Dissertation zur Erlangung des Doktorgrades
der Fakultät für Chemie und Pharmazie
der Ludwig-Maximilians-Universität München

Development and application of advanced single molecule fluorescence methods using PIE-MFD

Wolfgang Kügel

aus

München, Deutschland

2012

Bibliografische Information der Deutschen Nationalbibliothek
Die Deutsche Nationalbibliothek verzeichnet diese Publikation in der Deutschen Nationalbibliografie; detaillierte bibliografische Daten sind im Internet über
http://dnb.d-nb.de abrufbar.

ISBN 978-3-8439-0601-2

Erklärung
Diese Dissertation wurde im Sinne von § 7 der Promotionsordnung vom 28. November 2011 von Herrn Prof. Dr. Jens Michaelis betreut.

Eidesstattliche Versicherung
Diese Dissertation wurde eigenständig und ohne unerlaubte Hilfe erarbeitet.

München, den 01. August 2012

_____
(Wolfgang Kügel)

Dissertation eingereicht am: 26. Juni 2012
1. Gutachter: Prof. Dr. Jens Michaelis
2. Gutachter: Prof. Dr. Christoph Bräuchle
Mündliche Prüfung am: 17. Juli 2012

1. Auflage 2012

Abstract This thesis focuses on the development of new advanced techniques for multiparameter fluorescence detection (MFD) experiments and shows first applications to important biological problems. The main goal is to develop methods that yield reliable and precise single molecule FRET data to allow for a detailed insight into the shape and dynamics of biological complexes.

The first project focuses on the observation of intra-molecular dynamics. A new global approach to extract transition rates from fluorescence correlation spectroscopy (FCS) data is presented. Using this technique in combination with single-molecule burst analysis shows that the transition rates as well as the state distributions of double labeled DNA hairpins are influenced by the selected dye combination.

In a second project, single molecule burst analysis of multiparameter fluorescence detection (MFD) experiments is combined with the nano-positioning-system (NPS). NPS allows for the triangulation of unknown molecule parts in large biomolecules using a network of FRET based distance measurements. Till the experiments presented here an NPS analysis typically included experimental donor anisotropy, acceptor anisotropy and FRET efficiency data. Here, an additional utilization of experimental FRET anisotropy data is for the first time demonstrated to clearly improve the positioning accuracy.

To this end single-molecule burst analysis was applied and new methods based on the specific fluorescence properties of each individual burst were developed to allow for an unambiguous identification and separation of the desired population. Furthermore, a robust way to extract residual anisotropy data as well as a new graphics processing unit (GPU) based software implementation of the probability distribution analysis (PDA) is presented. This allows for a fast and reliable evaluation of FRET efficiency data.

The last part consists of three sub projects that are in general all based on the application of single molecule burst analysis to recent questions regarding the various pathways that control the accessibility of nucleosomal DNA in a cell. In this chapter, the active repositioning of nucleosomal DNA (remodeling) as well as changes in nucleosome stability caused either by chemical modifications of distinct residues or by the incorporation of alternatively spliced histones

are investigated.

First, a method to obtain information about the remodeling throughput from single molecule data is introduced. This technique is then applied to questions regarding the two ISWI ATPases present in human cells, namely Snf2H and Snf2L resulting in data that shows distinct differences between the two enzymes.

The second nucleosome project is focused on the alternatively spliced histone variant H2A.Z.2.2. The experiments presented show that incorporation of H2A.Z.2.2 into nucleosomes leads to a significant destabilization compared to nucleosomes carrying H2A.Z.2.1 or canonical H2A.

Finally, nucleosomes can also be chemically modified to alter their stability. Here, nucleosomes either methylated or acetylated on the lysine at position 64 of the H3 histone are investigated and compared to unmodified nucleosomes for differences in their stability.

Contents

Chapter 1

Introduction

All truths are easy to understand once they are discovered; the point is to discover them (Gallielo Gallilei).

This famous citation nicely describes the difficulty on the way to the current success of mankind which is based on our desire to understand the world around us.

Over the centuries knowledge was gained about all kinds of objects from the size of a single atom ($\sim 10^{-10}m$) to the dimension of galaxies ($\sim 10^{18}m$). In order to observe and manipulate this wide range of distances numerous techniques where developed. Despite these developments we are however still unable to defeat one of the probably biggest threats to human life, diseases.

Common to many diseases is a change in cellular processes, starting by accidental DNA errors which amongst others can cause cancer and ending with systematic cell reprogramming caused by viral infections.

Over the years more or less effective treatments for many known diseases have been developed. A huge number of these substances were developed in a trial and error manner and oftentimes till today nobody exactly understands all details of the pathways influenced.

Such understanding is in most cases already limited by our knowledge of the cellular processes themselves and not by a lack of will to study the effect of the respective compound.

To better understand cellular processes, standard bulk assays used in biology can allow for a first insight into the function of various proteins e.g knock out experiments can reveal which proteins are essential for a successful transcription and a change in the transcription rate of a gene can be detected by monitoring the respective mRNA concentrations. While bulk experiments provide good tools to monitor the average effect (in the above example altered transcription activity) the inherent averaging might oftentimes hide the individual steps involved.

In contrast, single molecule experiments provide a direct access to individual molecules and hence allow to overcome the averaging problem. There are basically two types of single molecule experiments characterized by the way the property of interest is detected (direct or indirect). Examples for techniques that allow for a direct measurement of single molecule properties are atomic force microscopy (AFM) or optical tweezers. Compared to that, indirect methods always require the attachment of a reporter system such as e.g. fluorescent dyes used for single molecule fluorescence.

The attachment of such dyes is necessary to allow for a detection of the molecule of interest and its properties. Unfortunately this modification by chemical compounds will always to some extent bias the bio-molecule under investigation. In this work a sample system related to the biologically relevant ribozymes, i.e. a single stranded DNA capable of forming a hairpin, was used to compare several dye pairs and to evaluate their effects on transition rates and state distributions on a single molecule level. In this context the choice of the dye molecule is shown to significantly influence the outcome of the experiment(chapter 4.2).

While the existence of flexible parts in bio-molecules is oftentimes essential for protein function such parts can hardly be resolved form x-ray crystallography data. This problem was addressed in recent years by using förster resonance energy transfer (FRET) to measure distances from known molecule parts to unknown positions. Combining several different distance measurements to one and the same point then allows for a triangulation of the unknown position in an analysis termed nano-positioning-system (NPS) [86].

In chapter 4.3 the parts of the RNA polymerase II (PolII) not resolvable by x-ray crystallography but previously estimated in NPS experiments were further refined using FRET anisotropy data obtained from multiparameter fluorescence detection (MFD) experiments. The increased resolution showed new features of the model system studied, namely the formation of hairpins on the non-template strand which could also be shown in control experiments. In addition a new PolII sample system not forming DNA hairpins was designed for further investigations and successfully tested.

Gene transcription by a polymerase is however by far not as easy as a polymerase walking along the DNA while transcribing it. There are numerous obstacles caused by the compaction of the DNA into chromatin fibers which is in a first step done by a wrapping around nucleosomes. Specialized enzymes, the so called chromatin remodeling factors (remodelers) rearrange these nucleosomes on the DNA and grant access to polymerases and other enzymes. Numerous remodelers exist oftentimes with only slightly different structure but strikingly different functions. While the biological function of many remodelers has been studied extensively over the recent years, till today, for some of them it is not even completely clear how they bind and whether they act as mono- or multi-mers. In order to address this lack of knowledge the two human ISWI ATPases SNF2H and SNF2L are compared and distinct differences are revealed in chapter 5.3.

While the transcription despite the chromatin structure is made possible by the described remodelers, nucleosomes also provide a variety of mechanisms to control gene activation and repression of which two are addressed in this work.

A well studied way to change nucleosome stability is the incorporation of non canonical histones such as H2A.Z. This histone has recently been found to be alternatively spliced in humans and the resulting H2A.Z.2.2 is demonstrated to significantly destabilize nucleosomes in chapter 5.4.

In addition methylation or acetylation of histones has been shown to influence gene activity but the actual effect of such a post translational modification strongly depends on the position it occurs. Here, the change of salt depended nucleosome stability upon methylation

or acetylation of a lysine in position 64 on histone H3 (H3K64me, H3K64ac) is studied in chapter 5.5. It is found that the strong nucleosome positioning sequence (widom 601) used to obtain a uniform sample is likely to superimpose any effect induced by these modifications.

To allow for such insights into the stability of complexes (chapter 5), inter- and intra-molecular dynamics (chapter 4.2) or even a reconstruction of molecule parts too flexible for x-ray chrystallography (chapter 4.3) several new tools had to be developed (chapter 4.1) and new techniques have been implemented (chapters 4.2.3, 4.3.4, 4.3.5, 4.3.6, 4.3.8, 5.2.7).

Chapter 2

Basics of fluorescence microscopy

Already in 1961 separate droplets containing fluorescent molecules could be detected [106]. It took however almost 15 years until the first fluorescently labeled single molecules were resolved [40]. At this time still many dyes (∼100) were attached to a single structure of interest to obtain a high enough brightness. First real single molecule detections in solid phase were reported in 1989 [81] followed already a year later by the first in single molecule experiments in solution [96]. From this stage of development again 6 years of development were necessary until the first successful single molecule FRET (smFRET) experiments were published [37]. Numerous reasons for this long period of development time can be given but always have to be seen as a whole. To measure smFRET the fluorescence signal from a donor and acceptor dye, attached to the complex under investigation had to be detected in two different spectrally distinct detection channels. To obtain this goal it was necessary to have access to FRET pairs with sufficiently high quantum yields as well detectors with high sensitivity in the corresponding wavelength and last but not least laser light sources of sufficient power at a wavelength compatible to the donor dye molecule.

Today, single molecule Förster resonance energy transfer (smFRET) is a powerful and widely used technique to study conformational dynamics of biological complexes [12] as well as transient structural properties [4] [86] [107] [115] (see also chapter 4.3). The following chapters will give a brief overview on the basic principles of fluorescence and fluorescence resonance energy transfer required to understand the experiments based on smFRET presented in this thesis. For an extensive overview see [64].

2.1 Fluorescence

The term Fluorescence describes the transition of a molecule from an excited state to the ground state by the emission of a photon. It was first mentioned by Sir John Frederic William Herschel in 1845 and the processes involved are typically summarized in a Jablonski diagram (see figure 2.1).

External energy such as a photon can excite a molecule from its electronic ground state S_0 to an excited state. This transfer usually does not occur directly to the lowest vibrational states but the vibrational ground states are reached by energy loss through collisions with other molecules on the timescale of $\sim 1ps$. The lowest excited S_1 state is then depopulated on the timescale of nanoseconds by various pathways.

A decay into higher vibrational states of the ground state S_0 occurs either by emission of a photon or by non radiative processes ($\sim 1 - 10ns$). These higher vibrational levels are then again depopulated by collisions with other molecules.

This simple description is already sufficient to explain the basic principles of fluorescence spectra. To this end however some approximations have to be made.

The Born-Oppenheimer approximation states that excited electrons have a small mass compared to the nuclei which means that the positions of the nuclei do not change throughout the electronic transition. This leads to different equilibrium positions of the nuclei at identical vibrational levels on different electronic states. Hence

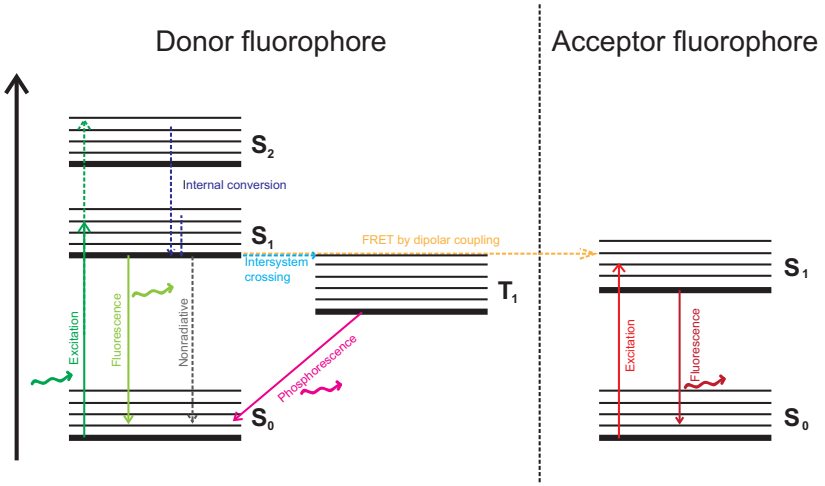

Figure 2.1: Jablonski Diagram. Two Fluorophores involved in a FRET experiment are marked as Donor (left) and Acceptor (right). The electronic ground state S_0, the excited states S_1 and S_2 as well as the tripplet state T_1 are depicted by big black lines, corresponding vibrational states are indicated by thinner lines. The excitation and de-excitation pathways are indicated by arrows.

according to the Franck-Condon principle an excitation to S_1 or S_2 usually does not occur to the vibrational ground state but to higher vibrational levels. As the vibrational states of S_0, S_1 and higher electronic states have a highly similar structure the emission spectra are approximately a mirror image of the excitation spectra of the respective fluorophore (Mirror image rule). In addition, since vibrational states are involved and their energy is lost by non-radiative internal conversion the absorption spectra will always be shifted towards higher energies as compared to the emission spectra (Stoke's shift). Finally, the emission of a photon to de-excite the S_1 state always occurs from the lowest vibrational level, and the emission spectra is therefore independent of the excitation wavelength (Kasha's rule).

These properties of fluorescence are the reason that single molecule fluorescence experiments in solution are possible since they allow for

a spectral separation of excitation and fluorescence.

In addition to the decay pathways described above the fluorophore can also enter a triplet state T_1 which is a spin forbidden transition that requires a change of the electron spin and takes place on the micro-second timescale. Since a relaxation from this triplet state requires another electron spin change it is slow compared to fluorescence and takes place on timescales ranging from milliseconds to hours.

The amount of photons emitted by a fluorophore relative to the amount of photons absorbed is commonly quantified by the so called quantum yield (QY). It is described by the rates of radiative k_r and non-radiative k_{nr} de-excitation:

$$QY = \frac{k_r}{k_r + k_{nr}}. \tag{2.1}$$

2.2 Fluorescence lifetime

Another important fluorescence property is the time a molecule spends in the S_1 state also refered to as fluorescence lifetime τ. In terms of the rates required to define the QY τ is given by

$$\tau = \frac{1}{k_r + k_{nr}} \tag{2.2}$$

It can be determined by measuring the time resolved probability to detect a photon at a timepoint t after a pulsed excitation (see chapter 3.2.4.6). This data can in the simplest case be described as an exponential decay of the photon flux $I(t)$.

$$I(t) \propto exp\left(-\frac{-t}{\tau}\right) \tag{2.3}$$

2.3 Förster resonance energy transfer

If a second dye with an absorption spectra that at least partly overlaps the first dyes emission spectra (figure 2.2) is located in close proximity

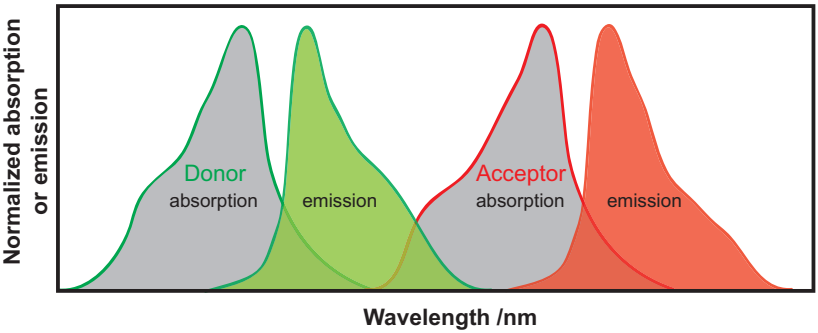

Figure 2.2: Exepmlary absorption and emission spectra. Sketched absorption (grey surface) and emission (colored surface) spektra of two dyes. Since the donor (green) emission and acceptor (red) absorpion partly overlap this dye pair is capable of showing FRET.

to an excited dye an alternative energy pathway called förster resonance energy transfer (FRET)[1] [26] exists. In the theoretical description of this process it is assumed that the fluorophores are infinitely small pointlike dipoles and the energy is transfered from the initially excited dye (donor) to the second dye (acceptor) via dipolar coupling of the electronic systems.

The process can also be sketched in a Jablonski diagram as shown in figure 2.1. The excited donor returns to its ground state by transferring its energy to an acceptor which in return is excited from the S_0 to the S_1 state. The excited acceptor can then itself return to the ground state by all the processes previously described for the donor.

According to [26] the energy transfer between two fluorophores can be described by a rate that is given as

$$k_{FRET} = \frac{1}{\tau_D}\left(\frac{R_0}{d}\right)^6 \tag{2.4}$$

where R_0 is a characteristic length scale for the respective system called Förster Radius, d is the distance of the two fluorophore dipoles

[1] sometimes also referred to as fluorescence resonance energy transfer

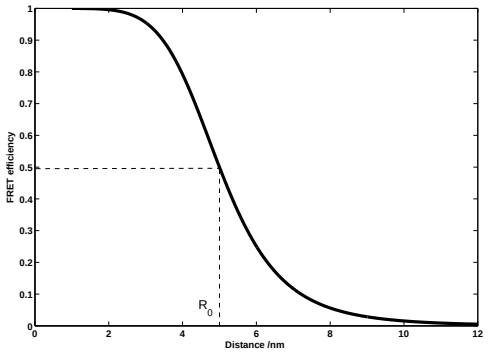

Figure 2.3: Simulated relation of FRET efficiency and distance. A simulation of the FRET efficiencies obtained for a donor-acceptor system with $R_0 = 5nm$ as a function of the dye-dye distance is shown.

and τ_D is the fluorescence lifetime of the donor dye. Based on this rate the FRET efficiency can be defined as the fraction of energy absorbed by the donor and transmitted to the acceptor

$$E = \frac{k_{FRET}}{k_{FRET} + k_r + k_{nr}} = \frac{1}{1 + (d/R_0)^6}. \tag{2.5}$$

Since the donor-acceptor distance appears in the sixth power in equation 2.5 the relation of E and d is highly nonlinear (see figure 2.3). If good distance resolution is required it is therefore essential to choose dye pairs with R_0 values approximately matching the expected distances (see chapter 4.3.3). It has to be noted here that measurements of dye pairs with FRET efficiencies close to 1 have to be handled with care since the FRET theory might not be sufficient for such constructs [62][63].

Using the above definition (equation 2.5) the FRET efficiency can directly be calculated from single molecule data either using fluorescence intensities (I)[2] or fluorescence lifetimes (τ) (equation 2.6)

[2]typically due to imperfect experimental setups correction factors have to be applied, see chapter 3.2.4.3

$$E = \frac{I_A}{I_A + I_D} = 1 - \frac{\tau_{D_A}}{\tau_{D_0}}. \tag{2.6}$$

In the above formula the fluorescence intensity of the acceptor after donor excitation is indicated by an A and the donor fluorescence is marked as D. For the fluorescence lifetimes τ_{D_A} describes the lifetime of the donor in presence of the acceptor and τ_{D_0} is the donor lifetime if no acceptor is present.

Using the wavelength in nm the Förster radius is given by

$$R_0^6 = 8.79 * 10^{-5} \frac{\text{Å } cm\ M}{nm^4} * \frac{\kappa^2\ QY_D\ J}{n^4\ N} \tag{2.7}$$

where n is the refractive index of the surrounding medium, N is the Avogadro number, QY_D is the quantum yield of the donor, J is the overlap integral of donor emission and acceptor absorption spectra in units of $M^{-1}cm^3nm^4$ and κ^2 is the orientation factor [64].

This orientation factor can be calculated for fixed relative dye orientations as

$$\kappa^2 = (cos\Psi_{DA} - 3cos\Theta_D\ cos\Theta_A)^2. \tag{2.8}$$

Here Ψ_{DA} describes the angle between the transition dipole moments of the respective dyes. The angle between the respective donor or acceptor fluorophores dipole moment and the line interconnecting the two dyes is given by Θ_D and Θ_A respectively (see figure 2.4).

To simplify calculations it is oftentimes assumed that both fluorophores rotate freely on timescales faster than the fluorescence lifetime of the donor in presence of the acceptor. This assumption causes the orientation effects to vanish and κ^2 becomes $2/3$. A Förster radius determined based on these assumptions is called isotropic Förster radius R_0^{iso}. If κ^2 is known it can be used to calculate R_0 by equation 2.9

$$R_0 = R_0^{iso} \sqrt[6]{\frac{3}{2}\kappa^2} \tag{2.9}$$

In this thesis $\kappa^2 = 2/3$ is assumed for precise FRET efficiency determination from data obtained in confocal single molecule exper-

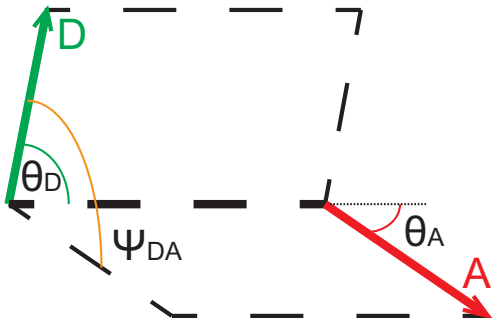

Figure 2.4: Relative orientations of two dyes. A pair of two FRET fluorophores is shown. The donor (D, green) and the acceptor (A, red) have a fixed orientation relative to each other. This orientation is described by the angle between the two dyes Ψ_{DA} and the angle of each dye to the line directly connecting the two fluorophores $\Theta_{D,A}$.

iments using probability distribution analysis (PDA). A detailed description of PDA and the custom implementation developed for this work can be found in chapter 4.1.2.

2.4 Fluorescence anisotropy

As just discussed the orientation of dyes is of fundamental importance for FRET experiments. Usually dyes attached to bio-molecules are not completely fixed but can change their orientation within certain boundaries. A measure for this orientational freedom is the anisotropy.

The anisotropy r can be defined by the fluorescence intensities parallel $I^{\parallel}$ and perpendicular to the excitation $I^{\perp}$ as

$$r = \frac{I^{\parallel} - I^{\perp}}{I^{\parallel} + 2I^{\perp}}. \tag{2.10}$$

If a MFD setup with pulsed excitation sources as used in this work is applied, anisotropy can also be measured as a function of time rela-

tive to the laser pulse (see chapter 3.2.4.5). In this case one commonly uses the term *time resolved anisotropy*.

Time resolved anisotropy data will always start at the value of the fundamental anisotropy r_0

$$r_0 = \frac{3cos^2\Psi - 1}{5}. \tag{2.11}$$

where Ψ is the angle between absorption and emission dipole, followed by a decay to a so called residual anisotropy r_∞. An r_∞ value of zero is approached if the fluorophore can rotate without any constraints. In contrast, fluorophores with rotational restrictions will show $r_\infty \neq 0$.

Such time resolved measurements are important since so called steady state anisotropy usually obtained in single molecule experiments is only a fluorescence intensity weighted average which strongly depends on the fluorescence lifetime. To better understand this issue assume two dyes with identical r_0 and r_∞ as well as an identical rotational decay time τ_{rot} but one with a long and one with a short fluorescence lifetime compared to τ_{rot}. Even though both dyes have identical rotational freedom the one with the lower lifetime will show a much higher steady state anisotropy than the one with the higher lifetime since its r_0 will contribute much stronger to the average.

For a FRET experiment in principle three different anisotropies can be determined which are the anisotropy of the donor, the anisotropy of the acceptor and the FRET anisotropy. Especially the latter anisotropy needs to be discussed in a bit more detail. In contrast to the anisotropy of a single dye where the absorption and emission dipoles of fluorophores are usually assumed to be nearly identical ($r_0 = 2/5$) for a FRET process these dipoles are not restricted in any way.

In the simplest case the relative orientation is fixed and under the assumption of a randomly oriented ensemble of FRET pairs with their transition dipole moments tilted by a constant angle Ψ_{DA} the FRET anisotropy can be calculated according to [17] as

$$r_{FRET} = \frac{2}{5}\frac{3cos^2\Psi_{DA} - 1}{2}.^3 \tag{2.12}$$

In reality the problem however becomes much more complicated as each of the dyes can rotate and hence the assumption of fixed relative orientations usually does not hold.

One of the ways to treat this problem is based on the assumption of a *dynamic orientational averaging* limit. For the precise FRET measurements presented in this work the model derived by [17] as implemented in the nano-positioning-system (NPS) analysis by [87] is used.

In brief: It is assumed that the *dynamic orientational averaging limit* is fulfilled, i.e. the reorientation of the dyes is fast compared to the energy transfer leading to a situation where the absorption and emission have different and independent transition dipole moments even though the relative dye positions are maintained. In this case the average $\langle \kappa^2 \rangle$ can be calculated based on the average axial depolarizations

$$\langle d^x_{D,A} \rangle = \sqrt{\frac{r_{D,A\ \infty}}{r_{D,A\ 0}}} \tag{2.13}$$

and

$$\langle d_{FRET} \rangle = \langle d^x_D \rangle \frac{1}{2}(3cos^2 \langle \Psi_{DA} \rangle - 1) \langle d^x_A \rangle = \frac{5}{2} \langle r_{FRET} \rangle \tag{2.14}$$

as

[3] according to this equation the upper and lower limits for the FRET anisotropy are equal to the boundaries for the donor and acceptor anisotropies $2/5$ and $-1/5$. r_{FRET} will become 0 when the transition dipole moments are tilted by the magic angle ($arccos(1/\sqrt{3}) \approx 54.7°$)

$$\begin{aligned}\left\langle \kappa^2 \right\rangle = (cos\,\langle \Psi_{DA} \rangle - 3cos\,\langle \Theta_A \rangle\, cos\,\langle \Theta_D \rangle)^2\, \langle d_A^x \rangle\, \langle d_D^x \rangle \\ +(1/3 + cos^2\,\langle \Theta_D \rangle\, \langle d_D^x \rangle)(1 - \langle d_A^x \rangle) \\ +(1/3 + cos^2\,\langle \Theta_A \rangle\, \langle d_A^x \rangle)(1 - \langle d_D^x \rangle).\end{aligned} \tag{2.15}$$

With this model the information contained in the FRET anisotropy can be used to calculate more precise distances from FRET experiments as theoretically shown in [85] and [87] and applied to experimental data in chapter 4.3.

Chapter 3

Experimental setup and methodology

3.1 Förster radius determination

The isotropic Förster radii (R_0^{iso}) were determined following the standard procedure by [130] as has been done previously in our lab described in detail by [2].

In brief, the *quantum yield (QY)* of the donor was determined in bulk experiments recording the emission (F900, Edinburgh Instruments) and absorption spectra (Cary 50, Varian) of the donor only sample as well as a separate reference dye. Additionally the absorption spectra of the acceptor were recorded (Cary 50, Varian) to determine the overlap integral. A summary of spectral ranges and reference dyes for the *QY* (table 3.1) and overlap integral (table 3.2) measurements is given below.

A slight modification of the initial protocol was made since for the PolII experiments presented in chapter 4.3 the percentage of bound RNA polymerase II (PolII) cannot be determined in bulk experiments and the amounts needed to apply a large enough excess of PolII to assume 100% binding could not be supplied. Hence these bulk measurements were performed using samples not containing RNA poly-

Table 3.1: Spectral ranges and reference dyes for the QY calculation.

Donor dye	reference dye [EtOH]	ref. QY [EtOH]	λ_{ex} $[nm]$	$\lambda_{min} - \lambda_{max}$ $[nm]$
Alexa555	Rhodamine 101	100%	550	555-700
Tamra	Rhodamine 101	100%	550	555-700
Atto520	Rhodamine 19	95%	515	520-700

Table 3.2: Spectral ranges and reference dyes for the overlap integral calculation. ϵ values from *www.genaxxon.com/docs/pdf/tamra_data.pdf*, *www.atto − tec.com*, *en.wikipedia.org/wiki/Alexa_Fluor*, March 2012. Detector nonlinearities were corrected for all spectra.

Dye	$\lambda_{ex}[nm]$	$\lambda_{min} - \lambda_{max}$ em. $[nm]$	$\lambda_{min} - \lambda_{max}$ abs. $[nm]$	ϵ $[cm^{-1}M^{-1}]$
Alexa555	525	528-700	400-700	150000
Tamra	525	528-700	400-700	95000
Atto520	515	520-700	400-700	110000
Alexa647	/	/	400-700	239000

merase II (PolII) and the measured QY did not necessarily represent the situation in the protein. To exclude false QY as a source for errors, the directly measured QY of the labeling positions furthest appart from the active center of the protein was assumed to be equal to that of the DNA only sample and were used as a basis to normalize the relative QY results obtained from gamma determination as explained in detail in chapter 4.3.7.

These corrected QYs, the donor emission spectra, the acceptor absorption spectra, a refractive index n = 1.3492 and κ^2=2/3 were then used in the freely available software PhotochemCAD to compute (R_0^{iso}).
(www.photochemcad.com, Version 2.1, 03.06.2009)

3.2 Multi parameter fluorescence detection

Single molecule FRET as well as fluorescence correlation spectroscopy (FCS) measurements were performed on a custom-built confocal microscope setup based on a Nikon TE300 (Nikon) inverted microscope. This section will give a detailed description of the confocal microscopy setup used to collect multiparameter fluorescence detection (MFD) data and the analysis techniques required to make use of the information detected. Techniques which required a custom implementation for this thesis are explained in detail while techniques where an already existing software could be used are only summarized in brief and a reference to the manuscript of the initial implementation is given for details. General techniques used for several projects are summarized in this section while more specific developments can be found associated to the respective projects as separate discussions in chapters 4 and 5.

3.2.1 Confocal microscopy

In a confocal microscope only one spot is illuminated by focused light and only light originating from that spot is detected using a point detector. Light from different planes is rejected by a (confocal) pinhole in the image plane of that spot. First experiments based on this technique were performed already in the 1950s when Marvin Minsky [80] patented his approach to obtain an image by scanning a sample through a confocal spot. While the fundamental arrangement has not changed since this first confocal microscope, consisting of a lamp, a lens and a pinhole, technical advances especially in the field of light sources (laser) and point detectors have increased the sensitivity of such setups to the single fluorescent molecule level.

The two most important parameters to describe a confocal setup are the lateral ($d_{r,FWHM}$) and axial ($d_{z,FWHM}$) dimensions of the observed volume. In the following only a short summary of the most important equations is given. A full discussion and the derivations of the below equations can be found in [91]. The lateral resolution is mainly determined by the refraction limit of the excitation volume

which can have a minimal lateral dimension of

$$d_{r,FWHM} = 0.51\frac{\lambda_{ex}}{NA}. \tag{3.1}$$

Here, NA is the numerical aperture defined as $NA = n * sin(\alpha)$ with α being the maximum collection angle of the objective and n being the refraction index of the immersion medium. Assuming an infinitely small pinhole and the water immersion objective used in this work (NA=1.2, n=1.33) one could theoretically achieve a minimum lateral expansion of

$$d_{r,FWHM} = 0.37\frac{\overline{\lambda}}{NA}. \tag{3.2}$$

Note that in this case the mean wavelength of excitation and emission $\overline{\lambda}$ has to be used.

As depicted in Eq: 3.1 and 3.2 a pinhole in the image plane of the laser focus does not have a huge effect on the lateral focal volume dimensions. It can however significantly improve the axial resolution. This is caused by the fact that a pinhole placed in the image plane can only be passed by light originating from the focal plane while light not originating from that plane will be blocked. However the axial resolution is usually at least by a factor of 2 lower than the lateral resolution.

Numerous equations describing the axial resolution can be derived [127]. They are however only valid for special cases. Hence only the simple equation 3.3 describing the axial resolution for the case that the pinhole size is larger than 1 Airy unit which is the distance between the maximum and the first intensity minimum in axial direction is given here as:

$$d_{z,FWHM} = \sqrt{\left(\frac{0.88 * \lambda_{em}}{n - \sqrt{n^2 - NA^2}}\right)^2 + \left(\frac{\sqrt{2} * n * PH}{NA}\right)^2}. \tag{3.3}$$

Here λ_{em} is the wavelength of the emitted light, n is the index of refraction, NA is the numerical aperture of the objective and PH

describes the pinhole diameter in μm.

3.2.2 Pulsed interleaved excitation (PIE)

While one can in principle use any light source for single molecule detection, more and more restrictions apply the more information one wants to gain throughout one measurement. For single molecule FRET experiments the excitation light should be monochromatic and far enough shifted to higher wavelengths that a possible direct excitation of the acceptor is minimized and a clear separation of donor fluorescence and laser light is possible. In order to gain additional information on the Stoichiometry of donor and acceptor labels on a sample one needs a second laser to directly excite the acceptor. If there is a possibility for FRET in the respective sample these two lasers have to be alternated to allow for a separation of donor and acceptor excitation. The duration of these laser pulses and the delay time becomes important as soon as lifetime information is required since every lifetime fit requires sound knowledge about the excitation timepoint of the individual molecule. This timepoint can only be known with sufficient precision if the laser pulse is significantly shorter than the fluorescence lifetime, allowing for an excitation of the dyes only in this short window. To this end pulsed interleaved excitation (PIE), a technique established by Barbara Müller et. al [84] fulfilling all of the above requirements was used for all smFRET experiments presented here.

The implementation of PIE used for this thesis was based on two lasers with wavelengths of 532 nm (frequency-doubled 1064 nm solid state, Pico-TA 530 Picoquant, Berlin, Germany) and 640 nm (LDH-D-C-640, Picoquant, Berlin, Germany) emitting short laserpulses ($\sim$300 ps) at a repetition rate of 26.66 MHz (see Figure 3.1). The lasers were triggered by a Multichannel Picosecond Diode Laser Driver "Sepia I" (Picoquant, Berlin, Germany) with a delaytime of the red laser of $\sim$15 ns also providing a sync pulse for the TCSPC cards (see chapter 3.2.3). The lasers were fibercoupled to singlemode fibers (Schäfter + Kirchhoff), combined using a wavelength division multiplexer (WDM-12P-111-532/647-3.5/125-PPP-50-3A3A3A-3-1,1,2, OZ

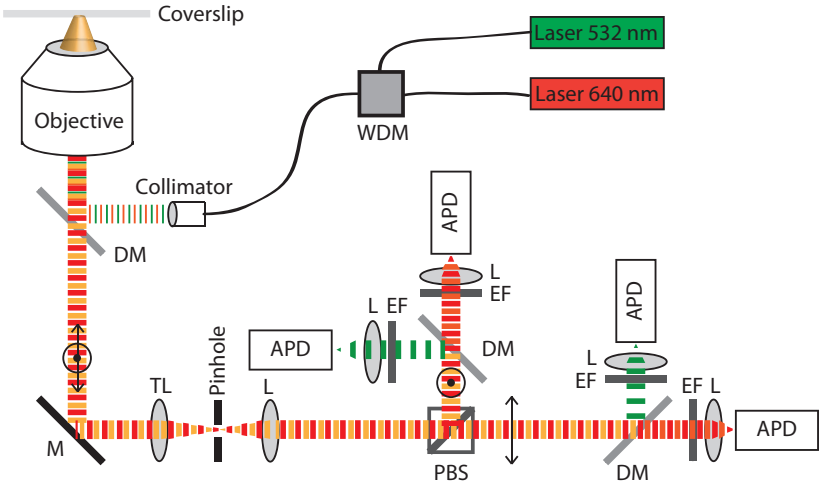

Figure 3.1: Schematic of the confocal setup. The lasers beams are merged using a Wavelength Division Multiplexer (WDM) and deflected into the objective by a Dichroic Mirror (DM). Fluorescence is reflected by a Mirror (M) onto a Tubus Lens (TL) and recollimated after the Pinhole by a Lens (L). Orthogonal polarizations are split by a Polarizing Beam Splitter (PBS) followed by a color separation based on Dichroic Mirrors. Emission Filters (EF) are cleaning the photon stream before focusing on an Avalanche Photo Diode (APD)

Optics) and collimated using a fiber collimator (60FC-4-RGB11-47, Schäfter + Kirchhoff). The linearly polarized light was finally cleaned up by a linear polarizer positioned directly after the fiber collimator and reflected into the objective (Nikon Plan Apo VC 60x 1.20WI) by a multiline dichroic mirror (DualLine z532/635, AHF Analysentechnik AG, München, Germany) .

3.2.3 Detection pathway

Assuming a one photon excitation as used throughout this work one can model the volume from which the fluorescent light is detected by the so called point spread function (PSF). This function can be

approximated by a three dimensional gaussian characterized by the lateral (ω_r) and axial (ω_z) distances from the center at which the detection efficiency has decreased to $1/e^2$.

$$PSF_{xyz} = \exp\left(\frac{-2(x^2+y^2)}{\omega_r} - \frac{2z^2}{\omega_z}\right) \tag{3.4}$$

Fluorescence from the PSF was collected by the same Nikon water immersion objective (Nikon Plan Apo VC 60x 1.20WI) and separated from the excitation beam by the same multiline dichroic mirror (DualLine z532/635, AHF Analysentechnik AG, München, Germany) described in chapter 3.2.2. The confocal volume was defined by focusing onto a d = 50 μm pinhole using a f = 200 mm focal-length lens. In order to gain information on color as well as rotational freedom and orientation of the molecules, fluorescence was split by polarization (PBS3, Thorlabs) and color (laser beam-splitter 640DCXR, AHF Analysetechnik AG, München, Germany) and cleaned up by a set of filters (green detection channels: Brightline HC582/75 ; red detection channels: ET700/75, AHF Analysetechnik AG, München, Germany). Four single photon counting avalanche photodiodes (green channel AQR-14, red channel AQR-16, PerkinElmer) were used for fluorescence detection and connected to four single-photon-counting modules (Becker&Hickl SPC-154) (see Figure 3.1). The photon acquisition in all 4 cards was triggered simultaneously by an external trigger (USB-6008, National Instruments) and data was recorded using a software provided by Becker&Hickl. For each TCSPC module the arrival time of a photon relative to the sync pulse (provided by the Sepia I, see chapter 3.2.2) is recorded (microtime) together with the number of sync pulses since the last photon in the respective channel (macrotime). The microtime information can be used to further subdivide the red parallel and perpendicular channels in red detection after red excitation (RR) and red detection after green excitation (GR). Together with the parallel and perpendicular green detection after green excitation (GG) channels this results in a total of 6 independent photon streams available for data analysis (RR$\parallel$, RR$\perp$, GR$\parallel$, GR$\perp$, GG$\parallel$ and GG$\perp$) as exemplarily depicted in Figure 3.2.

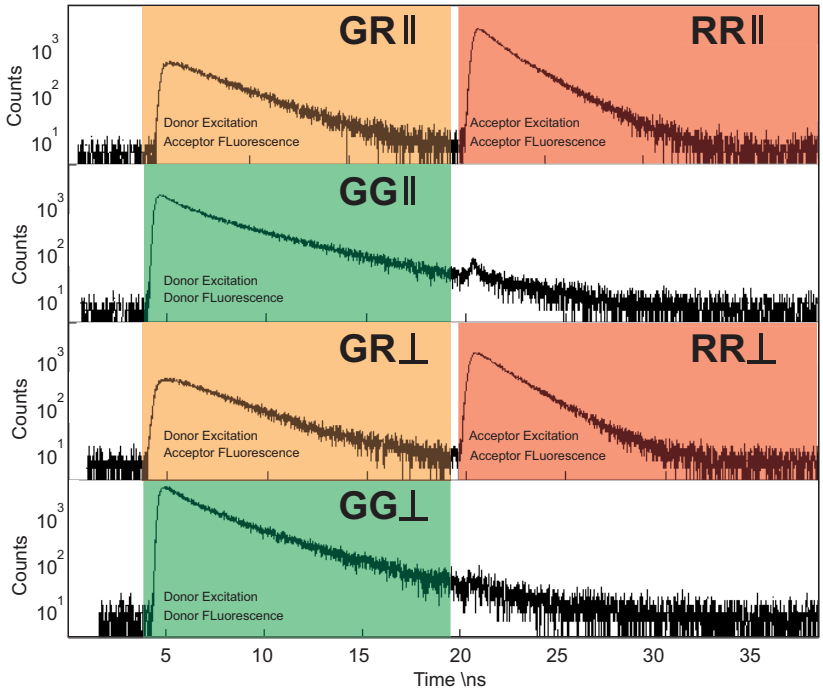

Figure 3.2: Pulsed interleaved excitation. A schematic microtime histogram for the four detection channels is shown with an overlay of the microtime ranges used to differentiate green detection after green excitation (GG), red detection after green excitation (GR) and red detection after red excitation (RR). The upper two panels show photons parallel to the excitation while the lower two panels arise from perpendicular photons.

3.2.4 Data analysis

In this work, confocal microscopy is not used to raster an image but to detect parameters such as the FRET efficiency, stoichiometry, fluorescence lifetime and anisotropy of freely diffusing molecules. Since these molecules only reside a very short period of time inside the focal volume ($\sim$0.5-5 *ms*) the number of photons detected per molecule (typically $\sim$50-500 photons) and channel (typically $\sim$0-300 photons) is rather low and hence the detection of single molecule events and calculation of the desired parameters is not in all cases straight forward. All data analysis described here is done using MATLAB and custom build software developed in our lab. This section will give an overview on burst search algorithms and the tools as well as corrections required to calculate the parameters of interest with high accuracy.

3.2.4.1 Burst search

Currently there are three widely used algorithms for burst detection [113]. They all rely on the overall photon stream independent of the channel the photons were detected.

The most straight forward approach is to divide the total photon stream into time bins with a length T. All photons in a time bin are summed up and bursts are selected by requiring a minimum number of photons. The amount of information can be maximized by applying a lower threshold to bins next to detected bursts, hence reducing the possible loss of data by partially filled bins [84].

Another method has been suggested by Enderlein et. al. [23] applying a *Lee Filter* to smooth the data followed by a threshold of the inter photon times.

For this work, photon bursts were selected using an all-photons burst search (APBS) [90]. This method applies a sliding window of fixed duration T (instead of simply binning the whole data trace) and requires a minimum number of M photons in a time window to be detected as part of a burst. Additionally a minimum total number of L photons in all windows consecutively detected within a burst is required.

Depending on the sample (dye brightness, diffusion constant of the protein or DNA and background) values for M (5-50 photons), T (0.2-5 ms) and L (>30 Photons) where optimized for the individual experiments presented here and are depicted in the corresponding methods section.

Each burst consists of a number of photons which have three properties: macrotime, microtime, and channel. This information can be used to calculate various parameters of which the most important ones will be explained in the following.

3.2.4.2 FRET efficiency

Probably the most commonly used property of double labeled sample molecules is the *FRET efficiency (E)* since it can be related to the dye-dye distance (refer to chapter 2.3). To calculate E from MFD data usually the photons detected in the parallel and perpendicular channels of each color are summed up to obtain a total signal (see chapter 4.3.8 for limitations of this approach)

$$S_{xy} = S_{xy}^{\parallel} + S_{xy}^{\perp}. \tag{3.5}$$

yielding the donor (S_{GG}), acceptor (S_{RR}), and FRET (S_{GR}) photons. Including corrections for spectral crosstalk (cr), direct excitation of the acceptor (de) and the different detection efficiencies in the red and green channel γ (see chapter 3.2.4.3 for details) the FRET efficiency of each burst can be calculated according to Eq: 3.6 [65]

$$E = \frac{S_{GR} - cr * S_{GG} - de * S_{RR}}{S_{GR} - cr * S_{GG} - de * S_{RR} + \gamma * S_{GG}}. \tag{3.6}$$

For some applications in this work also the uncorrected FRET efficiency, referred to as *proximity ratio* ϵ

$$\epsilon = \frac{S_{GR}}{S_{GR} + S_{GG}} \tag{3.7}$$

is calculated (see chapters 4.3.6 and 4.2.4.1).

3.2.4.3 Correction factors

A number of correction factors are required to calculate the variables of interest as accurate as possible.

The γ factor: The probably most important correction factor in FRET experiments is the γ factor. It corrects for the different QY of the donor (Θ_D) and acceptor (Θ_A) as well as the different detection efficiencies (η_{DA}) of the respective colors

$$\gamma = \frac{\eta_A * \Theta_A}{\eta_D * \Theta_D}. \tag{3.8}$$

An easy method to determine the γ factor has been developed by Kapanidis et. al. [53]. It is assumed that for a given dye combination and protein but different labeling positions the QY of the dyes stay constant. Under these assumptions if the correct γ factor is used the *stoichiometry (Sto)* should be identical for all molecules independent of their FRET efficiency (i.e. in a two dimensional histogram E and Sto should be uncorrelated). Hence by measuring a high- and a low-FRET sample one can adjust the γ factor until a minimal correlation of E and Sto is reached (see figure 3.3B-C).

A more reliable way to determine a gamma factor in cases where the assumption of constant QY is proven to be wrong can be found in chapter 4.3.7.

The spectral crosstalk (cr): Filters and dyes are limited by chemical and physical properties causing some imperfections in the spectral separation of the channels which have to be accounted for.

To this end the cr is defined as the fraction of photons emitted by the donor but - due to incomplete spectral separation - detected in the acceptor channel. It can be determined by measuring a donor only sample and determining the photons detected after donor excitation in both channels

$$cr = \frac{GR_{D\_only}}{GG_{D\_only}}. \tag{3.9}$$

For FRET experiments this calibration was additionally verified for the actual sample since each sample measured contained at least 10% donor only labeled molecules and therefore *cr* could be determined on the fly[1].

The direct excitation of the acceptor (de): Another error source when performing FRET measurements is caused by the limited spectral separation of the dye excitation spectra (see chapter 4.3.3). The requirement to have a sufficiently high spectral overlap of donor emission and acceptor absorption can in some cases lead to a *direct excitation of the acceptor (de)* by the donor laser. It is however possible to implement corrections for this effect as shown for the calculation of the FRET Efficiency (chapter 3.2.4.2) and Stoichiometry (chapter 3.2.4.4). In a PIE experiment the *de* can be defined as

$$de = \frac{GR_{\text{A\_only}}}{RR_{\text{A\_only}}} \tag{3.10}$$

and determined by measuring an acceptor only (*A_only*) sample (or the acceptor only population of a burst experiment). Since this effect is small it is easily biased by scattered light originating directly from the donor laser which is however also intrinsically accounted for in the *cr* correction. One possibility to account for this issue is to determine the spectral crosstalk of a buffer only sample which can then be used as weight for the subtraction of the correct amount of scattered photons throughout the *de* calibration, Eq: 3.11

$$de = \frac{GR_{\text{A\_only}} - \left(\frac{GR_{\text{Buffer}}}{GG_{\text{Buffer}}} * GG_{\text{A\_only}}\right)}{RR_{\text{A\_only}}}. \tag{3.11}$$

Please note that the definition of *de* involves two different excitation lasers and hence the calibration of this factor has to be done using the same laser powers as in the actual experiment. Typical values for *de* in this work range from 0% to 5%.

[1]The above description is equal to requiring that $E_{D\_only} = 0$ for a correct *cr*

The β factor: The β correction factor is required to allow for the accurate calculation of anisotropies (see chapter 3.2.4.5). It corrects for the different detection efficiencies of the parallel and perpendicular channels and is defined as

$$\beta_{\mathrm{xy}} = \frac{\eta_{xy}^{\perp}}{\eta_{xy}^{\parallel}}. \tag{3.12}$$

It can be determined by measuring a fast rotating molecule such as a free dye with preferably high lifetime and requiring that the residual anisotropy quickly decays to 0 within the first few *ns*. In this work it was determined using Atto532 or Atto520 for the donor channel and Atto647N for the acceptor channel. The β factor was iteratively optimized till r_{∞}=0 (see chapter 3.2.4.5). Typical β values were β_{GG} = 1.075 and β_{RR} = 1.325. Since the same detection pathways are used and the orientation of the linearly polarized light is identical for the two colors $\beta_{\mathrm{GR}} = \beta_{\mathrm{RR}}$. Please note that the β factor was slightly depended on the calibration of the setup and varied for the individual experiments in a range of +-0.025 based on the values given here.

Microscope depolarization: The factors $l_1 = 0.0308$ and $l_2 = 0.0368$ are pre-determined factors used to correct for the microscope's depolarization [59].

3.2.4.4 Stoichiometry

When FRET samples are measured, single molecule bursts containing double labeled molecules can be separated from background events using a Stoichiometry threshold depending on the respective dye pair. To this end the *stoichiometry (Sto)* of green and red dyes in each burst has to be calculated Eq: 3.13 [53]

$$Sto = \frac{\gamma * S_{\mathrm{GG}} + S_{\mathrm{GR}} - cr * S_{\mathrm{GG}} - de * S_{\mathrm{RR}}}{\gamma * S_{\mathrm{GG}} + S_{\mathrm{GR}} - cr * S_{\mathrm{GG}} - de * S_{\mathrm{RR}} + S_{\mathrm{RR}}}. \tag{3.13}$$

Based on Eq: 3.13 donor only molecules will show *Sto* = 1, acceptor

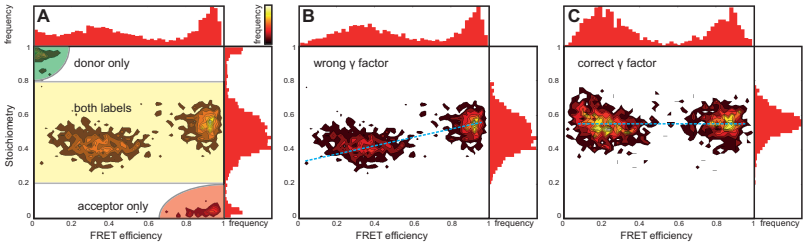

Figure 3.3: Two dimensional stoichiometry-FRET efficiency histogram: A sample containing two dsDNA species with different dye-dye distances (one showing high FRET and one low FRET) was measured (see chapter 4.1.2.4 for details). In addition the sample contained donor (Sto∼1) and acceptor only (Sto∼0) impurities (A). After removing these impurities by a Sto threshold (B), the γ factor can be corrected by minimizing the correlation between FRET efficiency and Stoichiometry (C).

only molecules will have $Sto = 0$ and double labeled molecules will be somewhere in between (see figure 3.3A). The actual value of the double labeled molecules is determined by the QY, detection efficiencies and laser powers of the respective channels. Hence by applying an appropriate lower and upper threshold the molecules of interest can be separated.

Additionally the Sto can be used to estimate the gamma factor as described in the previous section (chapter 3.2.4.3) and exemplarily depicted in figure 3.3B-C.

3.2.4.5 Anisotropy calculation

The lifetime weighted anisotropies, r (see chapter 2.4) can be calculated for each burst using Eq: 3.14

$$r_{xy} = \frac{\beta_{\mathrm{xy}} S^{\parallel}{}_{\mathrm{xy}} - S^{\perp}{}_{\mathrm{xy}}}{(1 - 3l_2)\beta S^{\parallel}{}_{\mathrm{xy}} + (2 - 3l_1) S^{\perp}{}_{\mathrm{xy}}} \tag{3.14}$$

where the index xy depicts the respective channel (GG, GR or RR) and β_{xy}, l_1 and l_2 are correction factors correcting for the different detection efficiencies (β) of the parallel and perpendicular channels

as well as the microscope objective depolarization [59].

Time resolved anisotropies were calculated throughout several of the experiments described in the following in order to extract the non-lifetime biased residual anisotropy (r_∞). To this end the burst subpopulation of interest was selected and the corresponding photons were exported for further calculations (see chapter 4.1.1). Out of these photon streams a microtime histogram was built for each channel and an anisotropy value was calculated for each timebin of the microtime histograms[2] Eq: 3.15

$$r_{xy}(\tau) = \frac{\beta_{xy} S^{\parallel}{}_{xy}(\tau) - S^{\perp}{}_{xy}(\tau)}{(1-3l_2)\beta S^{\parallel}{}_{xy}(\tau) + (2-3l_1) S^{\perp}{}_{xy}(\tau)}. \tag{3.15}$$

Since the electric wiring of the detection path will never be exactly identical for two TCSPC channels the microtimes were shifted by an offset value till the rising flank of the two polarization histograms matched at half maximum as good as possible.

From this time-resolved anisotropy $r_{xy}(\tau)$ the r_∞ value was extracted by calculating the weighted mean from that timepoint at which no decay of $r_{xy}(\tau)$ could be fit anymore. This method assumes that in contrast to the fast rotating dye, the labeled molecules under investigation in the respective chapter have rotational correlation times significantly higher than the observed 10-15 *ns*. Therefore after a short time period in which the rotation of the dye itself occurs (2-4 *ns*) the remaining 6-13 *ns* will appear quasi static in terms of the rotation of the labeled molecule. The data filtering necessary prior to the calculation was individually developed for each project and will be described in the respective methods sections.

3.2.4.6 Lifetime fit and implementation

The microtime (i.e. the relative arrival time of the photons after a syncpulse, see chapter 3.2.3) contains information about the fluorescence lifetime. This microtime is recorded for every photon with a

[2]For the experiments presented here the microtime histograms consisted of 4096 bins covering a total of 37.5 ns. for more details see chapter 3.2.4.6.

resolution of 4096 bins spanning a timerange from sync pulse to sync pulse of 37.5 *ns* (∼10 *ps* time resolution). In order to extract the lifetime information one has to fit a model function, usually a single exponential decay. If many photons are recorded (e.g. in an ensemble measurement) the bins are sufficiently populated and can be easily fit using a least squares algorithm. In contrast for burst analysis experiments with only 10-200 total photons per channel most of the bins will be empty and hence a more complicated approach has to be used. To this end a maximum likelihood estimator (MLE) was applied which is explained in full detail in [111] [60].

In brief, only a single exponential decay is assumed for the fluorescence intensity since information contained in a single burst is too low (i.e. there are not enough photons) to allow for a robust multi exponential description. The time-dependent model of the signal $M(\tau)$ is defined as the sum of the fluorescent component $F(\tau)$ and the background signal from scattered light $B(\tau)$ (Eq. 3.16)

$$M(\tau) = (1 - \alpha)F(\tau) + \alpha B(\tau). \tag{3.16}$$

The overall contributions of these two signals are determined by a proportionality factor α. $F(\tau)$ is constructed by a convolution of the single exponential decay and the predetermined instrument response function (IRF), obtained from the scattered light of a water only sample.

The comparison of data and model is done using the likelihood function Eq. 3.17

$$L(S|M(x)) = \prod_{i=1}^{k} \omega(S_i|M_i(x)). \tag{3.17}$$

Here, x is the set of model parameters for M, S is the experimental decay histogram and ω is the probability to detect S_i photons in the ith out of k TCSPC channels. Throughout the fit the normalized fit quality parameter $2I^*$ is minimized Eq. 3.18

$$2I^* = -2\frac{L(S|M(x))}{k - \zeta - 1} \tag{3.18}$$

where ζ is the number of model parameters. This fit quality parameter is basically comparing the likelihood function $L(S|M(x))$ to the likelihood $L(S|S) = 1$. A derivation of the $2I^*$ equation for a MFD setup was done by [60] resulting in Eq. 3.19

$$2I^* = \frac{2}{k-\zeta-1}\left[\left(S^{\parallel} ln\frac{S^{\parallel}}{M^{\parallel}} + S^{\perp} ln\frac{S^{\perp}}{M^{\perp}}\right) + \sum_i S_i^{\parallel} ln\frac{S_i^{\parallel}}{M_i^{\parallel}} \sum_i S_i^{\perp} ln\frac{S_i^{\perp}}{M_i^{\perp}}\right]. \tag{3.19}$$

The custom written fit algorithm used in this work calculates 10 values of the $2I^*$ parameter on an evenly spaced grid ranging from 0 to 9 *ns* which is a sufficient range for all dyes in use. The two datapoints next to the one with the lowest $2I^*$ are set as new outer boundaries and 10 new evenly spaced $2I^*$ values are calculated. This is iteratively done until the difference of the boundaries reaches 10 *ps*. At this stage the point with the lowest $2I^*$ is taken as result.

In order to speed up the lifetime determination of huge measurements where a lifetime fit has to be performed for up to 1 million molecules some optimizations have been applied.

First, since only few photons are sorted to a huge amount of channels (k=4096) this binning has been reduced to k=256 channels, reducing the amount of data to be processed.

Second the background share α was set to a fixed value of 0% which is close to the actual value throughout the high countrates of a burst to avoid an additional fit parameter.

Third, instead of Eq. 3.19, the less computationally expensive Eq. 3.20 by [111]

$$2I^* = \frac{2}{k-\zeta-1}\sum_i S_i ln\frac{S_i}{M_i}. \tag{3.20}$$

was used for the $2I^*$ calculation. Since this equation does not include corrections for anisotropy related effects occurring in an MFD experiment (i.e. different decays in parallel and perpendicular channels due to the polarized excitation) the signal had to be preprocessed prior to the lifetime fit. To this end the total fluorescence signal of

each channel $S_{xy,i}$ (xy = GG, RR or GR) was calculated including corrections for different detection effieciencies (β) and microscope objective depolarization ($l_{1,2}$ see chapter 3.2.4.3) which however has to be done only once prior to the fit iterations

$$S_{xy,i} = (1 - 3l_2)\beta S^{\parallel}_{xy,i} + (2 - 3l_1)S^{\perp}_{xy,i}. \tag{3.21}$$

Since out of the two polarizations perpendicular to the excitation polarization only one can be detected, equation 3.21 counts perpendicular photons $S^{\parallel}$ twice compared to the parallel photons $S^{\perp}$ hence removing possible artifacts from high anisotropy molecules.

Results obtained using this simplification are comparable to the ones obtained using Eq: 3.19 and including α as a free fit parameter (see chapter 4.3.5, Table 4.10) but can be calculated significantly faster. Since only a slight loss in precision and no differences for the separation of populations could be detected for the simplified method it is used throughout this work if not stated otherwise.

3.3 Fluorescence correlation spectroscopy

The technique fluorescence correlation spectroscopy (FCS) was first introduced by Magde et. al in the early 1970s [74] [73].

FCS experiments are performed at significantly higher concentrations than burst analysis experiments. Concentrations are usually chosen such that on average 2-10 molecules are inside of the focal volume which leads to a relatively constant average count rate. In FCS the fluctuations of the fluorescence signal are directly related to properties of fluorescent molecules diffusing through the focal volume. It allows access to the number of particles in the focal volume (N), the diffusion coefficient (D), photophysics, to inter molecular interactions and as demonstrated in chapter 4.2 intra molecular dynamics.

3.3.1 Theory and implementation

A correlation is a mathematical measure for the similarity of two signals and the correlation function of a fluorescence signal can be

thought of as a representation to detect a photon at the time $t + \tau$ if a photon has been detected at the time t. If the two signals S are identical this correlation of a signal over time with itself is called auto-correlation. It is defined as

$$G(\tau) = \frac{\langle \delta S(t) \delta S(t+\tau) \rangle}{\langle S(t) \rangle^2} \tag{3.22}$$

where $\delta S(t) = S(t) - \langle S(t) \rangle$ is quantifying the fluctuations by calculating the difference of the signal S at timepoint t and the average intensity.

If one calculates the correlation of two distinct signals the resulting function is called cross-correlation and Eq. 3.22 changes to

$$G(\tau)_{XX*YY} = \frac{\langle \delta S_{XX}(t) \delta S_{YY}(t+\tau) \rangle}{\langle S_{XX}(t) \rangle \langle S_{YY}(t) \rangle}. \tag{3.23}$$

Photon-arrival-time correlations were computed using a fast correlation algorithm [131] implemented into our software Pie Analysis in MatLab (PAM) PIE Analysis with MatLab (PAM, by M.Höller, M. Sikor and W. Kügel) and described in detail in [41]. FCS error bars were determined by segmenting the total measurement time for a dataset into eight parts, performing independent correlations for each of these segments and calculating the mean and the standard error.

Based on the assumption of a point spread function (PSF) given by a three dimensional gaussian (see Eq. 3.4) a general model to describe the contributions of the correlation function arising from diffusion can be derived (see Eq. 4.7, [46]). Additional models for intramolecular dynamics (Eq. 4.8, 4.9 and 4.10, [125]) and triplet kinetics (Eq. 4.11, [134]) have also been published and are discussed in chapter 4.2. A detailed summary of derivations for diffusion and triplet correlation functions can be found in [41].

3.3.2 Limitations and experimental considerations

Even though FCS itself is not limited with regard to processes occurring on extremely short timescales (e.g. rotational diffusion $\sim 10^{-7} - 10^{-9}$ s or antibunching $<10^{-9}$ s) such measurements are in

most cases limited by the capabilities of the equipment used for data acquisition. While the laser repetition rate is defining the lowest accessible time range which can be easily circumvented by using a cw-laser, in most cases especially the detectors are limiting.

On the one hand an effect called after-pulsing causes an increased probability of a dark count for a few hundreds of nanoseconds after a photon is detected and with that a detector dependent correlation on this timescale is introduced.

Additionally typical dead times of APDs are on the range of 100 *ns* which means that after a photon has been detected it is impossible to detect another photon within this time. Since no signal is detected the correlation will drop to zero resulting in a strong anti correlation that hides any fluctuation faster than the dead time. The most commonly used approach to overcome such issues is to either implement a 50:50 beam-splitter or as in this work a polarizing beam-splitter (PBS) and cross-correlate the signals of the two detectors. In this case only the fluctuations of the fluorescence signal will be detected as instrument effects of two independent detectors are uncorrelated.

If the polarization splitting is used the resulting cross correlation function will additionally allow for a determination of the molecules rotational correlation time.

Since rotational correlations encoded in the polarization were not of interest for the FCS experiments presented in this work and the processes investigated are sufficiently slow that no interference with the detector effects has to be expected the recorded photon streams of one color but different polarization were merged. Photons in the acceptor channel were further split into two channels according to their arrival times, that is, after the 640 *nm* laser pulse RR or after the 532 *nm* laser pulse GR as explained in chapter 3.2.3. Correlations between photons streams are from here on abbreviated as green autocorrelation (GGxGG) FRET green cross correlation (GRxGG) FRET autocorrelation (GRxGR) red autocorrelation (RRxRR).

3.4 Bayesian data analysis

To determine structural properties from smFRET data numerous uncertainties have to be accounted for which in case of the NPS is done by applying Bayesian data analysis. Since a good and extensive introduction into Bayesian data analysis can be found in [116] and the application to the problem of position estimation from FRET data is explained in detail in [87] only a short description of Bayes' theorem [7] is given here:

In Bayesian data analysis, the information about the expected data given a model of the physical process is encoded in the likelihood, p(d| Θ,I). This probability density connects the measured data, d, with the parameters, Θ, that quantify the model. The so-called background information, I, summarizes all information available to the experimenter (such as FRET theory, photon counting statistics, anisotropy etc.). The state of information of the experimenter before the experiment was performed, p(Θ |I), is called prior. It contains all knowledge about the model parameters, for instance constraints imposed by physical laws or information from previous measurements.

The information contained in the data can be combined with the prior information by using Bayes' theorem (equation 3.24) [47][116].

$$p(\Theta \mid d, I) \propto p(d \mid \Theta, I)\, p(\Theta \mid I) \tag{3.24}$$

Here, the probability density $p(\Theta \mid d, I)$ denotes the updated information after data analysis and is called posterior.

It is worth to note here that Bayesian inference does not rely on the optimization and local approximation of an objective function. Furthermore, it allows to directly include "prior information" in the analysis, for example the result of calibration experiments, simplifying error propagation.

3.5 Nested sampling

The following description is based on [87] and parts of it have been previously published in [61].

When Bayesian inference (see chapter 3.4) is used and the model is described by many parameters, it is oftentimes infeasible to evaluate the posterior probability density systematically (for example, on an evenly spaced grid) to account for every combination of model parameter values. In most cases, the computed densities would be close to zero, indicating that the particular values of the model parameters are very unlikely. Instead, one chooses to represent the posterior by a large-enough set of samples in the parameter space drawn from the posterior distribution, that is occurring with the posterior probability. To generarte such sample sets for bayesian data analysis of problems in moderate- and high-dimensional parameter spaces oftentimes advanced numerical tools are required.

In this work nested sampling [117], an algorithm that searches the region of the parameter space that contains the major part of the posterior probability, was applied[3]. This numerical approach for Bayesian analysis was used until recently, mainly in astrophysics, but has also been applied to the localization of unknown molecule parts [85], instrument noise evaluation [76], and model selection [11].

A full description of the nested sampling algorithm is beyond the scope of this work, hence only a brief summary of the essential knowledge required to understand the results presented later on is given here. For a full description of the algorithm and its implementation please refer to [87].

3.5.1 Background

Nested sampling starts with an initial set of samples randomly drawn prom the prior. Out of these samples the one with the lowest likelihood L_1 is continuously saved and replaced with a new sample drawn from the prior and required to have a new likelihood L_2 higher than the replaced one ($L_2 > L_1$). Following this procedure the algorithm compresses the samples in areas with high likelihoods.

Each of the samples is attributed to a weight w given by

$$w_i = L_i * (\xi_{i-1} - \xi_i) \tag{3.25}$$

[3]The algorithm used throughout this thesis was developed by Adam Muschielok

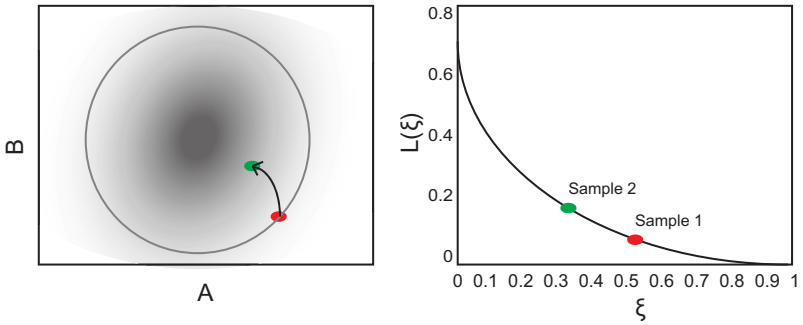

Figure 3.4: Schematic of an improvement in the parameter space (left, *A*,*B*) and in the corresponding sorted likelihood function $L(\xi)$ (right). The arrow indicates the generation of a new sample (Sample 2) replacing the old sample (Sample 1) within the new constraints (grey circle). Adapted from [87].

where L_i is the likelihood of the ith sample and ξ is the position of the sample in the sorted prior volume (see figure 3.4). Basically this formula leads to a situation where in the beginning of a sampling run the weights of the samples will be low since the low likelihood of the replaced samples is dominating the weight (figure 3.5, sample weight). After a while the likelihood will increase and the volume of the sorted prior volume excluded by replacing this sample ($\xi_{i-1} - \xi_i$) is also still sufficiently high to yield high weights (figure 3.5, sample weight, peak). At the end of the sampling the weights will be low again even though the likelihood is high since now the weight is dominated by the low volume exclusion. Please note that the precise position of the samples on the ξ axis can only be estimated. A description of how this estimation is done in the algorithm applied in this work can be found in [87].

Since nested sampling produces samples with varying weight [117] (figure 3.5), a subset of samples is chosen by drawing from this set of samples, with a probability proportional to the sample weight under the constraint that each sample can only be drawn once [116]. All samples obtained in this way possess equal weights and are therefore called equally weighted samples. These samples are used to repre-

sent the posterior in scatter plots, histograms and to compute NPS volumes.

3.5.2 Implementation

The custom implementation of the nested sampling algorithm used in this work is based on Metropolis Markov chain Monte Carlo written in MATLAB (The MathWorks) and C. The algorithm was originally developed to compute the position of unknown domains in macromolecular complexes in an analysis termed nano-positioning-system (NPS) [85], see chapters 3.6 and 4.3. In this work it is additionally applied to extract kinetic information from FCS experiments (chapter 4.2)[4].

3.6 Nano positioning system (NPS)

The nano-positioning-system (NPS) is a technique developed in the Michaelis lab [86] [85] [87] that uses FRET to determine the position of unknown molecule parts.

To this end positions known from crystal structures are labeled with one dye referred to as satellite in analogy to the GPS system. The unknown position is labeled with a FRET partner of this first dye called antenna. Measuring several satellite-antenna distances then allows for a triangulation of the unknown position. A full description of the NPS can be found in [87] and only a brief summary of the steps involved is given below:

The transformation of FRET efficiencies to actual distances involves several parameters which have to be determined. The most important one is the isotropic förster radius R_0^{iso} (chapter 3.1). Since R_0^{iso} assumes a free reorientation of the dye which is not the case for a protein or DNA bound dye molecule the restricted rotational freedom has to be included in the model. This was initially done by using not one fixed förster radius but a distribution obtained by a MonteCarlo

[4]The C++ code of the corresponding likelihood function can be found in the Appendix figures A.9-A.12

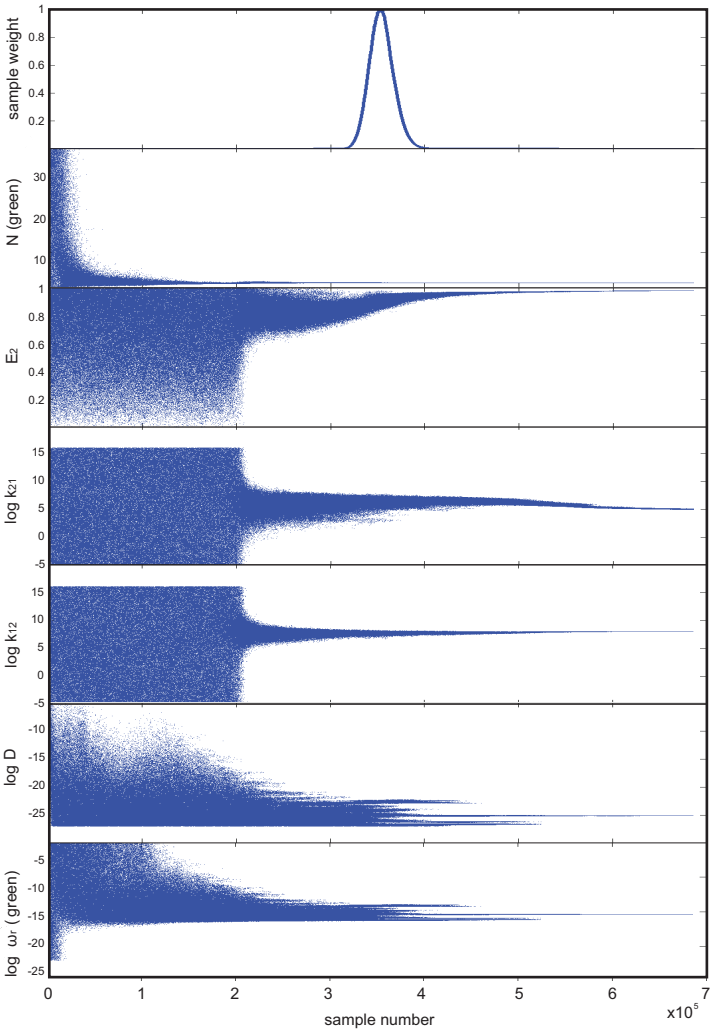

Figure 3.5: Exemplary sampling trace of the time-evolution of the Nested Sampling analysis algorithm. Displayed is the computed sample weight as well as the computed samples of some representative parameters (fitting kinetics in correlation functions, see chapter: 4.2) during the fit of an Atto532-Atto647N hairpin sample containing 10 mM NaCl measured at 60 μW laser power showing the convergence.

simulation based on the measurable value of the anisotropies [86] but is nowadays directly included in the analysis based on the equations given in chapter 2.4 (see also [87] for details). In brief, it is assumed that the dyes rotate much faster than their fluorescence lifetime such that they sample all accessible positions multiple times before energy transfer takes place and a photon is emitted. Under this assumption the observed data can be described by a static dye position and an average dye orientation (see also chapter 2.4).

The flexibility of the dye linker is accounted for by using a so called accessible volume instead of one fixed dye position. In case of the antenna dyes, these accessible volumes are boxes around the protein large enough to allow any reasonable position and restricted only by the volume occupied by the known protein and DNA coordinates.

For the satellites the attachment point is known and the accessible volume can be explicitly calculated in these cases. While a MD simulation would be the most accurate way to determine such a volume it is computationally expensive and hence not feasible for multiple positions. Instead a simplified method approximating the linker by a freely jointed chain is used in this work. The information about the accessible volume of the satellite is included in the analysis as boundary for the satellite position which is also optimized (together with its orientation) throughout the fit.

Since every measurement induces some errors and the transformation from FRET to actual dye-dye distances includes several experimental data bayesian inference (chapter 3.4) is used to include all information and the associated error. The results from this analysis are probability densities which in this thesis are shown at a surface contour of 68% credibility. In order to compute these densities nested sampling (chapter 3.5) is applied. All credibility volumes presented in this work were calculated using the NPS Software (V3.1) by Adam Muschielok, 2011.

Chapter 4

New developments and applications

4.1 New software developments

This section will give a technical description and brief usage information of the two main software tools developed for this work.

4.1.1 The Burst Explorer software

The Burst Explorer is a software tool that allows an easy analysis of multidimensional data. It is optimized to handle huge amounts of bursts obtained using MFD but can also be used to get an insight into correlations of sampling results.

All Burst analysis data processed for this work was analyzed using this software. A detailed description of the software, its functinality and its usage can be found in the Appendix chapter A.1.

4.1.2 Probability distribution analysis (PDA) on a GPU

The quantitative analysis of single molecule fluorescence resonance energy transfer experiments oftentimes requires complex statistical

methods such as PDA, whose numerical implementation are computationally expensive. Here, the GPU parallelization using the Matlab 2010b GPU implementation and CUDA applied throughout this work is explained. Benchmarks were performed to demonstrate the significant reduction of the computation time necessary for performing PDA and parallelization on a single GPU is shown to be much faster than parallelization on current desktop CPUs.

4.1.2.1 Introduction

Probability Distribution Analysis (PDA) [5] [5] [50] [52] [75] is a modern and powerful technique commonly used to analyze smFRET data obtained using point detectors such as single photon counting avalanche photo-diodes. PDA can be used to differentiate noise inherent in the photon-counting process from noise arising from dynamic fluctuation, such as photo-physics or structural changes. In PDA the probability of detecting each possible ratio of donor photons detected after donor excitation (S_g)[1] and acceptor photons after donor excitation (S_f), $P(S_g/S_f)$ is calculated for any given model. The resulting probability distribution can then be directly compared to measured data and the model parameters can thus be optimized.

Calculations to generate the probability distributions are both, straight forward and computationally expensive. Importantly, common fitting algorithms require multiple evaluations of the fit function and with that also the frequent computation of $P(S_g/S_f)$ to find an optimum solution. Therefore, parallelizing either the fitting routine or the fit function can significantly reduce the time required for data analysis.

New architectures and an increasing amount of processing cores have transformed Graphic Processing Units (GPUs) into powerful tools for highly parallel computation. This computation power is utilized in various areas of biophysical research, e.g. in super resolution microscopy [118], for molecular modeling [120] [119] [66] and

[1] For the readability of the formulas presented in this chapter the index GG usually applied to donor photons after donor excitation has been replaced by g only and the index GR usually meaning acceptor photons after donor excitation has been replaced by f (for FRET).

in sequence scanning of large biological databases [69]. However, until now most applications require complex software tools and GPU processing is not yet generally applied.

While CUDA (www.nvidia.com) is an advanced programming environment that allows for the easy parallelization of C, C++ and fortran code, Matlab (the mathworks, Natick, US) is a commonly used top level programming environment. Since the Matlab release 2010b the computation power of CUDA enabled GPUs can be used to run (some of the) Matlab functions and it is possible to implement CUDA code into existing programs without the need to transfer data to the GPU using separate C code. This makes GPU programming easily accessible also to researchers without extensive programming experience.

In the following an implementation of GPU computation for PDA using Matlab GPU commands and CUDA code is demonstrated to drastically reduce the calculation times compared to single- or multicore CPUs.

4.1.2.2 PDA theory

In a FRET experiment using a confocal microscope the probability to detect a ratio of green to red photons (S_g/S_f) can be calculated as given by [5]

$$P\left(\frac{S_g}{S_f}\right)_i = \int P(\epsilon^*(R_{DA})) \sum_{all\ N,F_f,B_g,B_f yielding (S_g/S_f)_i} P(N) P_{\epsilon^*}(F_f|N-B_g-B_f) P_{\langle B_g \rangle}(B_g) P_{\langle B_f \rangle}(B_f) d\epsilon^* \tag{4.1}$$

where a Gaussian distribution of distances with an average distance $\overline{d}_{DA}$ and a standard deviation of σ_R originating from dye movement due to long linkers is assumed. Based on this assumption $P(\epsilon^*(R_{DA}))$ the probability to detect molecules with an apparent background corrected FRET efficiency ϵ^*, given a dye distance $\overline{d}_{DA}$ can be calculated

$$P(\epsilon^*(R_{DA})) = \frac{R_0}{6\sqrt{2\pi\sigma_R}}\gamma^{1/6}\frac{1}{(1-\epsilon^*)^2}\left(\frac{1}{1-\epsilon^*}-(1+cr)\right)^{-7/6} exp\left\{-\frac{1}{2\sigma_R^2}\left[R_0\gamma^{1/6}\left(\frac{1}{1-\epsilon^*}-(1+cr)\right)^{-1/6}-\overline{d}_{DA}\right]^2\right\}. \tag{4.2}$$

As a result the observed histograms of the apparent FRET efficiency ϵ^* as would be calculated from the detected fluorescence photons of donor (F_g) and acceptor (F_f)

$$\epsilon^* = \frac{F_f}{F_g + F_f} \tag{4.3}$$

are broadened in excess of the shot noise limit.

It has to be mentioned here that this apparent broadening could also be due to numerous other reasons such as e.g. acceptor photophysics [5] [51].

The Förster Radius (R_0) required to convert distances to FRET efficiencies (or vice-versa) can either be determined as described in chapter 3.1 or, if the absolute distance is not critical (e.g. if one is only interested in relative probabilities of different states), it can be estimated from literature values[2].

Moreover, $P(N)$ is the probability of detecting exactly N photons and $P_{\langle B_{g,f}\rangle}(B_{g,f})$ is the probability of detecting $B_{g,f}$ donor and acceptor channel background photons given an average number of $\left\langle B_{g,f}\right\rangle$ counts and can be calculated from poissonian statistics

$$P_{\langle B_{g,f}\rangle}(B_{g,f}) = \frac{\left\langle B_{g,f}\right\rangle^{B_{g,f}} e^{-\langle B_{g,f}\rangle}}{B_{g,f}!}. \tag{4.4}$$

Finally the probability to detect exactly F_f red photons out of a total $F = N - B_g - B_f$ fluorescence photons $P_{\epsilon^*}(F_f|N-B_g-B_f)$ can

[2]here: $R_0 = 60$ Å, www.atto-tec.com, cr = 3%

be calculated using a binomial distribution

$$P_{\epsilon^*}(F_f|F) = \frac{F!}{F_f!(F-F_f)!}\epsilon^{*F_f}(1-\epsilon^*)^{F-F_f}. \tag{4.5}$$

4.1.2.3 Implementation

To calculate the probability distribution $P(S_g/S_f)$ a simple, straightforward approach using nested loops was applied. The nested loops were arranged in the following order: detected photons (N), green and red background photons (B_g, B_f) and detected red photons (F_f) to compute all meaningful combinations of the involved probabilities. In order to minimize the computational expense all probabilities not depending on fit parameters are calculated once before the fitting routine is called and the respective results are used directly in the nested loops. The final probability distributions are generated by performing a numerical integration calculating values for each bin. All results of $P(S_g/S_f)$ yielding equal FRET efficiencies are directly summed up into a result vector. Calculations are further sped up by taking only background photon numbers with a probability larger than 0.001 into account.

CPU implementation: The analysis was done using Matlab 2010b x64. CPU parallelization was achieved using the parfor function in Matlab. In order to optimize the performance all nested loops except of the parfor loop were written in C++ and the corresponding mex file is called from Matlab. The C++ code used to calculate the probabilities is shown in the Appendix figure A.5.

GPU implementation: For parallelization using a GPU all nested loops were written in CUDA. The CUDA function call, as well as the data transfer to and from the GPU, is implemented using standard Matlab commands. Due to our implementation of the parallelization it is possible that two or more GPU cores try to add their result to the same position of the result vector within a small enough time window to cause a loss of data. This problem is avoided by applying

the AtomicAdd command of CUDA that allows each core to use the respective memory address exclusively. Hence, other cores that try to work on the same address will wait until the add operation is complete. While this approach might slightly reduce the GPU throughput the effect on the implementation used here will usually be negligible as the writing operation is only a minor part of the performed calculations. The CUDA code used to calculate the probabilities can be found in figures A.6-A.8.

4.1.2.4 Methods

Sample system: For generating the experimental FRET data to be analysed by PDA, DNA oligomers with a forward strand 5′ GACC TATG CTAT TTAT TAAC CCCT ***T1*** A ***T2*** ATTC CTCG ACGA C and a reverse strand 5′ GTCGTCGAGGAATATAAGGGGTTAA ***T1*** AAATAGCA ***T2*** AGGTC (IBA GmbH, Göttingen) were used. Two different labeling position combinations both for the donor (backward strand Atto532) as well as for the acceptor (reverse strand, Atto647) were used as indicated.

The DNA strands were annealed in TE (pH 7.6) by heating to 60°C and cooling down by 2°C per minute to 4°C. For the experiments a 1:1 mixture of the two double labeled dsDNA samples was used at a final concentration of 60 pM in TE (pH 7.6) buffer. Samples were loaded into Lab-Tek II chambers (Nalge Nunc In. Corp. Naperville, USA) and experiments were performed as described in chapter 3. A laser power of 75 μW in front of the objective was applied and single molecule bursts were identified requiring at least 100 photons per burst and at least 4 photons per 500 μs.

An approximately 1:1 mixture of dsDNA molecules 1 and 2 was prepared and the fluorescence was measured using the confocal microscope described in chapter 3.2. For the PDA dirt was removed by a stoichiometry threshold ($S = 0.4 - 0.7$) and selected bursts were then divided into time-bins of 1 ms. Bursts (and burst fragments) shorter than 1 ms were disregarded from further analysis. From the detected green fluorescence photons (S_g) and detected red fluorescence photons (S_f) the proximity ratio ϵ was calculated according to

equation 3.7.

Fits were done using predetermined values for the crosstalk = 3%, the relative detection efficiencies γ =0.7, the mean background rates B_g = 300 Hz, B_f = 300 Hz, the polarization correction described in chapter 4.3.8 and a Förster distance R_0 = 60 Å. A threshold for the maximum number of photons N allowed in each 1ms time bin was applied in the analysis to control the problem size. The data was analyzed using PDA requiring two Gaussian distributions for a best fit yielding distances of $d_1 = 54.0$ Å, $d_2 = 78.1$ Å, distribution width of $\sigma_1 = 7.2$ Å and $\sigma_2 = 7.6$ Å and relative amplitudes of $A_1 = 0.58$ and $A_2 = 0.42$.

CPU experiments: Experiments were performed on three different CPUs, namely the Intel Core i7 2600k (3.4 GHz, 16 GB DDR3 1333 MHz), the Intel Core2 Duo E6550 (2.33 GHz, 8GB DDR2 800 MHz) and the AMD Athlon II X4 635 (2.9 GHz, 8GB DDR3 1333 MHz).

GPU experiments: The GPU computations were performed on an Intel Core2 Duo E6550 system running Windows 7, 64bit. Graphic cards were running in a single monitor configuration (resolution: 1680* 1050, driver version: 270.61) with Windows Aero enabled. Disabling of Windows Aero however did not change the results. We compared different standard GPUs, namely the Zotac GTX 260[2] 768 MB, with 216 CUDA cores (core clock 576.0 MHz, memory clock 1998 Mhz, 448 bit GDDR 3) and the Gainward GTX 560 Ti Phantom 1GB with 384 CUDA cores (core clock 835 Mhz, memory clock 2050 Mhz, 256 bit GDDR5) [3]. Note that the timeout detection of the windows operating system had to be disabled in order to perform the time consuming calculations.

[3]since these two graphic cards have to some extent different architectures their expected calculation speeds cannot be directly compared by number of CUDA cores and core clock.

4.1.2.5 Experiments and results

Since the properties of the fit results are discussed in detail in chapter 4.3.8 here only the values described above (see methods, chapter 4.1.2.4) are used to compare GPU and CPU calculation speeds. A graphical representation of data and fit can be found in figure 4.1B.

In a PDA fit routine most of the computation time is needed for generating the respective photon distribution. Using the algorithm described here and assuming that only 0 and 1 background photons have a sufficiently high probability, the generation of one complete distribution with 50 bins and 150 photons requires 4.5 million evaluations of $P(S_g/S_f)$. In order to reduce the time required for the PDA analysis, the computation of $P(S_g/S_f)$ was parallelized as described above (chapter 4.1.2.3).

The implemented parallelization of the nested loops on a GPU can be easily understood by looking at a simple example (figure 4.2). In this example one considers three nested for-loops which represent a three dimensional parameter space. In this parameter space each point can be calculated independently. CUDA allows the addressing of individual threads in an up to three-dimensional space and thus this provides a perfect example how parallelization can be done. In order to apply this idea to the PDA problem, each possible combination of the three outer for-loops (in this implementation the bins of the numerical integration, the number of total photons N and the number of green background photons B_g) was positioned in a three-dimensional space, thus allowing to perform highly parallel calculations.

Computing $P(S_g/S_f)$ for the example shown in figure 4.1B (using 50 bins and a maximum signal threshold of 150 photons) took 11.5 seconds on the slowest single core CPU (E6550) and 2.1 seconds on the fastest CPU using 8 threads on 4 cores (i7 2600k, Hyper Threading) (figure 4.3). In contrast, the same calculations can be performed on a moderately fast GPU (GTX 560 Ti) in 0.8 seconds, which is sufficiently fast for running a fit algorithm within a reasonable time. Even a comparatively weak GPU like the GTX 260 is capable of finishing the calculations faster than a standard office PC dual core CPU (4.1

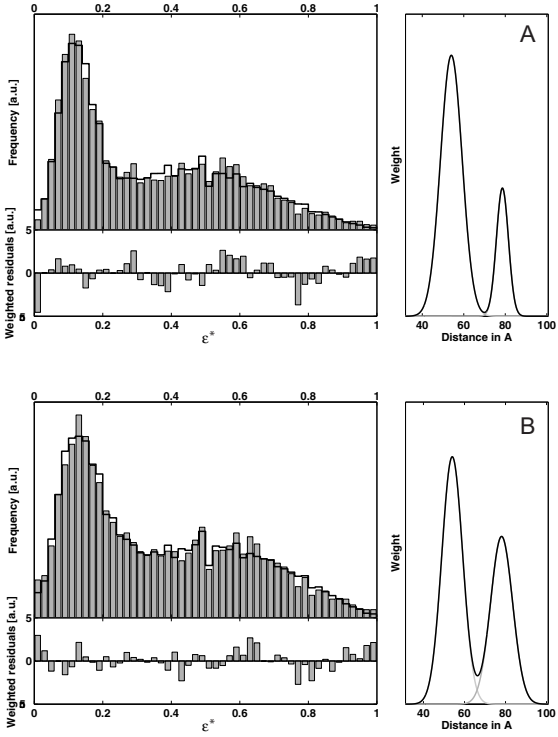

Figure 4.1: PDA analysis of smFRET measurement of a mixture of DNA molecules. Histograms of apparent FRET efficiencies (grey) and the corresponding PDA fit (black line) obtained for a sample containing a mixture of two dsDNA molecules with dye labels separated by 20 and 9 base pairs, respectively. For the PDA analysis the fluorescence signal for donor and acceptor was calculated using, equation 4.19 (A) or equation 4.20 (B). PDA yielded the following fit results: distances $d_{1A} = 54.0$ Å, $d_{2A} = 78.6$ Å, $d_{1B} = 54.0$ Å and $d_{2B} = 78.1$ Å, distribution widths $\sigma_{1A} = 7.4$ Å, $\sigma_{2A} = 4.1$ Å, $\sigma_{1B} = 7.2$ Å and $\sigma_{2B} = 7.6$ Å and relative amplitudes $A_{1A} = 0.79$, $A_{2A} = 0.21$, $A_{1B} = 0.58$ and $A_{2B} = 0.42$, where A and B denote the analysis in the respective panels.

```
for a = 1:N1
    for b = 1:N2
        for c = 1:N3
        Calculate function of (a,b,c)
        end
    end
end
```

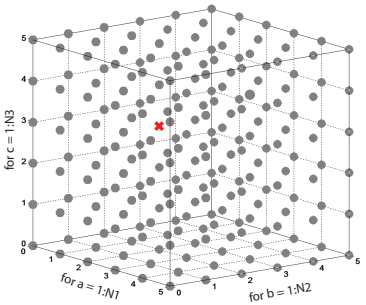

Figure 4.2: Cartoon describing the nested loop parallelization. A nested loop can be imagined as a three dimensional cube where each individual point represents one state of the nested loop (e.g. the red cross represents $a = 3$, $b = 2$, $c = 1$). Given that the calculations do not rely on each other each point can be evaluated individually. Such a three dimensional pattern is perfectly suited for GPU parallelization.

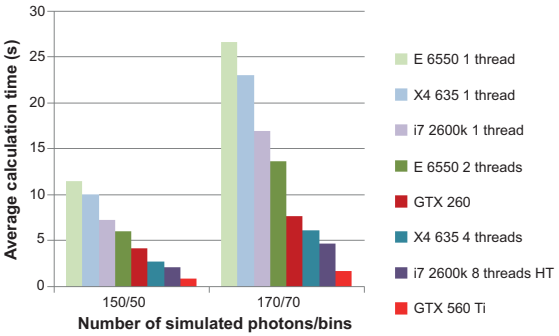

Figure 4.3: Comparison of time required to compute one distribution for several CPUs and GPUs. The average calculation time required to compute the probability distribution for the smFRET histogram of Figure 1 with 50 bins and a maximum signal threshold of 150 photons (left) and 70 bins with a maximum signal threshold of 170 photons (right) using a variety of different CPU and GPU parallelizations.

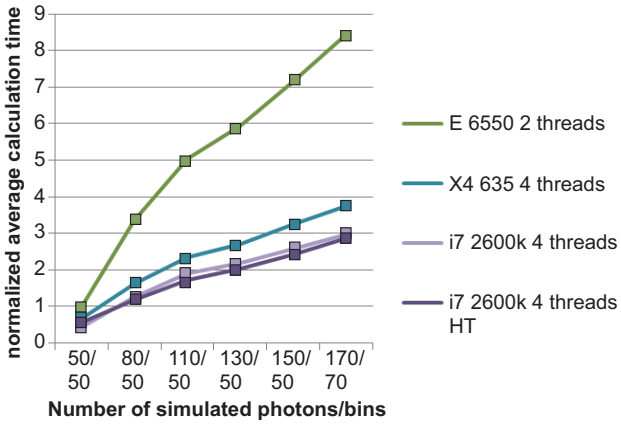

Figure 4.4: Comparison of CPU and GPU computation times as a function of problem size. The average CPU calculation time for different maximum signal threshold (photon numbers) and bins is normalized to the GTX 560Ti calculation time at the respective photons/bin combination demonstrating the superior scaling of the GPU approach with the problem size.

seconds).

The advantage of the GPU over the CPU becomes even more dramatic when computing more complex distributions. For example when calculating the probability distribution $P(S_g/S_f)$ for the data shown in figure 4.1B for 70 bins and a maximum signal threshold of 170 photons the GTX 560 implementation requires 1.6 seconds as compared to 4.6 seconds needed by the quad-core CPU (figure 4.3). Hence, computing the distributions on a GPU instead of a CPU leads to a significant speed increase.

It should be pointed out that the advantage of the GPU depends on the size of the required computation. For smaller problems (e.g. 50 bins and a maximum signal threshold of 50 photons) the time required to transfer data to the GPU is an important factor for the overall calculation speed. Additionally, the mapping of threads on the GPU can be done more efficiently when larger problems are ad-

dressed. This causes the GPU to scale significantly better with the problem size than the CPU (figure 4.4).

While the i7 2600k CPU is almost twice as fast as the graphics card for a maximum signal threshold of 50 photons and 50 bins this changes already at a maximum signal threshold of 80 photons and 50 bins where the GPU becomes slightly faster. When computing the distribution for 70 bins and a maximum signal threshold of 170 photons the GPU outperforms the i7 2600k CPU (8 threads, 4 cores) by a factor of 2.9. In comparison, the same calculation on a standard office PC (E6550) using two cores takes about 8.4 times longer than on the GPU and if only a single core were to be used the PDA computation would take 16.4 times longer.

4.1.2.6 Discussion

The analysis of PDA data is a complicated and computational expensive task. Oftentimes several experimental models have to be compared and thus it becomes important to develop novel algorithms that make PDA implementation both easier and faster. Here, the application of GPU programming to PDA using standard programming and data analysis software packages was presented. To demonstrate the speed increase possible by upgrading the CPU or buying a GPU an office PC running on an Intel Core 2 Duo E6550 CPU and equipped with a Gainward GTX 560 Ti Phantom 1GB was used. It was compared to a system running on an Intel Core i7 2600k. While this CPU (ignoring the need for a new motherboard) is currently $\sim$25% more expensive than a GTX 560 Ti it delivers less computation power and scales significantly worse with the problem size applied than the GPU. Therefore implementing a GPU parallelization as shown above is a fast and easy way to speed up calculations required to perform a PDA.

4.2 Influence of dye selection on DNA hairpin dynamics

Parts of this chapter have been published prior to this work in.

Bayesian-Inference-Based Fluorescence Correlation Spectroscopy and Single-Molecule Burst Analysis Reveal the Influence of Dye Selection on DNA Hairpin Dynamics
by Wolfgang Kügel, Adam Muschielok and Jens Michaelis [61]

Fluorescence correlation spectroscopy (FCS) is a powerful tool to gain information about dynamics of biomolecules. However, the key problem is to extract the rates hidden in the FCS data by fitting the data to a meaningful model. A number of different fitting approaches have been described in recent years but the extraction of relevant information to date has still been limited by numerous experimental problems and the fact that the set of starting parameter values chosen could often predefine the result. In this chapter a new way to globally analyze FCS data based on Bayesian inference is established to overcome these issues. Moreover, the influence of other remaining experimental error sources, for example, photo physics, is excluded by additional means. Using this approach in combination with the results from single-molecule burst analysis, the kinetics of DNA hairpins labeled with a variety of different fluorescent probes were investigated as a function of the salt concentration. It is shown that the rates of hairpin opening and closing as well as the equilibrium constant of the transition depend on the characteristics of the dye molecules used to label the hairpin. Thus, great caution has to be used when utilizing dye molecules as reporters for the kinetics of dynamic macromolecular structures.

4.2.1 Introduction

Throughout the last years, with the growing interest in the quantitative understanding of dynamic processes in living systems, also the studies of conformational dynamics of biological molecules have seen

an increasing attention. Prominent examples include investigations of the dynamics of DNA hairpins [10][125], RNA secondary structures [68], nucleosomes [8][35], motor proteins [129], DNA translocases [44] as well as a large variety of other proteins [79][92][88][133].

To study conformational dynamics, oftentimes a pair of local probes is attached to the molecule of interest, in particular a pair consisting of a dye molecule and a quencher. The term "exited-state quencher" is commonly applied to a molecule that accepts energy from an excited dye. Quenchers are either non-fluorescent [10][49] or fluoresce themselves [125].

Dynamic processes which bring about changes in the distance between the two probes cause fluctuations in the brightness of the emitted fluorescent light. Brightness fluctuations of the quenched probe can be monitored for both fluorescent and non-fluorescent quenchers while additional brightness fluctuations of the quencher are observed only if a fluorescent acceptor is used.

There is a large variety of different experimental techniques which make use of the attachment of local probes for the investigation of dynamics of a biomolecule, including proximity ratio auto-correlation [132][36], melting temperature analysis [94], photon counting histogram [48] and FCS [10]; however, they all suffer from the same experimental complication. Does the attachment of probes reporting about the conformational dynamics lead to changes in the underlying energy landscape?

In particular for investigations of DNA or RNA molecules, where single nucleotide changes are known to influence the dynamics [10], extreme caution has to be used. While the influence of different dye–quencher pairs on the melting temperature of DNA hybrids has been investigated previously [77], little is known about their influence on the steady-state distribution and on the transition rates of dynamic processes. Amongst the different biomolecules that have been investigated in dynamic studies, nucleic-acid hairpins have attracted large interest, since understanding their dynamics is required for understanding important biological processes, such as the dynamic nature of four-way junctions or processes driven by ribozymes [140][141].

Moreover, commercially available single DNA or RNA strands

capable of forming hairpin structures are readily available with a large variety of different labels and are thus a good model system to study dynamics. Previous studies have observed repeated opening and closing of hairpins with rates depending on the sequence, stem length and salt concentration [10][121][43][49].

For the proper interpretation of such experiments it is important to determine the influence of the attached probes on these transitions. A common technique for studying dynamic processes from the sub-microseconds to the hundreds-of-milliseconds time-scale is FCS (see chapter 3.3). In FCS, the computed correlation functions contain information about all dynamic processes, in particular diffusion, photo physics as well as conformational dynamics. It is therefore important that the respective contributions can be separated from each other. Unfortunately, diffusion and kinetics oftentimes occur on similar timescales, making it difficult to extract the parameter of interest with high accuracy. Conformational kinetics and diffusion can be distinguished by comparing measurements of double-labeled samples (with a quenchable molecule and a corresponding quencher) to those with only a single label (the quenchable molecule of the double-labeled samples) as shown by Bonnet et al. [10].

Only the double-labeled sample is sensitive to dye–quencher distance changes, while all other fluctuations are common to both samples. Thus, by dividing the auto-correlation function of the double-labeled sample by that of the single-labeled one, one obtains the desired information about the conformational dynamics. A drawback of this method is that other dynamic processes are removed entirely only if the concentration of molecules as well as the excitation and detection volumes are identical for both measurements. In contrast, identical concentrations are intrinsic when performing PIE experiments.

In PIE, one directly excites the quencher and calculates its auto-correlation function. By dividing the donor auto-correlation function containing the conformational dynamics signal by the auto-correlation function of the acceptor after direct excitation, diffusion kinetics can be removed. There are, however, other challenges that remain such as intrinsic photo physics of the labels (causing a “false” kinetic signal)

and the requirement that the confocal volumes of the two different colors need to be identical. While FCS is an excellent tool for the investigation of transition rates, the information about the underlying state distributions is very limited. Single-molecule burst analysis, in contrast, allows for a direct measurement of the FRET states and thus gives access to intra-molecular distances between donor and quencher. In this chapter confocal microscopy of DNA hairpins is combination with FCS and burst analysis techniques to investigate the influence of different dye molecules on the distribution of states and rate constants. Additionally a novel approach to extract kinetic rates by globally analyzing a set of five correlation curves including a separate donor-only measurement using Bayesian inference is demonstrated.

4.2.2 Experimental procedures

Experimental setup: Confocal measurements were performed on the setup described in chapter 3 at 21 °C. Laser powers were 25 μW (measured directly before the beams enter the objective lens) for FCS and 100μW for the burst measurements if not stated otherwise.

Nucleic-acid hairpins: DNA hairpins containing the acceptor at the 3′ end and the donor at the 5′ end (sequence CCCAA-$(T)_{21}$-TTGGG) attached via a C6 linker (see figure 4.5) were purchased from IBA GmbH. A separate set of DNA molecules with identical sequence but containing only dye molecules at the 5 ′ end were used for donor-only reference measurements. As fluorescence donors, Atto532, Alexa532, 6-Tamra and Cy3 were used, while Atto647N, Alexa647 and Cy5 (NHS) served as acceptors (see Appendix A.3 for dye structures).

In solution experimental conditions: In solution experiments (chapters: 4.2.3.2, 4.2.4.1) were performed in 1x TE buffer (100 mM Tris, 1 mM EDTA, pH 7.6) at varying NaCl concentrations of 10, 160 or 320 mM within Lab-Tek II chambers (Nalge Nunc In. Corp. Naperville, USA). Nucleic acid concentrations were 100 pM for the burst analysis and 1–10 nM for the FCS measurements. Correction

factors were determined as described in detail in chapter 3.2.4.3 assuming that the dye properties do not change upon opening and closing of the hairpin. Since this assumption has been proven to be wrong for Cy3 [77][108] Cy3-Cy5 Burst analysis data is presented without any corrections.

Table 4.1: Correction factors for the dye combinations under investigation

Donor	Acceptor	γ	*cr*	*de*
Alexa532	Alexa647	0.35	0.04	0.01
Alexa532	Atto647N	0.90	0.04	0.01
Atto532	Alexa647	0.30	0.04	0.01
Atto532	Atto647N	0.60	0.04	0.01
6-Tamra	Alexa647	0.60	0.08	0.01
6-Tamra	Atto647N	1.20	0.08	0.01
Cy3	Cy5	/	/	/

In gel experimental conditions: For the in gel burst-analysis experiments (chapter: 4.2.4.2) 6% poly-acryl-amide gels were casted containing 400 mM NaCl, running in 0.4% TBE (see Buffers, pH 8, 400 mM NaCl). All equipment (casting racks, Cover slides) in contact with the gels were cleaned using a 2% Hellmanex (Hellma GmbH & Co. KG) solution. To this end the respective equipment was heated in the solution to 100°C, washed with distilled water (Millipore), heated to 100°C in distilled water and washed again. Additionally all gels were prerun for 30 minutes (30-40 V) to remove remaining impurities. A total volume of 8μl (4μl Ficoll (GE Healthcare) and 4μl DNA Hairpin (100 nM)) was loaded. 5xGelPilot loading dye (Quiagen) was used as a marker on a separate lane as far appart of the samples as possible.

After the gel was run the respective lanes were cut and mounted between two clean cover slides. This sample was then manually scanned to determine the maximum count rate position which was taken as origin for moving upwards (opposing the gels running direction), downwards (in the gels running direction) and right until a

count rate of ∼2-4 kHz was reached and a burst measurement was performed.

Table 4.2: Gel composition for in gel burst-analysis

Gel composition	
9.8 ml	H_2O
0.85 ml	5xTBE Buffer
2.67 ml	Polyacrylamide (Rotiphorese Gel 30, 37.5:1, Roth)
60 μl	10% Ammoniumperoxodisulfate (APS)
12 μl	N,N,N′,N′-Tetramethylendiamine (TEMED)

UV measurements: All UV spectra were acquired in TE pH 7.6 using a Varian Cary 5000 UV-VIS-NIR spectrophotometer and UVette (Eppendorf) cuvettes at a constant temperature of 20 $^{\circ}C$ (PCB-150, Agilent).

Data processing: Data were analyzed using custom software written in MatLab (MathWorks) and C (see chapter 3.5). Correlations were performed as described in chapter 3.3. For the donor-only sample, only photons after donor excitation were auto-correlated (green autocorrelation donor only sample (GGdxGGd)) while for the double-labeled samples, donor photons after donor excitation GGxGG, acceptor photons after acceptor excitation RRxRR and acceptor photons after donor excitation GRxGR were auto-correlated. In addition, the cross-correlation function of donor and acceptor photons after donor excitation GRxGG was computed. All correlation functions containing conformational dynamics were limited to timescales of 10 μs in order to be insensitive to photophysical effects of the labels (see chapter 4.2.3.1). For in solution data the burst analysis (see chapter 3.2.4.1) was performed with thresholds of at least 30 photons within a time interval of 1.2 ms and a total burst size of at least 60 photons. Due to the higher background in gel bursts were selected using a threshold of at least 20 photons within 500 μs and a minimum number of 100 total photons.

FRET efficiency (E), stoichiometry (S), lifetime weighted fluorescence anisotropy (r) and fluorescence lifetime (τ) were calculated for each burst as described in chapters 3.2.4.2, 3.2.4.4, 3.2.4.5, 3.2.4.6).

Fit Parameter	Lower boundary	Upper boundary
N	0	20
log(D)	-27($\sim 1.9e-12$)	-5($\sim 6.7e-3$)
log(ω_r)	-22($\sim 2.8e-10$)	-5($\sim 6.7e-3$)
log(ω_r)	-22($\sim 2.8e-10$)	-5($\sim 6.7e-3$)
f_{isc} (RRxRR)	0	0.999
log(τ_{isc}) (RRxRR)	-23($\sim 1.0e-10$)	-7($\sim 9.1e-4$)
log(k_{xy})	-5($\sim 6.7e-3$)	16($\sim 8.8e6$)
$E_{1,2}$	0	1

Parameter	*FF*	*GF*	*GG*	*GGd*	*RR*
N					
D					
ω_R					
ω_z					
τ_{isc}					
f_{isc}					
k_{12}					
k_{21}					
E_1					
E_2					

Table 4.3: Boundaries and status of variables used in the Bayesian parameter estimation of the FCS data: A summary of the parameter boundaries used throughout the Nested Sampling is given in the upper panel. Boundary values in brackets are the exponential of the used log values given for easier comparability.
An overview of the fit parameters and their global or local status in the fit is shown in the lower panel. Globally optimized variables are indicated in black and individually optimized variables in grey. White fields indicate parameters not included in the analysis of the respective correlation function.

Bayesian inference: In order to be insensitive to experimental parameters that could vary when changing the samples, a prior was used where none of the model parameters were predetermined. Instead the parameters were limited to a reasonable range (see table 4.3 upper panel). A Jeffreys prior [47] was used for all variables (see table 4.3 lower panel), except for N, E and f_{isc}, where a flat prior was used to reduce the computational expense since feasible values can vary only in a narrow range. Furthermore $E_1 < E_2$ was imposed such that state 1 has without loss of generality the smaller FRET efficiency.

Buffers: The composition of the Buffers used in this chapter can be found in Tables 4.4 and 4.5.

Table 4.4: Composition of the 1xTBE Buffer

TBE Buffer	
90 mM	Tris Base
90 mM	Boric Acid
2 mM	EDTA-Na_2

Table 4.5: Composition of the TE Buffer

TE Buffer	
10 mM	Tris Base
1 mM	EDTA-Na_2

4.2.3 Global FCS analysis

DNA hairpins consisting of a 21-base loop and a five-base-pair stem were investigated in a custom-built PIE–FCS setup. The dye labels were positioned on opposite ends of the DNA construct allowing for a maximum FRET efficiency change upon hairpin opening and closing (see chapter 4.2.2). In order to extract the kinetic information the auto-correlation function of the green photon stream of a donor-only sample after donor excitation (GGdxGGd) was analyzed globally with the correlation functions obtained from a double-labeled sample, namely, the GGxGG, RRxRR, GRxGR and the cross-correlation GRxGG using Bayesian parameter estimation (figure 4.5 B–F).

4.2.3.1 Theory and application

All correlation functions have the general form:

$$G_{\mathrm{xy}}(\tau) = M_{\mathrm{xy}}(\tau) X_{\mathrm{xy}}(\tau) \tag{4.6}$$

where the indices x and y depict the photon streams that are correlated, X_{xy} describes the conformational kinetics of interest and M_{xy} is the diffusion term given by [46]

$$M_{\mathrm{xy}}(\tau) = \frac{\alpha}{\langle N_{\mathrm{xy}} \rangle} \left(\frac{1}{1 + \frac{4D\tau}{\omega^2 \mathrm{r_{xy}}}} \right) \left(\frac{1}{1 + \frac{4D\tau}{\omega^2 \mathrm{z_{xy}}}} \right)^{1/2} \tag{4.7}$$

Here, $\langle N_{\mathrm{xy}} \rangle$ is the average number of observed molecules in the focal volume, D denotes the diffusion constant,$\omega_{\mathrm{r_{xy}}}$ and $\omega_{\mathrm{z_{xy}}}$ are the lateral and axial dimensions of the focal volume and α is a correction factor depending on the focal volume geometry (here $\alpha = 2^{-3/2}$ since a three-dimensional Gaussian is assumed, see Eq. 3.4). A two-state model as depicted in figure 4.5 was used to describe the conformational dynamics of the DNA hairpin. The transition between states of FRET efficiency E_1 and E_2 lead to a kinetic contribution to the FCS signal described by Eq: 4.8, 4.9 and 4.10 [125]:

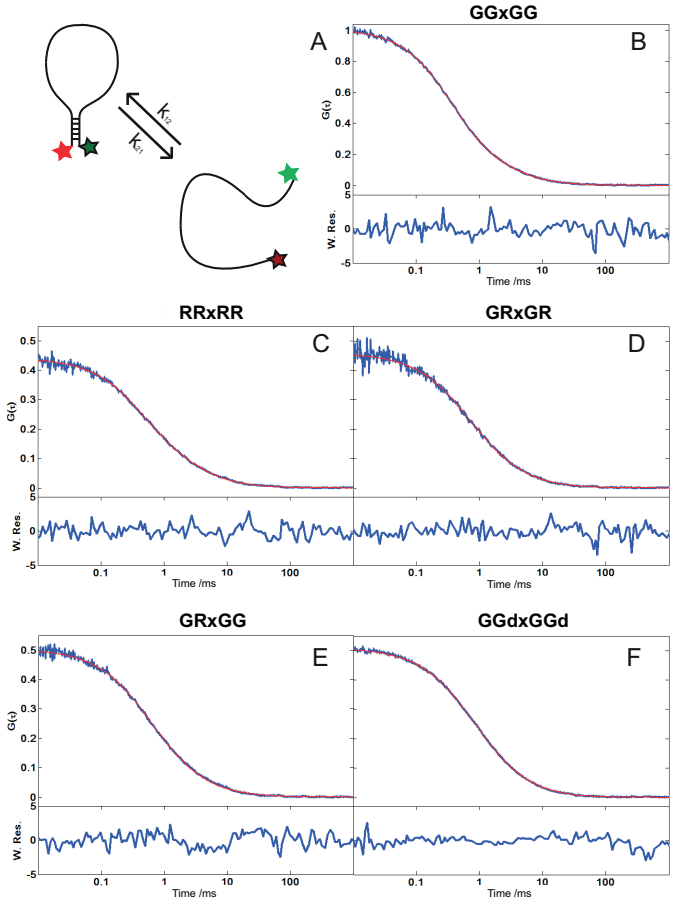

Figure 4.5: Hairpin opening dynamics identified by global analysis of correlation functions. (A) Schematic drawing of the two-state model used to describe the dynamics observed in the five correlation functions that were used for a global analysis to the recorded data (B-F). The forward and backward rates are denoted as k_{12} and k_{21}, the red and green dye positions are depicted by colored stars. Exemplary set of auto-correlation functions (B: donor-donor, C : acceptor-acceptor, D: FRET-FRET, and F: donor only sample) as well as cross-correlation (E) data for DNA hairpins labeled with Alexa532-Atto647N containing 10 mM NaCl measured at 16 μW laser power (blue). The corresponding results of the global analysis are shown in red and the weighted residuals (W. Res. (a.u.)) are given below each correlation curve.

$$X_{\mathrm{GGxGG}}(\tau) = 1 + A_{\mathrm{GGxGG}}(\tau) = 1 + \frac{k_{12}k_{21}(E_1 - E_2)^2}{[k_{21}(1 - E_1) + k_{12}(1 - E_2)]^2} e^{-(k_{12}+k_{21})\tau} \tag{4.8}$$

$$X_{\mathrm{GRxGR}}(\tau) = 1 + A_{\mathrm{GRxGR}}(\tau) = 1 + \frac{k_{21}k_{12}(E_1 - E_2)^2}{(k_{21}E_1 + k_{12}E_2)^2} e^{-(k_{12}+k_{21})\tau} \tag{4.9}$$

$$X_{\mathrm{GRxGG}}(\tau) = 1 + A_{\mathrm{GRxGG}}(\tau) = 1 - \frac{k_{21}k_{12}(E_1 - E_2)^2}{[k_{21}(1 - E_1) + k_{12}(1 - E_2)](k_{21}E_1 + k_{12}E_2)} e^{-(k_{12}+k_{21})\tau} \tag{4.10}$$

where k_{12} and k_{21} are the transition rates between the two conformational states and A_{XY} is the amplitude of the conformational kinetic signal. In contrast, the auto-correlation function of photons emitted by the acceptor dye after direct excitation (RRxRR) is insensitive to the hairpin dynamics and can be described by Eq. 4.11:

$$X_{RRxRR}(\tau) = 1 + \frac{f_{isc}}{1 - f_{isc}} e^{\frac{-\tau}{\tau_{isc}}} \tag{4.11}$$

with f_{isc} being the probability for a molecule to enter the triplet state upon excitation and τ_{isc} describing the triplet lifetime. To minimize computational expense, no additional triplet term was fit to the GGxGG, GRxGR and GGdxGGd correlation curves; instead, the experimental data was limited to a time range not showing donor photophysics. Since the donor-only labeled samples are insensitive to the conformational dynamics (assuming no changes in brightness), there is no kinetic term in these data sets (i.e. $X_{GGdxGGd}(\tau) = 1$).

It is important to note that not all correlation functions are equally sensitive to kinetics of a particular FRET transition (figure 4.6). This means that the signal amplitude detected in each channel depends

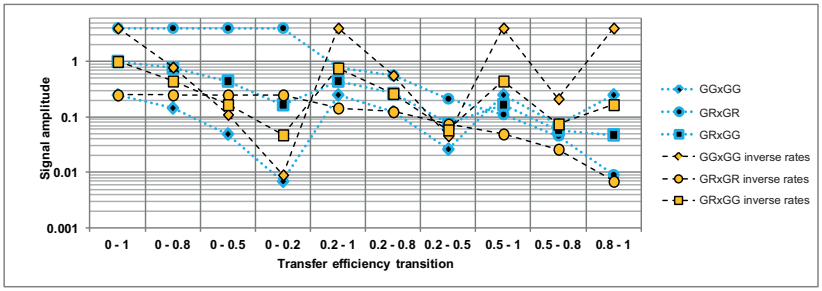

Figure 4.6: Comparison of expected kinetic signal amplitudes for different FRET states and kinetic rates. Simulated amplitudes A (Eq. 4.8–4.10) of the three correlations containing a kinetic term, namely, the donor GGxGG, and acceptor GRxGR auto-correlations and the cross-correlation and GRxGG calculated for the time point $\tau = 1e^{-8}s$, which is chosen to be significantly smaller than the timescale of molecular dynamics encoded in the correlation functions. Results are shown for different FRET transitions at rates of $k_{12} = 4000s^{-1}$ and $k_{21} = 1000s^{-1}$, and vice versa (inverse rates).

on the parameters of the investigated transition. Thus, by globally analyzing all correlation functions that contain a kinetic term, one avoids missing apparent transitions, an important advantage of the global analysis.

To globally fit all the correlation functions (Eqs. 4.6– 4.11) to the experimental data, 20 model parameters have to be determined (a summary of the variables and their status in the global analysis is given in Table 4.3 on page 61). Commonly, one aims at finding the global optimum of an objective function, which is typically the χ^2 function in a least-squares fit or the likelihood function in maximum likelihood estimation (MLE) [76][11]. The confidence bounds of the estimate are calculated from a local property of the objective function evaluated at the found optimum, namely, the second derivative matrix of χ^2 or the logarithm of the likelihood, respectively. While this approach is usually reasonable for a few model parameters, it can become inappropriate if the data is described by a more complex model with considerably more, possibly interdependent, parameters. In this case, the local approximation of the objective function used

to compute the errors of the estimate breaks down due to possible multidimensional correlations of the parameters, rendering the determined error bars inappropriate. Indications of such failure are slow convergence of the optimization and several equally "good" optima found (i.e. with different final parameters) in separate optimization runs started at different initial positions in the parameter space, both of which were observed for the FCS data presented here. A solution to these problems is Bayesian inference, a general data analysis method (which contains least squares and MLE as special cases, see chapter 3.4).

Therefore, Bayesian inference was used to globally determine all the parameters and experimental uncertainties [4]. To calculate the likelihood of the data uncorrelated experimental noise on top of the theoretical autocorrelation functions (Eqs. 4.6– 4.11) was assumed. It was assumed that this noise is normally distributed with zero mean and a known, time-dependent amplitude, so that the likelihood is proportional to $exp(-\chi^2/2)$, where χ^2 is the weighted sum of the squared residuals. An example for the result of a global Bayesian analysis of the GGxGG, RRxRR, GRxGR, GRxGG and GGdxGGd correlation functions is shown in figure 4.5 B–F. Importantly, the residuals for all correlation functions show no apparent correlation.

Dye molecules typically show photo-physical effects which lead to an auto-correlation signal that is difficult to distinguish from a kinetic signal if it is on the same time scale. Since the fit will optimize for the best possible result the description of the conformational kinetics becomes problematic if the photo-physical signal of one dye is significantly stronger than the global kinetic signal. One solution would be to add additional triplet terms to the model which in practice however increases the fit complexity and did not yield reproducible results on triplicate measurements (data not shown).

As for this reason the model used here does not account for triplet kinetics of the donor (and acceptor encoded in the GRxGR function), which could be mistaken for conformational kinetics of the hairpin, it is important to ensure that the results are independent of the laser

[4]The C++ code of the likelihood function used can be found in the Appendix figures A.9-A.12

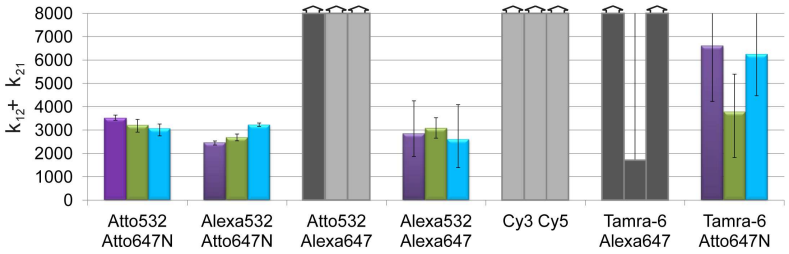

Figure 4.7: Influence of incidence laser power on the extracted kinetic rates. Resulting $k_{12} + k_{21}$ values for different dye combinations at laser powers of 16 μW (violet), 25 μW (green) and 60 (bright blue) μW in the presence of 10 mM NaCl (corresponding fit errors determined as described in main text). Results not containing any useful kinetic information are marked in bright- (dominating photo-physics) and dark grey (no kinetic signal detected). A rate-dependence on the laser power exceeding the statistical and systematic error of the measurements cannot be detected.

intensity. To this end all hairpin dye combinations were analyzed at 10 mM NaCl using 16 μW, 25μW and 60 μW of laser power (before the objective). The samples (see figure 4.10 and figure 4.7) showed no significant dependence on the laser intensity exceeding the statistical and systematic error of the measurement.

In order to prove that the data was not falsified by donor photo physics for any of the samples and salt concentrations under investigation, the donor-only hairpin (GGdxGGd), its fit function $G_{GGdxGGd}(\tau)$ and the fit function $G_{GGxGG}(\tau)$ of the FRET sample (figure 4.8) were compared.

Since the concentration for single- and double-labeled measurements is not required to be identical, the number of molecules in the confocal volume $\langle N \rangle_{xy}$ of the FRET sample was set to the respective value of the donor only sample for this overlay. Examples of a successful analysis of samples not affected by donor triplet kinetics are given in Figures 4.8 A,B, where a good fit of both correlation curves was obtained and a clear difference between donor-only (grey) and FRET (dashed black) maximum posterior results can be observed. Here, the donor-only data (grey circles) can be described

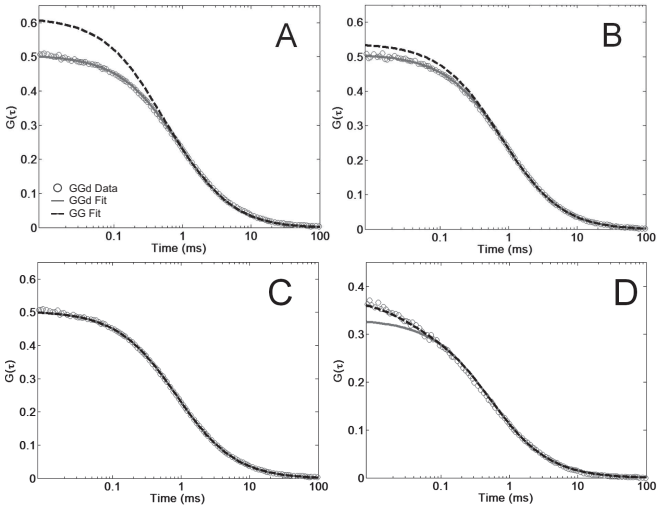

Figure 4.8: Comparison of conformational kinetics and photophysics. The experimental auto-correlation for the A) Atto 532 and B) Alexa 532 donor-only sample $G_{GGdxGGd}$ is shown (grey circles) together with the analysis results calculated using Eq. 4.7 (solid grey line). Overlayed are the kinetic results obtained from the global analysis of the A) Atto532–Atto647N and B) Alexa532–Alexa647-labeled hairpins (dashed black line). All four samples were measured at 10 mM NaCl and 16μW laser power. For the overlay, the number of molecules in the confocal volume (*N*) of the FRET sample was set to the respective value of the donor-only sample, since concentrations of single- and double-labeled measurements were not precisely identical. For short times, one clearly observes a difference between donor-only and FRET results, indicating the presence of additional kinetics. C) Atto532–Alexa647 hairpin sample correlation functions (measured under the same conditions and presented using the same color codes as in A) showing a different behavior. Here, the results from the donor-only and the FRET sample are indistinguishable over the complete accessible time range. Thus, there is no apparent signal of conformational dynamics. D) Correlation functions of Cy3–Cy5 labelled hairpins measured at 100 mM NaCl and 25 μW laser power shows a situation where the global analysis yields parameters that cannot describe the short-time behavior observed in the donor-only sample. In contrast, the kinetic parameters obtained in the global analysis for the FRET sample describe well the observed signal of the donor-only sample (again using *N* from the donor-only sample).

by the simple diffusion model, while a clearly visible kinetic contribution is contained in the FRET result. For different datasets (figure 4.8 C), the data from the donor-only and the FRET sample are indistinguishable over the complete accessible correlation time range. Thus, there is no apparent signal of conformational dynamics in the GGxGG correlation function.

A completely different behavior can be seen in figure 4.8 D. In this example, using a Cy3–Cy5 dye pair, the global analysis yields parameters that cannot describe the fast dynamics observed in the donor-only sample which instead is described by the kinetic parameters obtained in the global analysis for the FRET sample. This can be understood if photophysical effects of the donor have a stronger effect on the correlation function than the conformational dynamics. In such cases, during the global analysis, the kinetic term in Eq. 4.8 is misused to describe the photophysical signal instead of the conformational dynamics. Moreover, Cy3 is known to be sensitive to the local environment, resulting in lifetime and brightness variations upon e.g. switching from double to single strand [77][108]. Therefore, the Cy3–Cy5 dye pair was excluded from further FCS Analysis.

Additionally the results obtained for the acceptor photophysics using Eq. 4.11 were directly compared to the fit results obtained for the kinetic signal of the GRxGR correlation function (Eq. 4.9 to exclude dominating acceptor photophysics. However, none of the rates obtained for the different dye pairs was affected by acceptor photophysics.

4.2.3.2 Results

By performing a global analysis using Bayesian inference, all necessary parameters can be determined even without in-detail prior knowledge; however, some of the parameters are correlated and thus there is not enough information in the recorded data to accurately determine these parameters individually, most notably the rates k_{12} and k_{21} (figure 4.9 A).

Here, the uncertainties in the amplitude of the experimental correlation function caused by for example, poor statistics make it impossi-

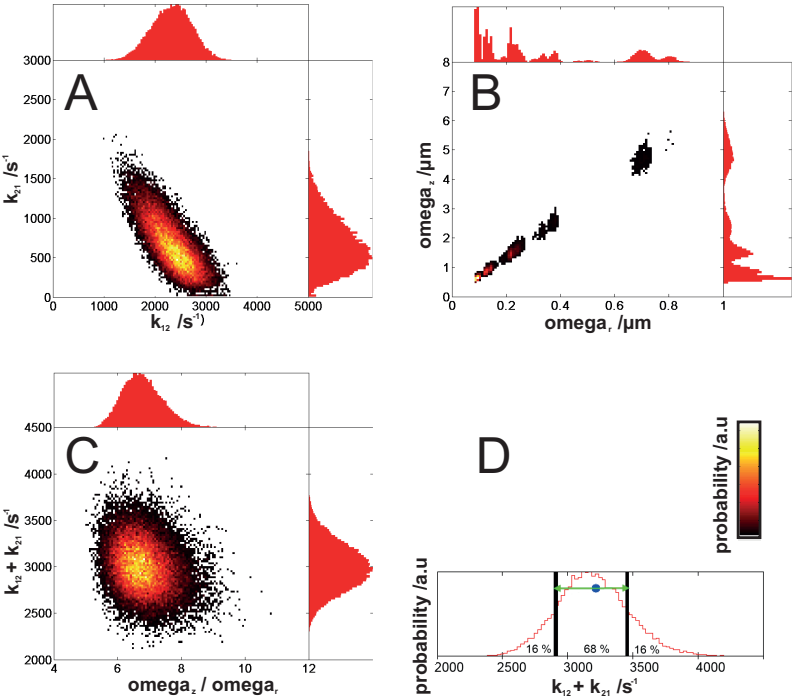

Figure 4.9: Correlations of experimental parameters. A) Two-dimensional histogram of the equally weighted samples obtained for the rate constants k_{12} and k_{21} for an Atto532–Atto647N sample containing 10mM NaCl measured at 60μW laser power. The top and side show the corresponding one-dimensional projection. The two parameters are strongly correlated. B) Green focal volume results showing a strong correlation between $\omega_\mathbf{r}$ and $\omega_\mathbf{z}$. C) Two-dimensional histogram and one-dimensional projections of the sum of transition rates versus the structural parameter ($\omega_\mathbf{z}/\omega_\mathbf{r}$). In contrast to the individual rates, the sum of rates as well as the structural parameter can be determined accurately. D) Schematic representation of the fit-error determination. Errors are given as the distance of the best fit-ting sample (blue point) to the lower and upper boarders that mark 1σ of the distribution (black lines). Since this best fitting sample is not required to show an equal distance to both boarders, the greater of the two distances was used as fit error for weighted averaging of the results.

ble to resolve parameters relying on small changes in this amplitude (this is problematic also for E_1 and E_2, data not shown). Instead, the sum of the rates $k_{12} + k_{21}$ (rate constant of the exponential decay in Equations 4.8– 4.10) can be determined with high accuracy (figure 4.9 C). Likewise, the structural parameter defined as the ratio of length ω_z to width ω_r of the focal volume (see figure 4.9 B and C) can be determined accurately while ω_z and ω_r are highly correlated.

To summarize the accuracy of the parameter estimation, the fit error was always defined as the distance of the maximum posterior sample to the points in the distribution including 68 % of the probability as shown in figure 4.9 D. Note that for this type of multidimensional analysis, oftentimes the best fitting sample (i.e. maximum posterior) is not positioned exactly in the middle of that interval; in fact, it does not even need to lie inside it.

Both the choice of dye molecules and the salt buffer conditions (i.e. the salt concentration) have an effect on the equilibrium constant, as well as on the kinetics between open and closed states for DNA hairpins. For the particular hairpins used in this work, assuming a perfect two-state (open-closed) system, one expects transitions from the open state with ∼10–20 % FRET (depending on the Förster distance of the respective dye pair) to the closed state with ∼100 % FRET.

The results obtained for the kinetics of hairpins labeled with different dye pairs and measured at different salt concentrations are summarized in figure 4.10. The total rate shows almost no dependence on the dye pair at 10 *mM* salt. At 160 *mM* NaCl, only the Alexa532-Alexa647 dye combination has a significantly higher rate whereas at 320 *mM* NaCl, more distinct influences of the dye molecules are observed:

Hairpins labeled with Atto647N show slow transitions but no differences between the donor dyes (6-Tamra, Alexa532, Atto532). Changing the red dye to Alexa647 leads, however, to a significant rate increase. In this case, Atto532 and 6-Tamra labeled hairpins show equal rates while hairpins with Alexa532 open and close much faster but at rates similar to the ones found for 160 *mM* NaCl.

To test the validity of the two state model the fit residuals were

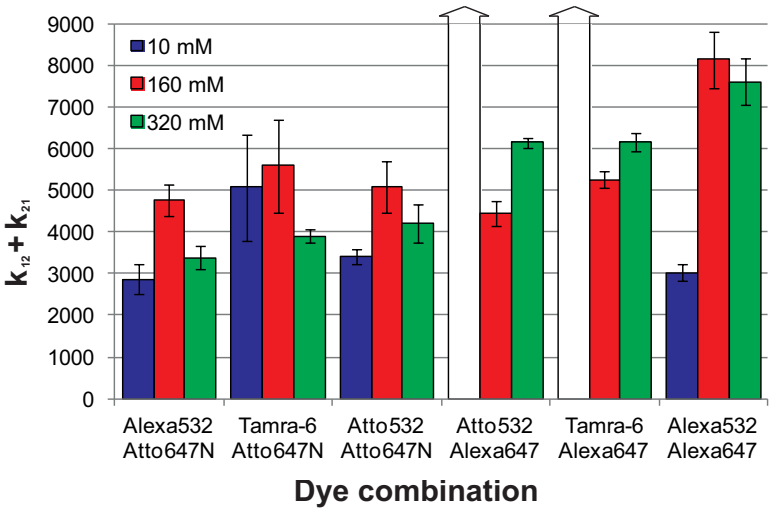

Figure 4.10: Summary of the kinetic results obtained from the FCS experiments. Overview of the determined hairpin kinetic rates for a variety of dye combinations and salt concentrations; determined sum of kinetic rates k_{12} and k_{21} for 10 mM (blue), 160 mM (red) and 320 mM (green) NaCl. Experiments were performed in triplicates and error bars were calculated for the fit-error-weighted averages. Samples not showing useful kinetic information are marked in white (dominating photophysical effects : Atto532 Atto647N 10 mM, no kinetic signal detected : Tamra-6 Alexa647 10 mM).

used. If the two state model is valid no systematic fluctuations should be observable. While the FCS data presented in figure 4.5 show the typical situation for hairpins containing Alexa647, which can be described using a simple two-state model, it was found that using Atto647N instead causes unexpectedly high residuals of the fits to the correlation functions (figure 4.11).The observed anti-correlations of the residuals from the fits to the donor auto-correlation and to the donor-FRET cross-correlation show an anti-correlation on a timescale of a few 100 μs (figure 4.11 B), which has previously been described as an indicator for the presence of additional kinetics [125]. More than two states have been reported for a five-base-pair T_{21} DNA hairpin,

A

	Alexa647		Atto647N	
	160 mM	320 mM	160 mM	320 mM
Atto532	No	No	Yes	Yes
Alexa532	No	No	Yes	Yes
6-Tamra	No	No	No	Yes

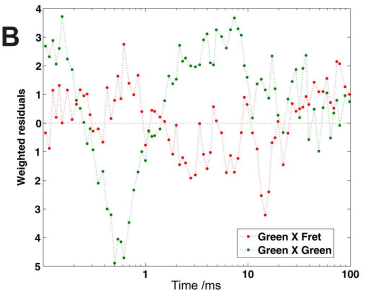

Figure 4.11: Summary of FCS datasets showing systematic deviations from the simple two-state dynamic model. A) Summary of data with (Yes, light grey) and without (No, dark grey) significant remaining residuals after globally fitting to a two-state dynamic model as described in chapter 4.2.3, B) Exemplary overlay of GGxGG auto-correlation (green) and GRxGG cross-correlation (red) residuals (Atto532-Atto647N, 320 mM NaCl) showing anti-correlated behavior.

but until now only one transition had been observed by conventional FCS [49].

4.2.4 Burst analysis experiments

Due to the discussed difficulties in extracting E_1 and E_2 from the FCS datasets, additional measurements with reduced DNA concentrations were performed, so that single-molecule fluorescence bursts could be observed. With the analysis of these bursts it was possible to gain insight into the distribution of states for each dye pair.

4.2.4.1 Burst experiments in solution

Data was collected for the double-labeled DNA hairpins in TE pH 7.6 at salt concentrations of 10, 160, and 320 mM NaCl (for details see methods in chapter 4.2.2).

Assuming a two-state kinetic system, one expects a gradual change of the equilibrium from a completely open NDA hairpin conforma-

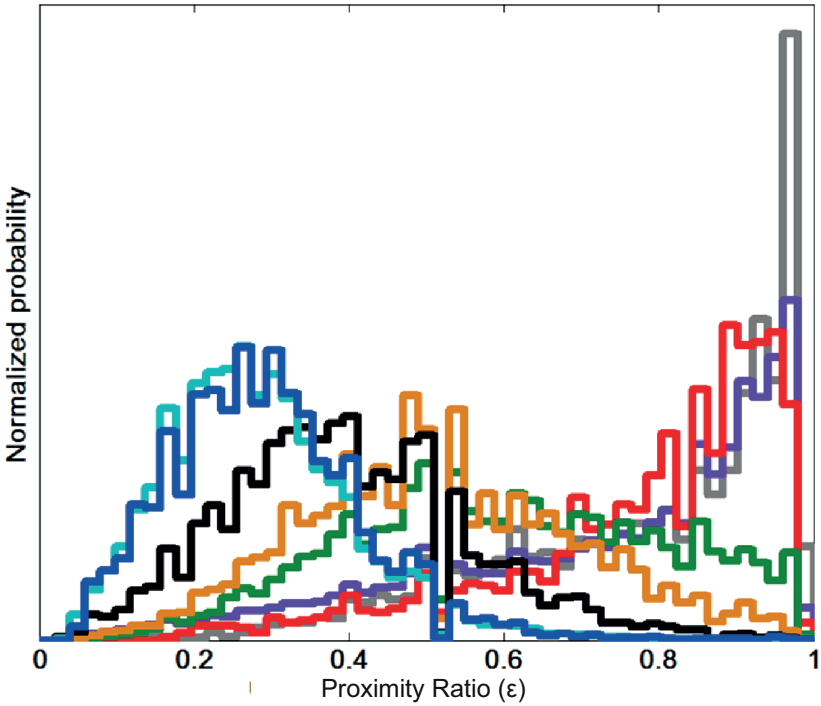

Figure 4.12: Proximity ratio distributions for hairpins labeled with the Cy3–Cy5 dye pair obtained from single-molecule burst analysis experiments. Comparison of the FRET efficiency distributions for the Cy3–Cy5 double-labeled hair-pins recorded at 0 mM (dark blue), 10 mM (light blue), 20 mM (black), 40 mM (gold), 80 mM(green), 100 mM (red), 160 mM (purple), and 200 mM (grey) NaCl concentration. Note that since for all salt concentrations only one populations exists an estimation of the γ factor was not possible (see chapter 3.2.4.3 for details). Hence the presented Proximity ratios have not been corrected for differences in fluorescence quantum yield, differences in detection efficiency, crosstalk and direct excitation.

tion at low salt (low-FRET-state-populated) to a completely closed conformation at high salt concentrations (high-FRET-state-populated) due to a shielding of the DNA backbone charge by the salt ions. From the kinetic rates determined in the FCS analysis (figure 4.10) one can estimate 3–8 transitions during the average burst duration of ~ 1 *ms*. Therefore, the mean FRET efficiencies per burst are likely to be averaged out and one expects only one distinct peak at any salt concentration, with the position of the peak determined at the respective equilibrium value [90]. For a two state system this peak position is directly related to the ratio of the rates since the FRET efficiency of this peak is the result of a dynamic averaging over the states present throughout the duration of each burst

The hairpins labeled with the Cy3–Cy5 dye combination match this expected behavior, starting from a single low FRET population at low salt and reaching almost 100% population of the closed state at ~ 100 *mM* NaCl (figure 4.12). In contrast, for a variety of combinations of 6-Tamra, Atto and Alexa dyes, different FRET histograms were observed (figure 4.13 A-F). While at low salt concentrations the histograms for all dye combinations show the expected shape, this is no longer true for elevated salt concentrations.

At 10 *mM* NaCl all hairpins are found predominantly in the open state and the main peak of the histogram is at low FRET efficiencies ($\sim$10-20%) with few observations of high FRET bursts. For high salt concentrations (160 *mM*), the different dye pairs lead to distinct histograms. Under such conditions (at least) two distinct peaks are observed. These distributions cannot be explained using a simple two-state model, in agreement with deviations from the simplistic picture in the FCS fit residuals discussed above (see figure 4.11).

A method to analyze whether a population is static or dynamic has been suggested recently by Santoso et. al. [110][109]. This method relies on the calculation of numerous proximity ratios (ϵ) for each burst by using a sliding window that contains always a constant number of photons (here 10 photons). From these proximity ratios (ϵ) one can calculate a standard deviation of the mean σ_ϵ for each burst. This σ_ϵ can then be compared to the theoretical shot noise limited

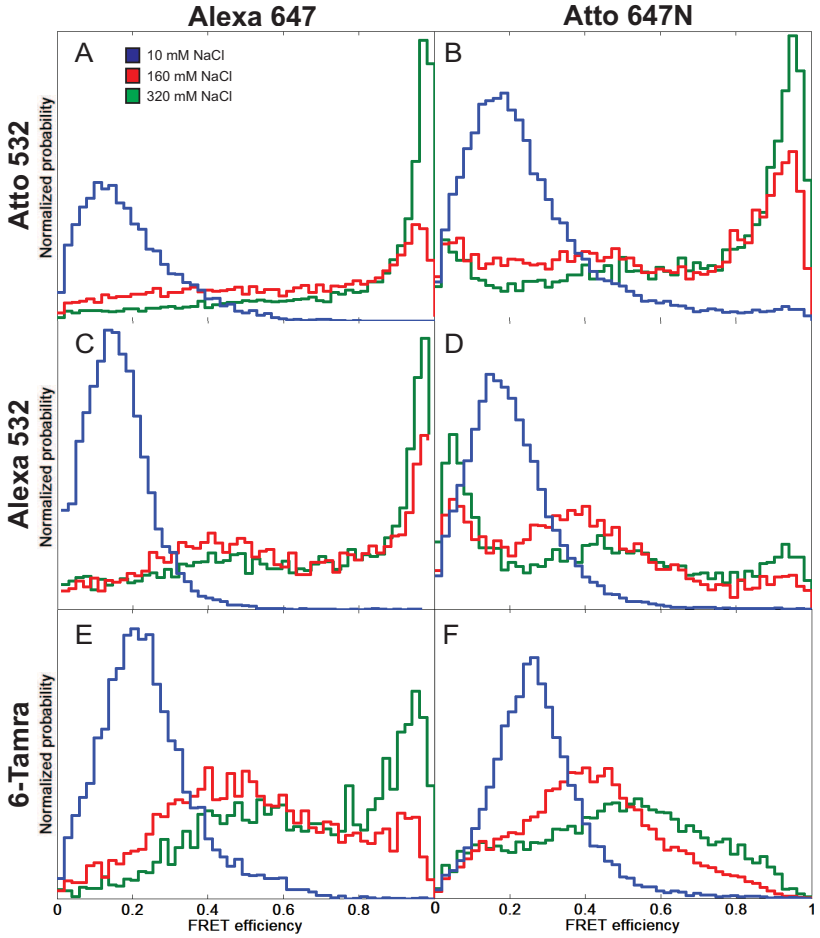

Figure 4.13: FRET distributions of DNA hairpins as a function of salt and choice of dye pair obtained from single-molecule burst analysis experiments. FRET-efficiency distributions for different FRET pair combinations measured at 100 μW laser power with NaCl concentrations of 10 mM (blue), 160 mM (red) and 320 mM (green). Shown are burst analysis data for Atto532–Alexa647 (A), Atto532–Atto647N (B), Alexa532–Alexa647 (C), Alexa532–Atto647N (D), 6-Tamra–Alexa647 (E), and 6-Tamra–Atto647N (F).

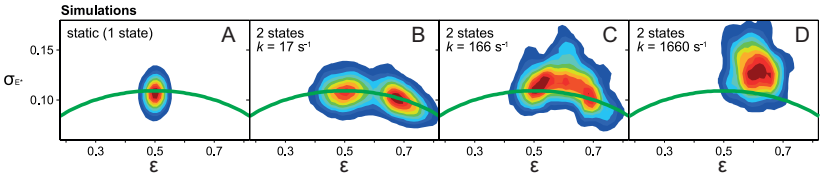

Figure 4.14: Standard deviation analysis simulations (Adapted from [109]). A burst analysis was performed on simulated timetraces requiring at least 6 photons within 500 ms and a total of 30 photons per burst. Data shown was additionally limited to bursts longer than 4 ms. The theoretical shot noise limit $\sigma_{\epsilon SN}$ (green parabola) was calculated for a 20 photon sliding window as was also used for the calculation of σ_ϵ presented here as a function of ϵ in a two dimensional contour plot. Simulated was a one state system (A), an systems fluctuating between two states of $\epsilon = 0.5$ and $\epsilon = 0.7$ at rates much slower than the diffusion through the focal volume (17 s^{-1}, B), approximately equal to the diffusion time (166 s^{-1}, C) and faster than the diffusion time (1660 s^{-1}, D). For a full description of the simulation experiment see [109].

standard deviation $\sigma_{\epsilon SN}$ (see Eq. 4.12[5]).

$$\sigma_{\epsilon SN} = \sqrt{\frac{\epsilon(1-\epsilon)}{1+GG+GR}} \tag{4.12}$$

For a whole burst analysis dataset this is usually done in a two dimensional plot of σ_ϵ and ϵ (see figure 4.14) [109].

From the simulations in figure 4.14 it becomes obvious what to expect from experimental data. Shot noise limited static bursts and bursts with dynamics slower than the diffusion time will appear close to the theoretical $\sigma_{\epsilon SN}$ calculated for the respective ϵ (green line). In contrast dynamic bursts with rates faster than the diffusion time will show a σ_ϵ exceeding the shot noise limit.

One drawback of this method however is the limitation to proximity ratios which, for different dyes, are not as easily comparable as FRET efficiencies since no corrections for the differing quantum

[5]Since a sliding window of 10 photons is used for the data presented here $GG + GR = 10$.

yields, and spectra are applied. Hence the information gained from actual experiments (see figure 4.15) is limited to a comparison of the relative amount of dynamic events and populations clearly shot noise limited between the different datasets.

Here, especially the 6-TAMRA dye combinations and Alexa532-Atto647N are mostly distributed around the shot noise limit indicating sub-populations stable on the timescale of the observation window ($\sim$2 *ms*) for these samples which are discussed in the following chapter.

In contrast Atto532-Alexa647, Alexa532-Alexa647 and to a lower extent Atto532-Atto647N show clear indications of dynamic averaging due to fast interchanging states as indicated by the burst populations significantly exceeding the shot noise limit.

To further resolve the nature of the individual sub-states, in the next chapter in gel burst analysis experiments will be used to allow for a separation of open and closed hairpins.

4.2.4.2 Burst experiments in a gel

In solution experiments (see chapter 4.2.4.1) showed that a pure two state system is not sufficient to describe the distributions obtained from single molecule burst analysis experiments. Additionally there are indications (see figure 4.15) that the observed intermediate populations are caused by both, systems that interchange fast as well as more long lived intermediate states. One method to gain further insight is to try a separation of possible subpopulations by running a gel and perform an in gel burst analysis experiment. These experiments were performed as described in chapter 4.2.2 collecting burst data in 6% Poly-acryl-amide gels at *pH* 8.0 and 400 *mM* NaCl. The reproducability of the results was tested for each dye combination by runing triplicates on non consecutive days in independent gels using fresh buffers.

When analyzing FRET histograms obtained from solution and in gel measurements it is important to note that for a currently unknown reason the peak positions of identical samples do not exactly match. The most likely reason is that the local environment somehow influ-

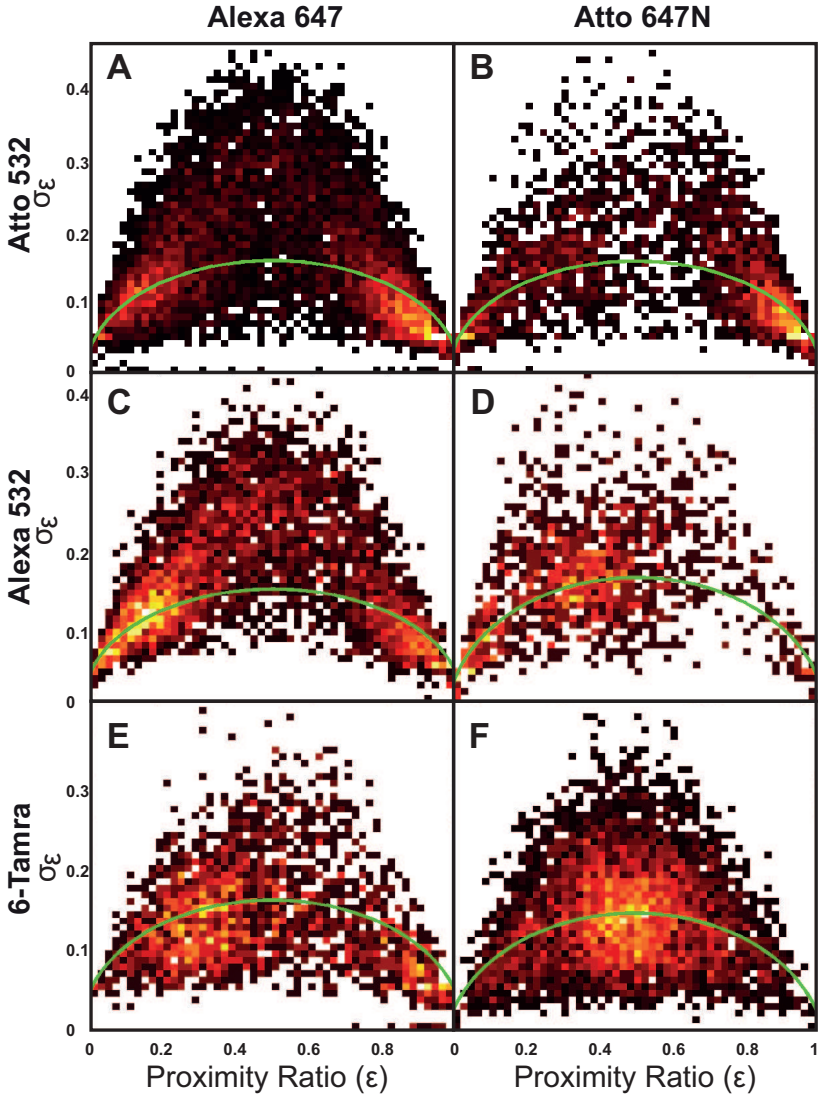

Figure 4.15: $\sigma_\epsilon / \epsilon$ distributions of DNA hairpins for different dye combinations are compared for data measured at 100 μW laser power with NaCl concentrations of 160 mM. The shot noise limit $\sigma_{\epsilon SN}$ as a function of ϵ is highlited (green line). Shown are burst analysis data for Atto532–Alexa647 (A), Atto532–Atto647N (B), Alexa532–Alexa647 (C), Alexa532–Atto647N (D), 6-Tamra–Alexa647 (E), and 6-Tamra–Atto647N (F).

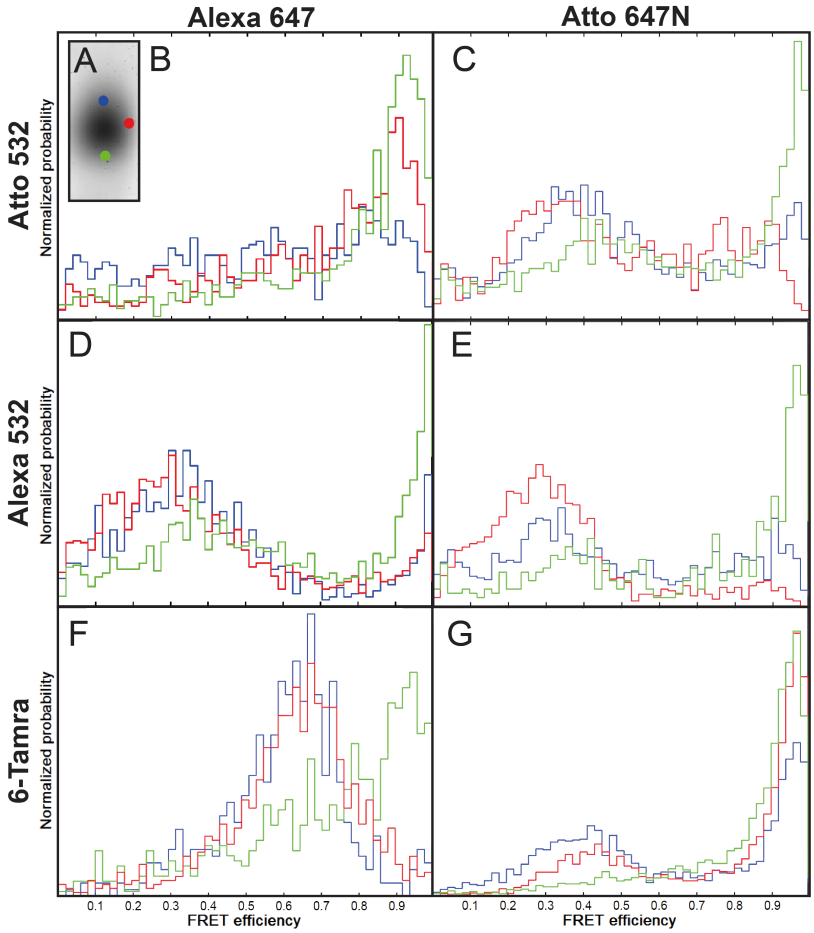

Figure 4.16: FRET distributions of DNA hairpins in a Poly-acryl-amide gel. In gel FRET efficiency distributions for different FRET pair combinations measured at 80 μW laser power in presence of 400 mM NaCl. Gels were 6% Poly-acryl-amide, running in 0.4% TBE (pH 8, 400 mM NaCl). Measurement points were located above (blue), at the edge (red) and below (green) the maximum count rate in the respective gel as indicated (A). Shown are burst analysis data for (B) Atto532-Alexa647, (C) Atto532-Atto647N, (D) Alexa532-Alexa647, (E) Alexa532-Atto647N, (F) 6-Tamra-Alexa532 and (G) 6-Tamra-Atto647N. For all dye pairs, the sub-population that moves faster through the gel shows a significant increase in the population of the closed conformation. Note that these state distributions are stable for hours at room temperature.

ences the dye properties hence biasing the Förster radius. Despite this differences between in solution and in gel measurements, assuming equal changes in the local environment for open and closed DNA hairpins it is however still possible to compare the general shape of the FRET distributions.

Before the discussion is focused on positions in the gel, lets first look at the overall features of the distributions obtained (see figure 4.16).

All gels run at 0 mM NaCl show only one low FRET population comparable to the in solution data at all measurement positions and is hence not discussed here (data not shown). The same was true for in gel burst data measured at 200 mM NaCl.

At elevated salt concentrations (400 mM)[6] almost no open hairpins (i.e. no low FRET population) can be observed anymore (see figure 4.16). Instead now a distinct high FRET population as expected for the fully closed hairpin and except for Atto532-Alexa647 (figure 4.16B) an additional intermediate state are detected.

Importantly all distinct populations observed in the gel (400 mM) experiments are also clearly visible in solution (160 mM, 320 mM). This is true for for all the dye combinations under investigation except 6-Tamra-Atto647N (compare figure 4.16G and 4.13F) which shows a significant high FRET population in gel that does not appear in solution. Such a stabilization of the closed hairpin conformation as observed for 6-Tamra-Atto647N is most likely caused by the elevated salt concentrations and the higher pH of the in gel experiments.

The most important changes however can be seen when comparing data obtained for one and the same sample but at different measurement positions within the gel. In the following the measurement positions will be described as upper (blue), lower (green, leading edge) and right (red) which is always meant relative to the intensity maximum detected in the respective band (see figure 4.16A).

With respect to these measurement positions all dye pairs show a similar behavior namely a high share of conformations showing

[6]The different NaCl concentrations required for DNA hairpin closure in gel and in solution are most likely a result of the different buffer conditions (TE, TBE, see chapter 4.2.2) but the actual origin has not been investigated in detail.

low to intermediate FRET ($0 - 80\%$ FRET efficiency) at the upper and right positions compared to an enrichment of high FRET molecules at the lower measurement position.

This data is in good agreement with the in gel distribution one would expect since the more compact and less flexible closed state (showing high FRET) can be mainly found at the leading edge while the slower diffusing more open DNA strands are found up-shifted. The only exception to this behavior was found for Cy3-Cy5 where only an intermediate FRET population could be observed at 400 mM NaCl in gel (data not shown) and which required 600 mM NaCl to show first signs of a distinct closed conformation(see Appendix A.5 figure A.16).

The most important feature of this observation is the fact that this spacial separation is stable for hours. A possible explanation for this behavior can be found in the presence of the dye molecules. In principle one can think of several possible effects that might influence the hairpin stability.

One possibility is that the two dyes directly interact with each other. Since all dyes have an extended π system one could think of two dyes π stacking which would cause a stabilization of the closed high FRET state. On the other hand, if the dyes are both positively or negatively charged they would repel each other causing a destabilization of the closed DNA hairpin.

A similar effect should be observed for a stacking of one or both dyes to a base of the stem sequence hence causing a hindrance of closure. In the two latter cases highly dynamic bursts originating from molecules attempting to close should be observed while in the first case only a stable high FRET population should be visible (For a more extensive discussion of these possibilities see chapter 4.2.5).

4.2.4.3 Atto532 causes two distinct stoichiometries

Throughout the experiments presented above only one Stoichiometry population was obtained for all dye combinations (see Table 4.1) except for hairpins labeled with Atto532 as a donor (figure 4.17) where two distinct stoichiometries were observed. Neither the choice of the

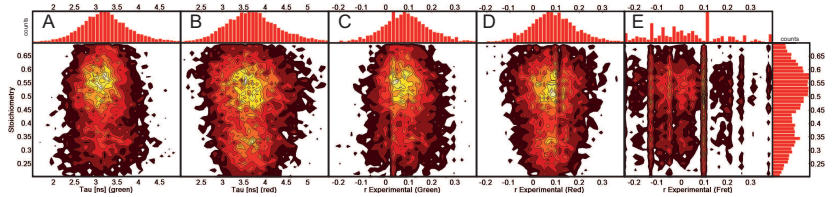

Figure 4.17: Comparison of Stoichiometry, Lifetime and Anisotropy. Atto532-Atto647N sample measured at 10 mM NaCl showing two distinct Stoichiometries (y-Axis) one centered around $Sto = 0.35$ and one centered around $Sto = 0.55$. No apparent correlation of the Stoichiometry can be detected for the fluorescence lifetime *Tau* (A,B) and anisotropy *r* (C-E) and neither for the red (B,D,E) nor for the green dye (A,C).

acceptor (Atto647N or Alexa647) nor the salt concentration influenced these two populations. They also showed indistinguishable fluorescence lifetime (figure 4.17A,B) and anisotropy (figure 4.17C-E) for the donor as well as the acceptor.

Differences could only be detected in the countrates (see figure 4.18) showing not only a decreased donor countrate (clearly visible in the low FRET samples figure 4.18B,F) but also an increased acceptor countrate (figure 4.18C,G,K,O) for the low stoichiometry population.

In order to explain these findings one might speculate about two slowly interchanging conformations of Atto532 which have the same lifetime and anisotropy (since it is chemically the same molecule maintaining its charge and π system extension). However one of the states is more quantum efficient and hence brighter. For such a case one would expect a higher FRET efficiency for the donor conformation with the higher QY (in this theory attributed to the brighter donor dye, i.e. the population with the higher Stoichiometry). The fact that the samples measured here show the exact opposite behavior (figure 4.18A,E) meaning a slightly higher FRET efficiency for the population with the lower stoichiometry however renders the above simple hypothesis inappropriate.

One way to extend the theory to match the observed data would be to assume that the brighter state (higher stoichiometry) by what-

ever mechanism quenches the acceptor dye comparatively stronger than the darker state. Using this addition to the initial theory one could explain the differing countrates in the donor (two differently bright donor states) as well as the different countrates of the acceptor (the brighter state quenches more efficiently). This quenching then could also be used to explain the observed lower FRET efficiency despite higher donor brightness since the acceptor quenching is independent of the excitation and hence a quenched acceptor would also emit fewer FRET photons. Support for the acceptor quenching hypothesis can be found in the red (i.e. the RR channel) countrate (figure 4.18C,G,K,O) as well as in the FRET (i.e. the GR channel) countrate (figure 4.18L,P) which indeed are noticeably lower for the low stoichiometry population[7].

If this effect is strong enough it might superimpose the higher energy transfer caused by the increased donor QY assumed and result in a lower observed FRET efficiency. Hence in such a case both stoichiometry populations would require an individual γ factor (see chapter 3.2.4.3) to be comparable.

Nevertheless the above model is only a hypothesis and the true origin of these two populations remains unclear and would require further investigations e.g. using NMR or comparable techniques to resolve a possible structural heterogeneity.

4.2.5 Discussion

FCS and single-molecule burst analysis experiments of DNA hairpins labeled with different dye molecules were performed to understand the effect of the probe molecules on DNA hairpin dynamics. For the FCS datasets, a global analysis approach using Bayesian-parameter estimation was developed to accurately extract kinetic information. With this approach, significant differences between hairpins labeled with different probes were observed, not only for the population of the individual states but also for the kinetics.

[7]The lower FRET countrate is only clearly visible for the high FRET samples (figure 4.18L,P). In contrast due to the few GR photons detected for the low FRET samples (figure 4.18D,H) these samples do not clearly show a correlation between stoichiometry and FRET countrate.

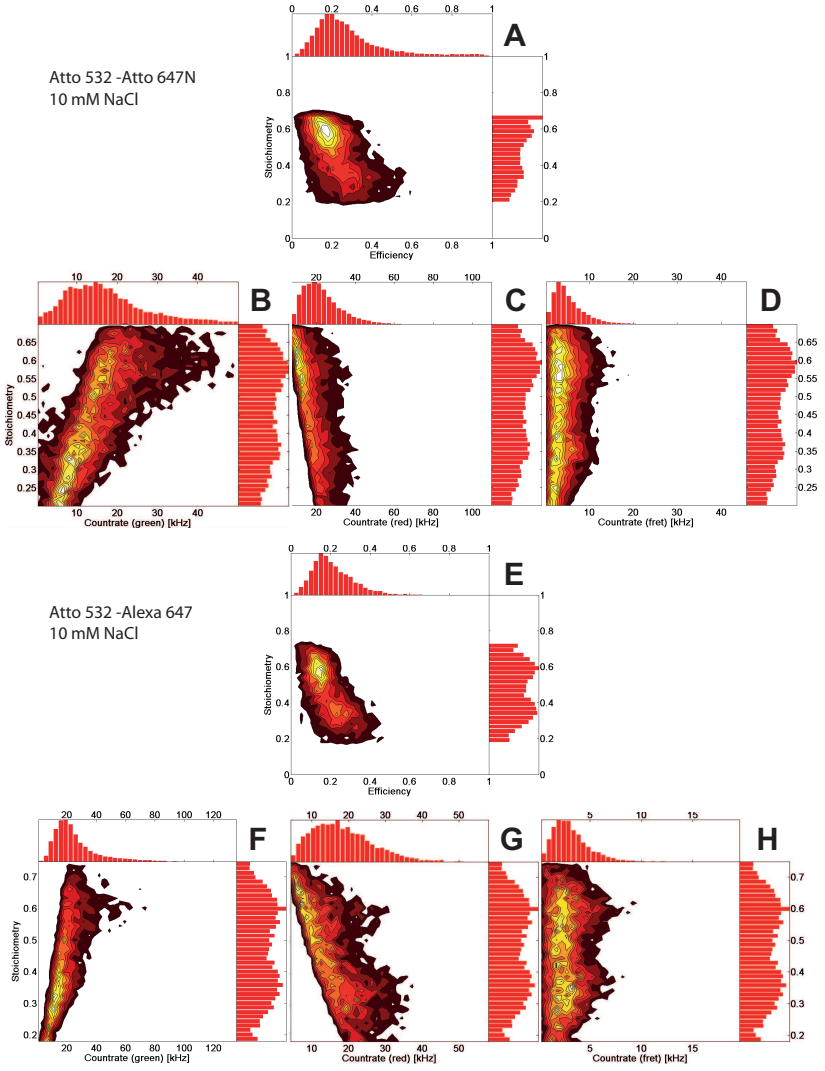

Figure 4.18: Comparison of stoichiometry and countrates in the different channels at 160 mM NaCl. Data obtained from Atto532-Atto647N (top) and Atto532-Alexa647 (bottom) show 2 stoichiometry populations at low (10 mM NaCl, left) as well as high (160 mM NaCl, right) salt concentrations. The differences in the stoichiometry clearly correlate not only with the donor countrate but also with the acceptor countrate. For an extensive discussion see chapter 4.2.4.3

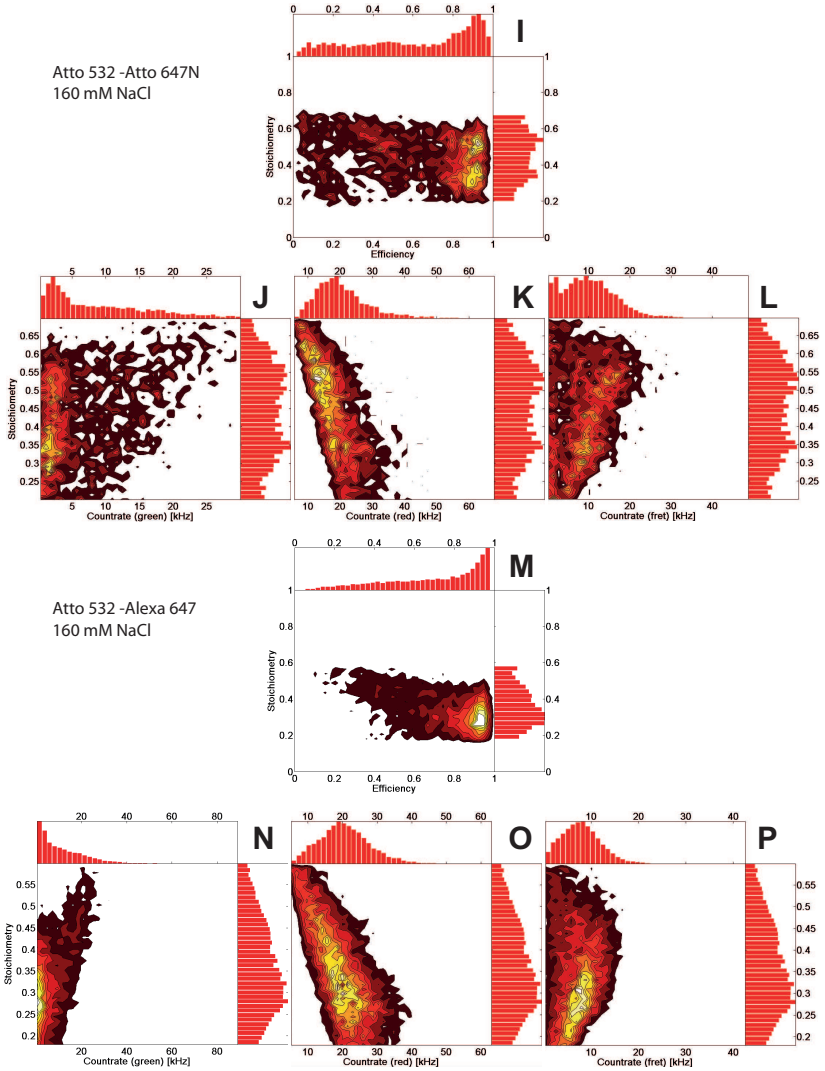
Atto 532 -Atto 647N
160 mM NaCl
I
J
K
L
Stoichiometry
Efficiency
Countrate (green) [kHz]
Countrate (red) [kHz]
Countrate (fret) [kHz]
Atto 532 -Alexa 647
160 mM NaCl
M
N
O
P

A related approach to globally fit FCS data has been published recently [102], where the number of fit parameters was reduced by assuming a transition between 0% and 100% FRET efficiency as well as by predetermining several parameters such as the triplet kinetics, focal volume and diffusion constants. By globally fitting a set of correlation functions with the remaining variables, it was possible to determine the kinetic rate. This approach has its limitations since it requires a perfect overlap of the green and red detection volumes and is only applicable to systems known to switch between 0% and 100% FRET. In contrast, the approach developed here uses a global analysis of the correlation functions without any restrictions. Even in the absence of a reliable calibration of the lateral and axial focal dimensions, it is possible to extract information such as kinetic rates and the structural parameter.

With this approach and in combination with the differing FRET efficiency distributions found in burst analysis experiments it could be shown that the opening and closing of DNA hairpins is influenced by the choice of dye molecules (figure A.4). The results show a significant influence of the dye pair on transition rates as well as on the equilibrium constant for the DNA hairpins investigated. At low salt concentrations, where the hairpins are expected to exist predominantly in the open conformation and therefore the dyes are expected to be far away from each other, all hairpins behave in a similar fashion. In contrast, a change to higher salt concentrations leads to distinct differences depending on the dyes selected. No stable hairpin is formed for Alexa532-Atto647N as well as 6-Tamra-Atto647N, even for the highest investigated salt concentrations (320 mM NaCl). Possible reasons include a sterical hindrance of hairpin formation or a repulsive interaction of the dye molecules. In contrast, other combinations of dye molecules, especially Cy3–Cy5 (and to a lower extent Alexa532–Alexa647, Atto532–Alexa647 and Atto532–Atto647N) stabilize the closed-loop conformation already at 160 mM NaCl while the 6-Tamra–Alexa647-labeled hairpins require 320 mM NaCl to show a distinct high FRET peak. Moreover, at higher NaCl concentrations, the FCS data show that not only the equilibrium state but also the kinetics are influenced by the dye pair.

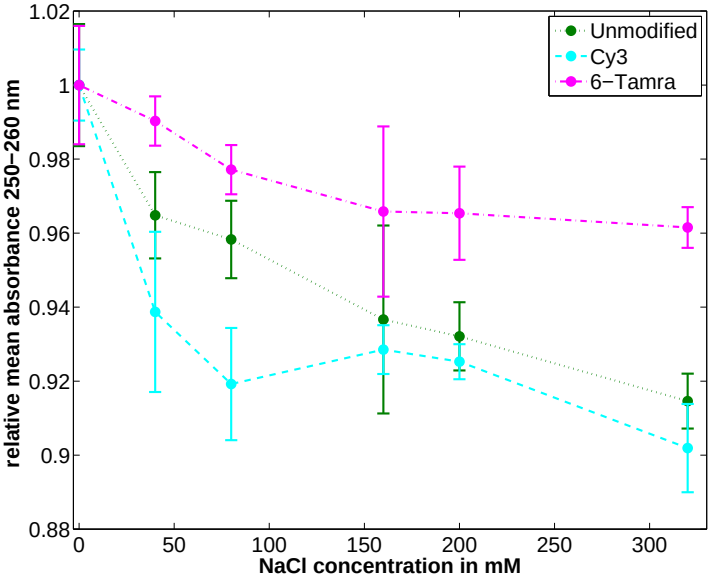

Figure 4.19: Relative absorption of selected DNA hairpins as a function of salt concentration. UV absorption (250 nm - 260 nm) for unlabeled and donor only labeled hairpins at various salt concentrations normalized to the mean of the respective 0 mM NaCl measurements are shown. Data was averaged from 2-3 independent samples per salt concentration, each measured 5 times and the computed standard deviations are shown as error bars. While the unlabeled and Cy3 labeled hairpins behave similar within the the measurement error showing a loss in UV absorption of about 9% at elevated salt concentrations, 6-Tamra shows an absorption loss of only 4% indicating less DNA being in a closed conformation.

The investigated hairpins can be classified into two groups according to their rates at 320 *mM* NaCl. The first group shows 3000–4000 transitions per second and contains all molecules labeled with Atto-647N. In contrast, all Alexa647-labeled hairpins show significantly higher rates (6000–7500 per second). Moreover, samples with Atto-647N showed a decrease in the rates while Alexa647 led to a rate increase when going from 160 to 320 *mM* NaCl, indicating that the molecular reason for the observed effects is quite complicated and has to include several different physical properties of the dye molecule, including hydrophobicity, charge, rigidity and size. Similar results come from the burst analysis data, where we find comparatively high populations of low FRET states (open hairpin) for Atto647N, even at elevated salt concentrations, but not for Alexa647. These data suggests that Atto647N strongly interacts with the DNA bases, thus hindering the DNA hairpin closure.

More insights into the effects of the dye combinations are gained by comparing the number of states that are required to describe the data for the different hairpins. The FRET distributions observed for Cy3–Cy5 labeled hairpins match the shape expected for a direct transition from an open to a closed state at a rate faster than the observation time (figure 4.12). To describe the behavior of the hairpins labeled with the other investigated dye molecules, at least one additional intermediate state is required. Previously, a three-state model was required to describe the dynamics for a hairpin labeled with Rhodamine6G and Dabcyl and containing a four-base-pair stem detected using FCS. In contrast, the same hairpin containing a five-base-pair stem could be described by a two-state model [49] [94]. It was found that for the five-base-pair system, fluctuations were too slow to be detected using FCS [94] while photon counting histogram experiments revealed the existence of a third state. The data presented here supports this interpretation, since no additional correlations are found in the residuals of the fits to the correlation functions for the 160 and 320 *mM* NaCl FCS datasets for the Alexa647 dye combinations, while the Atto647N dye combinations show (weak) additional fluctuations in the range of a few 100 μs (see figure 4.11). The latter data, as well as the burst analysis data of all Atto647N and Alexa647 dye combina-

tions, can only be explained if at least three states are used. A possible model is to introduce a semi-closed inter-mediate state consisting of numerous partially or mis-folded hairpins. In such a model, the slow process can be attributed to the formation and disruption of the fully closed stem while the fast process describes the transitions between an inter-mediate and a fully open structure.

While simple repulsion of the dye molecules would lead to a highly dynamic interchange between the three possible states, a sterical hindrance to hairpin closure, for example, caused by a dye molecule stacking to a base of the DNA, could yield a more long-lived state. DNA interactions have been reported for different dye molecules such as Tamra [22] or TexasRed [128]. For such a case, one expects a static heterogeneity, as observed in the burst analysis data. This hypothetic model is supported by in-gel burst analysis experiments, in which, depending on the position along a band, distinct FRET distributions can be identified (figure 4.16). One should note that there are other experimental techniques that can also be used for testing the influence of a dye molecule on the equilibrium value of the open versus closed state.

For example, one can exploit hypochromicity to compare the salt dependence of DNA hairpin closure in unlabeled and labeled samples. In exemplary experiments it was found that while the Cy3-labeled and the unlabeled hairpins behave quite similar, 6-Tamra-labeled samples show a deviation (figure 4.19), consistent with the interpretation that in these samples the hairpin closure is hindered.

DNA hairpins are known to be highly sensitive to changes in the stem or even the loop sequence [10]. Due to their similarity to RNA structures in ribozymes and t-RNA, understanding the effects of external reporter systems on the energy landscape is essential for numerous applications. In summary the results presented above show that the attachment of a reporter system (here, two dye molecules) clearly influences the results for the DNA hairpins investigated.

Even if the dye influence on bigger systems such as proteins is less pronounced than the influences reported here, it is important to realize that the results will depend on the choice of dye molecules. Thus, trying and comparing several dye combinations whenever working

with dynamic systems is recommended. Based on the findings presented here the use of Alexa647 as an acceptor and, if photophysics are properly accounted for, Cy3 as the donor can be suggested as good (initial) candidates for studies of molecular dynamics.

4.3 Using the nano-positioning-system (NPS) with multiparameter fluorescence detection (MFD) data

4.3.1 Introduction

The transcription of a gene to the messenger RNA (mRNA) is the first step towards the expression of a protein. Early publications concerning this topic where the term "RNA polymerase" is used to name the involved enzyme are e.g. [27][32] .

Numerous distinct RNA polymerases are known in eukaryotes, pro-karyotes and archeal bacteria. Especially eukaryotes have been shown to possess several specialized RNA polymeraseses of which the most prominent are RNA polymerasese I, II, III and IV. These four polymerases have specialized functions and yield different products such as rDNA (I), mRNA (II) and small non coding RNAs (III). The function of RNA polymerase IV is not fully understood but it is assumed to be involved in gene silencing by RNA-directed DNA methylation [123].

Despite these different functions the polymerases described above consist of comparable subunits as summarized in [16] (see table 4.6).

This chapter will focus on RNA polymerase II (PolII) which is the protein directly involved in eukaryotic gene expression.

Transcription: The transcription cycle of this enzyme can be described by three consecutive steps of which the first step is called initiation. It is dependent on several cofactors (TFIIA - TFIIH) and involves the recognition of a promoter sequence and DNA binding to form the so called preinitiation complex (PIC) [95][33]. The double stranded DNA is melted to form a transcription bubble allowing the template strand to be positioned inside the cleft of the polymerase resulting in a state commonly referred to as open complex [21] [126]. From this state the polymerase starts its transcription. After some ten bases of RNA are synthesized a release of the factors required for initiation occurs which marks the entry to the elongation state.

Table 4.6: Comparison of polymerases in different species and their subunits. according to [16]

RNA polymerase	Archea	Bacteria	PolI	PolII	PolIII
Total number of subunits	12	5	14	12	17
Molecular weight in kDa */species*	380 */P. furious*	375 */T. aquaticus*	589 */S. cerevisiae*	514 */S. cerevisiae*	693 */S. cerevisiae*
Core (10 subunits)	A′+A″	β'	A190	Rpb1	C160
	B′+B″	β	A135	Rpb2	C128
	D	α	AC40	Rpb3	AC40
	L	α	AC19	Rpb11	AC19
	K	ω	Rpb6 (ABC23)	Rpb6	Rpb6
	H	-	Rpb5 (ABC27)	Rpb5	Rpb5
	-	-	Rpb8 (ABC14.5)	Rpb8	Rpb8
	N	-	Rpb10 (ABC10β)	Rpb10	Rpb10
	P	-	Rpb12 (ABC10α)	Rpb12	Rpb12
	-	-	A12.2	Rpb9	C11
Rpb4/7 complexes	F	-	A14	Rpb4	C17
	E′	-	A45	Rpb7	C25
TFIIF	-	-	A49	Tfg1/Rap74	C37
	-	-	A34.5	Tfg2/Rap30	C53
PolIII specific	-	-	-	-	C82
	-	-	-	-	C34
	-	-	-	-	C31

Throughout the elongation phase the polymerase moves unidirectionally along the DNA template and produces a RNA transcript. To allow for a transcription despite the chromosomal compaction of the DNA this process also is supported by numerous other enzymes (see

chapter 5).

As soon as a termination sequence usually located shortly after the end of the respective gene is reached, the transcription is terminated and the final transcript is released for further processing by other enzymes.

Structure: The structure of PolII in the different states has been subject to numerous studies. First structural data was already published in 1991 with a resolution of about 16 Å[18] followed by studies showing an open and a closed conformation of the polymerase in 1997 [6]. More recently crystallographic studies were able to refine the structure of the elongation complex with nearly atomic resolution [55] [16].

In addition to the protein the structure by [55] showed the template strand from positions +9 to -10 and the non-template strand from positions +2 to +9 relative to the active center. Since an artificially assembled elongation complex was investigated also parts of the RNA strand (+1 to -8) could be refined.

The missing parts of the incorporated DNA and RNA were too flexible to be resolved by crystallographic techniques. Hence sm-FRET (TIRF) experiments were performed using fluorescently labeled DNA in elongation state constructs. These data were used in the so called nano-positioning-system (NPS) (see chapter 3.6) which revealed the position of the non template strand up to base -18 [86] [3] [4].

In this manner also the knowledge of the mRNA exit pathway could be extended to position +29 [3].

Scope of this chapter: The NPS technique used to estimate the positions of molecule parts from FRET efficiency measurements has evolved over the years. Most recent advances nowadays allow for a use of all measured FRET efficiencies in a network and includes information contained in the FRET anisotropy to further increase the positioning accuracy [85].

The improvement in resolution by applying the network analysis on the initially published data [4] has been demonstrated in [87]. To this end data of seven unknown position measured to eight known

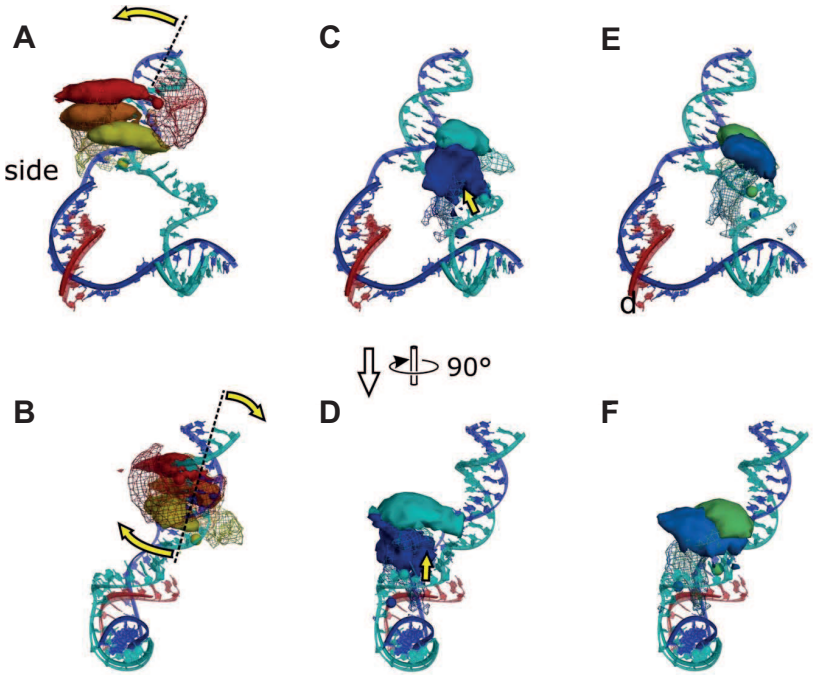

Figure 4.20: Nontemplate DNA, proposed changes in the model according to [87]. The 68% credible volumes of the marginal antenna position posterior (surfaces) analyzed globally are shown together with the obtained positions (meshes) based on the molecular model (transparent cartoons) previously proposed by [4]. The color code is nt+1 (C, D; dark blue), nt-2 (E, F; midnight blue), nt-4 (C, D; bright blue), nt-7 (E, F; green), nt-12 (A, B; yellow) nt-15 (A, B; orange) and nt-18 (A, B; red). In addition the nucleic acids observed in the crystal structure 1Y1W are shown (opaque cartoons). The global analysis suggests that the upstream DNA double strand must be tilted to form a larger angle with the downstream DNA double strand (A, B), and that the single-stranded nontemplate DNA should be located further away from the downstream part of the template DNA (C-F). Figure and caption adapted from [87]

positions was used (figures 4.21A). As a result of the improved resolution slight changes in the modeled DNA pathway were proposed (see figure 4.20). However it was stated that these results should be seen as preliminary since neither precise residual anisotropies for the donor could be measured (see chapter 4.3.3) nor was FRET anisotropy data included in the analysis [87].

Regarding the FRET anisotropy at that time only simulations showing a positive effect of FRET anisotropy measurements on the NPS resolution but no proof on experimental data could be performed (figure 4.21B-C [85]).

In this thesis a different donor dye is used to overcome the problems of insufficient donor anisotropy precision (chapter 4.3.3). In combination with MFD and the ability to measure FRET anisotropies this allowed for the first time[8] a demonstration of FRET anisotropy utilization in an NPS analysis of experimental data.

To this end single molecule MFD experiments were performed. Since FRET efficiencies as well as the FRET, donor and acceptor anisotropies should be determined as accurate as possible, multiple new developments and custom implementations of already known techniques were required.

In the following the necessary modifications of the dye pair (chapter 4.3.3), methodological developments and implementations (chapters 4.3.4, 4.3.5, 4.3.6, 4.3.7, 4.3.8) as well as the surprising finding of a DNA hairpin in the RNA polymerase II (PolII) structure are described (chapter 4.3.9).

In addition a new DNA construct that is not able to form such a hairpin is presented and demonstrated to be suitable for future experiments (chapter 4.3.9.6).

4.3.2 Experimental procedures

All measurements were performed using the confocal setup as described in chapter 3.2 at 80 μW laser power before the objective, sample concentrations of $\sim$ 50-80 pM and room temperature (RT) (i.e. 21°C $\pm$ 1°C) if not stated otherwise. The sample chambers (Lab-Tek

[8] to the authors best knowledge

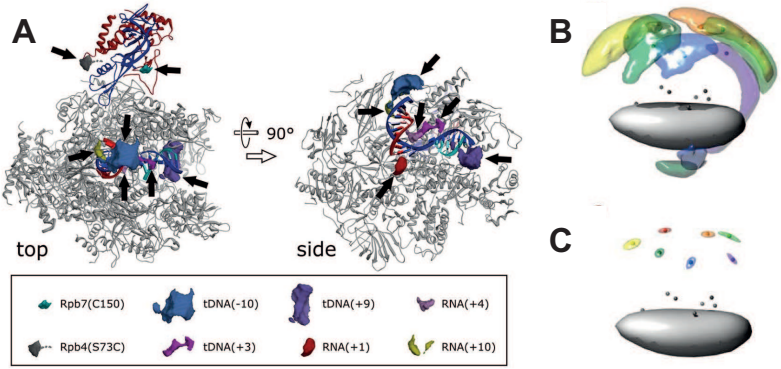

Figure 4.21: Nontemplate DNA, satellite position priors and comparison of analysis methods. (A) Nontemplate DNA, satellite position priors as published in [4]. The accessible volumes of the satellite fluorophores (indicated by arrows) are shown in top view (left) and side view (right) of the Pol II elongation complex. The position priors were flat within these volumes.
(B,C) Images of the fluorophores used to compute synthetic data are shown as spheres relative to a hypothetical macromolecule (gray surface). The antennas (unknown positions) are shown in color, the sattelites (known positions) in gray. The result of the global analysis of the FRET network without FRET anisotropy information is shown in (B). In (C) the network was analyzed like in (B), but FRET anisotropy data was used in addition to FRET efficiency data. B and C were computed with infinitely small satellite position priors. Figures and caption adapted and slightly modified from [87]

II, Nalge Nunc In. Corp. Naperville, USA) were incubated with 20 μl BSA solution (10 mM) for 10 minutes which was removed prior to sample loading.

RNA polymerase II (PolII) experiments: DNA hairpins were assembled by mixing 2 μl template strand (t)-DNA (100 μM, IBA GmbH, Göttingen), 2 μl non-template strand (nt)-DNA (100 μM,IBA GmbH, Göttingen), 2 μl RNA (100 μM,IBA GmbH, Göttingen) and 4 μl H_2O followed by heating to 95°C and slowly (2°C/min) cooling to 4°C if not stated otherwise.

The resulting double labeled DNA hairpin was diluted to a concentration of approx 50pM in Assembly buffer (Tab: 4.7) containing 10 mM Dithiothreitol (DTT) and 0.1mg/ml BSA. A total volume of 20 μl was loaded to the measurement chamber and measured for 1h prior to the addition of 2 μl PolII stock solution (1.5$pmol/\mu l$). After an incubation time of 10 minutes the sample was measured for 2-4 h.

A burst search was performed on the resulting photon streams with thresholds of 5 photons within a time interval of 0.5 ms and a total burst size of at least 60 photons (see chapter 3.2.4.1). The resulting bursts where then refined using fluorescence stoichiometry, lifetime, anisotropy and the time deviation signal (TDS) as described in the following chapters.

Protein induced fluorescence enhancement experiments: protein induced fluorescence enhancement (PIFE) DNA oligo-meres where obtained from IBA GmbH, Göttingen (Alexa647 samples) and H. Hwang and S. Myong (Cy3 samples). The DNA was annealed using 10 μl labeled forward strand and an excess of 20 μl unlabeled reverse strand (100 μM) to minimize labeled ssDNA in the final sample. This mixture was heated to 95°C and slowly (2°C/min) cooled down to 4°C. The resulting sample was diluted to a final concentration of 80 pM using BamH1 Binding Buffer (Tab: 4.8) containing 1% 2-Mercaptoethanol (BME) (Cy3 experiments) or 1% DTT (Alexa647 experiments) to maintain comparability to the original publicaction (Cy3, BME) [45] and the PolII measurements (Alexa647, DTT). Please note

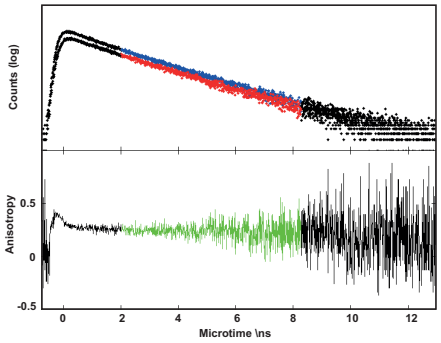

Figure 4.22: The timerange selected for the calculation of the residual anisotropy is exemplarily given for the red detection after red excitation of a sample containing Alexa647 labeled DNA bound to BamH1 with a dye-protein distance of 1 basepair. The selected timerange is marked in the Microtime histograms (upper panel) for the parallel (blue) and perpendicular (red) detection as well as in the corresponding time resolved anisotropy graph (lower panel, green).

that this buffer contains Ca^{2+} instead of Mg^{2+} to prevent the restriction enzyme BamH1 from cleaving the DNA. Data were collected by measuring a total volume of 20 μl of this dillution for 1.5 h. Finally 0.5 μl BamH1 stock (800 nM, Invitrogen) were added to the respective sample and after an incubation time of 10 minutes another measurement of 1.5 h was performed. The high excess of BamH1 was required to guarantee 100% binding of the DNA construct.

A burst search was performed looking for at least 5 photons within a time interval of 0.5 ms and a total burst size of at least 60 photons (see chapter 3.2.4.1). The lifetime fit was performed on each individual burst as described in chapter 3.2.4.6 and the lifetime weighted anisotropies for each burst where calculated (see chapter 3.2.4.5). From the resulting histograms the lifetime and lifetime weighted anisotropy values where extracted using a Gaussian fit. The residual anisotropy (r_∞) was determined by generating micro-time histograms of the bursts and calculating the fluorescence intensity weighted mean anisotropy after a relaxation time of 2 ns as indicated in figure 4.22 assuming a

fast reorientation of the dye within its boundaries in the first 2 *ns* (see also chapter 4.3.6).

Buffers: A summary of the Buffers used in this chapter can be found in the Tables below.

Table 4.7: Composition of the Assembly Buffer

Assembly Buffer	
50 *mM*	HEPES
40 *mM*	$(NH_4)_2SO_4$
5 μM	$ZnCl_2$
5%	Glycerol
5 *mM*	DTT

Table 4.8: Composition of the BamH1 binding Buffer

BamH1 binding Buffer	
50 *mM*	Tris-HCl pH 8.0
10 *mM*	$CaCl_2$
100 *mM*	NaCl

4.3.3 Dye selection

The choice of an appropriate dye combination is critical when accurate distances measurements shall be performed.

Due to the sixth power dependence of FRET efficiency and actual distance (see equation 2.5) an important criteria for good sensitivity is to find a dye pair that has a R_0^{iso} in the range of the expected distances. Additionally the dye pairs of choice are required to absorb and fluoresce at a wavelength compatible with the available equipment to be minimally perturbing the investigated system (see chapter 4.2).

To this end the initial studies on RNA polymerase II (PolII) were performed using a dye combination of Alexa555 and Alexa647 with

R_0^{iso} values determined to be in the range of 45-54 Å depending on the sample [2][4].

According to equation 2.7 R_0^{iso} depends on two parameters also relevant for dye selection namely the overlap integral and the quantum yield (QY) of the donor dye.

The fluorescence lifetime and QY are related since a low lifetime usually means that there are effective deexcitation pathways that allow the dye to loose energy on a timescale faster than fluorescence would occur (e.G. internal rotation of a dye, see equations 2.1 and 2.2). A loss of energy through non-fluorescent pathways causing a low fluorescence lifetime hence also lowers the QY.

To allow for an easier understanding of this effect assume two dyes with similar spectra and identical natural lifetime[9] [64]. Since in this case only the non-radiative decay rates are important for the observed lifetime, a dye with a high observed lifetime as required for the desired experiments would also have a high QY as compared to a dye with a low observed lifetime. In terms of changing the donor dye and maintaining the acceptor this means that a donor with similar wavelength but higher fluorescence lifetime would, under the above assumption, cause a higher R_0^{iso}.

The donor dye used for the experiments in [4], Alexa555 has a relatively low lifetime of only $\sim 0.3ns$ [10] which is approximately equal to the full width half maximum (FWHM) of the setups instrument response function (IRF) (see chapter 3.2). Combined with the poor quantum yield of only about 10% causing poor statistics, this short lifetime made it difficult to extract residual anisotropies from single molecule experiments (see chapter 4.3.6). Since the determination and use of residual anisotropies throughout an NPS analysis was essential for this project an alternative for Alexa555 had to be found. To minimize changes compared to the initial experiments a new donor dye compatible with Alexa647 as an acceptor and showing R_0^{iso} values of

[9] i.e. the lifetime a dye molecule has without non-radiative decay paths. It is defined as $\tau_n = 1/k_r$ and can be calculated from the QY and lifetime of the dye according to [64] $\tau_n = \tau/QY$.

[10] http://de-de.invitrogen.com/site/de/de/home/References/Molecular-Probes-The-Handbook/tables/Fluorescence-quantum-yields-and-lifetimes-for-Alexa-Fluor-dyes.html, 13.04.2012

approximately 45-54 Å was required.

To overcome the problem described above an Atto520 dye with a fluorescence lifetime of $\sim 3.6ns$ and a QY of 90% [11] which is blue shifted as compared to Alexa555 was used. This blue shift causes a decrease in the overlap integral with Alexa647 leading to an R_0^{iso} in the desired range (see tables 4.11 and 4.12).

4.3.4 The time deviation signal (TDS)

This method was used in an unpublished collaboration with the group of Prof. Dr. Gernot Längst (Universität Regensburg). To allow for a full understanding of the work presented in the thesis of Josef H. Exler parts of this chapter can also be found in the appendix of [24]. It additionally has been published as part of a collaboration with the group of Sandra Haake (Ludwig-Maximilians-University, Munich) [9].

A general problem with single molecule measurements are the binding constants of the respective sample contents. For many biomolecules concentrations typically used in burst analysis or even FCS measurements are lower than the binding constant hence requiring some additional effort to allow for a successful experiment.

While for FCS measurements the focal volume dimensions can be reduced thereby allowing the sample concentration to increase [54] this is not possible for burst analysis methods where a rather long residence of the molecule in the focal volume is desired. Additionally, nucleosomes as under investigation in chapter 5 are prone to become instable at low concentrations as well as when interacting with surfaces, thus in order to avoid artifacts the duration of the experiment has to be minimized while the concentration should be maximized.

Oftentimes a tradeoff has to be found where one has to keep in mind that with increasing concentrations the occurrence of multimolecule bursts is not negligible. For a homogeneous population with only a single FRET species this is not a problem. In contrast, if

[11] determined in PBS pH 7.4, http://www.atto-tec.com/fileadmin/user_upload/Katalog_Flyer_Support /Dye_Properties_01.pdf, 13.04.2012

several FRET states exist, multi-molecule events of different species will alter the determined FRET values. Moreover, impurities such as complexes labeled with only donor or acceptor observed simultaneously with double-labeled complexes will also lead to changes in the detected FRET efficiencies.

However, as two independently diffusing complexes don't enter and exit the excitation volume exactly at the same time it is possible to differentiate these multi-molecular events from single molecule events and to exclude them from further analysis. Independently diffusing molecules involved in a multi-molecule event will yield different values for the mean-macro-time (MMT) (i.e. the time where 50% of the respective photons have arrived, see Figure 4.23) for all photons of a burst, as compared to that for the photons of one color. Therefore a characteristic time deviation signal (TDS) can be calculated by defining:

$$\begin{aligned} TDS = &((D_{\text{all}} - D_{\text{green}}) + |T_{\text{all}} - T_{\text{green}}|) * (1 - \epsilon) \\ &+ ((D_{\text{all}} - D_{\text{FRET}}) + |T_{\text{all}} - T_{\text{FRET}}|) * \epsilon * \gamma \end{aligned} \tag{4.13}$$

where D_x is the burst duration, T_x is the MMT, γ is a factor correcting for the different detection efficiencies and QYs in the red and green channels (see chapter 3.2.4.3) and ϵ is the proximity ratio given by the number of photons in the burst as defined in equation 3.7.

Independently diffusing molecules involved in a multi molecule event will cause a deviation of the MMT calculated for all photons of a burst and the MMT for the individual photons of one color. As these burst properties are used to calculate the TDS for each burst by analyzing the differences between the values calculated from all photons and the ones calculated for individual channels one has to make sure that there is no influence of the respective FRET efficiency. E.g. for a high FRET burst where only very few green photons are detected a simple green TDS calculated according to $TDS_{\text{green}} = ((D_{\text{all}} - D_{\text{green}}) + |T_{\text{all}} - T_{\text{green}}|)$ will be very noisy due to the poor statistics and does not contain much useful information. Similarly, for low FRET complexes a TDS calculated according to

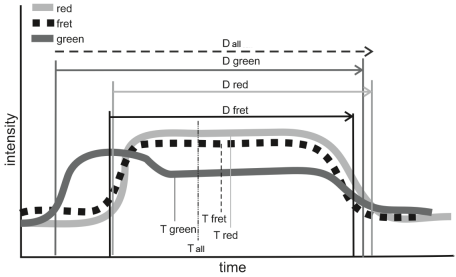

Figure 4.23: Schematic of mean-macro-time and burst duration. The schematic development of fluorescence intensity with time is used to exemplarily summarize the definitions of duration and MMT. For this schematic a theoretical multi-molecule event containing a donor only and a double labeled high FRET species is assumed. Positions of the MMT (T_x) as well as the durations, defined as the time difference between the first and the last photon in the respective channel of a burst (D_x), are marked.

$TDS_{\mathrm{FRET}} = ((D_{\mathrm{all}} - D_{\mathrm{FRET}}) + |T_{\mathrm{all}} - T_{\mathrm{FRET}}|)$ would be noisy due to the fact that in this case only few photons are detected in the red channel after green excitation. Therefore the TDS of these two channels is computed simultaneously and the relative value of the green versus the red TDS is adjusted according to the percentage of photons detected (see equation 4.13).

Equation 4.13 is generally applicable to burst analysis data and allows for detection of almost all cases of bursts containing more than one molecule at a time except multi molecule events containing low (0%) FRET double labeled and donor only molecule mixtures. The latter species can only be identified using an experimental setup that employs PIE [84] [65]. Using a PIE setup one can define a second criterion using the additional information of red detection after red excitation (RR).

$$TDS_{\mathrm{red}} = ((D_{\mathrm{all}} - D_{\mathrm{red}}) + |T_{\mathrm{all}} - T_{\mathrm{red}}|) \tag{4.14}$$

Here, the number of photons detected in the RR channel will be independent of the FRET efficiency.

Together these two parameters (TDS, TDS_{red}) can then be used to remove multi-molecule events from burst analysis data by excluding bursts with a TDS and or TDS_{red} above a given threshold from the further analysis.

To demonstrate the capabilities of this method a sample containing 23-NPS1-67 nucleosomes (see chapter 5.3, Ex0 Buffer chapter 5.2.3) as well as impurities of donor only and acceptor only complexes was measured. In order to stress the discussed effects for these test experiments the concentration of molecules was chosen to be high enough that most bursts detected show multi-molecule characteristics ($\sim$150pM double labeled nucleosomes).

Previously, it had been common practice that data cleanup was done by selecting bursts through a stoichiometry criterion only [65]. For example in the described experiment histograms would have been calculated from bursts with stoichiometry values between $\sim$0.45 and $\sim$0.77 (Figure 4.24 A, red) leading to a washed-out FRET efficiency histogram especially in the medium FRET area and an unnaturally sharp cut off in the stoichiometry distribution. In comparison using stringent thresholds of TDS <0.1 and TDS_{red} <0.1 a clean stoichiometry distribution is received showing peaks of distinct FRET efficiencies (Figure 4.24 B). In addition the resulting FRET histogram is almost identical with data measured at far higher dilutions as shown in figure 4.24E.

While these tests were performed at concentrations higher than normal they nicely visualize the capabilities of this method. Under regular conditions where only a few percent of all events are multi-molecular the appropriate TDS thresholds are determined by iterative optimization of Stoichiometry-TDS_x and Efficiency-TDS_x plots. Throughout this optimization one usually tries to find thresholds that remove as many multi-molecule events (stoichiometries higher or lower than the double labeled population) while maintaining as many events as possible. For the experiments presented in this thesis a starting value of 0.7 for TDS and TDS_{red} turned out to be a good initial guess.

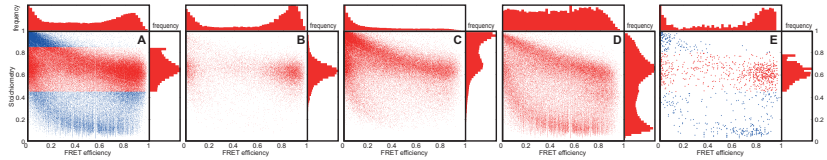

Figure 4.24: Effects of the TDS filter. The two dimensional plot of Stoichiometry versus FRET Efficiency recorded with a mononucleosome sample containing 6-NPS1-67 nucleosomes (A-D, $\sim 150pM$, Ex0 Buffer). (A) Bursts within a limited Stoichiometry area (S = 0.45-0.80) that would have previously been selected for data analysis are highlighted in red and were used for one dimensional projections of FRET efficiency (top) and stoichiometry (right). Besides dual labeled nucleosomes, the sample contained also impurities of donor and acceptor only complexes. The high concentration of molecules in the sample combined with the significant amount of single labeled impurities cause strong multi-molecular trailing. (B) A significant improvement of the data quality is reached by removing the multi-molecule events using TDS <0.1 and TDS_{red} <0.1 (B). The events removed by TDS_{red} <0.1 (C) and TDS <0.1 (D) as well as a sample measured at far higher dilution (E, $\sim 15pM$) are additionally shown to allow for an easier understanding of the TDS effect.

4.3.5 Protein induced fluorescence enhancement (PIFE): A measure for protein binding

A mayor problem with the assay used for the PolII experiments presented below is that both dye labels are located on the DNA. Hence colocalization of the two dyes does not prove the presence of the protein of interest and a separate measure had to be developed.

One commonly used way is to add a label on the protein, which however might be accompanied by new problems such as an additional FRET path and low labeling efficiencies. Recently, a fluorescence lifetime and brightness increase upon reduction of the distance to a protein has been shown for Cy3, Cy5 and DY547 bound to a DNA [45]. It is speculated that since this effect can only be observed for dyes with a Cyanine based structure (Figure A.4) it might be caused by a hindrance of light induced cis trans isomerization [108]. This would cause the dye to spend more time in its bright trans state and

additionally reduce the importance of a non radiative energy loss pathway leading to an increased fluorescence lifetime. Following this model, one would also expect an increase in fluorescence anisotropy due to the hindrance of dye motion. Hence, for DNA constructs with dye positions known to be in close proximity to a protein a two dimensional parameter change should be observable in a MFD experiment. Such a change could then be used for separating what will in the following be referred to as free DNA from protein bound DNA. Please note that brightness changes are not sufficiently sensitive in confocal experiments and cannot be used as additional separation parameter.

Proof of principle: For the NPS analysis Atto520-Alexa647 was chosen as FRET pair (see chapter 4.3.3). Importantly Alexa647 is also a Cyanine dye (Figure A.4) and should therefore show similar behavior than Cy3 or Cy5 upon protein binding.

In order to prove the applicability of PIFE on the Alexa647 PolII system, samples consisting of a dsDNA with a BamH1 binding site in a distinct distance to the 5′ dye label (see table 4.9) were prepared. Measurements were performed in a buffer containing Ca^{2+} instead of Mg^{2+} to prevent BamH1 from cleaving the DNA sample (for details see chapter 4.3.2) hence resulting in stable constructs with a well defined dye-protein distance.

Using this approach two dyes namely Cy3 (Provided by H. Hwang and S. Myong) and Alexa647 (IBA GmbH, Göttingen) were measured and analyzed (see chapter 4.3.2 for measurement conditions).

To maintain comparability with the original experiments by [45] the Cy3 sequence complementary strands were one base pair shorter than the forward strand and hence the labeled 5′ Thymine was not basepaired. Differing from that, the complementary strand of the Alexa647 sample was the same length as the forward strand in order to exclude possible artifacts from a non-paired base close to the dye.

As expected not only a change in fluorescence lifetime but also in anisotropy could be monitored upon a change of the BamH1-Dye distance for Cy3 as well as Alexa647 (Figure 4.25). A direct comparison of the absolute Cy3 lifetime values presented here with the results

Distance	Forward strand sequence
1 bp	Cy3-T T**GG ATC C**AT AGT AGC GTA GCG TAG CGT AGC GTA GCG TAG C
	Cy5-T T**GG ATC C**AT AGT AGC GTA GCG TAG CGT AGC GTA GCG TAG C
3 bp	Cy3-T TAT **GGA TCC** ATA CGT AGC GTA GCG TAG CGT AGC GTA GGC G
5 bp	Cy5-T TGT AT**G GAT CC**A TAC GTA GCG TAG CGT AGC GTA GCG TAG G
7 bp	Cy3-T AGC GTA T**GG ATC C**AT ACG TAG CGT AGC GTA GCG TAG CGT A
	Cy5-T AGC GTA T**GG ATC C**AT ACG TAG CGT AGC GTA GCG TAG CGT A
15 bp	Cy3-T CGT ATA TAC GTA GCG **GGA TCC** TAG CGT AGC GTA GCG TAG G

Table 4.9: DNA sequence used in the BamH1 Experiments. The forward strands for various Dye-Protein distances are listed with their 5′ labeling possibilities and the BamH1 recognition site depicted in bold letters.

Sample	Hwang et. al	Std. Lifetime Fit	Ext. Lifetime Fit
1 bp	0.64 $\pm$0.09 *ns*	0.77 $\pm$0.01 *ns*	0.76 $\pm$0.01 *ns*
1 bp BamH1	1.26 $\pm$0.27 *ns*	1.74 $\pm$0.1 *ns*	1.88 $\pm$0.02 *ns*

Table 4.10: Summary of lifetime fit results obtained for samples with 1 bp distance to the BamH1 binding site. Exemplary results from [45] are indicating lower lifetimes than obtained using single molecule subpopulation selection and the simplified fit used throughout this work (Standard Lifetime Fit, chapter 3.2.4.6 equation 3.20) or the Extended Lifetime Fit (chapter 3.2.4.6 equation 3.19)[111][60].

published by Hwang et. al. shows similar lifetimes within the error of the measurement for the DNA only constructs. In contrast a systematic deviation from the published data towards longer lifetimes slightly exceeding the measurement error is found for the BamH1 bound construct (see Table 4.10).

To exclude that this effect is caused by the simplified lifetime fit used here (see chapter 3.2.4.6) the 1 basepair distance data was reanalyzed using a software applying the more complex equation 3.19 including a background compensation published by [111] [60] (Software: MFD_Paris, AK Lamb). Since the results obtained in this way match the results from our simplified algorithm the different results can only be caused by the sample itself. The most likely reason is dirt causing events with a short fluorescence lifetime (e.g. scatter). Such events could not be treated at all by the bin-wise method used

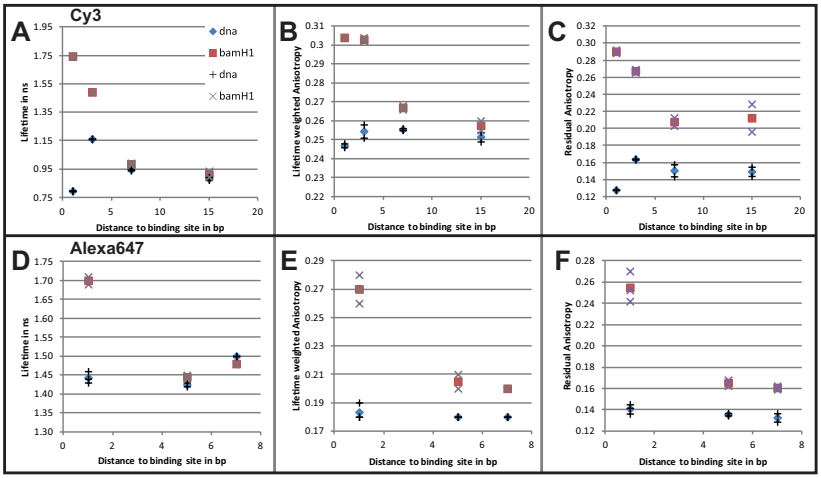

Figure 4.25: Summary of Alexa647 and Cy3 PIFE results. The BamH1-Dye distance dependence of lifetime (left), lifetime weighted anisotropy (middle) and residual anisotropy (right) is shown for Cy3 (upper panels) and Alexa647 (lower panels). Samples containing DNA only are marked as blue diamonds (mean value) and black crosses (individual measurements). Data obtained from DNA bound to BamH1 is depicted as red squares (mean value) and grey crosses (individual measurements).

by Hwang et. al. while for the experiments presented here, short lifetime background events were efficiently removed by single molecule burst analysis and subpopulation selection.

Nevertheless, since only relative changes are of importance for PIFE the difference in the absolute values does not change the finding that PIFE works for Cy3 as well as Alexa647.

Interestingly a lifetime dependence on the DNA sequence can also be detected (i.e. different fluorescence lifetimes for the same dye but different DNA construct, see DNA only measurements (blue data points in figure 4.25A and D). This can either be caused by increased stacking to neighboring bases, by differing DNA end melting or by increased quenching by a distinct base in close proximity to the dye [78]. Due to this lifetime dependence on the DNA sequence it is not

sufficient to analyze the lifetime weighted anisotropy as as discussed before (see chapter 3.2.4.5 and Eq. A.1 in the appendix).

The residual anisotropy, the anisotropy a system decays to after averaging over all degrees of freedom, is however by definition independent of the lifetime and is hence a good measure to compare the mobility of a dye in an otherwise equally sized system[12] (figure 4.25C,F).

The data clearly shows that not only the lifetime rises with the proximity of the protein but also the anisotropy increases and hence the average mobility of the dye decreases. While there is a difference between the residual anisotropy and the lifetime weighted anisotropy (compare figure 4.25 B,E and C,F) the effect of an increasing anisotropy upon protein binding is obvious in both values and hence the much easier accessible lifetime weighted average (figure 4.25B,E) will be used in combination with the lifetime (figure 4.25A,D) for the selection of PolII bound DNA strands.

Application to the PolII system: Having proven the general applicability of PIFE to Alexa647 labeled DNA it is important to demonstrate the sensitivity of the system for the NPS experiments. To this end a sample containing *Bubble*1 labeled at positions nt-12 (Alexa555) t+3 (Alexa647) was measured before (figure 4.26A) and after the addition of PolII (figure 4.26B-D).

As expected the addition of PolII caused an increased lifetime and anisotropy of Alexa647 upon protein binding (compare figure 4.26A and B, green). Importantly also many DNA strands remained unbound as indicated by the population with lifetime and anisotropy values (figure 4.26B, blue) identical to the values detected before the protein was added (figure 4.26A).

[12]The samples investigated here have a molecular weight of about $\sim 25kDa$ resulting in an estimated rotational correlation time of $\sim 15ns$. Since this is on the timescale of the experiment the dyes residual anisotropies will be slightly biased by the rotation of the whole system. Hence the discussion of the results is limited to a comparison of equally sized systems where the rotation of the whole construct is assumed to have an equal influence. (http://www.nmr2.buffalo.edu/nesg.wiki/NMR_determined_Rotational_correlation_time, 8.6.2012)

To exclude that this population with unchanged parameters was also protein bound but did not show the PIFE effect, the burst events where separated by lifetime, anisotropy and FRET efficiency[13]. In order to gain information on the diffusion time the photon streams of RR corresponding to the respective populations were correlated. It is important to note that the PIE information of RR has to be used since it is the only photon stream not biased by FRET processes and possible intra molecular dynamics. Additionally the sample containing just the free DNA and no PolII was correlated and the resulting correlation function was used as a reference for free DNA. As expected the population with lower Fluorescence lifetime and lower anisotropy (see Figure 4.26E, bluecurve) shows a diffusion time similar to the free DNA (Figure 4.26E, red curve). In contrast, the population with higher lifetime and higher anisotropy shows a significantly increased diffusion time (Figure 4.26E, green curve) which can be easily explained by the increased hydrodynamic radius upon PolII binding.

In summary PIFE offers an easy way of separating free from protein bound DNA without the need for additional labellings and will be used in the following to ensure that only PolII bound DNA constructs are included in the NPS analysis.

4.3.6 Anisotropy determination

In order to calculate distances from FRET efficiencies it is necessary to possess information about the relative (average) orientation of the dyes. Such information can be gained by determining the residual anisotropy (see chapter 2.4) of a sample. The residual anisotropy can be determined from time resolved anisotropy measurements, which however are not in all cases straight forward. This chapter will explain the corrections necessary to minimize systematic errors when calculating the time resolved anisotropy from the lifetime decays recorded for polarizations parallel and perpendicular to the excitation of each

[13] An additional separation by FRET efficiency was only possible for this special sample showing two distinct FRET populations, one at $\sim$ 50% and $\sim$ 80% FRET efficiency. All other positions measured did not show clearly separated populations in the FRET prameter space and hence could only be separated by anisotropy and lifetime.

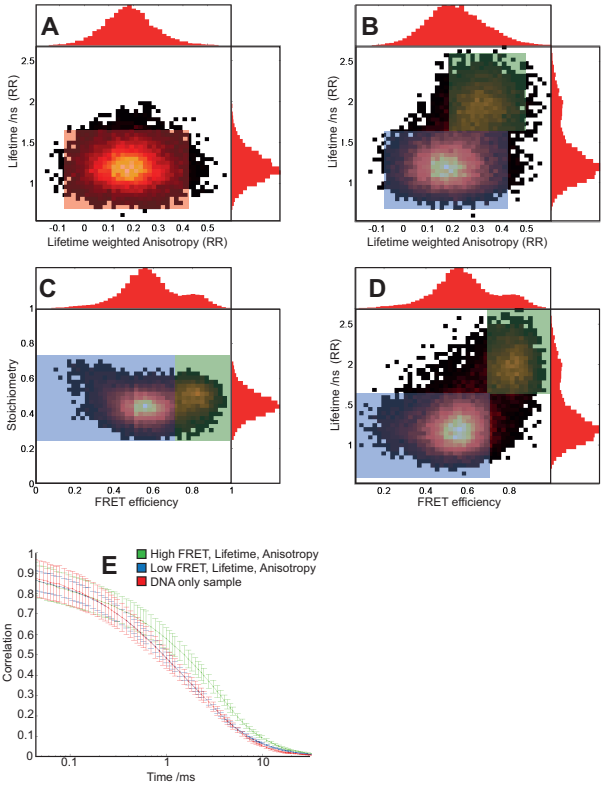

Figure 4.26: PIFE studies of PolII complexes. A sample containing *Bubble*1 **constructs labeled at positions nt-12 (Alexa555) and t+3 (Alexa647) was measured before (A) and after (B-D) the addition of PolII. Shown are the two dimensional histograms of parameter combinations important for the PIFE based separation of free and protein bound DNA together with their one dimensional projections. Only one population of fluorescence lifetime and anisotropy can be detected for the DNA only sample (A) while two distinct populations are found after PolII addition (B-D). The subpopulations are separated by FRET Efficiency (C,D), fluorescence lifetime (B,D) and anisotropy (B).**
(E) The auto-correlation functions of the red detection after red excitation (RR) channel were calculated for each subpopulation as indicated in the histograms by the respective color (green or blue) and compared to the autocorrelation of the free DNA sample (red). The data shown here was cleaned from multi molecule events and dirt using $0.25 \leq S \leq 0.7$**,** $TDS = 0.45$**,** $TDS_{red} = 0.5$ **and** $FRETcountrate \geq 5kHz$**.**

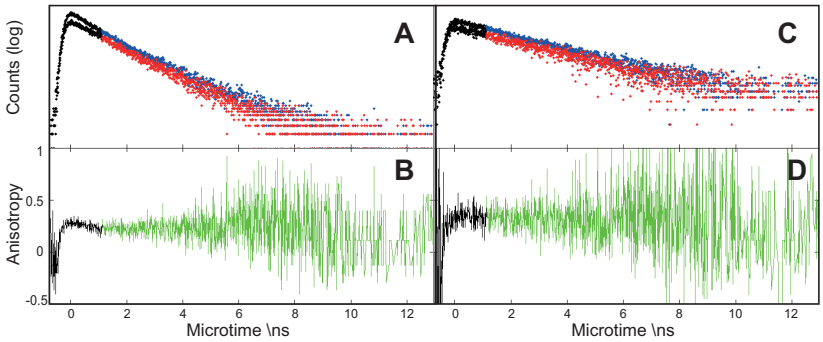

Figure 4.27: Effect of the microtime background subtraction. An example for the microtime and anisotropy decays is shown for a t+9 (Alexa647) nt-18 (Atto520) labeled sample containing 51% free DNA and 49% PolII bound DNA (see figure 4.28) before (A,B) and after (C,D) subtraction of the weighted DNA only microtime histograms. The microtime range selected for anisotropy calculation is shown in the RR histograms for parallel (blue) and perpendicular (red) (A,C). The corresponding anisotropy time range is depicted in green (B,D) resulting in r_∞=0.23 for the DNA only biassed dataset and r_∞=0.32 for the filtered data.

color. This is of particular importance since the residual anisotropy estimated from the time resolved anisotropy histogram will be used in the NPS analysis to gain information about the relative orientation of the dyes. All residual anisotropy data presented in this work were extracted by calculating the weighted mean of the steady part of the time resolved anisotropy decays (see figure 4.27B,D).

This method can be used under the assumption that the protein of interest rotates significantly slower than the lifetime of the fluorescent dye and the observation time frame of the experiment [14]. In this case the influence of protein rotation can be neglected since its rotation is too slow to add a measurable anisotropy decay on the observation timescale. Additionally it has to be ensured that the starting point for the calculation of this weighted mean is set such that the included

[14]The observation time frame was $\sim 18ns$ per channel. For 500kDa proteins which is about the weight of PolII [64] table 10.4 gives an approximate rotational correlation time of $\sim 200ns$ at 20°C.

data is not influenced by the instrument response function (IRF)[15].

It should be noted here that for the setup described in chapter 3.2 the IRF width was mainly dependent on the beam position on the APD. Hence during microscope alignment the detector positions were not only optimized for maximum intensity but also for a minimal IRF width.

Background correction: The mayor issue with the time resolved anisotropy from PolII data is that none of the datasets obtained throughout the experiments showed 100% protein binding. Hence always a subpopulation of free DNA is present in the data.

In this work this problem was treated by using selected parameters obtained in the MFD experiment to separate the bound from the unbound populations. Unfortunately most datasets did not clearly show two peaks in the FRET efficiency distribution as the one used for the identification of subpopulations in figure 4.26. Therefore only the lifetime and the lifetime weighted anisotropy of the directly excited red dye can be used to separate protein bound from free DNA by using PIFE (see chapter 4.3.5). While a sharp cut in these two dimensions is not problematic for the FRET efficiency determination using PDA (see chapters 4.3.8 and 4.1.2) where remaining impurities can be included in the fit, this is not possible for time resolved anisotropy. In this case if a simple lower RR anisotropy threshold is used to separate the populations, it will cause missing photons on the lower end of the gaussian distribution and lead to an overestimation of the actual anisotropy value.

To overcome this problem no threshold for the lifetime and anisotropy was set prior to exporting the photons for the time resolved anisotropy analysis.

Instead a gaussian distribution was assumed for both states in lifetime and lifetime weighted anisotropy of the RR channel and two 2-dimensional gaussian distributions (Eq. 4.15) were fit to the 2D histogram of these parameters (figure 4.28).

[15]Here IRF FWHM $\sim 300 - 500ps$ depending on the adjustment of the setup.

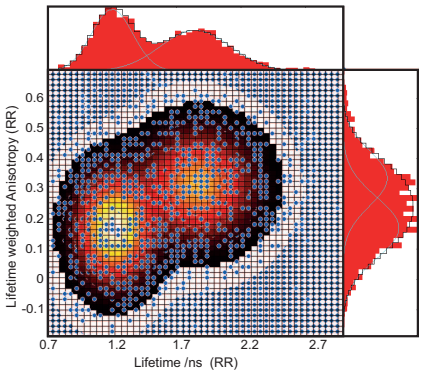

Figure 4.28: Exemplary fit of two 2-dimensional gaussians to an anisotropy-lifetime histogram. The two dimensional histogram (blue dots) shows RR lifetime versus RR anisotropy obtained from a t+9 (Alexa647) nt-18 (Atto520) labeled sample containing 51% free DNA and 49% PolII bound DNA. The corresponding gaussians fit is given as yellow to black gradient curve. Blue dots not visible have values lower than the fit function at the respective coordinate. The one dimensional projections show an overlay of the data (red bars), the fit result (black stairs) and the contributing individual gaussians (blue lines).

$$\begin{aligned} A(t,r) = a_1 * exp\left(\frac{-(t-t_1)^2}{2*\sigma_{t_1}^2} - \frac{(r-r_1)^2}{2*\sigma_{r_1}^2}\right) \\ + a_2 * exp\left(\frac{-(t-t_2)^2}{2*\sigma_{t_2}^2} - \frac{(r-r_2)^2}{2*\sigma_{r_2}^2}\right) \end{aligned} \tag{4.15}$$

where the fit variables are the width ($\sigma_{t,r,1,2}$), the peak position ($t_{1,2}$, $r_{1,2}$) and the amplitude ($a_{1,2}$). The two parts of the above equation describing the individual overlapping peaks were then integrated and the share of free and bound DNA was calculated.

Now that the shares of the contributing sub-populations could be determined, it was required to obtain the combined anisotropy decay as well as the anisotropy decay of the respective free DNA under

identical conditions. To this end one and the same sample was measured twice, once prior to the addition of PolII and once after PolII addition (see chapter 4.3.2 for details). A burst search followed by a removal of dirt molecules was performed using identical thresholds for both datasets and photons were exported to build a microtime histogram.

With the knowledge about the share and shape of the free DNA microtime histogram it was possible to subtract the correct amount of background directly from the PolII microtime histograms (see chapter 3.2.3). This allowed to calculate the residual anisotropy for PolII bound molecules only. An example of the results obtained in this way is given in figure 4.27 showing a significantly lower RR anisotropy and an initial decay caused by the 51% free DNA in the sample (A,B) and a higher constant value as expected for a large protein after the correction was applied (C,D).

Using this filtering finally reproducible residual anisotropies (r_∞) for identical dye positions could be obtained even for datasets with varying amounts of free DNA (see tables 4.11 and 4.12).

Crosstalk subtraction: A big issue for the anisotropy determination of the GR channel (also referred to as FRET anisotropy) is the spectral crosstalk (cr). Since the cr is defined as the percentage of donor photons detected in the acceptor channel (see chapter 3.2.4.3) the error caused by this effect is small for a high FRET molecule where the donor is quenched (small GG signal) and the acceptor is bright (high GR signal). In contrast the opposite is the case for low FRET samples where the GG signal is high while the GR signal is low.

If in the latter case even a small percentage of donor photons are detected in the acceptor channel this can lead to situations where even for low cr values the GR (FRET) anisotropy decay is dominated by GG photons.

Such errors can be avoided if the micro time histogram of the donor channel is known which is the case for the MFD experiments presented here.

In this work the GR anisotropy is corrected by subtracting the cr weighted GG microtime histogram for each polarization from the

respective GR histograms according to

$$GR_{\parallel,\perp,corrected}(\tau) = GR_{\parallel,\perp}(\tau) - cr * GG_{\parallel,\perp}(\tau) \tag{4.16}$$

prior to calculating the time resolved anisotropy. In the above equation $\parallel$ and $\perp$ indicate the parallel or perpendicular channel and τ is the time relative to the excitation laser pulse. While this procedure slightly increases the noise it yields reproducible results and minimizes the risk of falsified residual anisotropies in the GR channel.

Proximity ratio weighting: For FRET experiments it is oftentimes assumed that the width of the FRET distribution obtained is to some extent caused by dye movements within the limit of the linker [5] [51]. Since nonzero residual anisotropies are obtained for the samples measured here these movements are likely to be in some way confined (see also chapter 4.3.8).

In this context one has to consider that a dye might stick to some positions on the protein or DNA for timescales longer than the observation time (see chapter 4.2.4.2). If a free reorientation of the dyes is not given this will not only influence the width of the FRET efficiency distribution as discussed in chapter 4.3.8 but also the anisotropy.

In order to understand the underlying theory assume two dye pairs, one with an average donor and acceptor dipole orientation parallel to each other causing high FRET and one with average orientations tilted by a random degree showing a lower FRET efficiency.

Amongst many other possible orientations they are both contributing to the same FRET efficiency and anisotropy distribution that does not allow for a separation of subpopulations. Hence the corresponding photons would usually all contribute equally to the microtime histograms and connected to that the time resolved anisotropy. As a result, the parallel oriented dye pair with its many FRET photons would dominate the GR anisotropy while the tilted dye pair would only contribute to a lower extent.

To account for this effect and minimize possible errors from limited dye mobility the GR photons of each burst were attributed a

weight proportional to $1 - \epsilon$ (where ϵ is the uncorrected FRET efficiency also known as proximity ratio[16]). These reweighed photons were then used to build up the microtime histograms and to compute the time resolved anisotropy of the GR channel.

4.3.7 Gamma factor determination by quantum yield network analysis

To calculate actual distances from FRET measurements it is first of all critical to obtain unbiased data. However, in most cases due to numerous imperfections in the setups correction factors have to be applied in order to achieve this (see chapter 3.2.4.3).

Unfortunately the determination especially of the γ factor is not always straight forward. For surface based single molecule experiments it can be individually calculated for every molecule from bleaching steps [57] and molecule to molecule variations can be corrected. In contrast, for in solution measurements only an average factor can be estimated.

This factor is usually determined by measuring a high and a low FRET sample and assuming that the quantum yields (QY) of the respective dyes are identical for both samples. Since the stoichiometry is a measure for the relative number of photons detected after donor and after acceptor excitation one would expect identical Sto (see chapter 3.2.4.4) for both samples. Based on the assumption of constant QY one can hence minimize the correlation between FRET efficiency and stoichiometry by adjusting the γ factor as explained in detail in chapter 3.2.4.3.

The assumption of equal QYs is however not even valid for a DNA strand (see lifetime dependence of position in fig 4.25) and even less if in addition a protein is bound to the DNA (figure 4.31). In the following a method to obtain precise γ factors despite of different QYs will be presented and demonstrated.

[16] for the definition of ϵ see equation 3.7

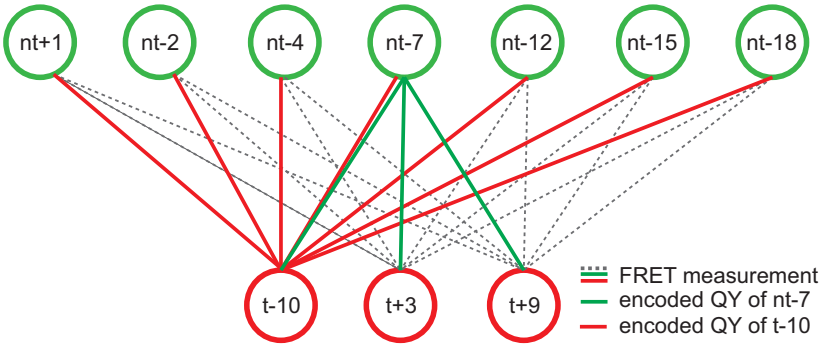

Figure 4.29: Exemplary illustration of the QY network used to estimate individual γ factors. The donor dye positions (green circles) and acceptor dye position (red circles) can be measured relative to each other. Since every donor and acceptor has an individual local environment they all have different quantum yields. The respective quantum yields however contribute to all measurements of one dye as exemplarily depicted for donor position $+7$ (green lines) and acceptor position -10 (red lines).

Quantum yield network analysis: An alternative to the simple approach of determining γ presented above opens up whenever a network of multiple distances to one and the same position is measured. Even though all of these measurements will require an individual γ factor, the QY of the dye located at this position will be encoded in each of that measurements γ factors (figure 4.29).

To utilize this information the definition of the γ factor for dye combination xy given in Eq. 3.8 can be rewritten to become

$$\gamma_{xy} = \frac{\Theta_{A_x}}{\Theta_{D_y}} * \frac{\eta_{A_x}}{\eta_{D_y}} \tag{4.17}$$

where η is the detection efficiency and Θ is the quantum yield of the donor (D) or acceptor (A). Since the spectra of dyes usually do not significantly change upon labeling a biomolecule, the ratio of the detection efficiencies η can be treated as an instrument constant Γ as long as the same dye combination is used and Eq. 4.17 becomes

$$\gamma_{xy} = \frac{\Theta_{A_x}}{\Theta_{D_y}} * \Gamma. \tag{4.18}$$

Please note that Γ also depends on the alignment of the setup. To avoid errors from differing alignment the setup was aligned and allowed to stabilize for at least 72h prior to measuring a series of datasets (see chapter 4.3.2).

Using individual QY for each dye together with a global Γ, a network of measurements can be optimized for one stoichiometry. For the case sketched in figure 4.29 this means that a total of 7 Θ_D, 3 Θ_A, 1 Γ and the unknown target stoichiometry have to be optimized at once. To this end nested sampling as described in chapter 3.5 was applied and the sample with the highest likelihood was taken as a result.

Note that if a large enough network is measured and the subsets are chosen in a way that no islands exist (i.e. a set of measurements not connected by at least one dye combination to the remaining data) it is in principle also possible to include several Γ values and target stoichiometries.

The C++ code of the likelihood function for a simple example only including a network of transcription elongation complexes labeled at $t-10$ $t+2$ $t+9$ and $nt-8$ $nt-13$ $nt-19$ is shown in the Appendix figures A.13-A.15.

Data cleanup: Prior to the parameter optimization described above, the desired species were identified using TDS (chapter 4.3.4) and stoichiometry thresholds in a way that donor and acceptor labeled complexes were included while single labeled complexes were excluded.

Since the samples were labeled with Alexa647 and thus sensitive to PIFE (see chapter 4.3.5), free DNA was separated from PolII bound DNA by applying a lower fluorescence lifetime threshold of 1.4 *ns* disregarding most of the free DNA bursts (see chapter 4.3.5 figure 4.28).

To reduce the computational expense not the stoichiometry of each individual burst was optimized but the total number of GG, GR and RR photons of the selected bursts were used to calculate and op-

timize an average stoichiometry (see Eq. 3.13) of each measurement.

Result verification: In principle the correct FRET efficiency could also be determined from the donor lifetime (see chapter 2.3 Eq. 2.6). While this method would be independent of the relative fluorescence intensities and no γ correction is needed it suffers from several other difficulties.

Due to the low photon numbers available for the lifetime fit (see chapter 3.2.4.6), the noise is relatively high compared to a FRET efficiency calculation using intensities. Additionally the number of GG photons decreases towards higher FRET values making a precise calculation of the donor lifetime more difficult for samples containing high FRET molecules [17]. Together these difficulties lead to bigger uncertainties than tolerable for e.G. an NPS analysis (see chapter 4.3).

In case of Atto520 used in this chapter a second important issue is the non-mono-exponential lifetime decay found for the labeling sites under investigation which makes it impossible to trust FRET efficiencies calculated from fluorescence lifetimes without additional information sources[18].

For these reasons the fluorescence lifetime was only used to verify that the intensity based FRET (Eq. 3.6) corrected with the quantum yield network analysis data and the FRET efficiencies calculated from fluorescence lifetimes are yielding on average comparable results.

Both, the lifetime of a donor only molecule and the donor lifetime in presence of an acceptor have to be known in order to calculate FRET efficiencies from fluorescence lifetimes according to Eq. 2.6.

To minimize the consumption of the PolII stock both required lifetimes were extracted directly from the respective dataset. This was possible since the sample labeling efficiency was not 100% and hence

[17] A good overview of how the error of a single molecule lifetime fit scales with the number of photons can be found in [60] figure 2.2.2.2-2.

[18] Only bulk experiments allow for a collection of enough photons to reveal non-mono-exponential fluorescence lifetimes in solution. Hence it cannot be completely excluded that individual dyes have a mono-exponential decay and that the observed non-mono-exponential slope is only a mixing of different subpopulations not resolvable in single molecule experiments due to the higher noise.

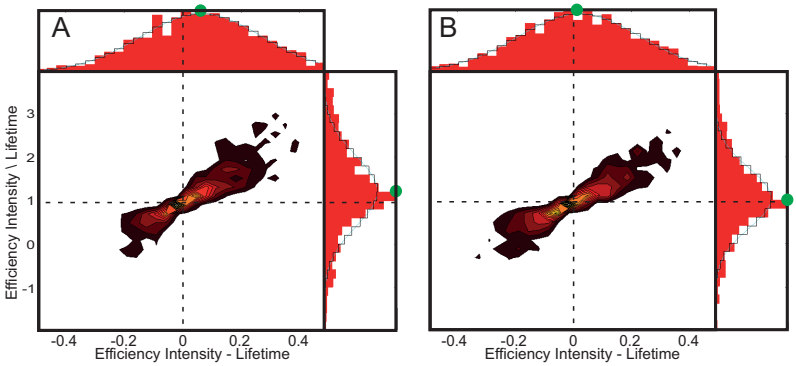

Figure 4.30: Comparison of smFRET efficiency histograms calculated from fluorescence intensities and lifetimes. An exemplary dataset of a nt-18 t+9 labeled DNA construct bound to PolII. Free DNA has been removed by a lower threshold of 1.4 ns for the RR fluorescence lifetime. The difference (x-axis) and ratio (y-axis) was calculated from FRET efficiencies obtained for each burst from fluorescence intensities (*Intensity*) and lifetimes (*Lifetime*). Shown are two dimensional histograms of uncorrected data (A, γ = 1, *cr* = 0) and data corrected with the results from the quantum yield network analysis (B, γ = 0.77, *cr* = 0.03). Peak positions of the gaussian fits (black stairs) are marked by green dots for better visibility. The theoretical position for a perfect match of lifetime and intensity calculated FRET are overlayed as dotted black lines. Remaining deviations from this ideal situation in figure B as well as the non single gaussian distribution of the ratio are most likely a result of the multi-exponential decay of Atto520 bound to DNA making a precise burstwise lifetime estimation difficult (see chapter 3.2.4.6).

the data measured always contained double labelled as well as donor and acceptor only molecules.

Here, the fluorescence lifetime based FRET efficiency was calculated for each double labeled molecule. To this end the molecules donor fluorescence lifetime was used together with the average fluorescence lifetime of the respective measurements donor only population (defined as all molecules with Sto > 0.9).

Oftentimes lifetime and intensity based FRET efficiencies are directly compared using a two dimensional plot. This representation however makes it difficult to instantly see how good two populations match. An easier way to judge whether two values are identical is to calculate the difference (Intensity FRET - lifetime FRET) or the ratio (Intensity FRET / lifetime FRET). Here assuming a perfect γ and lifetime fit the resulting FRET efficiencies should be equal and one would expect an average value of 0 for the difference and an average value of 1 for the ratio.

Hence by calculating ratio and difference for each individual burst and representing the results in a histogram (figure 4.30) one can easily compare the peak position of the resulting distribution to the expected values (0 or 1 respectively).

While an uncorrected intensity based FRET efficiency (γ=1, figure 4.30A) causes significant deviations from these expected values, the graph obtained after applying the results from the quantum yield network analysis (γ=0.77, cr=0.03) shows good correspondence of the expectations and the actual peak positions (figure 4.30B).

Note that due to the requirement of a sufficient amount of photons for the burst wise lifetime fit this comparison was only meaningful for low to medium FRET samples. As discussed above it was therefore not possible to simply use the lifetime based FRET efficiency to estimate the γ factor even though the non mono exponential lifetime decay does not seem to significantly bias the resulting distributions.

In this work lifetime based FRET was neither used directly as FRET result nor to explicitly calibrate the gamma factor. Instead the quantum yield network analysis successfully demonstrated above was used in all NPS experiments to accurately determine the γ factor.

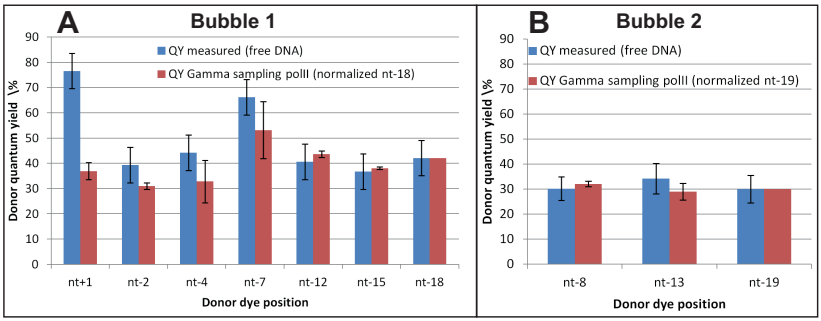

Figure 4.31: Comparison of quantum yields from DNA measurements and PolII quantum yield network analysis: The donor QY results obtained from measurements of DNA only for the various labeling positions of Bubble 1 (A) and Bubble 2 (B) are shown in blue. They are compared to the results of the quantum yield network analysis (blue) which are normalized to the labeling position with the largest basepair distance to the active center (Bubble 1, nt-18; Bubble 2,nt-19)

Quantum yields: The quantum yield network analysis results can not only be used to compute the γ factor for each individual measurement but they also allow for a determination of the correct QY which is important for the calculation of the Förster radius (see chapter 3.1).

For the project described here this is important since the common way to determine the QY requires bulk measurements. Hence due to the limited amounts of PolII it was only possible to directly determine the QY of the free DNA constructs in bulk (see chapter 3.1).

Fortunately, the fit described above optimizes on the ratio of Θ_A/Θ_D and hence yields information about the QY in presence of PolII. While it does not directly result in absolute values for the quantum yields, the network of donor and acceptor dyes fit contains the information about the relative values of donor and acceptor quantum yields to each other.

To make use of this information it is necessary to know at least one absolute QY value. Since as discussed above it was not possible to directly measure the QY in presence of PolII, here, the free DNA values were utilized.

To this end the fit results containing the desired relative QY were normalized to the quantum yield measured for the free DNA labeled at position nt-18 (Bubble 1) or nt-19 (Bubble 2) respectively (see figure 4.31). The choice for these dye positions was based on the assumption that the dye furthest away from the active center of the protein will encounter the least change in its local environment upon protein binding (i.e. Bubble 1, nt-18; Bubble 2, nt-19; figure 4.33).

The results for Bubble 1 show a slightly lower QY the closer the position is to the active center (see figure 4.31A). However the differences are within the experimental error for all positions except for nt+1 which is right at the active center of the protein. For this position the PolII bound construct shows only half the QY of the free DNA.

In contrast for Bubble 2 no significant changes of donor quantum yield upon protein binding were observed (see figure 4.31B).

All förster radii used in this chapter were determined using the normalized quantum yields derived from PolII bound molecules as shown here instead of the free DNA QY determined in bulk experiments (see chapter 3.1 for details)

4.3.8 Anisotropy corrected FRET

Throughout the development of a fast GPU based PDA analysis (chapter 4.1.2) test measurements were performed on a 1:1 mixture of high FRET and low FRET dsDNA constructs (see chapter 4.1.2.4). These DNA constructs had an identical sequence and differed only in their labeling positions. While the experiments clearly showed the two FRET populations, surprisingly neither the expected similar FRET distribution widths nor similar relative amplitudes could be observed.

This chapter will discuss reasons for these discrepancies in the result and demonstrates the effectiveness of the applied corrections.

Hindered dye rotation requires corrected FRET efficiency calculation: The data obtained for the 1:1 dsDNA mixture containing two types of constructs that show low FRET or high FRET (see chapter 4.1.2.4) was analyzed using PDA requiring two Gaussian distri-

butions for a best fit. Fits were done using predetermined values for the cr = 3%, the relative detection efficiencies $\gamma = 0.58$, the mean background rates B_G = 300 Hz, B_R = 300 Hz and the Förster distance R_0 = 60 Å. The initial fit results were: distances $d_1 = 54.0$ Å and $d_2 = 78.6$ Å, distribution widths $\sigma_1 = 7.4$ Å and $\sigma_2 = 4.1$ Å and relative amplitudes $A_1 = 0.79$ and $A_2 = 0.21$ (figure 4.1). When interpreting such data, it is important to note that the broadening beyond the shot noise limit given by the apparent distribution width can have various reasons including distance fluctuations [5] and acceptor photo-physics [51].

Interestingly, the PDA result neither yielded the intended 1:1 mixture, nor were the two determined widths, σ_1 and σ_2 similar, as would be expected for identical dye pairs used at differing labeling positions on the same dsDNA. Note, that in the described experiments polarized excitation was used and fluorescence photons parallel and perpendicular to the excitation were detected. For the analysis shown in figure 4.1A the total photon numbers S_{GG} and S_{GR} were calculated by adding the respective number of detected photons ($S_{GG,GR}$) in the parallel and perpendicular channel[19]

$$S_{xy} = S_{xy}\| + S_{xy}\perp, \tag{4.19}$$

following previous publications from other groups [5] [52].

For any polarization sensitive measurement it is important to realize that the total emitted fluorescence is the sum of the fluorescence emitted with a polarization parallel to the excitation and two times the fluorescence emitted perpendicular to the excitation polarization. If the dye molecules rotate fast with respect to the fluorescence lifetime these polarization effects are not important, otherwise it is easy to correct for them in the following equation[20]:

$$S_{xy} = (1 - 3l_2)\beta S_{xy}^{\|} + (2 - 3l_1)S_{xy}^{\perp}. \tag{4.20}$$

As PDA requires integer values, the photon numbers calculated using equation 4.20 were rounded to the nearest integer prior to fur-

[19] equation 4.19 is equal to equation 3.5 and reproduced here for better readability
[20] equation 4.20 is equal to equation 3.21 and reproduced here for better readability

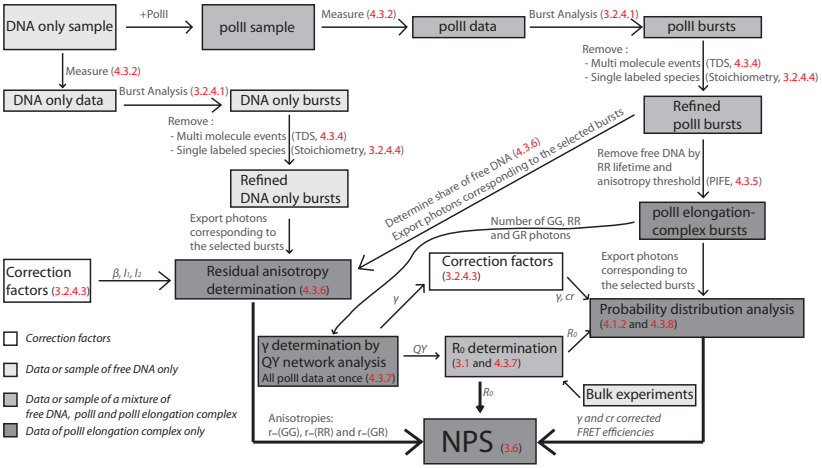

Figure 4.32: Schematic of the individual steps involved in the NPS experiments. Schematic showing an overview of the data acquisition and analysis steps performed to obtain data suitable for usage in the NPS. For easy referencing the chapter describing the respective step in detail is depicted in red letters. The process of isolating double labeled PolII elongation complex data from free DNA and other impurities is color coded in each step as indicated at the lower left corner.

ther usage.

Applying equation 4.20 to the measured FRET data resulted in a best fit with distances of $d_1 = 54.0$ Å and $d_2 = 78.1$ Å, distribution widths $\sigma_1 = 7.2$ Å and $\sigma_2 = 7.6$ Å and relative amplitudes $A_1 = 0.58$ and $A_2 = 0.42$. Note that in this case $\gamma = 0.7$ has to be used due to the experimentally determined differences in the detection efficiencies in the four detection channels ($\beta_G = 1.1$ and $\beta_R = 1.35$, see chapter 3.2.4.3). Thus, both, the correct approximately 1:1 ratio of the two different DNA molecules is recovered and the widths of the two distributions are similar (figure 4.1B).

Since most samples measured for the NPS experiments showed high anisotropies (see table 4.11) equation 4.20 was used for all experiments and results presented in the following.

4.3.9 Experiments and results

The method to determine fluorescence anisotropies for the NPS analysis used previously in the Michaelis laboratory [86] [4] [2] [33] suffered from three mayor drawbacks. First, it did not allow to measure the FRET anisotropy (see chapter 4.3.6), second the anisotropies were determined in bulk where it is impossible to separate individual subpopulations and third only lifetime weighted average anisotropies were obtained (compare chapter 3.2.4.5). In this thesis MFD is applied to simultaneously measure FRET efficiencies and anisotropies including the FRET anisotropy from double labeled and protein bound molecules. Additionally the residual anisotropy is used instead of the lifetime weighted anisotropy to avoid artifacts from differing lifetimes.

To this end new methods were developed (chapter 4.3.4, 4.3.5, 4.3.6, 4.3.7, 4.3.8) and a different donor dye as compared to [2] had to be used (chapter 4.3.3). An overview of the data acquisition and analysis process is shown in figure 4.32. For easy referencing the chapter containing detailed information on the respective step is highlighted in red.

All PolII experiments were performed on artificial partially mismatched dsDNA constructs with a 17 base pair (bp) RNA (IBA GmbH, Göttingen) hybridized to the template strand in the mismatch region referred to as "Bubbles" (Figure 4.33). To use such a Bubble construct it is assumed that the mismatched DNA region is of the same size as the region that would naturally be melted in the PolII state under investigation (here elongation state) and hence the non matching basepairs do not change the conformation of the polymerase.

The Bubble 1 sequence is identical to the sequences used in [55] and [4]. This approach allows for the construction of an "elongation complex" without the need for a TATA-box and initiation factors as the PolII can directly bind to the partially open construct. Note that in the constructs shown in figure 4.33 known positions from crystal structures are depicted as full circles (nt, green; t, blue; RNA, red). Bases are numbered according to their relative position to the active center. The labeling positions, marked by colored stars, will in

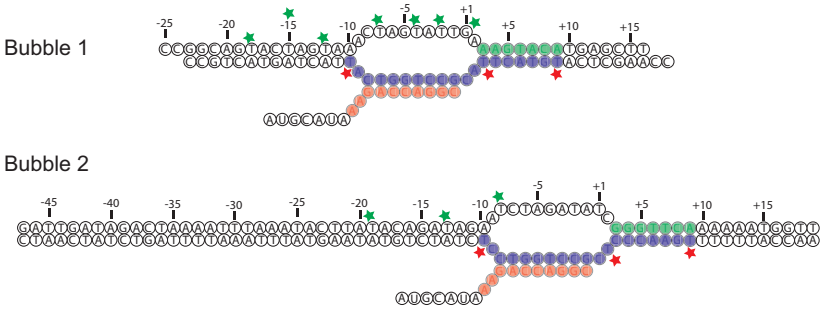

Figure 4.33: DNA constructs used in the PolII experiments. Labeling sites for donor (green stars) and acceptor dyes (red stars) are indicated. Positions visible in the 1Y1W crystal structure are highlighted as colored filled circles (nt, green; t, blue; RNA, red)

the following be abbreviated by these numbers in combination with *nt* indicating the non-template strand and *t* indicating the template strand.

4.3.9.1 Single molecule data used to determine positions of Bubble 1

A total of 21 donor(t-10, +3, +9)-acceptor(nt +1, -2, -4, -7, -12, -15, -18) dye pair samples were measured (see chapter 4.3.2 for details). Thresholds to separate the subpopulation of interest were applied (chapter 4.3.4, 4.3.5) and the anisotropies (chapter 4.3.6) as well as the FRET efficiencies (chapter 4.3.8) were extracted . Additionally, data measured by J, Andrecka using total internal reflection (TIRF) microscopy [2] were included in the analysis providing information on the distances of the unknown non template DNA strand to positions C150 on Rpb7 and C73 on Rpb4.

In accordance with previous observations ([87] figure 6.33) throughout the analysis for some t+3 datasets it was impossible to obtain a NPS result explaining the detected data (figure 4.34). While in the example shown here the measured and expected FRET anisotropy of the t+9 nt+1 position are in good agreement (figure 4.34A) large

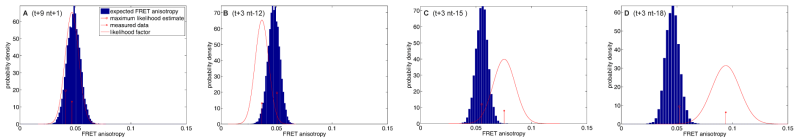

Figure 4.34: Comparison of NPS result and measured data. Exemplary comparison of expected FRET anisotropy based on the NPS result and actually measured data. The measured (red line) and expected (Blue bars) FRET anisotropy of the t+9 nt+1 position are in good agreement (A). In contrast the t+3 data (B-D) shows significant deviations of expected and measured FRET anisotropies.

inconsistencies appear for some t+3 datasets(nt-12- nt-15, nt-18 figure 4.34B-D) .

Possible reasons for these inconsistencies include a mis-assembled DNA-PolII complex due to the limited space available for a dye in position t+3 [21]. Hence the information obtained from t+3 experiments is not included in the following results and discussion. It has however to be noted that an inclusion of t+3 data despite the inconsistencies only changes the obtained positions globally but does not change the relative positions of the antenna dyes to each other and hence would not change the main result of this chapter (data not shown). A summary of all data included in the following NPS analysis is shown in table 4.11.

[21] For a full discussion on possible origins of these inconsistencies see [87]

Table 4.11: Data obtained for the NPS analysis of Bubble 2 samples. errors are SEM

FRET eff. %[2]				
nt+1	46	49	32	-
nt-2	41	44	35	-
nt-4	44	48	36	-
nt-7	49	53	54	-
nt-12	47	51	57	32
nt-15	46	50	48	29
nt-18	47	51	35	22
R_0^{iso} **Å**	t+9	t-10	Rpb7 C150[1]	Rpb4 C73[1]
nt+1	54.7	49.2	64	-
nt-2	44.5	48.0	62	-
nt-4	44.0	47.4	64	-
nt-7	50.3	54.2	64	-
nt-12	47.3	51.0	64	62
nt-15	46.2	49.9	64	63
nt-18	47.0	50.7	62	63
FRET anisotropy[3]				
nt+1	0.072	0.072	-	-
nt-2	0.075	0.088	-	-
nt-4	0.121	0.046	-	-
nt-7	0.099	0.039	-	-
nt-12	0.124	0.099	-	-
nt-15	0.151	0.062	-	-
nt-18	0.051	0.202	-	-
red anisotropy	0.323 ± 0.002	0.341 ±0.002	0.23	0.27
	nt+1	nt-2	nt-4	nt-7
green anisotropy	0.285 ±0.004	0.266 ±0.006	0.285 ±0.003	0.172 ±0.003
	nt-12	nt-15	nt-18	
green anisotropy	0.227 ±0.003	0.242 ± 0.003	0.268 ±0.003	

[1] For C150 and C73 FRET efficiency, R_0 and anisotropy data adapted from [2], for these measurements Tamra was used as a donor instead of Atto520

[2] An estimated FRET efficiency error of 3% was used in the NPS analysis. FRET values smaller than 10% were attributed an error of 5%

[3] An average error of ±0.030 was used for all fret anisotropies

4.3.9.2 NPS results indicate hairpin formation

Based on the data summarized in table 4.11 different NPS analyses were performed (see chapter 3.6) according to the guidelines given in [85] and [87].

Since a different dye combination as compared to the initial experiments by [4] was used (see chapter 4.3.3) in a first step the data was checked for its consistency with the previously published data. To this end a global NPS analysis was performed including all information except for the FRET anisotropy. The results obtained from the data measured in this thesis (figure 4.35C,D) should therefore be equal to the probability densities from a global reevaluation of the initial dataset as presented in [87] (figure 4.35A,B).

As expected the overall density arrangement was reproduced and only a slight shift of all positions away from the polymerase could be observed. This shift is most likely resulting from the fact that this new data only contains information from PolII bound complexes. In contrast, due to the way the experiments were performed a bias of the initial TIRF datasets ([4]) by free DNA can only be excluded for DNA-protein distances.

Including the FRET anisotropy however led to an unexpected result (figure 4.35E,F). While the densities from nt+1 to nt-12 maintained their position, completely different positions were detected for nt-15 and nt-18. The 68% probability densitiy of nt-15 is now found in between nt-7 and nt-4. An even larger position change occurs for the initially furthest outward density nt-18 which is now positioned in between nt-4 and nt+1.

Experiments were tested for simple measurement errors by measuring duplicates yielding virtually identical results.

4.3.9.3 Result verification

The DNA sequence used in the FRET studies presented here (figure 4.33, Bubble 1) was identical to the sequence used since the initial crystal structure [55] and throughout the following publications [2]. As the results were reproducible, the observed probability density positions were trusted and the question arose whether alternative struc-

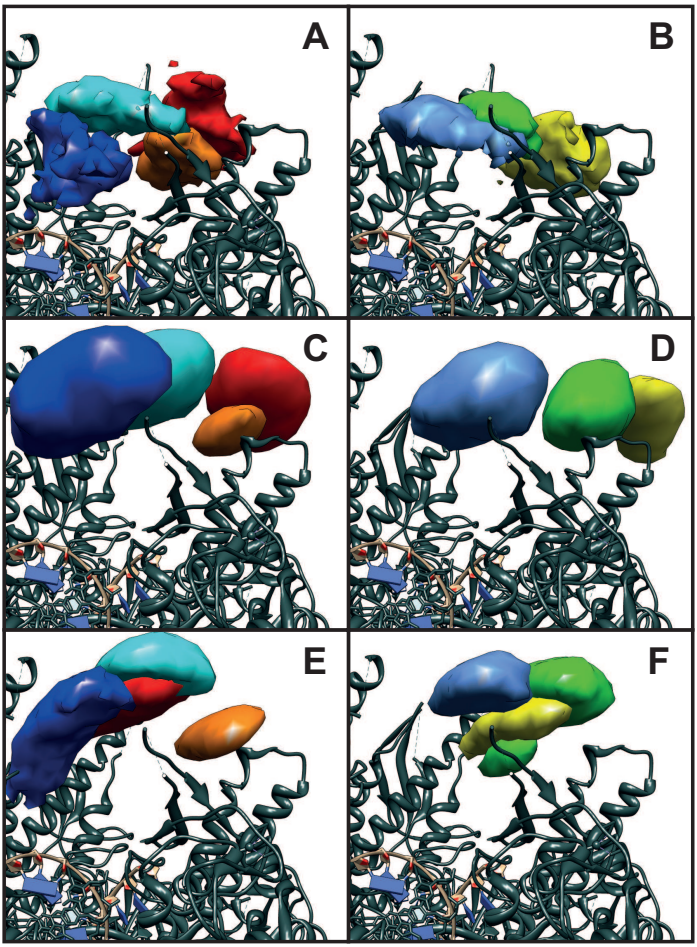

Figure 4.35: Comparison of results obtained for Bubble1. The 68% probability densities obtained for the Bubble1 PolII construct resulting from a global analysis are color-coded and separated for a better visibility in the following manner: The positions nt+1 (Blue), nt-4 (bright blue), nt-12(orange) and nt-18 (red) are shown in the upper row (A,C,E) while positions nt-2(midnight blue), nt-7(green) and nt-15(yellow) can be found in the lower row (B,D,F).
Positions based on the data presented in [2] as calculated in [87] (A,B) could be reproduced based on the data presented here if calculated without FRET anisotropy information (C,D). In contrast the additional FRET anisotropy information caused a different arrangement of probability densities (E-F) and indicates the presence of a DNA hairpin.

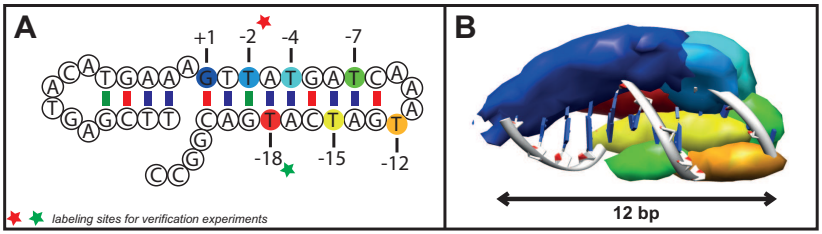

Figure 4.36: Comparison of NPS results and theoretical hairpin structure of the non template DNA. (A) The estimated most stable DNA hairpin consists of a 9 bp stem and a 4 bp loop. (B) The 68% probability densities obtained from the NPS analysis of Bubble 1 are overlayed with a 12 base pair long DNA structure (PDB: 1BNA). Dye positions are color coded as depicted in figure A. Base pairs are indicated as violet (A-T), red (G-C) and green (Hoogsteen G-T) lines. Labeling sites for verifying the existence of a hairpin as described in the following are marked as green (Atto520) and red(Alexa647) stars.

tures might be formed by the DNA sequence used. Reanalyzing the sequence revealed that the non template strand is capable of partially basepairing itself hence forming a relatively stable hairpin.

If the hairpin hypothesis is true secondary structure prediction algorithms [22] suppose that the most stable hairpin structure would consist of a 9 base pair stem followed by a 4 base loop (figure 4.36A).

An overlay of the PDB:1BNA structure in figure 4.36B reveals that the obtained densities span over a distance of approximately 12 basepairs of a dsDNA. This is in good agreement with the expected dimensions of the hairpin structure. In addition the relative positions of the densities nt-18 (between nt-4 and nt+1) and nt-15 (between nt-7 and nt-4) as discussed in the previous chapter also resemble the positions expected in the assumed hairpin.

To test the hypothesis of the existence of a hairpin under the experimental conditions applied, a special nt-DNA labeled with an acceptor at position nt-2 and with a donor at position nt-18 was used. A construct containing this non template strand and an unlabeled tem-

[22] http://eu.idtdna.com/analyzer/Applications/OligoAnalyzer/ (24.04.2012)

plate strand was designed (based on Bubble 1). This sample should show low FRET until a hairpin is formed which would cause a high FRET signal (compare figure 4.36A and figure 4.37A).

SmFRET data obtained from such a construct [23] can be found in figure 4.37B. The clearly dominant high FRET population confirms the presence of the hairpin structure in the free DNA construct (blue) as well as after PolII binding (red, successful binding is indicated by the increased RR fluorescence lifetime, see chapter 4.3.5). Interestingly the FRET distribution does not change upon protein binding indicating a negligible influence of the protein on the observed distribution. In addition the distribution is spread over almost the full FRET range which might be caused by dynamics in the sample (see chapter 4.2.4.1).

4.3.9.4 Optimization of conditions towards minimal hairpin formation

As discussed in chapter 4.2 the conformation of a hairpin can be controlled by the buffer conditions and the temperature. Hence, experiments with bubbles assembled at different conditions were performed aiming at a minimization of hairpin formation.

The local concentration of the self complementary nt-DNA parts is rather high compared to the concentration of the freely diffusing complementary template strand. Therefore a lower cooling speed should give the ssDNA more time to find and basepair to its counterpart instead of hairpin formation before the kinetics do no longer allow for a fast exchange. Indeed experiments showed that a modification of the annealing cycle to a sequence with slower cooling from 95°C to 4°C at only 1°C/min resulted in about equal amounts of Hairpin and correctly assembled Bubble 1 (compare figure 4.37B and C). A further reduction of the cooling speed did not result in increased correct annealing (data not shown).

In addition by changing the buffer from H_2O to TE (figure 4.37D) or Assembly buffer (figure 4.37E) the equilibrium for this construct

[23] annealed as described in chapter 4.3.2 and [2]

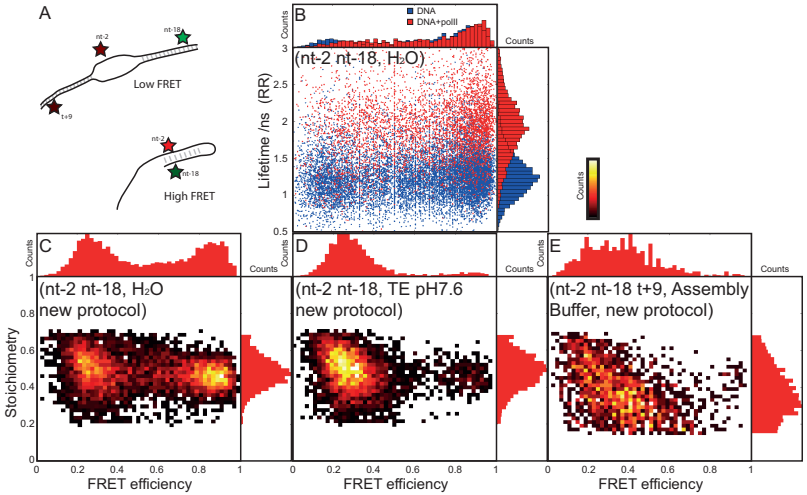

Figure 4.37: smFRET studies investigating DNA hairpin formation. (A) Schematic of the expected change in FRET efficiency upon hairpin formation. The first three experiments (B-D) were performed using a sample double labeled on the non-template strand (nt-2, Alexa647 and nt-18 Atto520 compare Bubble 1 figure 4.36). In contrast the last experiment (E) contained an additional Alexa647 dye at position t+9 on the template strand. (B) A two dimensional scatter plot of FRET efficiency and red detection after red excitation (RR) fluorescence lifetime measured before (blue) and after (red) the addition of PolII shows one main FRET population at ∼90% FRET efficiency and a shift in fluorescence lifetime but not the FRET efficiencies upon protein binding. The dominant high FRET population is associated with the formation of a hairpin and is not significantly influenced by PolII binding. A change in the Bubble annealing protocol as described in the main text improves the yield of non hairpin constructs as evidenced by the increased LF population (C). Using TE or Assembly buffer instead of water combined with this optimized protocol further reduces the hairpin formation (D). The shift in stoichiometry observed in E is caused by the presence of a second red dye at position t+9 and demonstrates that indeed a dsDNA is formed. Note that in panels C-E a two dimensional histogram instead of a scatter plot (B) is shown to allow for a better visibility of the distributions.

could furthermore be shifted to an almost complete formation of the correct Bubble 1.

To prove that the observed FRET efficiencies indeed result from the correct binding of a template strand and not only from hindered hairpin formation under these conditions, experiments with three labels were performed. The respective constructs contained the previously described double labeled nt-DNA and a single labeled t-DNA (t+9, Alexa647, see schematic figure 4.37A). Position t+9 was chosen here, since in a perfectly assembled DNA construct (figure 4.33 Bubble 1) it is furthest away from the two other dyes and should hence only cause a slight increase in FRET efficiency upon dsDNA formation. In contrast however the stoichiometry will decrease when the dsDNA is formed since now two red dyes are fluorescing upon direct excitation hence increasing the amount of RR photons per burst while the GG photons remain the same [24] (see chapter 3.2.4.4).

As expected the stoichiometry significantly decreased due to the double amount of acceptor dyes per molecule indicating correct Bubble 1 formation with these labeling positions and conditions (figure 4.37E).

4.3.9.5 Labeling positions influence the DNA annealing

Based on the results described in the previous chapter the measurements of Bubble 1 samples were repeated with the optimized preparation scheme. Surprisingly no major changes in FRET efficiencies or anisotropies were detected as exemplarily shown in figure 4.38. The distributions of nt-15 and nt-18 which would be expected to show the largest changes due to the largest distance change upon hairpin or dsDNA formation remain identical despite the changes in Bubble preparation.

While all other data looked identical only a slight change could be detected for nt-12 samples where the distance to t+9 changed towards higher FRET values.

[24] Assuming that direct excitation of the acceptor by the donor laser is negligible. Also the possibility of FRET towards this second acceptor plays a role but is not important for the analysis done here.

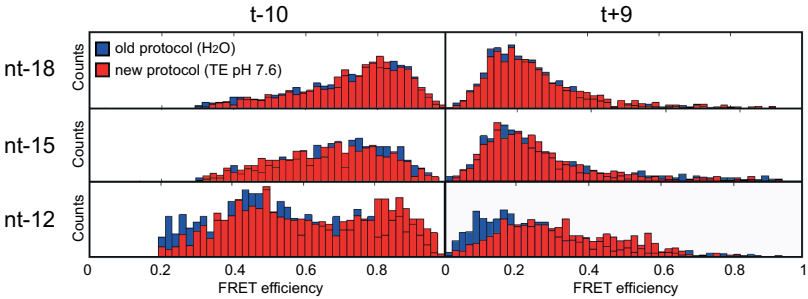

Figure 4.38: smFRET data obtained for different sample preparation protocols. The data obtained from measurements of Bubble 1 assembled with the traditional bubble annealing protocol (blue, see chapter 4.3.2) and assembled with the modifications described in the main text (red) are compared for acceptor labeling positions t-10 and t+9 and donor positions nt-18, nt-15 and nt-12. For these samples the positions which should change most upon hairpin formation. Except for nt-12 no significant FRET change could be observed.

How can these results be explained? Based on the results presented in chapter 4.2 one might speculate about an influence of the dye labels on hairpin or dsDNA formation.

If one assumes a sterical hindrance of DNA base pairing caused by the dyes attached then in case of the double labeled nt-DNA with labels in close proximity hairpin formation might simply be hindered as compared to the single labeled DNA constructs. If one furthermore assumes that the position of the dye labels influences the degree of sterical hindrance it could well be possible that different dye positions and combinations are not equally sensitive to the changes made in order to minimize hairpin formation.

4.3.9.6 Minimizing hairpin formation by thermodynamic considerations

Since the attempts to overcome hairpin formation by simply changing the conditions yielded either insufficient or unpredictable behavior of the sample, a new Bubble construct was designed.

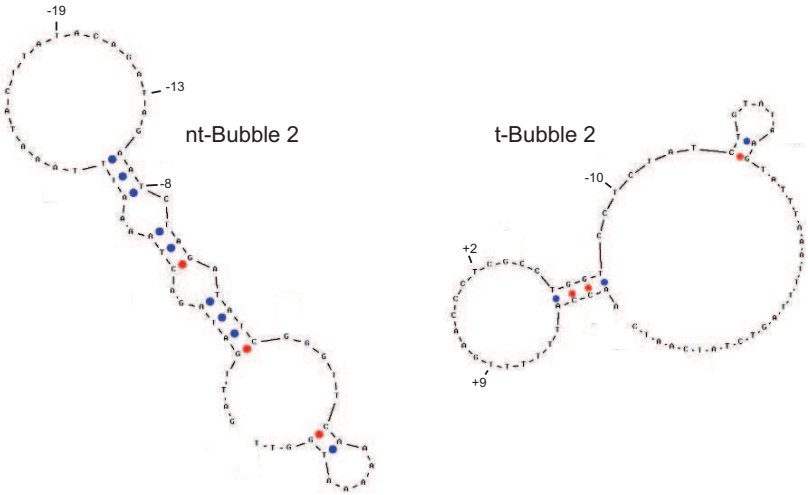

ssDNA	ΔG [*kcal/mol*]
nt Bubble 1	-7.88
nt Bubble 2	-2.99
t Bubble 2	-1.88

Figure 4.39: Most stable hairpin structure of Bubble 2 and theoretical ΔG values.. The most stable hairpin structure of Bubble 2 ssDNA as simulated at 20°C and 100 $mMNa^+$, 100 $mMMg^{2+}$ using *http://eu.idtdna.com/analyzer/Applications/OligoAnalyzer/* (24.04.2012) is shown for the non-template (left) and the template (middle) strand. Basepairs are indicated in red (G-C) and blue (A-T) and labeling positions are marked with their position relative to the active center of the polymerase. The corresponding ΔG values are summarized in the table (lower right corner) additionally including the value for the non template sequence of Bubble 1.

It is practically impossible to completely exclude DNA hairpin formation. Hence the goal for this new construct was to minimize the possibility for a hairpin which was achieved by minimizing the stability of the possible hairpin structures. Hence the sequence of Bubble 2 shows two important features.

First the most stable hairpin conformations have a significantly lower ΔG than the hairpin found for Bubble 1 (see table in figure 4.39).

Second, in contrast to Bubble 1 the hairpins expected still maintain large areas accessible for template DNA meaning that even if a hairpin is formed this does not completely prevent a binding of the complementary ssDNA strand. Hence throughout the assembly the more stable dsDNA will be formed instead of hairpin structures (see figure 4.39).

The sequence of this so called Bubble 2 can be found in figure 4.33.

4.3.9.7 Proof of principle Bubble 2

To check whether this new sequence changes the positions calculated in an NPS analysis, Bubble 2 samples were prepared and measured as described in chapter 4.3.2 except that the annealing was done in Assembly buffer using the modified cooling pattern (see chapter 4.3.9.4).

Due to the different sequence and the limitation of internal labeling to thymine bases slightly different labeling positions had to be used. The known satellite positions now were t+2, t+9, t-10 and Rpb7 C150 labeled with Alexa647. As exemplary unknown positions nt-8, nt-13 and nt-19 (Atto520) were chosen since especially the latter two should show large differences in their position as compared to the previous hairpin results (compare to positions nt-7, nt-12 and nt-18 of Bubble 1).

An NPS analysis based on Bubble 2 data (see table 4.12) was performed and resulted in three distinct probability densities (figure 4.40B). The arrangement with nt-8 closest to the protein followed by nt-13 and nt-19 corresponds to the expected behavior of DNA exiting the polymerase. In addition also the approximate distance spanned by the densities matches the dimensions expected (compare to the distance of the black arrows on the DNA sequence in

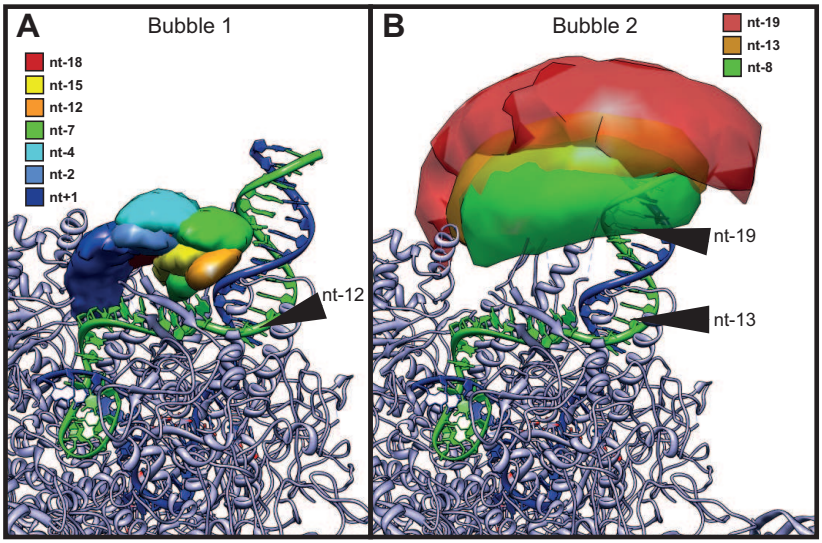

Figure 4.40: Comparison of NPS results and the previous model. The model derived according to the NPS results in [4] is overlayed to the results obtained for the Bubble 1 (A) and Bubble 2 (B) constructs presented here. The modeled non-template positions nt-12, nt-13 and nt-19 are marked with a black arrow to allow for an easier comparison with the 68% probability densities. Color codes for the dye position as shown in the figure.

figure 4.40). The absolute distance between the obtained densities and the polymerase is however larger than could be explained by any position of the DNA in the elongation complex, a fact that will be discussed in more detail in the following chapter.

Table 4.12: Data obtained for the NPS analysis of Bubble 2 samples. errors are SEM

R_0^{iso} Å	t+2	t+9	t-10	Rpb7 C150
nt-8	49.34	49.45	53.00	52.65
nt-13	50.52	50.63	54.17	53.86
nt-19	49.92	50.03	53.30	53.09
FRET eff. %[1]				
nt-8	46	42	88	9
nt-13	36[2]	33	85	6
nt-19	72	19	60	74
FRET anisotropy[3]				
nt-8	0.048	0.050	0.036	0.360
nt-13	0.054	0.096	0.023	0.188
nt-19	0.074	0.161	0.050	0.157
red anisotropy	0.301 $\pm$0.039	0.320 $\pm$0.023	0.350 $\pm$0.012	0.149 $\pm$0.086
	nt-8	nt-13	nt-19	
green anisotropy	0.313 $\pm$0.039	0.316 $\pm$0.023	0.314 $\pm$0.019	

[1] An estimated FRET efficiency error of 3% was used for the NPS analysis. FRET values smaller than 10% were attributed an error of 5%

[2] Two peaks were detected, the second peak had a total share of $\sim$ 27.6% and a FRET efficiency of 62%

[3] An average error of $\pm$0.030 was used for all fret anisotropies

4.3.10 Discussion and outlook

When interpreting new results one of the most important questions is whether current models remain valid.

The probability density positions obtained form MFD FRET datasets without FRET anisotropies were similar to the positions determined using surface based TIRF smFRET data, presented in [87]. This result indicates that neither the uncertainties caused by the experimental limitations of TIRF microscopy such as the amount of free

double labeled DNA not bound to a protein nor the uncertainties of the MFD experiments presented here (e.g. γ) did cause severe positioning errors.

However the inclusion of FRET anisotropies into the nano-positioning-system (NPS) analysis of the non template DNA strand in RNA polymerase II (PolII) caused distinct changes especially of positions nt-12, nt-15 and nt-18 (see figure 4.35).

This new data can be best described by a hairpin formation in the non template DNA strand, a situation completely different to that of the expected dsDNA strand exiting the PolII. Additional experiments further solidified the interpretation of the existence of this hairpin with and without PolII bound to the DNA.

Compared to the model derived from the initial probability densities [4] the hairpin detected here is positioned a bit further away from the polymerase even though the general direction of the nt-DNA seems to be similar (figure 4.40A).

On the one hand this is a great result since it is the first time that the importance of FRET anisotropy for distance measurements could be demonstrated on non simulated datasets. Furthermore, the fact that in separate experiments the detected hairpin structure was indeed found to be the dominating population proves the reliability of the NPS method.

On the other hand the results presented here require new experiments to be performed on the PolII elongation complex to verify the correctness of the DNA exit path model presented in [4].

To this end a new DNA construct not capable of forming stable hairpins was designed. First NPS experiments yielded probability densities with the correct order of nt-8 being closest to the polymerase followed by nt-13 and nt-19. The relative distances of the observed positions to each other are in good agreement with the distances expected for a dsDNA.

The distance of the probability densities to the polymerase is however about 6-10 basepairs larger than predicted by the previous model. Importantly this shift is too large to be consistent with an elongation complex where the distance of each base to the active center is limited by the length of the DNA (figure 4.40B).

One possible reason for such an outward shift is an error in the γ factor. To understand the problem note that, due to the way they are determined, all obtained γ factors are connected. Throughout the so called quantum yield network analysis (see chapter 4.3.7) a network of dye QYs is optimized together with an instrument constant such that in a perfect scenario all datasets yield identical stoichiometries. Since the target stoichiometry is unknown and also optimized throughout the sampling a too small network might allow for a too low or too high target stoichiometry caused by a single impurity in one measurement. This would shift all γ factors simultaneously towards higher or lower values respectively. As a result such an offset in the correction factor values would directly offset the FRET efficiencies obtained. The problem with this theory is that for the data presented here, even a relatively large γ offset of e.g. 0.3 would cause a distance shift of only about ~ 3 Å (assuming $\kappa^2 = 2/3$).

Hence, the γ factor alone is not sufficient to fully explain the observed shift away from the polymerase.

Another important factor in the calculation of distances from FRET efficiencies that could also contribute to the observed position shift are the anisotropies. In case of the NPS analysis it is assumed that the dyes reorient faster than their fluorescence lifetime and that the observed anisotropies are an average of all possible orientations.

One indication for a problem with that model describing the dye orientations is that only positive FRET anisotropies with approximately the same value (in most cases about 0.1) were detected. For dyes undergoing fast reorientation within fixed boundaries one would however also assume that conditions exist that cause negative FRET anisotropies (i.e. the two dyes are on average tilted by more than the magic angle).

The absence of such negative FRET anisotropies could for example be explained by assuming that several distinct average orientations exist for each dye position and that they interchange slower than the fluorescence lifetime. If the observed average anisotropies are caused by subpopulations of dyes temporally restricted in different positions instead of by one population re-orientating on timescales faster than the dyes lifetime, the static model applied in NPS would no longer be

valid.

Sub-states stable on the timescale of a burst can for example be detected by an anisotropy probability distribution analysis (PDA). For the data presented here and on a timescale of 1 *ms*, this analysis however revealed only one anisotropy population for each of the channels (donor, acceptor, FRET). It has to be noted that the absence of sub-states on that time-scale does not rule out the possibility of sub-populations stable for a few μs or shorter.

Nevertheless, further experiments will be necessary to fortify or disregard the above hypothesis of stable sub-states and if they in fact turn out to be an issue, the development of a different model accounting for such states might be required.

In order to verify or change the non template DNA exit path model it is necessary to precisely determine the distances in the in the PolII elongation complex. Based on the results presented in this thesis a combination of TIRF microscopy and MFD data might be a good approach to minimize remaining error sources.

Using such a combination would allow for an accurate γ correction of individual molecules by the TIRF experiments resulting in more precise FRET data. This data could then be combined with anisotropy (chapter 4.3.6) and R_0^{iso} (chapter 4.3.7) values from MFD experiments that can be filtered from artifacts caused by free dye or DNA not bound to PolII (chapter 4.3.5). In addition the MFD FRET efficiency data can be used to ensure that 100% of the labeled DNA are actually bound to the polymerase and PDA (chapter 4.1.2) might serve as a fallback for samples where this goal can not be achieved and a change in FRET efficiency upon protein binding is detected.

Chapter 5

Nucleosome dynamics and accessibility

5.1 Overview

Nature has developed a highly effective method to fit the DNA into the small compartment of the nucleus of a cell. The so called chromatin was first detected by Alexander Flemming at the end of the 19th century when he detected a stainable (chroma = colored) structure in the nucleus of a eucaryotic cell. Oftentimes the vast number of the 10000 fold DNA compaction is highlighted to be the most impressive feature of the chromatin. The simple compaction alone would be however rather useless if the second feature even more important for life would be missing.

What makes chromatin so outstanding is the combination of high compaction and maintaining the accessibility of the DNA. This not only allows for transcription but also for a regulation of genes by making some easier accessible than others.

Chromatin can be divided into two classes namely euchromatin which is the less condensed form mainly found in the center of the nucleus and the peripherally located heterochromatin. Both of these forms consist of the same "building block" structure called nucleo-

some.

Nucleosomes are the first step of DNA compaction reducing the DNA extension by a factor of about seven. This is achieved by wrapping the DNA on a length of 147 base pairs 1.7 times in a left handed superhelical manner around a protein complex [58].

This complex is stabilized by positively charged residues of four core histones, *H2A*, *H2B*, *H3* and *H4* interacting with the negatively charged DNA backbone at 14 histone DNA-Backbone contacts. The 11-16 kD core histones all show a similar combination of highly ordered α helices well conserved throughout species and rather unstructured N-terminal tails.

The next steps of compaction is associated to the linker histones H1 and H5. The H1 and H5 histones are involved in higher order compaction of chromatin and nucleosome spacing. They are not part of the nucleosome core and do not show good conservation between species.

The chromatin is thought to have a "beads on a string" like structure [93] commonly referred to as *11 nm fiber* followed by the *30 nm fiber* state. In this state neighboring nucleosomes are assumed to interact resulting in a more condensed structure. Till today the real structure of this *30 nm fiber* is unknown, however two competing models exist.

The solenoid model assumes that consecutive nucleosomes are located next to each other forming a helical superstructure [105] with only one start. In contrast the zigzag model proposes a structure where consecutive nucleosomes are in different helical stacks of a two start helix [56][112]. Further compaction of the *30 nm fiber* is necessary to achieve the 10000 fold compaction. This maximum chromatin condensation however only occurs during the metaphase and the structures involved are not fully understood yet [82].

A canonical nucleosome is formed by a histone octamere core consisting of two $H2A/H2B$ dimers, a $(H3/H4)_2$ tetramer [71] and a DNA wrapped around it. In addition also not fully assembled nucleosomes such as tetrasomes (only $(H3/H4)_2$ [1]) and hexasomes ($(H3/H4)_2$ and one $H2A/H2B$ [20]) are known to exist. Interestingly it was recently found [142] that hexasome formation coincides with

activity of PolII an enzyme responsible for transcription also studied in this work (see chapter 4.3).

In order to maintain and control accessibility of the nucleosomal DNA for transcription, replication and repair proteins, several mechanisms have evolved. [13] use transcription as an example that includes the most important of these processes all at once. They argue that the AT-rich regions of many PolII promoters are related to a bending of the DNA in a way that destabilizes nucleosomes. This destabilization causes a so called nucleosome free region (NFR) which is approximately 100 base pairs long and located at the transcription start site. The first nucleosome next to this NFR is oftentimes found to contain alternatively spliced H2A.Z instead of canonical H2A while the mayor part of the coding region is usually packed by canonical nucleosomes. Nucleosomes containing H2A.Z are thought to be less stable than canonical nucleosomes and might hence make the NFR more easily accessible. It is stated that the transition to the active state is accompanied by increased histone acetylation, nucleosome movements in the promoter and coding regions and nucleosome loss close to the transcription start site.

Following this example the easiest way of controlling DNA accessibility is related to the intrinsic instability of nucleosomes which allows for a detachment and reattachment of the DNA ends commonly referred to as breathing or transient DNA unwrapping [67]. Even though no additional proteins are involved in the breathing itself various pathways to control this process exist.

The two most important ways of controlling the nucleosome stability aiming to change the histone DNA affinity are alternatively spliced histones and post translational modifications mostly methylation or acetylation of amino-acids in close proximity to the DNA.

In chapter 5.5 the change in affinity caused by acetylation and methylation of a lysine on position 64 of the *H3* histone is investigated. The destabilizing effect is found to be negligible for strong positioning sequences such as the *Widom 601* sequence [70][122] used here [24].

Furthermore the stability of nucleosomes containing a novel alternatively spliced *H2A* variant (*H2A.Z.2.2*) or an other variant (*H2A.Z.2.1*)

is compared to the stability of canonical *H2A* in chapter 5.4.

Another way for an organism to guarantee accessibility of genes is active repositioning of nucleosomes on the DNA strand catalyzed by an ATP driven chromatin remodeling factor (remodeler). In the above example the remodeler is required to allow access of the PolII to the actual gene. This repositioning is also required for other processes e.g. to induce equal distances of nucleosomes on a DNA strand prior to further compaction oftentimes accompanied by gene silencing. An example for such a remodeler is the well studied *ACF* (ATP-utilizing Chromatin assembly and remodeling Factor) complex which is amongst other functions capable of equally spacing the nucleosomes on a DNA strand [138][104]. The mammalian ACF is assumed to be a tetramer consisting of two Snf2H (Surcorse non-fermenting 2 homolog) motor proteins and two ACF1 proteins [103]. While Snf2H is responsible for the actual repositioning of the nucleosome the ACF1 is supposed to control direction and speed of the repositioning [39].

In order to understand the individual functions of different remodeling enzymes it is important to understand the differences between them. To this end, the two ISWI ATPases present in human cells, namely Snf2H (ATPase of the CHRAC and ACF complexes) and Snf2L (ATPase of the NURF complex), were investigated in chapter 5.3 and different activity changes upon increasing dilution could be resolved.

5.2 Common methods

Many experimental methods such as sample preparation and handling as well as data filtering were commonly used for each of the nucleosome projects discussed in this section. This chapter will summarize and explain these techniques in one place. The term *nucleosome* will in the following generally be used for mono-nucleosomes since only such constructs were investigated. Any additional methods required for each of the projects are described in the respective experimental section.

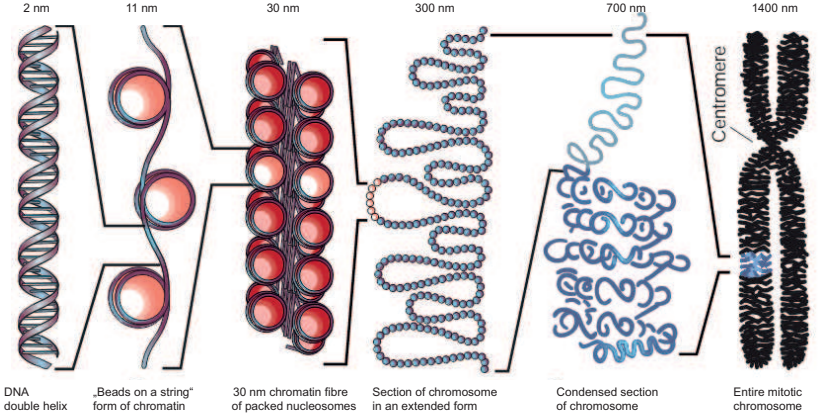

Figure 5.1: Levels of DNA compaction in chromatin. An overview of the different levels of compaction and the associated dimensions and names as described in this work.This figure was obtained from [25], Licensee: Wolfgang Kügel; License Date: Apr 4, 2012; License Number: 2881961027940

5.2.1 Labeling sites and DNA preparation

To perform single molecule experiments on nucleosome dynamics and accessibility it is crucial to have a well defined sample. This is necessary since a defined initial state is required to identify changes caused by modifications or remodeling enzymes.

Since on a random DNA sequence nucleosomes can usually be assembled at various locations special sequences have to be used to ensure only one well defined nucleosome position. The experiments discussed in the following are all based on an initial position of the nucleosomes on the DNA defined by the strongest known positioning sequence, namely the *Widom 601* [70] sequence if not stated otherwise. Random sequences were added at both ends (see figure 5.2) to obtain longer DNA constructs.

Since the *601* sequence will be significantly favored by the hisone octamer over the additional random sequences a well defined nucleosome position is assumed. All labeling sites were chosen to yield a maximum FRET efficiency change upon any movement of the nucleo-

some core or the DNA regardless of the reason for the movement (i.e. intramolecular dynamics or remodeling). This means that a transition from high FRET to low FRET state will occur if the initial nucleosome position on the DNA is changed or if the DNA (partly) unwraps from the nucleosome core.

A total of three labeling combinations is used (see figure 5.3):

- The *F+14* (Atto532) *F-64* (Atto647N) dye combination was used on a 200 base pair DNA to study the differences of Snf2H and Snf2L, two remodeling enzymes that reposition the nucleosome from the side to the center of a DNA strand (chapter 5.3). These labels are positioned such that a remodeling of the nucleosome to the center of the DNA will cause a clearly detectable FRET efficiency change.

- The *F-15* (Tamra) *R-60* (Alexa647) positions are located on the opposite side of the nucleosome as compared to *F-64 and F+14* and a bit further inward. They were used to study the changes of nucleosome stability in case of the incorporation of alternatively spliced *H2A* variants (chapter 5.4) as well as postranslationally modified *H3K64* (chapter 5.5) histones.

- The labeling positions *F-38* (Tamra) *R-40* (Alexa647) are chosen close to the dyad since a modification of the *H3K64* position (chapter 5.5) is most likely mainly affecting the inner loop turn of the nucleosomal DNA (see figure 5.11). These positions yield the most sensitive sample system for H3K64 modifications with labels only on the DNA .

It has been shown that it is possible to directly label histones and still obtain intact nucleosomes [98]. However, in this thesis no histones carrying additional modifications, such as a dye, were used. This was done since especially the experiments on nucleosome stability and dynamics discussed in chapters 5.4 and 5.5 were performed to detect effects of histone modifications which otherwise might be biased.

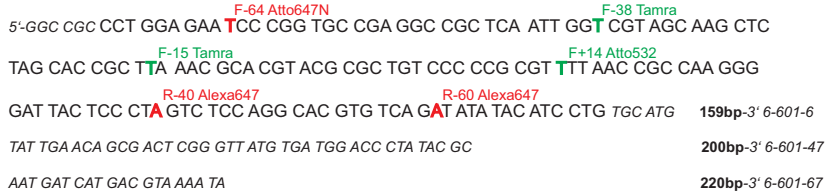

Figure 5.2: Summary of the DNA sequence and associated labeling sites used for Nucleosome experiments. The forward strand of the nucleosome positioning sequence *Widom 601* is highlighted (bigger letters). The base pairs added to obtain the 159-, 200- and 220 base pair constructs used are shown in smaller letters. A donor (green) or acceptor (red) labeling position is indicated in the respective color. The labeling sites are given with their respective dyes and positions relative to the nucleosome dyad counted towards the 3'end. Dyes located on the forward strand are indicated by an *F*, dyes on the reverse strand by an *R* in front of the number describing the dye position.

All necessary fully synthetic primers with and without labels used for DNA preparation by PCR in this chapter were obtained from IBA GmbH (Göttingen).

5.2.2 Nucleosome handling

All handling of samples containing histones or assembled nucleosomes was done using low binding pipette tips (LAd-Professional, Biozym Scientific GmbH, Hessisch Oldendorf, Deutschland) and low binding eppendorf cups (Biozym Scientific GmbH, Hessisch Oldendorf).

5.2.3 Nucleosome assembly

Nucleosomes were assembled by the respective collaboration partners using salt gradient dialysis and were used as supplied (for details see [24] and [9]). Assembled nucleosomes were stored at 4°C until usage.

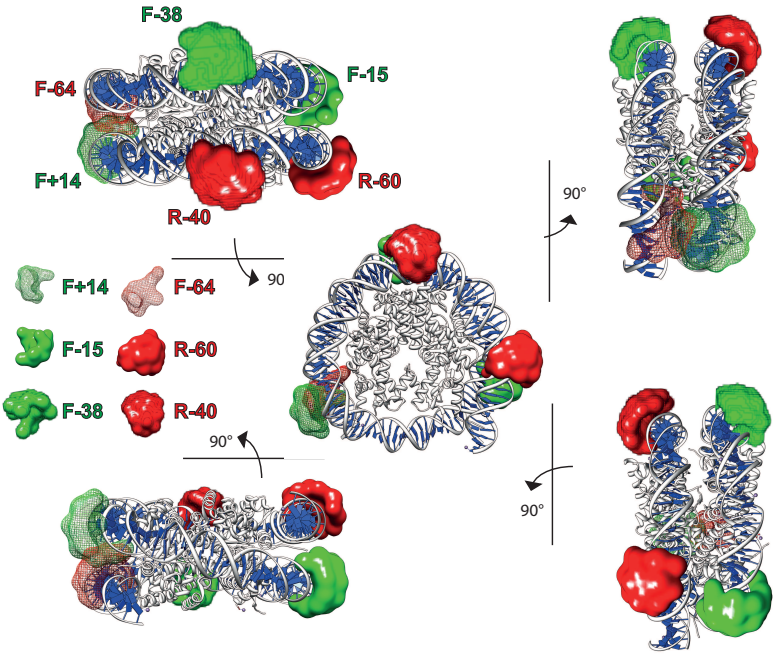

Figure 5.3: Location of the labeling sites on mono-nucleosomes. The crystal structure of a nucleosome (PDB: 3lz0) is used to represent the dye positions (68% credibility surfaces,see chapter 3.6) assuming that the *Widom 601* sequence used in this work is wraped around the nucleosome while additional DNA forms unbound overhangs at both ends (not shown, compare to figure 5.2). The top view is shown in the center allowing for a derivation of the other views by rotation around the respective axis as indicated. Dye pairs of donor (green) and acceptor (red) belonging together are shown in the same style i.e. a mesh (*F+14 F-64;* used in chapter 5.3), a solid surface (*F-15 R-60;* used in chapters 5.4 and 5.5) and a fuzzy surface (*F-38 R-40;* used in chapter 5.5).

5.2.4 Coverslip coating

Since nucleosomes are known to become instable upon contact with glass surfaces [72] different cover slip coatings were applied for the individual experiments minimizing the available glass surface. The following sections will describe the preparation of the cover slips using polyethylene glycol (PEG) and 1,2-Dioleoyl-sn-glycero-3-phosphocholine (DOPC).

5.2.4.1 Cleaning

Cover slips (Marienfeld) were heated to 100°C in a 2% solution of Hellmanex III (Hellma) and washed thoroughly using double distilled water (ddH_2O) to remove the detergent. After drying the coverslips in nitrogen flow possibly remaining dirt and water were removed by a butane-gas flame.

5.2.4.2 PEG coating

PEG coating was performed as described in [2]. The clean and dry cover slips were silanized for 30 minutes in a 2% solution of (3-aminopropyl)-triethoxysilane (Sigma-Aldrich, Schnelldorf) in spectroscopically clean acetone. After the coverslips were rinsed (ddH_2O) and dried (nitrogen flow) they were incubated for one hour in a solution of mPEG-succinimidyl propionate (40 $mg/100\ \mu l$,mPEG-SVA MW 5000 Da, Laysan Bio Inc.) in carbonate-bicarbonate buffer (pH 9.4). The coated slips were heated in ddH_2O to boiling and then rinsed thoroughly. Remaining ddH_2O was removed under nitrogen flow.

5.2.4.3 DOPC coating

The preparation of the vesicles necessary to allow for a coating of cleaned glass surfaces was performed as similarly described by [113]. First lipid films were prepared by dissolving 300 μg DOPC (Avanti Polar Lipids, Alabaster, USA) in chloroform and removing the solvent under nitrogen flow. Remaining chloroform was evaporated under vacuum for at least one hour.

The lipid films were redissolved in Ex0 Buffer (see chapter 5.2.6) for 1 hour at 4°C. The resulting solution of multilamellar vesicles was extruded (Liposofast Basic, Avestin Europe GmbH, Mannheim, Germany) through polycarbonate membranes (31 times, 200 nm pore diameter) resulting in a solution of unilamellar vesicles with a diameter of $\sim$200 nm.

A cleaned cover slip was incubated in the resulting solution for 1 hour after the addition of $CaCl_2$ (100 mM). The $CaCl_2$ causes the vesicles to become instable and form a DOPC layer on the glass surface.

The coated cover slip was thoroughly rinsed (ddH_2O) and dried using nitrogen prior to use.

5.2.5 Sample loading

Samples were loaded directly onto the coverslip as drops with volumes of 40μl. To minimize evaporation additional drops of pure water were positioned around the sample and a small cap with a total volume of $\sim$2 ml was put over the cover slide. Hence the air in this confined volume was saturated with water from numerous droplets and the loss of water from the actual sample required for saturation of the surrounding volume was reduced. This was sufficient to perform all measurements presented in this chapter without noticeable effects of sample evaporation.

5.2.6 Buffers

A summary of the Buffers used in this chapter can be found in the Tables below.

5.2.7 Dynamic filter

While the time deviation signal (TDS) filter described in section 4.3.4 is not biased by fast dynamics where changes occur several times throughout a burst, slow dynamics with rates similar to the diffusion time can be falsely detected as multi molecule events.

Table 5.1: Composition of the Ex-X Buffer

Ex-X Buffer	
20 mM	Tris-HCl pH 7.6
1.5 mM	$MgCl_2$
0.5 mM	EGTA
10 %	Glycerol
X mM	KCl

To better understand the problem recapitulate equations 4.13 and 4.14 and note that the TDS is based on differences in the mean-macrotime (MMT) (see figure 4.23) and burst duration of the individual channels (GG,GR,RR). For simplicity the following explanation uses the MMTs only. It is however worth noting that it is in principle also valid for the duration differences contributing to the TDS.

Now, assume a molecule switching between a high and a low FRET state. If several of these transitions occur while the molecule is in the focal volume only an average will be detected and the MMT of all three channels will be identical. Hence the values obtained for TDS as well as TDS_{red} will be close to zero.

In contrast if only few transitions[1] occur during the observation time of a single molecule burst the individual states are not averaged over the whole burst and the MMTs are different for the GG andGR channel hence resulting in a nonzero TDS signal[2]. Note that even though the RR signal is not affected by the dynamics under normal experimental conditions the TDS_{red} value observed for such an event will also be increased as compared to a non dynamic sample. This happens because usually the detection efficiencies in the green and red channels are not equal and hence the total counts detected for a high FRET or a low FRET state will differ (for better understanding

[1]The actual limit of transitions within one burst that still significantly bias the TDS signals strongly depend on the countrate of the respective sample and is hard to predict. In this thesis it is assumed that only 1 or 2 transitions have a significant effect and the discussion is limited to these two cases

[2]Due to the limited photon numbers in an actual experiment the values for TDS and TDS_{red} are unlikely to be exactly zero. The description given here assumes an infinitely high photon count to allow for a clearer description of the problem.

refer to chapters 3.2.4.3 and 3.2.4.4). Since the MMT of all photons (T_{all}) is not corrected for differences in detection efficiencies it is also biased by the slow dynamics and will change the value obtained for TDS_{red}.

Nucleosomes are known to be opening and closing at rates of about 25 s^{-1} which is significantly slower than the average observation time of 1 ms [124, 57]. Since some of the nucleosome modifications investigated in this thesis might not only change the nucleosome stability but also the kinetic rates, measures were taken to ensure the comparability of the respective data.

As discussed above, a transition from e.g. a high to a low FRET state occurring while the respective molecule traverses the confocal volume leads to differences in the individual MMT of the channels (T_{FRET}, T_{red} and T_{green}).

Additional sources for differing MMTs are photo-physical effects such as blinking and bleaching as well as the various multi-molecule events possible. Hence to exclude dynamic bursts from the TDS filter a possibility to identify such bursts had to be developed.

To this end the the differential signals (T_{green} - T_{red}, T_{FRET} - T_{red} and T_{green} - T_{FRET}) can be used. Each of these differential signals can be either positive (+)or negative (−), and these algebraic signs yield distinct patterns for dynamic bursts as explained in the following.

Regarding the expected sign (+ or −) patterns it is first of all important to note that multi-molecule events can cause all kinds of combinations depending on the timepoint the individual molecules enter and exit the focal volume and the species involved (donor only, acceptor only, high FRET, low FRET).

In contrast, a systematic analysis of the signs expected for photo physical events on high FRET (HF) and low FRET (LF) molecules as well as molecular dynamics with one and two transitions per burst shows distinct patterns for dynamics and photo-physics (see table 5.2 for a summary or Appendix A.2 figure A.4A-C for details). Using these sign patterns it is hence possible to clearly separate photo physics from molecular dynamics.

In this thesis to allow for an efficient removal of multi-molecule events while still maintaining dynamic events, bursts showing the

sign patterns $+-+$ and $-+-$ (T_{green} - T_{red}, T_{FRET} - T_{red}, T_{green} - T_{FRET}), which were identified to be caused by molecular dynamics (see table 5.2 dark grey), were excluded from the respective TDS thresholds (see schematic in figure 5.4A).

It is important to note that an exclusion of these specific bursts patterns will also bias the effectiveness of the TDS filter for multi-molecule events. This happens since multi-molecule events, as previously discussed, are expected to possess random sign patterns. To estimate the share of multi-molecule events influenced by the dynamic filter, the three differential signals can be assumed as a three dimensional cube with the 0 position in the center. Based on this imagined cube the sign combinations $+-+$ and $-+-$ cover $2/8$th of the total volume. Hence applying the dynamic filter described above will, in addition to the dynamic events, exclude $1/4 = 25\%$ of all randomly distributed bursts (i.e. multi-molecule events) from the TDS thresholds.

In a real experiment, data quality usually is not significantly reduced by activating the dynamic filter as demonstrated in figure 5.4B-D on a dataset collected for the H2A.Z project presented in chapter 5.4. Here, the data quality reached by applying a stoichiometry threshold is used as a starting point (figure 5.4B). Removing events with $TDS \geq 1$ and or $TDS_{red} \geq 0.6$ results in a much cleaner dataset as especially seen in the stoichiometry projection of the two dimensional scatter plot to a one dimensional histogram (figure 5.4C). Remarkably the data quality (easiest judged by the stoichiometry projection in this example) does not get significantly worse when the dynamic filter is applied (compare figure 5.4 C and D) while in the FRET efficiency region between the two main peaks where dynamic bursts would be expected slightly more events are maintained.

5.3 Chromatin remodeling enzymes

The work presented in this chapter was done in a collaboration with the group of Prof. Dr. Gernot Längst (Universität Regensburg). Since the data presented in this chapter were a minor part of this collabo-

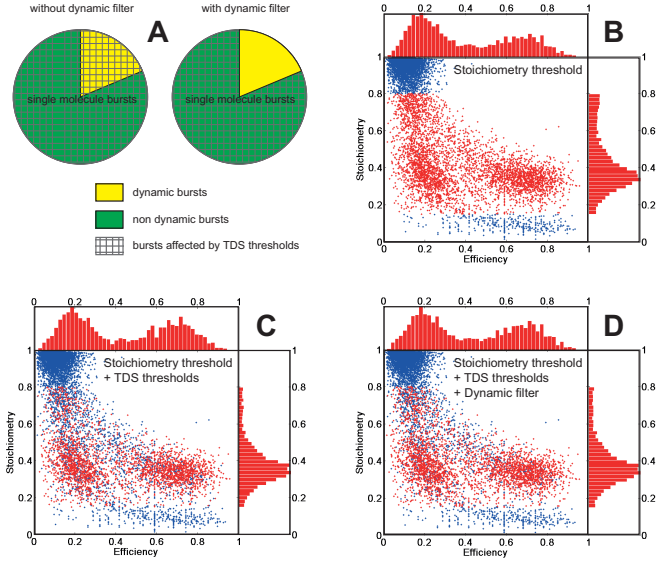

Figure 5.4: Application of the dynamic filter to smFRET data. (A) Schematic depicting the way the dynamic filter works on single molecule burst data. The total of all bursts detected is symbolized by the circle and the share of dynamic events is marked in yellow. The dynamic filter excludes such bursts identified to be dynamic (yellow) from the TDS thresholds (grey grid) which are then only applied to non dynamic bursts (green).
(B-D): Experimental data collected from a mono-nucleosome sample as described in chapter 5.4.2 (*H2A.Z*, nucleosomal DNA labeled at positions F-15 R-60, TE pH 7.6). Shown are two dimensional burst analysis data scatter plots of Stoichiometry versus FRET Efficiency, together with the one-dimensional projections. Besides dual labeled nucleosomes, the sample contained also impurities of donor and acceptor only complexes as can be seen by the $Sto = 0$ and $Sto = 1$ populations. The high concentration of molecules in the sample combined with the significant amount of single labeled impurities cause strong trailing between the individual populations clearly visible in the raw data (B). Bursts remaining after setting a threshold for the stoichiometry $S = 0.15 - 0.8$ (B), after time deviation signal (TDS) thresholds are set to $TDS < 1$ and $TDS_{red} < 0.6$ (C) and after activating the dynamic filter (D) are shown in red and given as projections. Note that the Stoichiometry threshold was set very loose here for better visibility of the effect of the dynamic filter. A significant improvement of the data quality is reached by removing the multi-molecule events (C) as can bee seen especially in the Stoichiometry projection. Importantly data quality does not get significantly worse when applying the dynamic filter (D).

	T_{green} - T_{red}	T_{fret} - T_{red}	T_{green} - T_{fret}
Dynamics HF -> LF	+	-	+
Dynamics LF -> HF	-	+	-
Dynamics LF -> HF -> LF HF state early in the burst	+	-	+
Dynamics LF -> HF -> LF HF state in the middle of the burst	0	0	0
Dynamics LF -> HF -> LF HF state late in the burst	-	+	-
Dynamics HF -> LF -> HF LF state early in the burst	-	+	-
Dynamics HF -> LF -> HF LF state in the middle of the burst	0	0	0
Dynamics HF -> LF -> HF LF state late in the burst	+	-	+
HF Donor blinking early in the burst	+	+	0
HF Donor blinking in the middle of the burst	0	0	0
HF Donor blinking late in the burst	-	-	+
HF Acceptor blinking early in the burst	-	0	-
HF Acceptor blinking in the middle of the burst	0	0	0
HF Acceptor blinking late in the burst	+	0	+
HF Donor bleaching	-	-	0
HF Acceptor bleaching	+	0	+
LF Donor blinking early in the burst	+	0	+
LF Donor blinking in the middle of the burst	0	0	0
LF Donor blinking late in the burst	-	0	-
LF Acceptor blinking early in the burst	-	-	0
LF Acceptor blinking in the middle of the burst	0	0	0
LF Acceptor blinking late in the burst	+	+	0
LF Donor bleaching	-	0	-
LF Acceptor bleaching	+	+	0

Table 5.2: Summary of possible signs for the mean-macro-time differences T_{green} - T_{red}, T_{FRET} - T_{red} and T_{green} -T_{FRET}. Expected MMT differential signals T_{green} - T_{red}, T_{FRET} - T_{red} and T_{green} - T_{FRET} signs caused by dynamics and photo-physical effects. The prefixes are shown to depend on the occurrence of the respective event within the burst (early, middle or late) and on the FRET efficiency of the burst i.e. high FRET (>50%, HF) as well as low FRET (<50%, LF). Importantly photo-physics (light grey) and dynamics (dark grey) show distinct prefix patterns allowing for a clear identification of such events. In the rare case that a transition independent of its origin (photophysics or dynamics) occurs exactly in the middle of a burst the prefix pattern will not allow for an identification of the event (white).

ration only the single molecule results obtained by the author will be discussed in detail. A brief summary of the associated data obtained by the collaborating group is however given in the following introduction. A full discussion of all experiments described in this section including the single molecule data shown here can also be found in [24].

5.3.1 Introduction

The term remodeler is commonly referred to as proteins or protein complexes which change the packaging state of chromatin. This process involves the hydrolysis of ATP to move, or restructure the nucleosome. An extensive review of the state of knowledge on remodelers can be found in [13] and only a brief summary aiming to allow for a better understanding of the experiments performed in this thesis is given in the following.

Classification Remodelers can be classified into four main families (SWI/SNF, ISWI, CHD, INO80) which all utilize Snf2 family ATPases but differ in their auxiliary subunits. This chapter will focus on the ISWI (imitation switch) family and the two ATPases occurring in humans which are the 127kDa Snf2H and the 126kDa Snf2L. While Snf2L is part of only the NURF complex Snf2H is found in various remodeling complexes (ACF, CHRAC, NoRC, RSF and WICH).

Domains All ISWI family ATPases have characteristic highly conserved C-terminal SANT and SLIDE domains responsible for nucleosome recognition. Moreover they have a HAND domain that is suspected to be important for oligomerization [104]. DEXDc and HELICc are the highly conserved ATPase domains not limited to the ISWI family but common to all ATPases (see figure 5.5).

Function While some ISWI-type remodelers are thought to assist chromosome assembly by adjusting the nucleosome spacing (ACF, CHRAC), NURF has an opposite effect since it randomizes nucleosome spacing. The Snf2L complex NURF is on the one hand known to

promote transcription activation while on the other hand also causing enhanced H1 loading to nucleosomes hence supporting chromosome compaction [15].

Even though ISWI complexes actively participate in DNA condensation some are assumed to be connected to transcription initiation by actively making DNA regions accessible to the proteins involved. In this context human Snf2H has been shown to promote DNA replication as part of the ACF complex [14] and to be active at the replication focus as part of the WICH complex [101].

Some remodelers are thought to be complexes containing only one ATPase domain acting as a monomer. There is however strong evidence that ACF acts as a dimeric system allowing for an easy switching between back and forth movement[103].

Current models for the mechanism of remodeling assume that the remodeler is anchored at the histone core moving the DNA around it. The SLIDE domain is currently thought to interact with the linker DNA while the ATPase domain binds the DNA approximately two turns from the nucleosome dyad [143] [137]. In this way the remodeler can push DNA from the linker towards the nucleosome forming a loop which is then actively propagated towards the dyad followed by a one dimensional diffusion to the other end of the nucleosome. Currently neither the manner of this process (concerted or sequential) nor the size of the propagating loop is known.

Regulation For the Snf2H containing remodelers it has however been shown that a regulation might be achieved through the interaction of the non catalytic subunits and the linker DNA [39].

ISWI remodelers in general are known to be regulated by histone modifications (e.G. H4K16 acetylation causes reduced activity for some ATPases while increasing the activity for others) and by the length of the DNA linker between two nucleosomes. Especially the second feature might be essential for the correct spacing of nucleosomes.

Differences between Snf2H and Snf2L Since the smFRET experiments described here were part of a collaboration the results obtained

by collaboration partners necessary to understand and interpret the data are shortly summarized in the following. All information on Snf2H and Snf2L reproduced in this paragraph was obtained from [24] and will not be cited separately again. Note that most of the summarized results were obtained using a nucleosome positioning sequence (refered to as *NPS1* sequence) which is only 87% identical to the *Widom 601* sequence used for the single molecule studies presented here (figure 5.2).

In humans Snf2L and Snf2H are the two known ISWI ATPases. While the DEXDc, HELICc, HAND, SANT and SLIDE domains are highly conserved (95%) significant differences are found at the N and C-terminal ends of the sequences (see figure 5.5). These differences result in somewhat different binding and remodeling behavior as summarized in the following.

Table 5.3: Summary of bulk results for Snf2H and Snf2L. Binding ($k_{1/2}$) and dissociation (k_d) constants as well as Hill-coefficient (n) results are discussed in detail in [24] and only summarized here

construct	Parameter	Snf2H	Snf2L
6-NPS1-47 nucleosomes	$k_{1/2}$ $[nM]$	304 $\pm$6	205 $\pm$21
6-NPS1-47 nucleosomes	n	7.3 $\pm$1.2	2.4 $\pm$0.6
6-NPS1-47 nucleosomes	k_d $[nM]$	7.7 $\pm$1.2	3.9 $\pm$0.4
6-NPS1-47 nucleosomes	n_d	1.7 $\pm$0.4	1.7 $\pm$0.3
22-NPS1-22 nucleosomes	$k_{1/2}$ $[nM]$	638 $\pm$16	471 $\pm$21
22-NPS1-22 nucleosomes	n	7.1 $\pm$1.0	3.6 $\pm$0.5
40-NPS1-40 nucleosomes	$k_{1/2}$ $[nM]$	647 $\pm$28	238 $\pm$13
40-NPS1-40 nucleosomes	n	7.2 $\pm$1.6	2.4 $\pm$0.3
77-NPS1-77 nucleosomes	$k_{1/2}$ $[nM]$	527 $\pm$26	308 $\pm$12
77-NPS1-77 nucleosomes	n	9.5 $\pm$4.0	3.6 $\pm$0.5
77-NPS1-77 free DNA	$k_{1/2}$ $[nM]$	7.7 $\pm$1.2	3.9 $\pm$0.4
77-NPS1-77 free DNA	n	1.7 $\pm$0.4	1.7 $\pm$0.3

The binding experiments revealed binding ($k_{1/2}$) and dissociation (k_d) constants both indicating a higher nucleosome affinity for Snf2L than for Snf2H (see table 5.3). Additionally a high cooperativity was detected for both enzymes. Interestingly Snf2H showed an almost

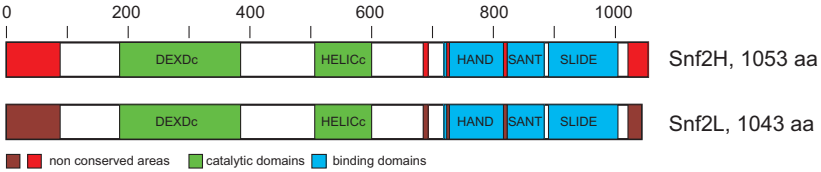

Figure 5.5: Snf2H and Snf2L are highly conserved. The catalytic (green) and binding (blue) domains are highly conserved between Snf2H and Snf2L. In contrast the N and C terminal ends show only low conservation (∼20% identity). This figure is based on [24], figure 5.1.

twice as high cooperativity as Snf2L.

At elevated enzyme concentrations (above 300 nM) agglomerates were observed. Snf2L caused distinct multimers resolvable using gel electrophoresis while Snf2H agglomerates were too large to enter a poly-acrylamide (PAA) gel.

Competitive binding experiments showed preferential binding to *0-NPS1-0 DNA* over *0-NPS1-0* nucleosomes (slightly bound) and *22-NPS1-22* nucleosomes almost unbound for both enzymes. Comparing *40-NPS1-40* to *77-NPS1-77* nucleosomes showed preferential binding of the latter one by Snf2H while Snf2L showed higher affinity to nucleosomes with a shorter overhang.

Native gel remodeling experiments indicated DNA overhang length dependent differences in remodeling activities. While Snf2H showed decreasing remodeling activity with decreasing linker length and no activity for a *0-NPS1-0* and even a 200 bp *33-NPS1-20* nucleosome, Snf2L remained active even without a DNA overhang. Interestingly Snf2H was highly active on a differently positioned 200 bp *6-NPS1-47* construct moving the nucleosome to the center of the DNA strand as was also done by Snf2L. Additionally experiments by other groups in human malignant cancer cell lines showed that a depletion of Snf2L led to growth inhibition and cancer cell death while a deletion of Snf2H had no effect [139].

Based on these results single molecule experiments were performed to further investigate the influence of substrate affinity on remodeling.

5.3.2 Experimental details

Sample preparation In order to perform single molecule experiments on the kinetics of nucleosome remodeling Snf2H and Snf2L were purified and nucleosomes were assembled from chicken histones by Josef H. Exler as described in [24]. It was ensured that both enzymes show comparable activity in standard in vitro assays by following the time course of ATP consumption upon remodeling 77-NPS1-77 nucleosomes (data not shown). Snf2 samples were used as provided.

Since the *6-NPS1-47* nucleosome alignment was the smallest construct under investigation still showing remodeling by Snf2H and Snf2L and only one well defined population before and one after remodeling, it was also used for the single molecule experiments presented here. The nucleosomal DNA was labeled with an Atto532 dye molecule at position *F+14* and with an Atto647N dye at position *F-64* relative to the dyad (chapter 5.2.1). It was assembled from 10 different overlapping oligo nucleotides by Barbara Treutlein (Group of Prof. Dr. Jens Michaelis, Ludwig-Maximilians-University, Munich) using a Ligase Chain Reaction (LCR). Note that despite the different statement in [24] the DNA used for the single molecule experiments had the *widom 601* based positioning sequence depicted in 5.2 (*6-601-47*) and not the slightly different *NPS1* sequence used for the bulk measurements.

Measurement and data filtering Confocal burst analysis measurements were performed at 100 μW laser power before the objective as described in chapter 3. Samples (40 μl) were transferred to a DOPC coated cover slide (see chapter 5.2.4.3) and data collection was started 30 s after the addition of 430 μM ATP.

Multi molecular events were removed from the data using TDS<0.45 and TDS_{red}<0.5 (see chapter 4.3.4) with activated dynamic filter as described in detail in chapter 5.2.7. Remaining donor and acceptor only bursts were excluded by a stoichiometry threshold.

5.3.3 Single molecule experiments

5.3.3.1 Agglomeration at enzyme concentrations higher than the binding constant

In the studies by [24] differences of Snf2 binding to *77-NPS1-77* nucleosomes were found. While Snf2L formed differently sized complexes separable in a native Polyacrylamide (4.5% PAA) gel, Snf2H formed aggregates too large to enter the gel.

In order to gain more insight into this behavior, single molecule experiments were performed on *6-601-47* nucleosome samples at concentrations above the binding constants (see table 5.3).

The expected agglomeration of nucleosomes and remodelers due to the high cooperativity could be shown for both enzymes.

An example for agglomeration of 220 basepair *6-601-67* nucleosome samples before and after the addition of 590 nM ATPase shows the results obtained (figue 5.6).

The detection of populations at about $20 - 50\%$ FRET efficiency (figure 5.6, blue) results from the formation of large aggregates formed after the addition of Snf2. These aggregates contain both high as well as low FRET molecules which results in the observation of an average FRET value. This interpretation is strengthened by the increased brightness and duration observed for these bursts. Hence the above experimental results indicate that agglomerates caused by the ISWI ATPases consist of high FRET 601 positioned nucleosomes as well as free DNA and all other nucleosomes contributing to the low FRET state prior to Snf2 addition (compare red and blue scatter plots in figure 5.6).

Additionally as expected differences between Snf2H and Snf2L could be detected. However since agglomerates are hard to quantify using confocal single molecule methods no reproducible dependence of agglomeration and concentration could be derived. To further investigate these agglomerates super resolution imaging (e.G. STED, STORM and PALM) or AFM might be the tool of choice for sufficiently large agglomerates.

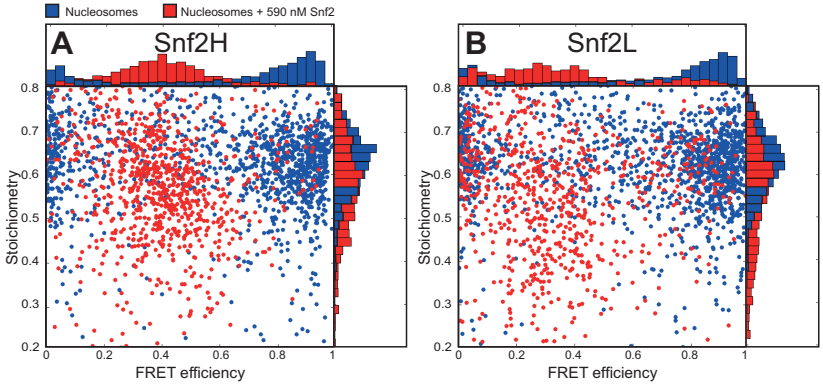

Figure 5.6: Agglomeration of nucleosomes induced by Snf2H and Snf2L. The FRET efficiency and stoichiometry distributions of 220 base pair *6-601-67* nucleosome samples before (blue) and 30 minutes after (red) addition of 590 nM Snf2H (left) or Snf2L (right) is shown by scatter plots and one dimensional projections.

5.3.3.2 Remodeling time depends on the concentration

While as just demonstrated concentrations above the binding constant cause agglomeration of the sample, the kinetic single-molecule studies presented in the following were performed under conditions where the available amount of remodeler was limiting.

Experimental considerations Using the 6-601-47 200 base pair DNA (see figure 5.2) for nucleosome assembly and assuming a perfect alignment with the *Widom 601* sequence[3] will bring both labels to positions in close proximity to each other and locate them near the nucleosomal entry/exit site (figure 5.3). Assuming the standard R_0 for an Atto532-Atto647N dye pair of 59 Å[4] and distance of 40-45 Å estimated from the crystal structure one expects to measure a FRET efficiency of 84-

[3]The crystal structure of a DNA with the 601 sequence wrapped around a histone core can be found in PDB:3LZ0

[4]www.atto-tec.com/fileadmin/user_upload/Katalog_Flyer_Support/R%280%29-Values_2011.pdf, 06.04.2012

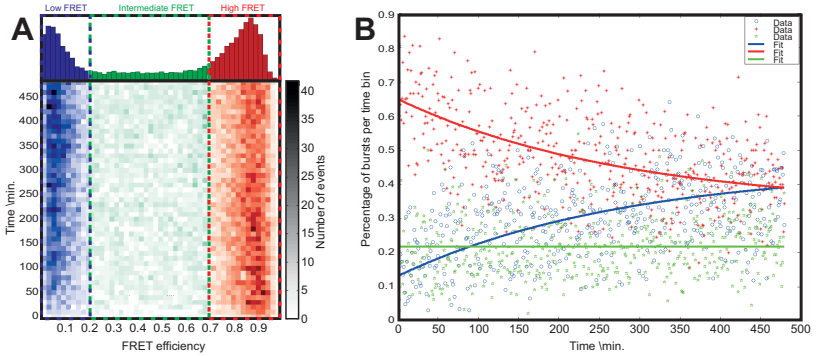

Figure 5.7: Identification of subpopulations and time evolution of nucleosome remodeling. (A) Two dimensional plot of FRET efficiency (color scale) versus time after addition of ATP with 17 nM Snf2H and 28 nM nucleosomes showing a change from high to low FRET with time. The histogram is segmented in three parts, low (0-20%) FRET efficiency, intermediate (20-70%) FRET efficiency and high (70-100%) FRET efficiency which are used for further analysis. The top shows the 1 dimensional FRET distribution histogram which is obtained by integrating over the complete measurement time.
(B) Percentage of fluorescence bursts of high, medium and low FRET as a function of time analyzed in time bins of 60 seconds. As a result of the remodeling reaction the high FRET fraction (red stars) decreases and simultaneously the low FRET population (blue circles) increases while the intermediate population (green stars) stays approximately constant. The high FRET and low FRET data can be fitted using single exponentials (solid lines).

91% for perfectly assembled nucleosomes.

The FRET efficiencies obtained for the high FRET (HF) population as shown in figure 5.7A are in good agreement with this expected FRET efficiency for perfectly assembled nucleosomes. One however has to note that usually every sample contains some amount of mis-assembled nucleosomes (mostly tetramers or hexamers) and free DNA. For this reason data collected from mono-nucleosome samples typically do not only show the expected high FRET population but also an additional low FRET peak. That was also true for the experiments presented here where always a small low FRET (LF) population was present already prior to remodeling.

Both ISWI ATPases under investigation (Snf2H and Snf2L) are known to translocate nucleosomes positioned at the ends of the DNA to the center upon addition of ATP [24]. In the experiments presented here, this will move the F-64 position out of the nucleosome core particle and away from the F+14 position hence causing a decrease in FRET efficiency. Since no change of the intermediate fret state (MF, figure 5.7 green) state was observed throughout all the experiments performed at concentrations below the binding constant it is assumed that the dye distance increases such that the remodeled nucleosomes show approximately 0-10% FRET efficiency. Therefore an analysis of the time evoultion of the HF and LF populations can be used to resolve remodeling reaction kinetics. To this end two dimensional histograms of FRET Efficiency versus time were calculated for each measurement (figure 5.7A) and segmented into three parts according to their FRET efficiency. These parts were defined as LF (0-20% FRET), medium FRET (MF) (20-70% FRET) and HF (70-100% FRET). The time trace was binned into 60 second intervals and the share of bursts in each of the three FRET areas was calculated for the respective interval (figure 5.7B, data points). The observed time decays were globally fit (figure 5.7B, lines) using a maximum likelihood estimation algorithm. To this end a constant fraction of medium FRET bursts (MF) not affected by the remodeler (falsely assembled complexes, e.g. tetramers) was assumed. The HF and LF time decays could then be described by a coupled exponential decay for the LF (Eq. 5.1) and HF (Eq. 5.2) populations

$$LF(\tau) = LF_{\infty} - C * e^{\frac{-\tau}{T_l}} \tag{5.1}$$

and

$$HF(\tau) = 1 - MF - LF(\tau). \tag{5.2}$$

where T_l is the characteristic remodeling time scale and C is an empirically determined constant factor of 0.3 required to best match the observed decays.

An example of such a fit is given in figure 5.7B where at time point t_0, which is 30 seconds after the addition of ATP (see chapter 5.3.2) the LF population starts to exponentially increase while simultaneously the HF population decreases.

Attributing the HF population to nucleosomes positioned on the *Widom 601* sequence and the LF population to free DNA and remodeled nucleosomes allows for a comparison of the two remodeling enzymes. To this end the remodeling velocity $v = 1/T_l$ was calculated for each sample and concentration and normalized to the samples with the highest remodeler concentration. The normalized velocity was then analyzed as a function of the relative amount of remodeler (figure 5.8A).

Results To gain information about the influence of binding and unbinding on the remodeling speed experiments were performed at concentrations well below the binding constant where none of the ISWI ATPases showed formation of stable complexes with the nucleosomes in gel experiments (see summary of previous results in chapter 5.3.1).

To this end, a 1:20 mixture of double labeled and unlabeled *6-601-47* 200bp nucleosomes[5] (see figure 5.2) was used at a total concentration of 28 nM and remodeler concentrations of 17, 23, 34 and 69 nM, respectively in Ex-4.55 Buffer. For comparison, the binding constants for 6-NPS1-47 nucleosomes as determined in [24] are for

[5] As previously described nucleosomes are prone to become instable at low concentrations. To avoid errors the total nucleosome concentration was increased by adding unlabeled nucleosomes.

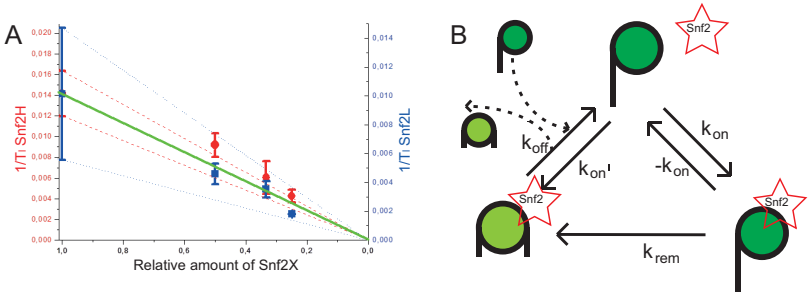

Figure 5.8: Concentration dependence of Snf2L and Snf2H remodeling speeds. Remodeling speed ($1/T_l$) for Snf2L (blue boxes) and Snf2H (red circles) as a function of the remodeler concentration (A). Experiments where performed in a regime where the remodeler is unbound most of the time. Thus, one expects a linear dependence of remodeling speed with remodeler concentration (green line). A deviation corridor based on the standard error of the first data point is shown by red dashed (Snf2H) and blue doted (Snf2L) lines. (B) Three state model used to explain the observed differences.

Snf2L $K_{1/2} = 205 \pm 21nM$ and for Snf2H $K_{1/2} = 304 \pm 6nM$. Under these conditions nucleosomes were stable for several hours and the remodeling process could be triggered by the addition of ATP.

Based on the limiting enzyme concentrations a simple three state model with only one remodeler bound at a time as depicted in figure 5.8B can be assumed. The binding of ATPase is the initial step followed by an ATP dependend remodeling of the nucleosome and dissociation of the enzyme. The limiting enzyme concentration in the experiments performed here will require several rounds of substrate binding, nucleosome movement and dissociation for each enzyme to achieve a complete conversion of the substrate (figure 5.8B). Following this model one would expect that a further reduction of concentration should lead to a decrease in observed velocity proportional to the total amount of remodeler finally ending at zero remodeling speed when no enzyme is in the solution (green line in figure 5.8A). This expected result is observed for Snf2L showing a decrease in velocity proportional to the concentration (see figure 5.8A, blue).

Since all data was normalized to the data measured at the highest Snf2 concentration, a deviation corridor was defined based on the standard error of this point. This corridor represents the expected deviation from the assumed decrease in remodeling speed. In contrast to Snf2L, a systematic deviation form the expected line exceeding the deviation corridor is observed for Snf2H (red), which can only be explained by either an increase in the rate of binding k_{on} and or an increase in the rate of unbinding k_{off}. Since, at these conditions k_{off} is rate limiting and an increase of k_{on} for decreasing enzyme concentration is also counterintuitive the data is likely to show a small increase in k_{off} for Snf2H over the investigated enzyme concentrations. As a result these experiments indicate that under the conditions used here k_{off} was rate limiting for the remodeling reaction and might be concentration dependent for Snf2H.

This result is in good agreement with the additional data presented in [24] where it was found by that Snf2L can use all positions of a 200 bp nucleosome as a substrate. In contrast, Snf2H has been shown to be unable to remodel e.G. a 20-NPS1-33 positioned nucleosome and also shows less stable binding to nucleosomes with reduced DNA linker length.

5.4 Non-canonical nucleosomes

The work presented in this chapter was done in a collaboration with the group of Prof. Dr. Sandra B. Hake (Ludwig-Maximilians-University, Munich). Results obtained by other members of this cooperation are summarized in the following introduction. Only the single molecule results obtained by the author will be discussed in the results section in detail. Since this work has previously been published all details regarding sample preparation steps not performed by the author of this work can be found in [9].

5.4.1 Introduction

In addition to the canonical histones also further specialized non-canonical variants have developed. The best studied amongst these is probably the H2A.Z histone family which has $\sim$ 60% sequence identity to canonical H2A [135] and is essential in most eukaryotes. Amongst other functions it is thought to improve accessibility of promoter sequences since it causes more open nucleosomes and is found to be globally enriched in regions flanking the transcription start site [34][13].

Incorporation in nucleosomes H2A.Z is known to be controlled by remodelers of the INO80 family. While H2A.Z-H2B dimers are inserted into chromatin by TIP60 and SRCAP the remodeler INO80 is known to also have the opposite effect, replacing H2A.Z-H2B with canonical H2A-H2B [13].

Alternative splicing Several forms of H2A.Z (e.g. H2A.Z.1 and H2A.Z.2) were already known prior to the studies presented in [9]. The investigated H2A.Z.2.2 is however the first alternatively spliced histone proven to exist in this group. This makes H2A.Z only the second histone family where alternative splicing has been observed. Only MacroH2A, another, larger form of H2A was known to be alternatively spliced before.

H2A.Z.2.2 In this chapter single molecule experiments on H2A.Z.2.2 are presented which are part of an extensive experimental effort on the detailed characterization of this protein. To allow for a better understanding of the results presented a summary of the additional experiments by other groups is given in the following. For a full discussion of these results refer to [9].

The necessary genes to allow for an alternative splicing of H2A.Z.2.2 are found in all primates and with some modifications also in horse, rabbit and panda-bear genomes. H2A.Z.2.2 could be shown to be expressed in human cells with a significant enrichment in brain tissues where it is found to make up up to $\sim$ 50% of all H2A.Z compared to

only 5-15% in other cells. Expression however could not be detected in mouse cells.

While H2A.Z.1 and H2A.Z.2.1 are highly conserved (98% identity, identical acetylation and ubiquitination patterns) H2A.Z.2.2 is 14 amino acids shorter and has an additional difference of 6 amino acids at the C-terminal end. This shortening causes also the loss of the two ubiquitination sites K129 and K121 which are part of the H3/H4 docking domain. The changed docking domain is found to prevent formation of a DNA free histone octamer while still allowing for stable H2A.Z.2.2-H2B dimer fomration.

Experiments showed that by itself neither the 6 changed amino acids nor the truncation by 14 amino acids were sufficient to cause this destabilization but only a combination of both. INO80 family remodelers could be shown to actively incorporate H2A.Z.2.2 into chromatin just as all other H2A.Z histones.

Interestingly fluorescence recovery after photo bleaching (FRAP) experiments indicated that H2A.Z.2.2 is primarily unbound in the cell nucleolus with only minor fractions incorporated into chromatin.

Nevertheless it was possible to obtain stable H2A.Z.2.2 mononucleo-somes containing all 8 histone subunits which were used for a variety of experiments. MNase experiments suggest that in case of H2A.Z.2.2 only a 120 bp DNA fragment is protected from digestion while the expected 146 bp were detected for canonical H2A. Moreover H2A.Z.2.2 was found to significantly destabilize nucleosomes containing H2A.Z.2.2. These digestion experiments suggest that the H2A.Z.2.2 containing nucleosomes are to some extent more dynamic and hence destabilized compared to canonical nucleosomes. This interpretation was also supported by molecule dynamics (MD) simulations comparing H2A.Z.1, a truncated *H2A.Z*.2.1[113] and H2A.Z.2.2. These MD simulations revealed a unique structural change in H2A.Z.2.2 that would cause an increased distance to the H3 histone. To experimentally resolve the differences in nucleosome stability the single molecule experiments described in the following were performed.

5.4.2 Experimental details

Sample preparation The DNA required to assemble a 159 bp *6-601-6* nucleosome construct for single molecule FRET experiments was labeled with a Tamra dye molecule at position *F-15* and with an Atto647N dye at position *R-60* relative to the dyad (see chapter 5.2.1). It was prepared by Monika Holzner (group of Prof. Dr. Jens Michaelis, Ludwig-Maximilians-University, Munich) using labeled custom made primers (IBA GmbH, Göttingen), dNTPs (Finnzymes) and the Phusion DNA-polymerase (Finnzymes) in a polymerase chain reaction (PCR).

In order to perform single molecule experiments histones and histone variants were purified and mono-nucleosomes were assembled by Clemens Bönisch as described in [9] using a mixture of labeled DNA and unlabeled DNA (molar ratio of 1:50). Samples were used as provided.

Measurement and data filtering To gain information on salt dependent nucleosome stability, single-molecule förster resonance energy transfer (smFRET) measurements of dual labeled nucleosomes freely diffusing through the focal volume of a confocal microscope were performed.

It is well known, that at ultra-low concentrations, nucleosomes are prone to become instable in typical experimental geometries [28]. To minimize such effects a 1 : 250 mixture of double labeled to unlabeled nucleosomes was prepared by adding an additional amount of unlabeled nucleosomes to the initial 1:50 mixture. Measurements were performed at a total concentration of 25 nM nucleosomes in commercially available TE buffer (Sigma-Aldrich, pH 7.6) containing 10 mM DTT and 0 mM , 300 mM, 400 mM, 500 mM, 600 mM and 700 mM NaCl, respectively.

The samples were incubated at the respective salt concentration for 1 hour at 21°C before a drop of 20 μl was put onto PEG coated (see chapter 5.2.4.2) cover slips for data collection.

Confocal measurements were performed as described in chapter 3 applying 80 μW power before the objective. Data were collected for

10 *min* and an all photons burst search (APBS) was applied with the criteria of detecting at least 3 photons within 500 μs with a total of at least 60 photons per burst (see chapter 3.2.4.1).

While it is clear that the gamma factor could change due to an increased salt concentration it was found to be constant for all samples (independent of the H2A variant) measured at identical salt concentration (data not shown).

As previously described (see chapter 3.2.4.3) the gamma factor for individual measurements is typically be estimated under the assumption that the low FRET and high FRET populations of the respective sample have identical QYs which is not necessarily true for free DNA and assembled nucleosomes as contribution to the populations in the samples presented here. Hence in this chapter since only differences between the H2A variants are compared for distinct NaCl concentrations an average $\gamma = 0.7$ was estimated and on the analysis of data from all samples. Additionally it was ensured that all samples of identical NaCl concentration were measured at the same day under identical conditions to exclude artifacts from differing detection efficiencies by changes in the setup.

Note that crosstalk and direct excitation correction was not necessary since the spectra of the dyes did not change due to the salt and no absolute distances were to be determined. Multi-molecular events were removed from the data as described in chapter 4.3.4 using $TDS < 1$ and $TDS_{red} < 0.6$ including the additional dynamic filter described in chapter 5.2.7. Remaining donor-only and acceptor-only bursts were removed using stoichiometry thresholds ($S > 0.15$ and $S < 0.55$).

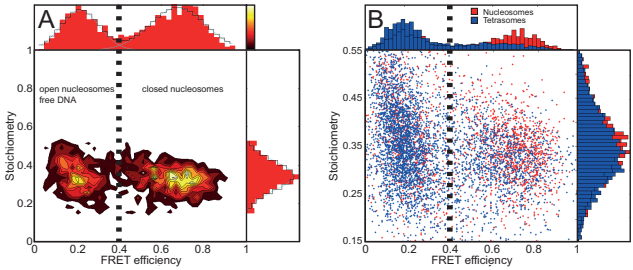

Figure 5.9: Analysis of samples containing different H2A variants. (A) Exemplary two-dimensional FRET efficiency versus stoichiometry histogram showing canonical *H2A* nucleosomes at 0 mM NaCl (TE pH 7.6). Data was filtered using $TDS < 1$, $TDS_{red} < 0.6$ and a stoichiometry threshold ($S = 0.15 - 0.55$). The separation between low (open nucleosomes and free DNA) and high FRET (closed nucleosomes) at a FRET efficiency of 40% used to analyze the data presented in the following is marked by a dotted black line. (B) Direct comparison of canonical *H2A* nucleosomes and tetrasomes assembled only from *H3*/*H4* showing that while most tetrasomes show low FRET, a small subpopulation also shows high FRET.

5.4.3 Results

Due to the chosen labeling positions on the nucleosome, closed nucleosomes have the donor and acceptor dyes positioned adjacent to each other leading to a high FRET state with an efficiency of $\sim$ 80% while open or incomplete nucleosomes show a very low FRET signal (see figure 5.3) . The fraction of closed nucleosomes was quantified for each salt concentration by analyzing how many of the detected fluorescence bursts have a FRET efficiency larger than 40% (figure 5.9A). The data was normalized to the fraction of closed molecules at 0 mM NaCl to allow for a comparison of the salt dependence for the three investigated samples (H2A, H2A.Z.2.1, H2A.Z.2.2, see figure 5.10).

Until 300 mM NaCl all experiments showed an approximately constant share of high FRET bursts. Above 300 mM NaCl this population decreased with increasing salt concentration and a clearly different slope becomes visible for H2A.Z.2.2 as compared to the other samples.

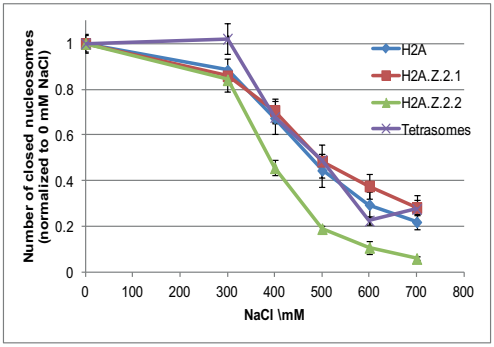

Figure 5.10: Salt dependent destabilization of nucleosomes containing different H2A variants. The fraction of mono-nucleosomes containing either canonical *H2A* (blue), *H2A.Z.2.1* (red), *H2A.Z.2.2* (green) or Tetrasomes (violet) is shown a a function of NaCl in the solution. For comparability data was normalized to the amount of closed nucleosomes at 0 mM NaCl. The standard error was calculated from 6 independent measurements of each data point.

Hence at elevated salt concentrations a decreased stability of *H2A.Z.2.2* loosing its compact structure at about 400 *mM* NaCl, could be resolved. In contrast nucleosomes assembled from canonical *H2A* and *H2A.Z.2.1* showed comparable stability within the error clearly losing their compaction at higher salt concentrations as compared to *H2A.Z.2.2*.

Interestingly also *tetrasomes* assembled from the *6-601-6* DNA and H3/H4 histones showed a small high FRET population (see figure 5.9). This population was stable to approximately 300 *mM* before the tetrasomes started to fall apart in a manner similar to *H2A* and *H2A.Z.2.1*. It however has to be noted that due to the low signal of only $\sim$ 20% intact tetrasomes at 0 *mM* NaCl the tetrasome data in figure 5.10 is more sensitive to differences in e.g. the surface coating quality than the nucleosome octamer data ($\sim$ 60% intact at 0 *mM*).

The differences obtained for nucleosome stability shown here also match results from bulk experiments that detected disintegration of H2A.Z.2.2 nucleosomes between 200 *mM* and 400 *mM* NaCl.

Prior to the experiments shown and discussed here [9] another shortened human H2A variant with an unusual C-terminus called *H2Abbd* was causing the least stable nucleosomes known [31]. However the observed H2A.Z.2.2 salt stability was even lower than found for *H2Abbd* which disintegrated at around 400 *mM* [9]. Hence the experiments discussed above revealed that *H2A.Z.2.2* is causing the strongest nucleosome destabilization known to date.

While the detailed functions of *H2A.Z.2.2* remain unclear, its enrichment in brain tissues combined with the severe nucleosome destabilization allows for the speculation that it is to some extent supporting primate brain development. However to fully understand its function further studies will be necessary.

5.5 Post translational modifications

The work presented in this chapter was done in a collaboration with the group of Tom Owen-Hughes (University of Dundee, Dundee, UK) and Dr. Robert Schneider (MPI, Freiburg, Germany).

5.5.1 Introduction

In addition to the two already described ways of controlling gene expression on a chromosome level, a third equally important pathway exists which includes the post translational modification of histones. While many different modifications are known, this chapter will focus on the acetylation and methylation of H3 histones, especially of the lysine on position 64.

Modification positions The N-terminal domains of the histones are positively charged and sticking out of the nucleosome surface making them accessible for post translational modifications. Since these tails are assumed to be involved in chromatin compaction [83], modifications can be used to control active gene expression or silencing.

In addition, also other modifications further inside the nucleosomes have been proven to exist [38] where mainly the positively

charged lysines that provide the binding of the negatively charged DNA can be post-translationally modified [56].

Acetylation and methylation function Acetylations are currently assumed to cause an activation of gene expression by shielding the positive lysine charge hence weakening the DNA histone contacts and reducing the nucleosome stability [83]. Additionally it has been shown that acetylation is used to control remodeling activities e.g. an acetylation of H4K16 causes reduced activity of ISWI ATPases [13].

Since not only a single but also di- and tri-methylations have been shown in vivo the role of methylation is not as easily described. Methylations are in some cases assumed to simply prevent lysine acetylation which is equal to silencing a gene. An example for such a situation is the methylation of H3K27 [38]. In other cases a mono-methylation e.g. of H3K4 causes an activation of genes and a tri-methylation of H3K4 is in addition to its activation effect found to be essential to maintain Hox gene expression patterns [136][13].

In this chapter the salt dependent stability of nucleosomes assembled with unmodified H3 histones (WT), K64 tri-methylated H3 histones (H3K64me3) and K64 acetylated H3 histones (H3K64ac) is compared to detect differences that might allow for conclusions on the biological function of the respective modification.

5.5.2 Experimental details

Sample preparation The DNA required to assemble a 200 bp *6-601-47* nucleosome construct for single molecule FRET experiments contained a Tamra dye molecule at position *F-15* and an Atto647N dye at position *R-60* relative to the dyad (see chapter 5.2.1). These positions were chosen since the construct had to be sensitive to changes close to the end of the 147 basepairs wrapped around the histone core.

In addition a second construct sensitive to changes close to the dyad axis was labeled with a Tamra dye molecule at position *F-38* and an Atto647N dye at position *R-40*.

Both DNA strands were prepared by Monika Holzner (group of Prof. Dr. Jens Michaelis, Ludwig-Maximilians-University, Munich)

using labeled custom made primers (IBA GmbH, Göttingen), dNTPs (Finnzymes) and the Phusion DNA-polymerase (Finnzymes) in a Polymerase Chain Reaction (PCR).

In order to perform single molecule experiments unmodified H3, H3K64me3 (tri-methylated, [114] and H3K64ac (acetylated, [89]) were provided by Dr. Robert Schneider (MPI, Freiburg, Germany) and assembled into mono-nucleosomes by Dr. Daniel Ryan (group of Tom Owen-Hughes, University of Dundee, Dundee, UK). Samples were used as provided.

Measurement and data filtering Experiments were performed using a 1 : 20 mixture of double labeled to unlabeled nucleosomes at a total concentration of $\sim 1nM$ in commercially available TE buffer (Sigma-Aldrich, pH 7.25) containing 10 mM DTT. Depending on the respective experiment in some cases BSA (12 μM) was added since it has been shown to stabilize nucleosomes at low concentrations [30].

The samples were incubated at the respective salt concentration for 12 hours at $4°C$ before a drop of 20 μl was put onto a PEG coated (see chapter 5.2.4.2) cover slip for data collection.

Confocal measurements were performed as described in chapter 3 applying 75 μW (*F-15 R-60*) or 80 μW (*F-38 R-40*) of laser power before the objective. Data were collected for 10 *min* and an all photons burst search (APBS) was applied with the criteria of detecting at least 4 photons within 500 μs and a total of at least 60 photons per burst (see chapter 3.2.4.1).

Correction factors were determined for each measurement as described in chapter 3.2.4.3. Since the data of the samples containing BSA was measured over a period of one month on non consecutive days the setup alignment slightly changed between the different measurement series. To exclude possible artifacts from these different alignments, an individual γ factor was determined and applied for each measurement, even though differences due to misalignment turned out to be small. A summary of the γ factors for the respective salt concentration and sample can be found in table 5.4.

For all measurements not containing BSA where the total NaCl concentrations were low and were all data were measured within

three consecutive days an average γ factor of $\gamma = 0.7$ was applied.

The crosstalk applied to all *F-15 R-60* datasets was $cr = 0.115$ and the direct excitation was $de = 0.065$. The *cr* and *de* were also determined for all *F-38 R-40* and found to be identical to the *F-15 R-60*. In this case these factors would however bring the two populations (high and low FRET) closer to each other making the definition of a separation threshold more difficult. Hence, they were not applied in order to slightly improve the sensitivity of the *F-38 R-40* experiments.

Table 5.4: Correction factors applied to H3K64 BSA data sets

mM **NaCl**	**0**	**50**	**100**	**200**	**300-900**	**1000**
WT $\gamma =$	1	1	0.9	0.8	0.7	0.6
H3K64ac $\gamma =$	1	1	0.9	0.8	0.7	0.6
H3K64me3 $\gamma =$	1	0.9	0.8	0.7	0.7	0.6

Multi-molecular events were removed from the data as described in chapter 4.3.4 using $TDS < 1$ and $TDS_{red} < 0.6$ including the additional dynamic filter described in chapter 5.2.7. Remaining donor-only and acceptor-only bursts were removed using a stoichiometry threshold (*F-15 R-60*, $S = 0.2 - 0.65$; *F-38 R-40*, $S = 0.15 - 0.55$).

5.5.3 Results and discussion

Previous studies have shown that a trimethylation of H3K64 causes a repression of genes during development [19]. In order to gain insight into this process single molecule experiments were performed comparing the salt stability of unmodified H3 histones (WT), K64 trimethylated H3 histones (H3K64me3) and K64 acetylated H3 histones (H3K64ac) as described above (see chapter 5.4.2).

F-15 and R-60 labeling sites Since it had been shown that the structural effect of histone acetylation is primarily on the outer part of the DNA [28] the initial experiments were performed using nucleosomes labeled at positions F-15 and R-60 (see figure 5.11). Samples contained 12 μM BSA to stabilize the nucleosomes at the low concentrations necessary for single molecule experiments (see chapter 5.5.2

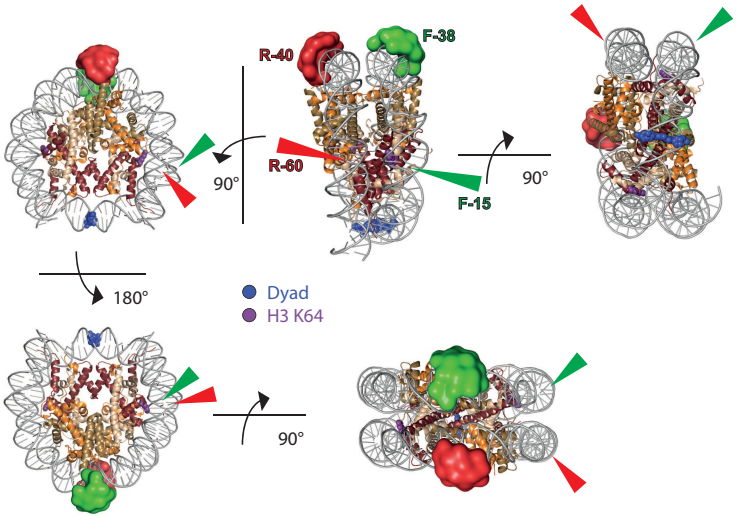

Figure 5.11: Labeling sites of H3K64 modified nucleosomes. The labeling sites *F-38* (rendered green) *R-40* (rendered red) are displayed relative to the dyad (blue balls) and the H3K64 position modified for the experiments discussed here (violet balls) using the PDB: 3lz0 crystal structure. For a better visibility of the H3K64 position positioned in the inner loop which otherwise would be hidden, the labeling position combination *F-15 R-60* is marked by a green and a red arrow respectively instead of a full rendered depiction as given in figure 5.3.

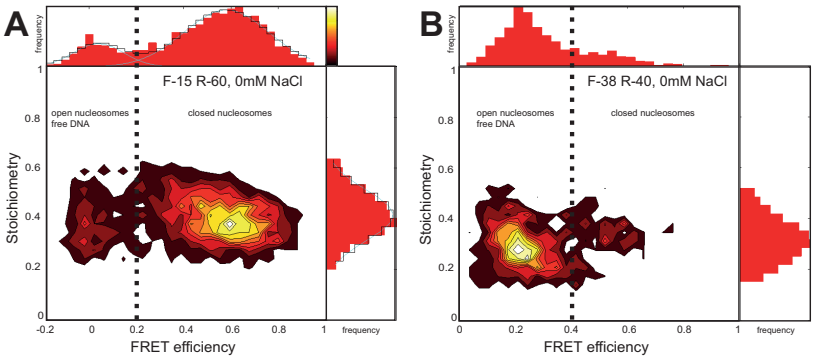

Figure 5.12: Analysis of samples with different H3K64 modifications and labeling positions. (A) Exemplary two-dimensional FRET efficiency versus stoichiometry histogram showing nucleosomes assembled using unmodified (WT) H3 and labeled at the *F-15 R-60* labeling sites. Measurements were performed at 0 mM NaCl concentration and correction factors were $\gamma = 1, cr = 0.115, de = 0.065$. (B) The exemplary two-dimensional FRET efficiency versus stoichiometry histogram of WT *F-38 R-40* nucleosomes measured under the same conditions clearly shows the low fraction of intact nucleosomes obtained from assemblies carrying labels at these positions. Correction factors were $\gamma = 0.7, cr = 0, de = 0$
All samples were measured at 0 mM NaCl (TE pH 7.25) and data was filtered using $TDS < 1$, $TDS_{red} < 0.6$ with activated dynamic filter and a stoichiometry threshold (S = 0.2 – 0.65). The separation between low (open nucleosomes and free DNA) and high FRET (closed nucleosomes) at a FRET efficiency of 20% (A) and 40% (B) as used to analyze the data presented in the following is marked by a dotted black line.

for experimental details). Two populations could be identified one at lower FRET ($< 20\% FRET$) originating from free DNA as well as only partially assembled nucleosomes and one at higher FRET efficiency ($> 20\% FRET$) associated with intact nucleosomes (figure 5.12, A). Analyzing the ratios of these fractions as a function of time. In contrast to the experiments presented in the previous chapter (see chapter 5.4) there was no visible change between 0 and 200 mM NaCl. To obtain better statistics here, the normalization was done to the average ratio obtained from 0-200 mM NaCl.

The results obtained in this way revealed a disassembly beginning at about 700 mM NaCl and no significant difference between all three investigated samples (figure 5.13).

Concentration has been shown to significantly influence nucleosome stability [28] however it is unclear whether the nucleosomes become unstable or if surface interactions become more important at lower concentrations. While the fact that BSA can be used instead of competitor nucleosomes [30] to achieve stabilization points to the surface hypothesis it can not be excluded that BSA does to some extent also directly interact with the nucleosomes and falsifies the result.

It has been shown that differences in salt stability can also be detected without competitor or BSA even though the required salt concentrations for disassembly were quite different [28]. Hence to exclude the possibility of artifacts the above experiments were repeated without BSA.

The results were normalized to the population ratio at 0 mM NaCl (figure 5.13B). The expected reduced salt concentrations required for nucleosome disassembly resulted in nearly full disappearance of the HF population already at 50 mM NaCl. Importantly again no differences in the stability of the individual modifications could be detected
.

One reason for the missing differences might be that the H3K64 which is located more on the inner loop of the nucleosome (see violet balls in figure 5.11) does not influence the nucleosome stability at the outer parts of the loop and hence by opening up the nucleosome the FRET efficiency of the F-15 and R-60 labeled samples is already close to zero before the differences in stability are becoming important.

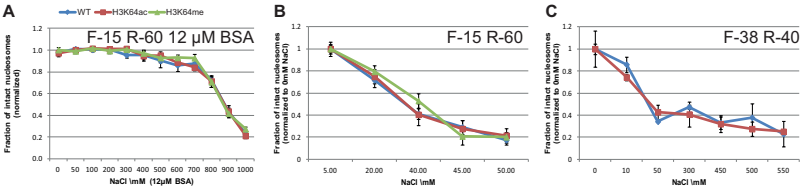

Figure 5.13: Comparison of salt stability for H3K64 wildtype and modified nucleosomes. The relative fraction of intact *WT* (blue), H3K64ac (red) and H3K64me3 (green) nucleosomes normalized to the mean of intact nucleosomes obtained for 0-200 mM NaCl (A) and normalized to the amount of intact nucleosomes at 0 mM NaCl (B,C) is shown as a function of salt concentration. Samples containing 12 μM BSA (A) show a decrease of high FRET events at higher salt concentrations than samples without BSA but labeled at the same positions *F-15* and *R-60* (B). Data obtained from samples labeled at *F-38* and *R-40* measured without the addition of BSA (C) shows comparable behavior. Importantly none of the datasets indicates significant differences between the individual modifications.

F-38 and R-40 labeling sites To overcome this issue nucleosomes were labeled close to the dyad at positions F-38 and R-40 which is the most sensitive position for modifications affecting the inner loop without further changing the system by labeling the histone core.

Unfortunately these labeling sites caused severe problems in nucleosome assembly resulting in only about 15-20% intact and or correctly positioned nucleosomes compared to $\sim$ 80% obtained for F-15 and R-60 labeled ones (compare figure 5.12 A and B). This led to a comparably poor dynamic range for these measurements.

For the three samples investigated here, one would expect the most severe influence for the H3K64ac modification since it shields the positive charge of the lysine and might cause a weakening of the histone nucleosome interactions. In contrast H3K64me3 should have a mainly steric effect and methylations are as already described assumed to sometimes simply prevent an acetylation of the respective position [38]. Following this argument the methylated sample should behave rather similar to the unmodified while the acetylated might be destabilized.

A direct comparison of salt dependent nucleosome stabilities between WT and H3K64ac nucleosomes labeled at F-38 and R-40 however showed a full nucleosome disassembly at salt concentrations of 50 *mM* as seen in the previous experiments and again no difference between the two samples (WT and H3K64ac; see figure 5.12C). Qualitatively similar results (but at higher salt concentrations) were also obtained for some test measurements additionally containing BSA (data not shown).

Conclusion The above results are in good agreement with studies performed on H3K56 acetylation (also using the *Widom 601* positioning sequence) where no differences in salt stability could be detected [89]. Importantly, in contrast to the H3K64 samples investigated here, for H3K56ac increased nucleosome breathing as compared to WT nucleosomes was found.

The lack of increased breathing observed here however can be easily explained by the position of the K64 modification on the inner loop of the nucleosome which would require an almost fully unwrapping of the nucleosome in a dynamic manner to become important for breathing.

Interestingly more recent experiments indicate that the lack of differences in salt stability might be caused by the strong 601 positioning sequence which seems to be masking the small differences caused by these modifications (Tom Owen-Hughes, personal communication).

Further investigations of the modifications on H3K64 using less stable positioning sequences will therefore be necessary in future experiments to better understand their biological function.

Chapter 6

Summary

This thesis was focused on the development and implementation of new and advanced techniques for confocal experiments that combine pulsed interleaved excitation (PIE) with a multiparameter fluorescence detection (MFD) scheme. Such setups can in principle be used to run numerous types of experiments of which here fluorescence correlation spectroscopy (FCS) and single molecule burst analysis were explicitly used.

FCS FCS was applied to investigate the opening and closing dynamics of DNA hairpins and their dependence on the dye combination used as a reporter system (chapter 4.2). This was possible since the FRET capable dye labels on both ends of the ssDNA used for the hairpin experiments cause fluctuations of donor and acceptor brightness upon opening and closing. When the correlation functions of the corresponding photon stream are calculated, these fluctuations cause a distinct signal that can be analyzed. Unfortunately, the intensity of this signal is dependent not only on the FRET efficiency of the states (E_1, E_2) but also on the rates at which they interchange (k_{12}, k_{21}). To make things complicated, also the detectability in the correlation channels is dependent on these parameters. This means that for some parameter combinations (E_1, E_2, k_{12}, k_{21}) it can happen

that a sufficiently strong signal is only found in one correlation function (e.g. the donor auto-correlation GGxGG) while almost no signal is present in the others (the acceptor auto-correlation RRxRR and the acceptor-donor cross-correlation GRxGG). Hence, to prevent the risk of missing the kinetics of interest one needs to globally analyze all three channels that are possibly carrying information about the kinetics of the system.

Here, a global approach to fit 5 correlation functions (GGxGG, GRxGR, GRxGG, RRxRR and GGdxGGd) with a total of 20 parameters that describe the kinetics as well as diffusion and photophysics of the molecules was developed (chapter 4.2.3).

The huge number of parameters - some highly correlated - made a simple least squares fit unreliable since the obtained fit result was strongly dependent on the starting values. Instead, an approach based on bayesian inference was chosen and nested sampling was applied to obtain not only the best fitting values but also to gain knowledge about the uncertainties for each individual parameter.

This FCS based method in combination with single molecule burst analysis in solution and in gel was then successfully applied to investigate how different dye pairs change the outcome of an experiment. It could be shown that the rates as well as the populations of the open and closed state strongly depend on the dye pair chosen as a reporter system.

Single-molecule burst analysis In the field of single molecule burst analysis several previously known techniques were implemented and new techniques were developed. All of these developments were targeted to enable the usage of MFD data in the nano-positioning-system (NPS) analysis. The NPS is a system developed in the Michaelis lab that allows to determine unknown positions within a known structure by a triangulation of several distances to known positions.

Since in a usual experiment every sample contains some impurities the first step in obtaining unbiased single molecule data is to identify and sort the detected events. This is usually done by defining parameters such as FRET efficiency, stoichiometry, fluorescence lifetime or anisotropy.

Commonly used parameters such as the stoichiometry allow for a separation of single and double labeled molecules as well as individual species. However, prior to the developments presented in this thesis no parameter existed that could treat multi-molecule events (i.e. more than one molecule at a time traverses the focal volume). Therefore the time deviation signal (TDS) was developed (chapter 4.3.4). TDS is a parameter based on fluorescence intensity time-traces that allows for an identification and removal of multi-molecule events. The TDS signal of a multi-molecule event and a molecule undergoing dynamic transitions on the timescale of the observation time are however quite similar. Hence, to allow a usage of the TDS on dynamic systems an additional filter was developed such that the TDS can be used also in presence of dynamic events (chapter 5.2.7).

Next, a method to clearly identify a desired population in heterogeneous samples was required. This was necessary since throughout the PolII elongation complex measurements both labels were located on the DNA and it hence was crucial to ensure that DNA-protein complexes were analyzed instead of free DNA. While oftentimes different species can be separated by their FRET efficiency the PolII system investigated in this thesis did not allow for such a separation and hence the capabilities of MFD became important.

For the NPS experiments presented here the acceptor dye was the cyanine dye Alexa647. It is known from literature that the fluorescence lifetime of some cyanine dyes (Cy3, Cy5) increases if the dye is in close proximity to a protein. Utilizing this effect a method to clearly identify protein bound as well as free DNA on a single molecule level was developed.

To allow for single molecule fluorescence lifetime experiments, a burst wise lifetime fit (chapter 3.2.4.6) and a software tool to efficiently analyze huge amounts of data in multidimensional parameter spaces (chapter 4.1.1) was written in Matlab.

Applying these tools, it could be shown that indeed the fluorescence lifetime and the anisotropy of Alexa647 (attached at the 5′ end of a dsDNA) increase upon protein binding (BamH1) in close proximity to the labeling site. Based on these initial experiments two populations with differing fluorescence lifetime and anisotropy values of

Alexa647 could be identified in the PolII data. They were successfully attributed to populations of free (low lifetime $\sim 1.0 - 1.3\ ns$ and anisotropy ~ 0.2) and protein bound (increased lifetime $\sim 1.7 - 2.0\ ns$ and anisotropy ~ 0.3) DNA (chapter 4.3.5) which then allowed for a separation of the respective events.

Now that the molecules of interest could be clearly identified, the next step was to extract the parameter of interest (FRET efficiency and residual anisotropy) with high accuracy and in a reasonable time.

The currently most accurate way of determining FRET efficiencies from single molecule burst data is the so called probability distribution analysis (PDA). This technique in principle relies on the explicit calculation how likely it is to observe a photon combination given the total number of photons in a burst, the background countrate and known correction factors of the experiment. Unfortunately, the calculations to generate these probability distributions are computationally expensive. Here, a new approach of highly parallelizing the required calculations on a GPU using Matlab 2011a and CUDA is presented and successfully demonstrated to greatly reduce the time required for data analysis (chapter 4.1.2).

When absolute distances shall be calculated from FRET efficiency data it is not sufficient to know only the FRET efficiency itself but one also has to gain information about the relative orientations of the dyes involved. A parameter containing such information is the residual anisotropy, the anisotropy a system decays to after averaging over all degrees of freedom. To this end, a new protocol to determine residual anisotropies has been developed. It allows to correct for inhomogeneous state distributions and impurities in the sample and yields residual anisotropy values reproducible over several independent measurements (chapter 4.3.6).

To obtain accurate information it is also crucial to precisely know the necessary correction factors. In a confocal experiment the γ factor, which corrects for the different detection efficiencies and quantum yields of the donor and acceptor channel, is oftentimes causing the biggest uncertainties. Standard procedures rely on the assumption that e.g. for different labeling positions on a DNA the quantum yields as well as the detection efficiencies stay constant. Based on

this assumption usually one global γ factor is optimized such that all data show equal stoichiometries (for details see chapter 3.2.4.3). However, the quantum yields are in many cases not constant for different positions. To address this possible error source a new approach to determine γ accounting for different quantum yields by a global analysis of a FRET measurement network (refer to figure 4.29) was developed in this thesis (chapter 4.3.7).

To this end it was assumed that the quantum yield for one and the same dye remains unchanged as long as it is located at the same position within a sample molecule independent of the location of the corresponding FRET partner. Now the contribution of the quantum yields to the γ factor (encoded in several measurements with differing FRET values for each position) could be directly optimized together with a global instrument constant (accounting for the constant relative detection efficiencies) to yield equal stoichiometries for the whole network. As a result one obtains individual γ factors for each measurement which are connected by the respective quantum yields and the relative detection efficiencies.

Application These single molecule burst analysis techniques were then applied to experiments on the PolII elongation complex (chapter 4.3.9). In this project the goal was to experimentally demonstrate that the knowledge of FRET anisotropies (i.e. the anisotropy of the acceptor after donor excitation) improves the accuracy of an NPS analysis. In order to be able to compare the results to some already published NPS experiments the position of the non template DNA strand in the RNA polymerase II (PolII) elongation complex was chosen to be redetermined.

As a result an increase in accuracy by including FRET anisotropy data in a NPS analysis could for the first time be shown on experimental data (chapter 4.3.9). The positions obtained from single molecule burst analysis data without FRET anisotropy reproduced the general alignment of the labeled bases as compared to the previously published positions with just a slight shift away from the polymerase. Interestingly, distinct differences were detected between the NPS analysis results with and without the FRET anisotropy. In

contrast to the result discussed before the positions obtained with the FRET anisotropy included revealed a completely different alignment of the labeled bases (chapter 4.3.9.2).

Throughout further experiments it could be shown that this new alignment is indeed correct and the results indicate the formation of a hairpin in the non-template strand (chapter 4.3.9.3). Importantly the DNA construct used for these experiments had a sequence identical to the constructs used for the initial crystal structure as well as the previously published NPS analysis.

Since of course such a non-template hairpin formation is unlikely to happen throughout transcription in a cell a new sequence unable to form a hairpin was developed (chapter4.3.9.6). First results indicate that this new construct indeed does not form a hairpin. Interestingly the new positions are however shifted away from the PolII such that they are no longer within the reach of the DNA which is limited by the distance to the active center.

Currently it is not completely clear what causes this shift. The two most likely reasons are uncertainties in the γ factor which alone are however not sufficient and or problems with the currently used static NPS model.

Nucleosomes As part of collaborations with other groups, studies on nucleosome accessibility were performed. Nucleosomes are the first step of DNA compaction in a cell and basically consist of a histone core (H2A,H2B,H3 and H4) around which the DNA is wrapped. Such a packaging of DNA however raises the question how enzymes as e.g. the PolII discussed above can process along the DNA despite these obstacles.

One possible pathway is an active movement of the nucleosome by a separate enzyme. Enzymes that catalyze such an active repositioning of nucleosomes are the so called remodelers. Here the two human ISWI ATPases Snf2H and Snf2L were compared (chapter 5.3) and single molecule burst analysis was applied to detect changes in the remodeling times for different enzyme concentrations. Throughout these experiments Snf2L showed the expected linear increase in remodeling time with increasing dilution while for Snf2H a signifi-

cant deviation towards shorter remodeling times was found. Based on additional experiments by cooperation partners a model was suggested that attributes these differences to a change in the Snf2H unbinding rate k_{off} upon dilution.

Of course, the processing along the DNA is hindered not only by one but by numerous nucleosomes. The high compaction of the DNA resulting from these nucleosomes however also restricts the initial binding of enzymes. In this work two ways of how a cell can control DNA accessibility by changing the nucleosome stability were investigated, namely alternative splicing or chemical modification of the histones forming the nucleosome core.

Here, H2A.Z.2.2 a recently discovered alternatively spliced H2A variant known to be enriched in brain tissues was for the first time investigated for its influence on nucleosome stability (chapter 5.4). In these experiments it could be successfully shown that an incorporation of such histones into nucleosomes leads to the least stable nucleosomes known to date.

Furthermore experiments were performed on chemically modified canonical nucleosomes (chapter 5.5). These samples were either trimethylated (H3K64me3) or acetylated (H3K64ac) at the lysine on position 64 of the H3 histone. Surprisingly at first no clear influence of these modifications on nucleosome stability could be detected. Compared to other modification sites previously studied by other groups, K64 is on the inner turn of the nucleosome close to the dyad. Thus it should require quite far unwrapping of the nucleosome to make a difference. One possible explanation for the absence of detectable changes is that the strong positioning sequence (601) commonly used to ensure homogeneous mono-nucleosome samples might have such a high affinity to the nucleosome core that it masks the influence of the modifications on the investigated position. Hence future experiments on this topic using a weaker positioning sequence are required to investigate these modifications. Indeed first experiments by Dr. Daniel Ryan (The Australian National University Canberra, unpublished results) that use the NucA positioning sequence instead of the 601 sequence seem to indicate that the acetylation (H3K64ac) causes a destabilization of the nucleosomes. Nevertheless more data will be

required to fully understand the importance of the above modifications.

Conclusion In summary this thesis presented new methods to analyze single molecule burst analysis as well as FCS data. These techniques were then successfully applied to biological questions including structural properties, dynamics and the stability of bio-molecular complexes.

Appendix A

Supplementary

A.1 Burst Explorer software manual

The Burst Explorer is a software tool that allows an easy analysis of multidimensional data. It is optimized to handle huge amounts of bursts obtained using MFD but can also be used to get an insight into correlations of sampling results.

All Burst analysis data processed for this work was analyzed using this software. GUI items not explained below are either adjusting the graphical representation (e.g. *Binning*[1], *Marker Size*, *BarWidth*, ...) or are in an experimental pre-alpha state and not desired for everyday use. Items of the GUI (figure A.1) referred to in this chapter are highlighted in italic letters.

Data: In order to minimize the data processed most variables are calculated throughout the initial burst search and only parameters derived from these variables are determined upon loading a file in *Burst Explorer*. Using this approach all data can be corrected for γ, *cr*, *de* and β directly in the Burst Explorer software without the need to redo the burst analysis (*Adjust Gamma*, *Adjust Anisotropy*) while

[1] In this case the binning refers to the one and two dimensional histograms presented in Graph 1 and Graph 2

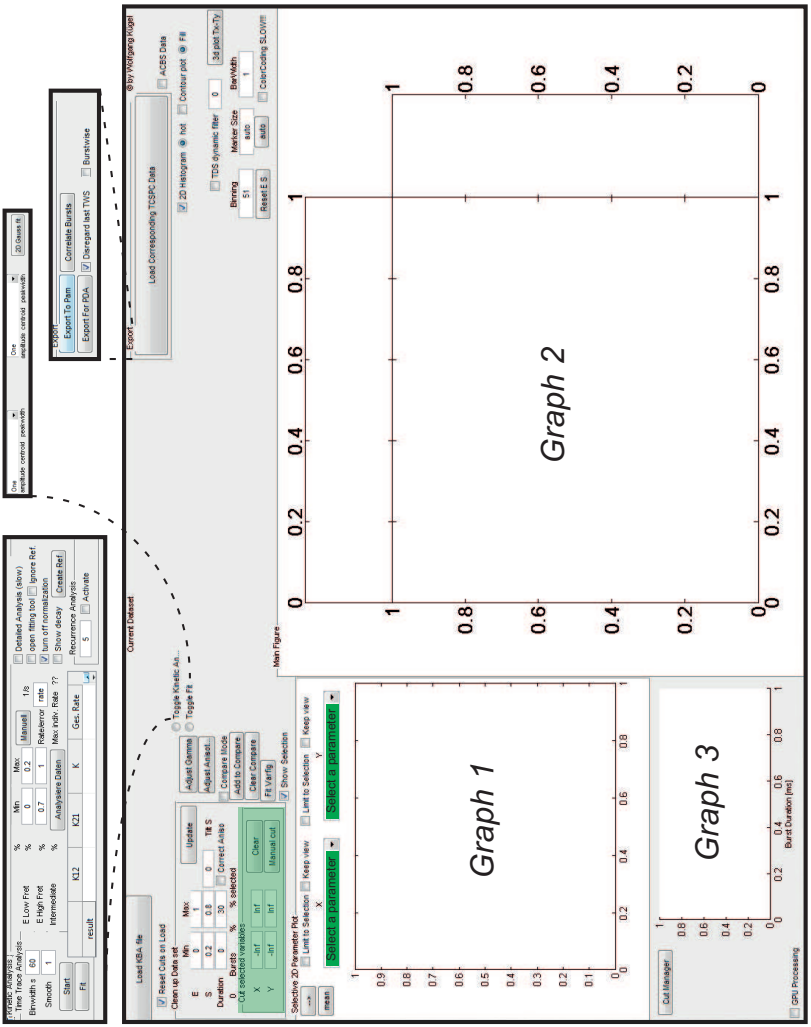

Figure A.1: Overview of the Burst Explorer user interface. The GUI is shown with the the three main images (*Graph 1,2,3*. The Area to enter boundaries for the variable selected in the drop down menu is highlighted in green. The three most important items overlayed upon selection are depicted as insets connected to the respective option.

there is still no need to permanently hold the whole photon-streams in memory. This reduced memory cost also is required to allow for a fast comparison of different measurements as explained later on.

GUI: The main window provides three separate Graphs (figure A.1, *Graph 1,2,3*). The smaller one with drop down menus (*Graph 1*) is allowing for a fast selection of the parameters of interest and has a range selection area directly associated to that graph (highlighted in green here). In this area filters can be generated which allow e.g. only bursts with a fluorescence lifetime between 2 *ns* and 5 *ns*. All data will be immediately filtered when an upper or lower threshold value is entered. Direct access to the parameters FRET efficiency (E), stoichiometry (Sto) and burst Duration as well as the possibility to activate the *Correct Aniso* which causes the usage of equation 4.20 instead of equation 4.19 for the calculation of the total signal per channel is located above this graph.

Since multi-dimensional representations are usually hard to understand from a two dimensional marginalization a second graph is provided (*Graph 2*) which is by default configured to show the FRET efficiency and the Stoichiometry. This graph additionally provides one dimensional projections of the data at the top and right hand side. All boundaries set to the variables selected in the small graph are immediately applied to the larger graph as well and can be switched on and off using the *cut manager* making it easy to understand high dimensional correlations even of subpopulations. If FRET efficiency and stoichiometry are not the most interesting variables of a dataset every desired variable combination can be projected to the big graph (–> button). The standard FRET efficiency-stoichiometry plot can always be easily restored using the *Reset E S* button. Finally the distribution of the burst duration is shown in *Graph 3*.

Compare to raw data: If a direct comparison of selected bursts and raw data is required the *Show Selection* as well as the *2D Histogram* check box can be unchecked switching *Graph 1* and *Graph 2* into a scatter plot mode overlaying the raw data (blue) and the selected data (red). An example of this overlay can be found in chapter 5.2.7

(figure 5.4 D-F) where the dynamic filter is introduced and demonstrated.

TDS dynamic filter: The check box *TDS dynamic filter* excludes all bursts with mean-macro-time patterns (see chapter 5.2.7 table 5.2) identifying them as dynamic from any TDSr(red) and TDSgf thresholds that might be set.

Fit: The *Toggle Fit* button will show a menu that allows the selection of up to 4 gaussian distributions to be fit to each of the one dimensional projections. The button 2D Gauss fit is used to fit two 2-dimensional gaussians to the two dimensional histogram of *Graph 2* (see figure 4.28). This information can be used to precisely quantify the shares of multi-dimensionally correlated but not fully separable populations as demonstrated in chapter 4.3.6.

Kinetic analysis: Alternatively the *Toggle Kinetic Analysis* button will open a menu that allows to analyze the time evolution of up to three subpopulations. To this end the lower and upper boundaries of the desired populations (defined by the variable on the x-Axis of *Graph 1*) can be entered in the *Min* and *Max* fields. Additionally a *Binwidth* and if required a *Smooth* factor can be supplied. After pressing the *Start* button the software will calculate the evolution of the entered subpopulations over time. The resulting graph is opened in a new window and automatically saved so the obtained evolution can be fit using the *Fit* button if required. An example for the application of this method can be found in chapter 5.3 where it was used to compare the concentration dependence of SNF2H and SNF2L remodeling speeds.

Recurrence analysis The *KineticAnalysis* also offers the possibility to perform a *recurrence analysis* of single particles (RASP). This analysis was initially developed by [42] and is capable of detecting dynamics that occur on timescales larger than the average diffusion time of a molecule through the confocal volume. It assumes that at a sufficient

dilution the same molecule is more likely to enter the focal volume again than a new one if the time between two bursts is sufficiently small.

To better understand the information gained by this method assume that two consecutive bursts with only a short delay show a different e.g. FRET efficiency. If error sources such as too high sample concentrations and photo-physical effects can be excluded then this can be directly related to a distance change of the two involved fluorophores on the timescale of the burst-burst distance.

The button *Activate* in the *Reentry analysis Diff. level* panel will use the parameter selected for the x-axis of *Graph 1* and show all events that fulfill the restriction that two consecutive bursts occurred within the number of milliseconds entered in the field right of the *Activate* button. The result will be presented on *Graph 2* showing the distribution of the respective parameter value of the first burst on the x-axis versus the following burst on the y-axis (see figure A.2, B).

Overlay theoretical curves: An overlay of theoretical curves can be added to the graphs by using the *Fit Varfig* Button. Implemented are:

- The perrin equation [99] [100] which basically describes the dependence of the lifetime weighted anisotropy $r(t)$ (see chapter 3.2.4.5) and the lifetime τ (see chapter 3.2.4.6) for spherical rotors [2]

$$r(\tau) = \frac{r_0}{1 + \frac{\tau}{\rho}}. \tag{A.1}$$

  Here r_0 is the fundamental anisotropy and ρ is the rotational correlation time of the sample molecule. Hence since the rotational correlation time is directly related to the rotational diffusion constant of a molecule D_r ($\rho = 1/(6D_r)$) the lifetime weighted anisotropy is not only influenced by the fluorophore lifetime but also the molecular weight of the sample (see also chapter 2.4 for details)

[2] An exponential decay of the time resolved anisotropy is assumed which is only true for spherical molecules

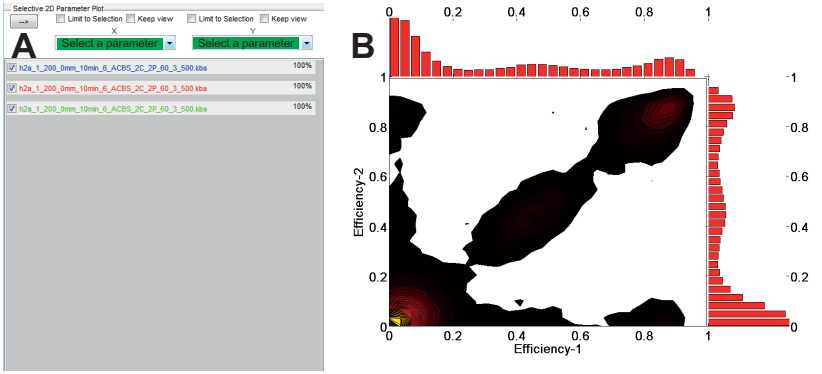

Figure A.2: Exemplary depiction of the compare mode selection (A) and a recurrence analysis (B). (A) The checkbox menu appearing instead of *Graphs 1* and *2* in the *compare mode* is shown with three exemplary datasets. It gives the color code of the scatterplots used to compare different datasets and allows for a selection of the files to be shown. If a range limitation for the selected parameters is entered the remaining share is shown as percentage of the total for each dataset. (B) An example for a *recurrence analysis* of a double labeled nucleosome sample (F+14 Atto532, F-64 Atto647N, see figure 5.3) measured at $\sim$15 pM concentration shows the FRET efficiency as parameter of interest. The maximum burst separation to be included in this graph was 100 ms. Clearly a transition from the low to the intermediate as well as the high FRET population is visible. In contrast no direct transitions between the high and intermediate FRET states seem to occur on that timescale (i.e. within the 100 ms burst separation).

- The empirically determined relation of FRET efficiency and donor lifetime in presence of the acceptor (τ_{D_A}) and in absence of the acceptor (τ_{D_0}) as derived by [29]

$$E = 1 - \frac{a + b * \tau_{D_A} + c * \tau_{D_A}^2 + e * \tau_{D_A}^3}{\tau_{D_0}} \tag{A.2}$$

- The shot noise limit of σ_{e^*} as shown and explained in chapter 4.15.

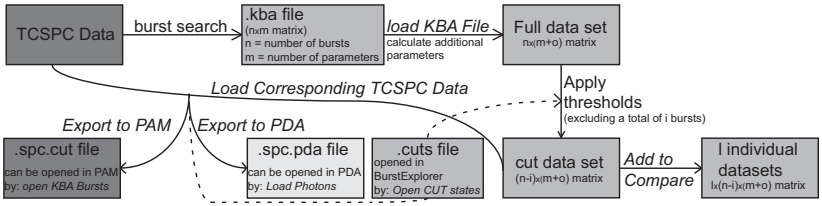

Figure A.3: Summary of data processing and file types of the BurstExplorer software. Data processed in the software PIE Analysis with MatLab (PAM, by M.Höller, M. Sikor and W. Kügel) is marked in dark grey, data processing in BurstExplorer is shown in medium gray and data processed using the PDA software described in chapter 4.1.2 is highlighted in light grey.

Export corresponding photons: Once the data is cleaned up from single labeled molecules, bleaching, blinking and multi-molecule events (see TDS, chapter 4.3.4) the desired populations can be selected and the photons corresponding to these bursts can be exported for further processing (e.g. time resolved anisotropy or PDA, figure A.1, top right, *Load Corresponding TCSPC Data*). Upon export an additional *.cuts* file is written containing the information of all restrictions applied at the time of export. This state can be restored at any time point and for any dataset by loading the *.cuts* file (Start -> Load CUT state). A summary of the data files read and written as well as the connections between the individual programs used throughout this work can be found in figure A.3.

Compare datasets: If several independent measurements are to be compared the so called *Compare Mode* can be used. Data can be added to this mode by pressing the *Add to Compare* button and cleared by *Clear Compare*. Please note that only the data filtered by the activated thresholds is added and not the whole dataset allowing this mode to be used for the comparison of subpopulations as well as datasets (see figure A.3). All data added is shown as an overlay using differently colored scatter plots and their projection for any variable of interest. The individual datasets can be hidden and shown using the checkbox list appearing instead of *Graph 1* and *3* upon entering the

Compare Mode (figure A.2, A). Additionally the percentage of bursts remaining in each dataset is shown since the range of variables can be set for all compared datasets at once as described already for the regular mode. In that way differences between samples or subpopulations can be easily analyzed.

A.2 Dynamic filter details

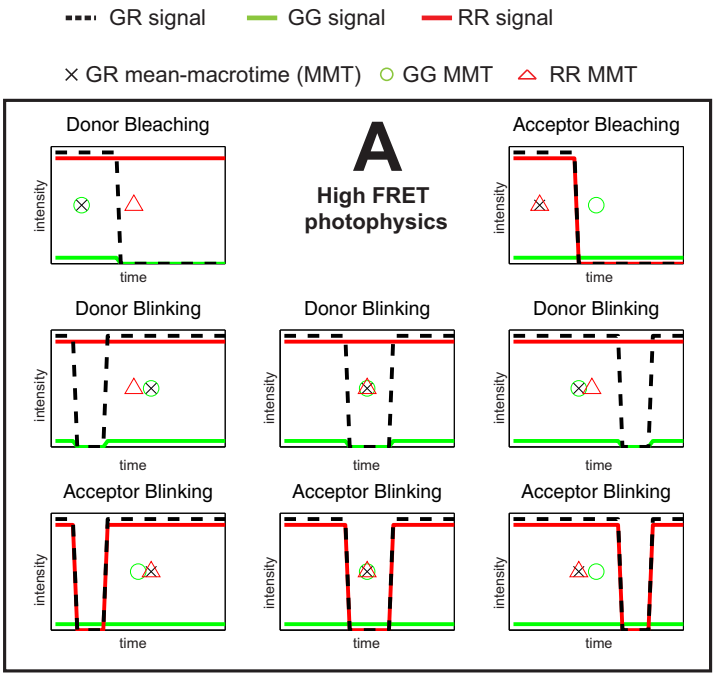

Figure A.4: Differential signal simulation for the Dynamic filter. Simulation of bleaching and blinking events of the donor or acceptor dye occurring on a high FRET sample (A) and on a low FRET sample (B). The mean-macro-time (MMT) resulting from the photon streams of the donor (green), acceptor (red) and FRET (dashed black) channels are depicted as black cross (FRET), green circle (donor) and red triangle (acceptor). The relative mean-macro-time values of dynamic transitions with rates lower or equal to the transition time of the respective molecule (C) clearly show patterns distinct from photo physics. A summary of the MMT differences can be found in table 5.2.

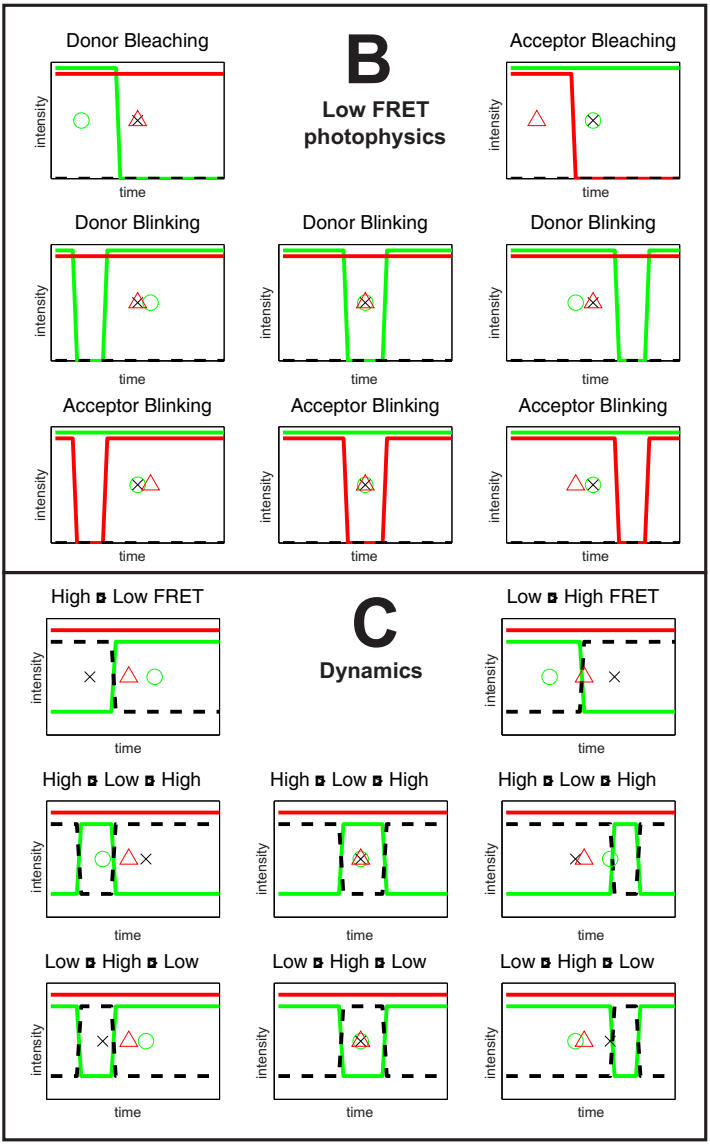
B
Low FRET
photophysics
Donor Bleaching
Acceptor Bleaching
Donor Blinking
Donor Blinking
Donor Blinking
Acceptor Blinking
Acceptor Blinking
Acceptor Blinking
C
Dynamics
High ◘ Low FRET
Low ◘ High FRET
High ◘ Low ◘ High
High ◘ Low ◘ High
High ◘ Low ◘ High
Low ◘ High ◘ Low
Low ◘ High ◘ Low
Low ◘ High ◘ Low
intensity
time

A.3 Dye structures

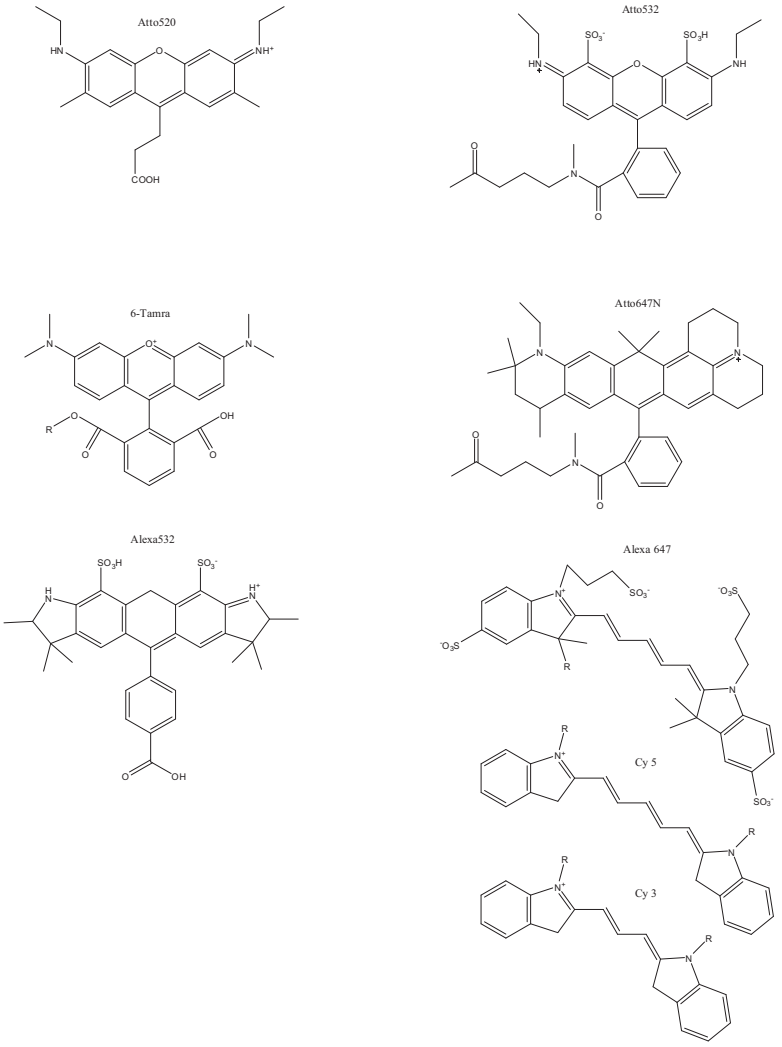

Figure A.4: Overview of dyes used in this work. Dye structures are shown for all dyes with publicly available structures. The dye structures are based on information available at www.atto-tec.com, www.invitrogen.com, www.wikipedia.com and [97]

A.4 Program code

Below the core code fragments calculating probability distributions for PDA analysis on a CPU (figure A.5) or a GPU (figures A.6-A.8) as well as the likelihood functions used for the global FCS kinetic analysis (figures A.9-A.12) and the quantum yield network analysis (figures A.13-A.15)

A.4.1 PDA C++ code

```
#include "mclcppclass.h" #include "mex.h" #include "matrix.h" #define _USE_MATH_DEFINES #include <math.h>
#include <float.h>
#include <stdlib.h> #include <stdio.h>
/* The gateway function */
void mexFunction(int nlhs, mxArray *plhs[],
                 int nrhs, const mxArray *prhs[])
{
    int Nsim, i, j, F, f, index, counter, PFsize1 ;
    double *minN, *maxN, *numelE, *E,*PN,*PF,*PBG,*PBR, *P, Nsim_x_epsi ,*NBGG ,*NBGR, *epsi;
    int notyet = 1;

    if (nrhs != 11)   // check proper number of input arguments
        mexErrMsgTxt("not enough input arguments.");

    // read in input arguments
    minN = mxGetPr(prhs[0]); //lower limit of photons in the simulation
    maxN = mxGetPr(prhs[1]); //upper limit of photons in the simulation
    numelE = mxGetPr(prhs[2]); //length of the vector containing all possible FRET efficiency values
    E = mxGetPr(prhs[3]); //vector containing all possible FRET efficiency values
    PN = mxGetPr(prhs[4]); //vector containing all possible P(N) values
    PF = mxGetPr(prhs[5]); //precalculated matrix containing all possible P(F) values
    PFsize1 = mxGetM(prhs[5]); // size of the P(F) matrix
    PBG = mxGetPr(prhs[6]); // vector containing all possible green background photon probabilities
    PBR = mxGetPr(prhs[7]); // vector containing all possible red background photon probabilities
    NBGG = mxGetPr(prhs[8]); // number of green background photons that have a likelihood larger than $1e^
{-3}$
    NBGR = mxGetPr(prhs[9]); // number of red background photons that have a likelihood larger than $1e^
{-3}$
    epsi = mxGetPr(prhs[10]); // equality condition


    //  generate MATLAB output
    plhs[0] = mxCreateDoubleMatrix(*numelE,1,mxREAL);     // allocate memory;
   P = mxGetPr(plhs[0]);


   for (i=0; i < *numelE; i++) {
       P[i] = 0.0;
   }

    counter = 0;
    for (Nsim = *minN; Nsim <= *maxN; Nsim++)  {
        for (i = 0; i <=*NBGG; i++)  {
            Nsim_x_epsi = (double)Nsim * *epsi;
            for (j = 0; j <=*NBGR-i; j++) {
                F = Nsim-(i+j);
                for (f = 0; f<=F; f++) {
                    notyet = 1;
                    index = 0;
                    do  {
                        if ((abs((double)(Nsim)*E[index] - ((double)(j+f))) < Nsim_x_epsi) && notyet) {
                           P[index] +=  (PN[counter] * PF[f+PFsize1*F]* PBG[i] * PBR[j]);
                           notyet = 0;
                        }
                      index ++;
                    }
                    while(index <= (*numelE)-1 && notyet == 1);
                }
            }
        }
        counter = counter+1;

    }

}
```

Figure A.5: PDA C++ code

A.4.2 PDA CUDA code

```
#include <math.h>
#include <float.h>
#include <stdlib.h>
#include <stdio.h>

__device__ double atomicAdd(double* address, double val)
{ double old = *address, assumed;
do { assumed = old; old = __longlong_as_double( atomicCAS((unsigned long long int*)address,
                          __double_as_longlong(assumed), __double_as_longlong(val + assumed))); }
while (assumed != old);
return old; }


// kernel definition
__global__ void PDA1(int* minN, double* NBGG,double* NBGR, int *numelE, double *E, double *Pe, double *PF,
double *PBG, double *PBR, double *PN, double *P, int *PFsize1, int *PFsize2, int *Ngauss,  int *N, double
*epsi, double *weight1)
{
    int j, F, f;
    double Nsim_x_epsi;
    int a = blockIdx.x * blockDim.x + threadIdx.x;
    if (a > *Ngauss) {return;}

    int counter = blockIdx.y * blockDim.y + threadIdx.y ;
    if (counter > *N) {return;}

    int i = blockIdx.z * blockDim.z + threadIdx.z;
    if (i > *NBGG) {return;}

    int Nsim = counter + *minN;
    int dim1;
    int dim2 = (*PFsize2) * (*PFsize1)* a;
    int index;
    double Prob = 0;
    int notyet = 1;


         Nsim_x_epsi = (double)Nsim * *epsi;
            for (j = 0; j <=*NBGR-i; j++) {
                F = Nsim-(i+j);
                dim1 = *PFsize1*F;
                for (f = 0; f<=F; f++) {
                    notyet = 1;
                    index = 0;
                    do  {
                        if ((abs((double)(Nsim)* E[index] - ((double)(j+f))) < Nsim_x_epsi) && notyet) {
                            Prob = ((PN[counter] * PF[f+dim1+dim2]* PBG[i] * PBR[j])*Pe[a] * (*weight1));
                            atomicAdd(&P[index], Prob);
                            notyet = 0;
                        }
                    index ++;
                    }
                    while(index <= (*numelE)-1 && notyet == 1);
                }
            }
        }
```

Figure A.6: PDA CUDA code part 1

```
// kernel definition
__global__ void PDA2(int* minN, double* NBGG, double* NBGR, int *numelE, double *E, double *Pe, double *PF,
double *PBG, double *PBR, double *PN, double *P, int *PFsizel, int *PFsize2, int *Ngauss, int *N, double
*epsi, double *weight1, double *Pe2, double *weight2)
{
    int j, F, f;
    double Nsim_x_epsi;
    int a = blockIdx.x * blockDim.x + threadIdx.x;
    if (a > *Ngauss) {return;}

    int counter = blockIdx.y * blockDim.y + threadIdx.y ;
    if (counter > *N) {return;}

    int i = blockIdx.z * blockDim.z + threadIdx.z;
    if (i > *NBGG) {return;}

    int Nsim = counter + *minN;
    int dim1;
    int dim2 = (*PFsize2) * (*PFsizel)* a;
    int index;
    double Prob = 0;
    int notyet = 1;

         Nsim_x_epsi = (double)Nsim * *epsi;
            for (j = 0; j <=*NBGR-i; j++) {
                F = Nsim-(i+j);
                dim1 = *PFsizel*F;
                for (f = 0; f<=F; f++) {
                    notyet = 1;
                    index = 0;
                    do  {
                        if (abs((double)(Nsim)* E[index] - ((double)(j+f))) < Nsim_x_epsi && notyet) {
                            Prob = ((PN[counter] * PF[f+dim1+dim2]* PBG[i] * PBR[j])*Pe[a] * (*weight1)) +
                                   ((PN[counter] * PF[f+dim1+dim2]* PBG[i] * PBR[j])* Pe2[a] * (*weight2));
                            atomicAdd(&P[index], Prob);
                            notyet = 0;
                        }
                     index ++;
                    }
                    while(index <= (*numelE)-1 && notyet == 1);
                }
            }

}
```

Figure A.7: PDA CUDA code part 2

```
// kernel definition
__global__ void PDA3(int* minN, double* NBGG, double* NBGR, int *numelE, double *E, double *Pe, double *PF,
double *PBG, double *PBR, double *PN, double *P, int *PFsize1, int *PFsize2, int *Ngauss, int *N, double
*epsi, double *weight1, double *Pe2, double *weight2, double *Pe3, double *weight3)
{
    int j, F, f;
    double Nsim_x_epsi;
    int a = blockIdx.x * blockDim.x + threadIdx.x;
    if (a > *Ngauss) {return;}

    int counter = blockIdx.y * blockDim.y + threadIdx.y ;
    if (counter > *N) {return;}

    int i = blockIdx.z * blockDim.z + threadIdx.z;
    if (i > *NBGG) {return;}

    int Nsim = counter + *minN;
    int dim1;
    int dim2 = (*PFsize2) * (*PFsize1)* a;
    int index;
    double Prob = 0;
    int notyet = 1;

         Nsim_x_epsi = (double)Nsim * *epsi;
            for (j = 0; j <=*NBGR-i; j++) {
                F = Nsim-(i+j);
                dim1 = *PFsize1*F;
                for (f = 0; f<=F; f++) {
                    notyet = 1;
                    index = 0;
                    do  {
                        if (abs((double)(Nsim)* E[index] - ((double)(j+f))) < Nsim_x_epsi && notyet) {
                            Prob = ((PN[counter] * PF[f+dim1+dim2]* PBG[i] * PBR[j])*Pe[a] * (*weight1)) +
                                   ((PN[counter] * PF[f+dim1+dim2]* PBG[i] * PBR[j])* Pe2[a] * (*weight2))+
                                   ((PN[counter] * PF[f+dim1+dim2]* PBG[i] * PBR[j])* Pe3[a] * (*weight3));
                            atomicAdd(&P[index], Prob);
                            notyet = 0;
                        }
                     index ++;
                    }
                    while(index <= (*numelE)-1 && notyet == 1);
                }
            }
}
```

Figure A.8: PDA CUDA code part 3

A.4.3 FCS global kinetic fit likelihood code

```
#include "compilerswitches.h"       // switches that determine used algorithm

#define _USE_MATH_DEFINES
#include <math.h>
#include <stdlib.h>

#include "nestedsampler.h"

// define data
#define ARG_T_RRxRR datap[0]    // time axis
#define ARG_D_RRxRR datap[1]    // data (correlation function)
#define ARG_W_RRxRR datap[2]    // weights

#define ARG_T_GGxGG datap[3]    // time axis
#define ARG_D_GGxGG datap[4]    // data (correlation function)
#define ARG_W_GGxGG datap[5]    // weights

#define ARG_T_GRxGR datap[6]    // time axis
#define ARG_D_GRxGR datap[7]    // data (correlation function)
#define ARG_W_GRxGR datap[8]    // weights

#define ARG_T_GGxGR datap[9]    // time axis
#define ARG_D_GGxGR datap[10]   // data (correlation function)
#define ARG_W_GGxGR datap[11]   // weights

#define ARG_T_GGonly datap[12]  // time axis
#define ARG_D_GGonly datap[13]  // data (correlation function)
#define ARG_W_GGonly datap[14]  // weights


// define parameter names

#define N1  par[0]       // number of molecules in the focus RRxRR
#define N2  par[1]       // number of molecules in the focus GRxGR
#define N3  par[2]       // number of molecules in the focus GGxGG
#define logD par[3]         // log diffusion constant
#define logRomega_r par[4]  // radial focal size parameter RRxRR
#define logRomega_z par[5]  // axial focal size parameter RRxRR
#define logGomega_r par[6]  // radial focal size parameter GGxGG
#define logGomega_z par[7]   // axial focal size parameter GGxGG
#define logGRomega_r par[8]  // radial focal size parameter GRxGR
#define logGRomega_z par[9]  // axial focal size parameter GRxGR
#define logGRGomega_r par[10]  // radial focal size parameter GGxGR
#define logGRGomega_z par[11]  // axial focal size parameter GGxGR
#define rrtrp  par[12]     // RRxRR amount of population in triplet state
#define logrrtrpT par[13]     // RRxRR logtriplet time
#define logk12 par[14]   // log(k12)
#define logk21 par[15]   // log(k21)
#define E1 par[16]       // FRET efficiency of state 1
#define E2 par[17]      // FRET efficiency of state 2
#define N4  par[18]     // number of molecules in the focus GGxGR
#define N5  par[19]     // number of molecules in the focus Green only GGxGG

static const double LOG_SQRT_2PI = 0.5*log(2*M_PI);   // log(sqrt(2*pi))

double loglikelihood(
                double *par        // position in parameter space
                #ifdef CALCULATE_SUPREMA
                ,double logLstar     // log-Likelihood constraint
                #endif
                )
{
    unsigned int i;                      // running indeces
```

Figure A.9: Likelihood function of the FCS global fit part 1. This likelihood function is used by the nested sampling algorithm throughout the parameter optimization.

```
double logL = 0;                // logarithm of the likelihood, initialize with 0
double negLogLx2;                // 2 times the negative of log likelihood
static double logWt;                    // weight
double e;                       // part of the exponent in likelihood
long double fun;                    // function value
double *tau, *dat, *wt;
#ifdef CALCULATE_SUPREMA
double negLogLx2max;          // maximum value of negLogLx2 imposed by logLstar constraint
#endif

// --- calculate (constant) normalization factor for the first run
if (firstrun)
    {
    logWt = 0.0;
    }

#ifdef CALCULATE_SUPREMA
negLogLx2max = -2*(logLstar - logWt);       // maximum value of negLogLx allowed in order to be above
logLstar
#endif


        // check whether remaining part of the likelihood has to be calculated
    if (E1 > E2) // if there is no chance to have large enough likelihood
        {
    return(logZERO);        // give up!
        }

// --- calculate likelihood without normalization factor ---
negLogLx2 = 0.0;


// --- RRxRR fit, no kinetics

    tau = (double*)(info[ARG_T_RRxRR]);     // initialize time axis pointer
    dat = (double*)(info[ARG_D_RRxRR]);     // initialize correlation data pointer
    wt  = (double*)(info[ARG_W_RRxRR]);     // initialize weight pointer

    for (i = 0; i < Ninfo[ARG_T_RRxRR]; i ++, tau ++, dat ++, wt ++)       // for each point in the
    RRxRR correlation
    {
    // calculate function value for data point i
    fun = (0.35355/N1*(1.0+(rrtrp/(1.0-rrtrp))*exp(-*tau/exp(logrrtrpT))) * (1.0/(1.0+4.0*exp(logD)
    *(*tau)/(exp(logRomega_r)*exp(logRomega_r)))*1.0/sqrt(1.0+4.0*exp(logD)*(*tau)/(exp(logRomega_z)*exp
    (logRomega_z)))));

    // -2*(exponent of the gaussian)
    e = *wt * (*dat - fun);

    // update likelihood
    negLogLx2 += e*e;

    #ifdef CALCULATE_SUPREMA
        // check whether remaining part of the likelihood has to be calculated
        if (negLogLx2 > negLogLx2max) // if there is no chance to have large enough likelihood
            {
            return(logZERO);        // give up!
            }
    #endif
    }
```

Figure A.10: Likelihood function of the FCS global fit part 2

```
  // --- GGxGG

      tau = (double*)(info[ARG_T_GGxGG]);     // initialize time axis pointer
      dat = (double*)(info[ARG_D_GGxGG]);     // initialize correlation data pointer
      wt  = (double*)(info[ARG_W_GGxGG]);     // initialize weight pointer


      for (i = 0; i < Ninfo[ARG_T_GGxGG]; i ++, tau ++, dat ++, wt ++)       // for each point in the
      GGxGG correlation
      {
      // calculate function value for data point i
      fun = (0.35355/N3*(1.0/(1.0+4.0*exp(logD)*(*tau)/(exp(logGomega_r)*exp(logGomega_r)))*1.0/sqrt
      (1.0+4.0*exp(logD)*(*tau)/(exp(logGomega_z)*exp(logGomega_z)))) * (1.0 + (((exp(logk12)*exp(logk21)*(E1-E2)
      *(E1-E2))/((exp(logk21)*(1.0-E1) + exp(logk12)*(1.0-E2))*(exp(logk21)*(1-E1) + exp(logk12)*(1.0-E2))))*exp
      (-(exp(logk12) + exp(logk21))*(*tau)))));

      // -2*(exponent of the gaussian)
      e = *wt * (*dat - fun);

      // update likelihood
      negLogLx2 += e*e;

      #ifdef CALCULATE_SUPREMA
          // check whether remaining part of the likelihood has to be calculated
          if (negLogLx2 > negLogLx2max) // if there is no chance to have large enough likelihood
              {
              return(logZERO);        // give up!
              }
      #endif
      }


// --- GRxGR

      tau = (double*)(info[ARG_T_GRxGR]);     // initialize time axis pointer
      dat = (double*)(info[ARG_D_GRxGR]);     // initialize correlation data pointer
      wt  = (double*)(info[ARG_W_GRxGR]);     // initialize weight pointer

      for (i = 0; i < Ninfo[ARG_T_GRxGR]; i ++, tau ++, dat ++, wt ++)       // for each point in the
      GRxGR correlation
      {
      // calculate function value for data point i
      fun = (0.35355/N2*(1.0/(1.0+4.0*exp(logD)*(*tau)/(exp(logGRomega_r)*exp(logGRomega_r)))*1.
      0/sqrt(1.0+4.0*exp(logD)*(*tau)/(exp(logGRomega_z)*exp(logGRomega_z)))) *(1.0 + (((exp(logk12)*exp(logk21)*
      (E1-E2)*(E1-E2))/((exp(logk21)*E1 + exp(logk12)*E2)*(exp(logk21)*E1 + exp(logk12)*E2)))*exp(-(exp(logk12) +
      exp(logk21))*(*tau)))));

      // -2*(exponent of the gaussian)
      e = *wt * (*dat - fun);

      // update likelihood
      negLogLx2 += e*e;

      #ifdef CALCULATE_SUPREMA
          // check whether remaining part of the likelihood has to be calculated
          if (negLogLx2 > negLogLx2max) // if there is no chance to have large enough likelihood
              {
              return(logZERO);        // give up!
              }
      #endif
      }
```

Figure A.11: Likelihood function of the FCS global fit part 3

```
   // --- GGxGR

        tau = (double*)(info[ARG_T_GGxGR]);     // initialize time axis pointer
        dat = (double*)(info[ARG_D_GGxGR]);     // initialize correlation data pointer
        wt  = (double*)(info[ARG_W_GGxGR]);     // initialize weight pointer

        for (i = 0; i < Ninfo[ARG_T_GGxGR]; i ++, tau ++, dat ++, wt ++)       // for each point in the
        GGxGR correlation
        {
        // calculate function value for data point i
        fun = (0.35355/N4*(1.0/(1.0+4.0*exp(logD)*(*tau)/(exp(logGRGomega_r)*exp(logGRGomega_r)))*1.
        0/sqrt(1.0+4.0*exp(logD)*(*tau)/(exp(logGRGomega_z)*exp(logGRGomega_z)))) *(1.0-(((exp(logk12)*exp(logk21)*
        (E1-E2)*(E1-E2))/((exp(logk21)*E1+exp(logk12)*E2)*(exp(logk21)*(1.0-E1)+exp(logk12)*(1.0-E2))))*exp(-(exp
        (logk12)+exp(logk21))*(*tau)))));

        // -2*(exponent of the gaussian)
        e = *wt * (*dat - fun);

        // update likelihood
        negLogLx2 += e*e;

        #ifdef CALCULATE_SUPREMA
            // check whether remaining part of the likelihood has to be calculated
            if (negLogLx2 > negLogLx2max) // if there is no chance to have large enough likelihood
                {
                return(logZERO);        // give up!
                }
        #endif
        }

    // --- Green only GGxGG

        tau = (double*)(info[ARG_T_GGonly]);     // initialize time axis pointer
        dat = (double*)(info[ARG_D_GGonly]);     // initialize correlation data pointer
        wt  = (double*)(info[ARG_W_GGonly]);     // initialize weight pointer


        for (i = 0; i < Ninfo[ARG_T_GGonly]; i ++, tau ++, dat ++, wt ++)       // for each point in the
        GGxGG correlation
        {
        // calculate function value for data point i
        fun = (0.35355/N5*(1.0/(1.0+4.0*exp(logD)*(*tau)/(exp(logGomega_r)*exp(logGomega_r)))*1.0/sqrt
        (1.0+4.0*exp(logD)*(*tau)/(exp(logGomega_z)*exp(logGomega_z)))) );

        // -2*(exponent of the gaussian)
        e = *wt * (*dat - fun);

        // update likelihood
        negLogLx2 += e*e;

        #ifdef CALCULATE_SUPREMA
            // check whether remaining part of the likelihood has to be calculated
            if (negLogLx2 > negLogLx2max) // if there is no chance to have large enough likelihood
                {
                return(logZERO);        // give up!
                }
        #endif
        }


        logL += (logWt - 0.5*negLogLx2);      // normalize

    return(logL);   // return the likelihood
}
```

Figure A.12: Likelihood function of the FCS global fit part 4

A.4.4 Gamma sampling likelihood code

```
#include "compilerswitches.h"       // switches that determine used algorithm
#define _USE_MATH_DEFINES
#include <math.h>
#include <stdlib.h>
#include "nestedsampler.h"

// define data
#define tm10m8 ((double*)(info[datap[0]]))
#define tm10m13 ((double*)(info[datap[1]]))
#define tm10m19 ((double*)(info[datap[2]]))
#define tp2m8 ((double*)(info[datap[3]]))
#define tp2m13 ((double*)(info[datap[4]]))
#define tp2m19 ((double*)(info[datap[5]]))
#define tp9m8 ((double*)(info[datap[6]]))
#define tp9m13 ((double*)(info[datap[7]]))
#define tp9m19 ((double*)(info[datap[8]]))

// define parameter names
#define Ead  par[0]
#define Qatp9  par[1]
#define Qatm10 par[2]
#define Qatp2 par[3]
#define Qdntm8 par[4]
#define Qdntm13 par[5]
#define Qdntm19 par[6]
#define S1  par[7]


static const double LOG_SQRT_2PI = 0.5*log(2*M_PI);   // log(sqrt(2*pi))
double loglikelihood(
                double *par        // position in parameter space
                #ifdef CALCULATE_SUPREMA
                ,double logLstar     // log-Likelihood constraint
                #endif
                )
{   double gamma28 = Ead*(Qatp2/Qdntm8);
    double gamma213 = Ead*(Qatp2/Qdntm13);
    double gamma219 = Ead*(Qatp2/Qdntm19);
    double gamma98= Ead*(Qatp9/Qdntm8);
    double gamma913 = Ead*(Qatp9/Qdntm13);
    double gamma919 = Ead*(Qatp9/Qdntm19);
    double gamma108 = Ead*(Qatm10/Qdntm8);
    double gamma1013 = Ead*(Qatm10/Qdntm13);
    double gamma1019 = Ead*(Qatm10/Qdntm19);


    unsigned int i;             // running indeces
    double logL = 0;            // logarithm of the likelihood, initialize with 0
    double negLogLx2;           // 2 times the negative of log likelihood
    static double logWt;        // weight
    double e, GG, GR, RR;       // part of the exponent in likelihood
    long double fun;            // function value
    double *tau, *dat, *wt;
    double sigma;
    #ifdef CALCULATE_SUPREMA
    double negLogLx2max;        // maximum value of negLogLx2 imposed by logLstar constraint
    #endif
```

Figure A.13: exemplary likelihood function used for the quantum yield network analysis page 1. This likelihood function is used by the nested sampling algorithm throughout the parameter optimization. The exemplary function shown here would be used to calculate γ factors for a network of $t-10$ $t+2$ $t+9$ and $nt-8$ $nt-13$ $nt-19$.

```
// --- calculate (constant) normalization factor for the first run
    if (firstrun)
        {
        logWt = 0;
        }

    #ifdef CALCULATE_SUPREMA
    negLogLx2max = -2*(logLstar - logWt);       // maximum value of negLogLx allowed in order to be above
    logLstar
    #endif



    // --- calculate likelihood without normalization factor ---
    negLogLx2 = 0.0;

  double de = 0.00;
  double cr = 0.03;
  sigma = 1;

    GG = tm10m8[0];
    RR = tm10m8[1];
    GR = tm10m8[2];
    fun = (GR-de*RR-cr*GG+gamma108*GG)/(GR-de*RR-cr*GG+gamma108*GG+RR);
    e = (S1-fun)/sigma;
    negLogLx2 += e*e;

    GG = tm10m13[0];
    RR = tm10m13[1];
    GR = tm10m13[2];
    fun = (GR-de*RR-cr*GG+gamma1013*GG)/(GR-de*RR-cr*GG+gamma1013*GG+RR);
    e = (S1-fun)/sigma;
    negLogLx2 += e*e;

    GG = tm10m19[0];
    RR = tm10m19[1];
    GR = tm10m19[2];
    fun = (GR-de*RR-cr*GG+gamma1019*GG)/(GR-de*RR-cr*GG+gamma1019*GG+RR);
    e = (S1-fun)/sigma;
    negLogLx2 += e*e;

    GG = tp2m8[0];
    RR = tp2m8[1];
    GR = tp2m8[2];
    fun = (GR-de*RR-cr*GG+gamma28*GG)/(GR-de*RR-cr*GG+gamma28*GG+RR);
    e = (S1-fun)/sigma;
    negLogLx2 += e*e;

    GG = tp2m13[0];
    RR = tp2m13[1];
    GR = tp2m13[2];
    fun = (GR-de*RR-cr*GG+gamma213*GG)/(GR-de*RR-cr*GG+gamma213*GG+RR) ;
    e = (S1-fun)/sigma;
    negLogLx2 += e*e;
```

Figure A.14: exemplary likelihood function used for the quantum yield network analysis page 2

```
    GG = tp2m19[0];
    RR = tp2m19[1];
    GR = tp2m19[2];
    fun = (GR-de*RR-cr*GG+gamma219*GG)/(GR-de*RR-cr*GG+gamma219*GG+RR);
    e = (S1-fun)/sigma;
    negLogLx2 += e*e;

    GG = tp9m8[0];
    RR = tp9m8[1];
    GR = tp9m8[2];
    fun = (GR-de*RR-cr*GG+gamma98*GG)/(GR-de*RR-cr*GG+gamma98*GG+RR);
    e = (S1-fun)/sigma;
    negLogLx2 += e*e;

    GG = tp9m13[0];
    RR = tp9m13[1];
    GR = tp9m13[2];
    fun = (GR-de*RR-cr*GG+gamma913*GG)/(GR-de*RR-cr*GG+gamma913*GG+RR);
    e = (S1-fun)/sigma;
    negLogLx2 += e*e;

    GG = tp9m19[0];
    RR = tp9m19[1];
    GR = tp9m19[2];
    fun = (GR-de*RR-cr*GG+gamma919*GG)/(GR-de*RR-cr*GG+gamma919*GG+RR);
    e = (S1-fun)/sigma;
    negLogLx2 += e*e;


        logL += (logWt - 0.5*negLogLx2);      // normalize

    return(logL);   // return the likelihood
}
```

Figure A.15: exemplary likelihood function used for the quantum yield network analysis page 3

A.5 In gel burst analysis 600 mM NaCl

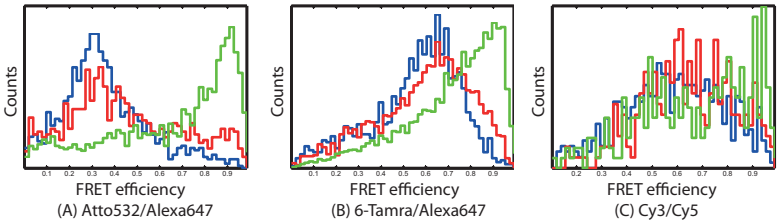

Figure A.16: Hairpin DNA measurements at $600mM$ NaCl in a PAA gel. Measurements were performed above (blue), below (green) and beneath (red) the point of maximum countrate.

Acknowledgement

First of all I want to thank my advisor Prof. Dr. Jens Michaelis for the possibility to do my PhD thesis in his group. Thanks for always having an open door and providing the perfect framework for scientific research. You made work in your group a real pleasure.
I also thank Prof. Dr. Christoph Bräuchle who provided big parts of the infrastructure and Prof. Dr. Don C. Lamb. It was great to have direct access to the expertise of three research groups at once.
In this context my thanks go to all members of these three groups for creating the friendly atmosphere we work in. It was a great help to have people around that always took the time to help with problems or answer questions.
Thank you Adam for answering all my stupid questions and for providing the nested sampling algorithm.
Without the help of Bärbel and Moni none of the nucleosome experiments would have been possible. The same holds for the PolII experiments where I was glad to have the support of Julia and Asia. It was great to have access to the readily prepared samples, thank you so much for all the time you invested.
Thank you Jochen for providing a second brain when complex problems had to be structured and thank you Christian for a great time in Illinois. Niko, thanks for all the help and the great time since the 7th grade.
Furthermore I would like to thank my Bachelor students Anders and Anna-Lena as well as my "F-Praktikant" Christoph and my collaboration partners Clemens, Daniel and Joseph for their contribution to the success of this work.
Finally I thank my parents for their overwhelming support and last but not least Eva for sharing all the good and not so good times of this PhD as my better half.

MMT mean-macro-time

TDS time deviation signal

MFD multiparameter fluorescence detection

PIFE protein induced fluorescence enhancement

PIE pulsed interleaved excitation

FRET förster resonance energy transfer

NPS nano-positioning-system

RT room temperature

PolII RNA polymerase II

BME 2-Mercaptoethanol

DTT Dithiothreitol

RR red detection after red excitation

GG green detection after green excitation

GR red detection after green excitation

bp base pair

nt non-template strand

t template strand

FCS fluorescence correlation spectroscopy

GGxGG green autocorrelation

GGdxGGd green autocorrelation donor only sample

GRxGG FRET green cross correlation

GRxGR FRET autocorrelation

RRxRR red autocorrelation

cr spectral crosstalk

de direct excitation of the acceptor

E FRET efficiency

Sto stoichiometry

IRF instrument response function

QY quantum yield

PSF point spread function

PBS polarizing beam-splitter

PDA probability distribution analysis

DOPC 1,2-Dioleoyl-sn-glycero-3-phosphocholine

PEG polyethylene glycol

remodeler chromatin remodeling factor

HF high FRET

LF low FRET

MF medium FRET

NFR nucleosome free region

PAA poly-acrylamide

FWHM full width half maximum

smFRET single molecule FRET

Bibliography

[1] M. Alilat, Sivolob, B. Revet, and A Prunell. Nucleosome dynamics. protein and dna contributions in the chiral transition of the tetrasome, the histone (h3-h4)2 tetramer-dna particle. *J Mol Biol*, 291(4):815–841., 1999.

[2] Joanna Andrecka. *Single molecule fluorescence studies of the RNA polymerase II elongation complex*. PhD thesis, Ludwig-Maximilians-Universität München, 2009.

[3] Joanna Andrecka, Robert Lewis, Florian Brückner, Elisabeth Lehmann, Patrick Cramer, and Jens Michaelis. Single-molecule tracking of mrna exiting from rna polymerase ii. *PNAS*, 105(1): 135–140, 2008.

[4] Joanna Andrecka, Barbara Treutlein, Maria Angeles Izquierdo Arcusa, Adam Muschielok, Robert Lewis, Alan C. M. Cheung, Patrick Cramer, and Jens Michaelis. Nano positioning system reveals the course of upstream and nontemplate dna within the rna polymerase ii elongation complex. *Nucleic Acids Research*, 37(17):5803–5809, 2009.

[5] M. Antonik, S. Felekyan, A. Gaiduk, and C. A. Seidel. Separating structural heterogeneities from stochastic variations in fluorescence resonance energy transfer distributions via photon distribution analysis. *J Phys Chem B*, 110(13):6970–8, 2006.

[6] F. Asturias, G. Meredith, C. Poglitsch, and R. Kornberg. Two

conformations of rna polymerase ii revealed by electron crystallography. *J. Mol. Biol.*, 272:536–540, 1997.

[7] Thomas Bayes. An essay towards solving a problem in the doctrine of chances. *Philosophical Transactions of the Royal Society of London*, 53:330–418, 1763.

[8] T. R. Blosser, J. G. Yang, M. D. Stone, G. J. Narlikar, and X. Zhuang. Dynamics of nucleosome remodelling by individual acf complexes. *Nature*, 462(7276):1022–7, 2009.

[9] Clemens Bönisch, Katrin Schneider, Sebastian Pünzeler, Sonja M. Wiedemann, Christina Bielmeier, Marco Bocola, H. Christian Eberl, Wolfgang Kügel, Jürgen Neumann, Elisabeth Kremmer, Heinrich Leonhardt, Matthias Mann, Jens Michaelis, Lothar Schermelleh, and Sandra B. Hake. H2a.z.2.2 is an alternatively spliced histone h2a.z variant that causes severe nucleosome destabilization. *Nucleic Acids Research*, online: doi: 10.1093/nar/gks267, 2012. doi: 10.1093/nar/gks267.

[10] G. Bonnet, O. Krichevsky, and A. Libchaber. Kinetics of conformational fluctuations in dna hairpin-loops. *Proc Natl Acad Sci U S A*, 95(15):8602–6, 1998.

[11] J. E. Bronson, J. Fei, J. M. Hofman, Jr. Gonzalez, R. L., and C. H. Wiggins. Learning rates and states from biophysical time series: a bayesian approach to model selection and single-molecule fret data. *Biophys J*, 97(12):3196–205, 2009.

[12] C. Bräuchle, D.C. Lamb, and J. Michaelis. *Single Particle Tracking and Single Molecule Energy Transfer*. Wiley-VCH Verlag, 2010.

[13] Cedric R. Clapier and Bradley R. Cairns. The biology of chromatin remodeling complexes. *Annual Review of Biochemistry*, 78 (1):273–304, 2009.

[14] Nadine Collins, Raymond A. Poot, Iwao Kukimoto, Custodia Garcia-Jimenez, Graham Dellaire, and Patrick D. Varga-Weisz. An acf1-iswi chromatin-remodeling complex is required for

dna replication through heterochromatin. *Nat Genet*, 32(4):627–632, 2002. doi: 10.1038/ng1046.

[15] Davide F. V Corona, Giorgia Siriaco, Jennifer A Armstrong, Natalia Snarskaya, Stephanie A McClymont, Matthew P Scott, and John W Tamkun. Iswi regulates higher-order chromatin structure and histone h1 assembly in vivo. *PLoS Biol*, 5(9):e232, 08 2007. doi: 10.1371/journal.pbio.0050232.

[16] P. Cramer, K.-J. Armache, S. Baumli, S. Benkert, F. Brueckner, C. Buchen, G.E. Damsma, S. Dengl, S.R. Geiger, A.J. Jasiak, A. Jawhari, S. Jennebach, T. Kamenski, H. Kettenberger, C.-D. Kuhn, E. Lehmann, K. Leike, J.F. Sydow, and A. Vannini. Structure of eukaryotic rna polymerases. *Annual Review of Biophysics*, 37(1):337–352, 2008. doi: 10.1146/annurev.biophys.37.032807.130008.

[17] R.E. Dale, J. Eisinger, and W.E. Blumberg. The orientational freedom of molecular probes. the orientation factor in intramolecular energy transfer. *Biophysical Journal*, 26:161–193, 1979.

[18] S.A. Darst, A.M. Edwards, E.W. Kubalek, and R.D. Kornberg. Three-dimensional structure of yeast rna polymerase ii at 16Å resolution. *Cell*, 66:121–128, 1991.

[19] Sylvain Daujat, Thomas Weiss, Fabio Mohn, Ulrike C Lange, Céline Ziegler-Birling, Ulrike Zeissler, Michael Lappe, Dirk Schübeler, Maria-Elena Torres-Padilla, and Robert Schneider. H3k64 trimethylation marks heterochromatin and is dynamically remodeled during developmental reprogramming. *Nature Structural & Molecular Biology*, 16:777–781, 2009.

[20] S. de la Escalera, M.A. Nieto, and E. Palacián. Preparation and structural characterization of nucleosomal core particles lacking one h2a.h2b dimer. *Biochem Biophys Res Commun*, 157(2):541–547, 1988.

[21] Pieter L. DeHaseth and John D. Helmann. Open complex formation by escherichia coli rna polymerase: the mechanism of polymerase-induced strand separation of double helical dna. *Molecular Biology*, 16(5):817–824, 2006.

[22] C. Eggeling, J. R. Fries, L. Brand, R. GÃ$\frac{1}{4}$nther, and C. A. M. Seidel. Monitoring conformational dynamics of a single molecule by selective fluorescence spectroscopy. *Proceedings of the National Academy of Sciences*, 95(4):1556–1561, 1998.

[23] J. Enderlein, D. Robbins, W. Ambrose, P. Goodwin, and R. Keller. The statistics of single molecule detection: an overview. *Bioimaging*, 5(3):88–98, 1997.

[24] Josef H. Exler. *Nuclearархitecture and structural dynamics - molecular basis ofchr omatin remodeling induced by human iswi machines -*. PhD thesis, Universität Regensburg, 2010.

[25] Gary Felsenfeld and Mark Groudine. Controlling the double helix. *Nature*, 421(6921):448–453, 2003. doi: 10.1038/nature01411.

[26] Theodor Förster. Zwischenmolekulare energiewanderung und fluoreszenz. *Annalen Der Physik*, 437:55–75, 1948.

[27] J. J. Furth, Jerard Hurwitz, and Monika Goldmann. The directing role of dna in rna synthesis. *Biochemical and Biophysical Research communications*, 4(5):362–367, 1961.

[28] A. Gansen, K. Toth, N. Schwarz, and J. Langowski. Structural variability of nucleosomes detected by single-pair forster resonance energy transfer: histone acetylation, sequence variation, and salt effects. *J Phys Chem B*, 113(9):2604–2613, 2009.

[29] A. Gansen, A. Valeri, F. Hauger, S. Felekyan, S. Kalinin, K. Toth, J. Langowski, and C. A. Seidel. Nucleosome disassembly intermediates characterized by single-molecule fret. *Proc Natl Acad Sci U S A*, 106(36):15308–13, 2009.

[30] Alexander Gansen, Florian Hauger, Katalin Täth, and Jörg Langowski. Single-pair fluorescence resonance energy transfer of nucleosomes in free diffusion: Optimizing stability and resolution of subpopulations. *Analytical Biochemistry*, 368(2):193 – 204, 2007. doi: 10.1016/j.ab.2007.04.047.

[31] Thierry Gautier, D. Wade Abbott, Annie Molla, Andre Verdel, Juan Ausio, and Stefan Dimitrov. Histone variant h2abbd confers lower stability to the nucleosome. *EMBO Rep*, 5(7):715–720, 2004.

[32] E. Peter Geiduschek, Tokumsa Nakamoto, and Samuel B. Weiss. The enzymatic synthesis of rna: Complementary interaction with dna. *PNAS*, 47(9):1405–1415, 1961.

[33] Dina Grohmann, Julia Nagy, Anirban Chakraborty, Daniel Klose, Daniel Fielden, Richard H. Ebright, Jens Michaelis, and Finn Werner. The initiation factor tfe a nd the elongation factor spt4/5 compete f or the rnap clamp during transcription initiation and elongation. *Molecular Cell*, 43:263–274, 2011.

[34] B. Guillemette and L. Gaudreau. Reuniting the contrasting functions of h2a.z. *Biochemistry and Cell Biology*, 84(4):528–535, 2006. doi: 10.1139/o06-077.

[35] K. Gurunathan and M. Levitus. Single-molecule fluorescence studies of nucleosome dynamics. *Curr Pharm Biotechnol*, 10(5): 559–68, 2009.

[36] Kaushik Gurunathan and Marcia Levitus. Fret fluctuation spectroscopy of diffusing biopolymers: Contributions of conformational dynamics and translational diffusion. *The Journal of Physical Chemistry B*, 114(2):980–986, 2009. doi: 10.1021/jp907390n.

[37] T.J. Ha, T. Enderle, D. Ogletree, D. Chemla, P. Selvin, and S. Weiss. Probing the interaction between two single molecules: fluorescence resonance energy transfer between a single donor and a single acceptor. *Proceedings of the National Academy of Sciences*, 93(13):6264, 1996.

[38] Sandra B. Hake, Benjamin A. Garcia, Elizabeth M. Duncan, Monika Kauer, Graham Dellaire, Jeffrey Shabanowitz, David P. Bazett-Jones, C. David Allis, and Donald F. Hunt. Expression patterns and post-translational modifications associated with mammalian histone h3 variants. *Journal of Biological Chemistry*, 281(1):559–568, 2006. doi: 10.1074/jbc.M509266200.

[39] Xi He, Hua-Ying Fan, Joseph D. Garlick, and Robert E. Kingston. Diverse regulation of snf2h chromatin remodeling by noncatalytic subunits. *Biochemistry*, 47(27):7025–7033, 2008. doi: 10.1021/bi702304p. PMID: 18553938.

[40] T. Hirschfeld. Optical microscopic observation of single small molecules. *Appl. Opt.*, 15(12):2965–2966, 1976.

[41] Matthias Höller. *Advanced Fluorescence Fluctuation Spectroscopy with Pulsed Interleaved Excitation*. PhD thesis, Ludwig-Maximil ians-Universität München, 2011.

[42] Armin Hoffmann, Daniel Nettels, Jennifer Clark, Alessandro Borgia, Sheena E. Radford, Jane Clarke, and Benjamin Schuler. Quantifying heterogeneity and conformational dynamics from single molecule fret of diffusing molecules: recurrence analysis of single particles (rasp). *Physical Chemistry Chemical Physics*, 13: 1857–1871, 2011.

[43] S. Hohng, T. J. Wilson, E. Tan, R. M. Clegg, D. M. Lilley, and T. Ha. Conformational flexibility of four-way junctions in rna. *J Mol Biol*, 336(1):69–79, 2004.

[44] T. Hugel, J. Michaelis, C. L. Hetherington, P. J. Jardine, S. Grimes, J. M. Walter, W. Falk, D. L. Anderson, and C. Bustamante. Experimental test of connector rotation during dna packaging into bacteriophage phi29 capsids. *PLoS Biol*, 5(3): e59, 2007.

[45] Helen Hwang, Hajin Kim, and Sua Myong. Protein induced fluorescence enhancement as a single molecule assay with short

distance sensitivity. *Proceedings of the National Academy of Sciences*, 108(18):7414–7418, 2011.

[46] C. A. M. Seidel J. Widengren. Manipulation and characterization of photo-induced transient states of merocyanine 540 by fluorescence correlation spectroscopy. *Phys. Chem. Chem. Phys.*, 2:3435 – 3441, 2000.

[47] Harold Jeffreys. *Theory of probability*. Clarendon Press, Oxford, 1939.

[48] J. Jung and A. Van Orden. A three-state mechanism for dna hairpin folding characterized by multiparameter fluorescence fluctuation spectroscopy. *J Am Chem Soc*, 128(4):1240–9, 2006.

[49] J. Jung, R. Ihly, E. Scott, M. Yu, and A. Van Orden. Probing the complete folding trajectory of a dna hairpin using dual beam fluorescence fluctuation spectroscopy. *J Phys Chem B*, 112(1): 127–33, 2008.

[50] S. Kalinin, S. Felekyan, M. Antonik, and C. A. Seidel. Probability distribution analysis of single-molecule fluorescence anisotropy and resonance energy transfer. *J Phys Chem B*, 111 (34):10253–62, 2007.

[51] S. Kalinin, A. Valeri, M. Antonik, S. Felekyan, and C. A. Seidel. Detection of structural dynamics by fret: A photon distribution and fluorescence lifetime analysis of systems with multiple states. *J Phys Chem B*, 114(23):7983–7995, 2010.

[52] Stanislav Kalinin, Suren Felekyan, Alessandro Valeri, and Claus A. M. Seidel. Characterizing multiple molecular states in single-molecule multiparameter fluorescence detection by probability distribution analysis. *The Journal of Physical Chemistry B*, 112(28): 8361–8374, 2008. doi: 10.1021/jp711942q.

[53] A. N. Kapanidis, N. K. Lee, T. A. Laurence, S. Doose, E. Margeat, and S. Weiss. Fluorescence-aided molecule sorting: analysis of structure and interactions by alternating-laser

excitation of single molecules. *Proc Natl Acad Sci U S A*, 101(24): 8936–41, 2004.

[54] L. Kastrup, H. Blom, C. Eggeling, and S. W. Hell. Fluorescence fluctuation spectroscopy in subdiffraction focal volumes. *Phys. Rev. Lett.*, 94(17):178104, 2005.

[55] H. Kettenberger, K.-J. Armache, and P. Cramer. Complete rna polymerase ii elongation complex structure and its interactions with ntp and tfiis. *Mol. Cell*, 16:955–965, 2004.

[56] Sepideh Khorasanizadeh. The nucleosome: From genomic organization to genomic regulation. *Cell*, 116(2):259–272, 2004.

[57] W. J. Koopmans, A. Brehm, C. Logie, T. Schmidt, and J. van Noort. Single-pair fret microscopy reveals mononucleosome dynamics. *J Fluoresc*, 17(6):785–95, 2007.

[58] Roger D. Kornberg. Chromatin structure: A repeating unit of histones and dna. *Science*, 184(4139):868–871, 1974. doi: 10.1126/science.184.4139.868.

[59] Masanori Koshioka, Keiji Sasaki, and Hiroshi Masuhara. Time-dependent fluorescence depolarization analysis in three-dimensional microspectroscopy. *Appl. Spectrosc.*, 49(2):224–228, 1995.

[60] V Kudryavtsev. *Development and applications of new fluorescence techniques to characterize single biomolecules in solution and living cells*. PhD thesis, Universität Düsseldorf, 2006.

[61] W. Kuegel, A. Muschielok, and J. Michaelis. Bayesian inference based fcs analysis and single molecule burst analysis reveal the influence of dye selection on dna hairpin dynamics. *ChemPhysChem*, 13(4):1013–1022, 2012. doi: 10.1002/cphc.201100720.

[62] Dexter D. L. A theory of sensitized luminescence in solids. *J. Chem. Phys.*, 21:836–850, 1953.

[63] Philip D. Laible, Robert S. Knox, and Thomas G. Owens. Detailed balance in förster-dexter excitation transfer and its application to photosynthesis. *The Journal of Physical Chemistry B*, 102 (9):1641–1648, 1998. doi: 10.1021/jp9730104.

[64] Joseph R. Lakowicz. *Plrinziples of Fluorescence Spectroscopy*. Kluwer Academic/Plenum Publishers, New York, 1999.

[65] N. K. Lee, A. N. Kapanidis, Y. Wang, X. Michalet, J. Mukhopadhyay, R. H. Ebright, and S. Weiss. Accurate fret measurements within single diffusing biomolecules using alternating-laser excitation. *Biophys J*, 88(4):2939–53, 2005.

[66] Benjamin G. Levine, John E. Stone, and Axel Kohlmeyer. Fast analysis of molecular dynamics trajectories with graphics processing units–radial distribution function histogramming. *Journal of Computational Physics*, 230(9):3556–3569, 2011.

[67] Gu Li and Jonathan Widom. Nucleosomes facilitate their own invasion. *Nat Struct Mol Biol*, 11(8):763–769, 2004. 10.1038/nsmb801.

[68] S. Liu, G. Bokinsky, N. G. Walter, and X. Zhuang. Dissecting the multistep reaction pathway of an rna enzyme by single-molecule kinetic "fingerprinting". *Proc Natl Acad Sci U S A*, 104 (31):12634–9, 2007.

[69] Weiguo Liu, B. Schmidt, G. Voss, A. Schroder, and W. Muller-Wittig. Bio-sequence database scanning on a gpu. In *Parallel and Distributed Processing Symposium*, page 8 pp., 2006.

[70] P. T. Lowary and J. Widom. New dna sequence rules for high affinity binding to histone octamer and sequence-directed nucleosome positioning. *J. Mol. Biol.*, 276(1):19–42, 1998.

[71] Karolin Luger, Armin W. Mader, Robin K. Richmond, David F. Sargent, and Timothy J. Richmond. Crystal structure of the nucleosome core particle at 2.8[thinsp]a resolution. *Nature*, 389 (6648):251–260, 1997.

[72] Alexandra Lusser and James T Kadonaga. Strategies for the reconstitution of chromatin. *Nature Methods*, 1(1):19–26, 2004.

[73] D. Magde, E. L. Elson, and W. W. Webb. Fluorescence correlation spectroscopy. ii. an experimental realization. *Biopolymers*, 13(1):29–61, 1974.

[74] Douglas Magde, Elliot Elson, and W. W. Webb. Thermo dynamic fluctuations in a reacting system - measurement by fluorescence correlation spectroscopy. *Phys. Rev.Lett.*, 29(11):705–708, 1972.

[75] K. Mapa, M. Sikor, V. Kudryavtsev, K. Waegemann, S. Kalinin, C. A. Seidel, W. Neupert, D. C. Lamb, and D. Mokranjac. The conformational dynamics of the mitochondrial hsp70 chaperone. *Mol Cell*, 38(1):89–100, 2010.

[76] P. Maragakis, F. Ritort, C. Bustamante, M. Karplus, and G. E. Crooks. Bayesian estimates of free energies from nonequilibrium work data in the presence of instrument noise. *J Chem Phys*, 129(2):024102, 2008.

[77] S. A. Marras, F. R. Kramer, and S. Tyagi. Efficiencies of fluorescence resonance energy transfer and contact-mediated quenching in oligonucleotide probes. *Nucleic Acids Res*, 30(21):e122, 2002.

[78] Salvatore A. E. Marras, Fred Russell Kramer, and Sanjay Tyagi. Efficiencies of fluorescence resonance energy transfer and contact mediated quenching in oligonucleotide probes. *Nucleic Acids Research*, 30(21):e122, 2002. doi: 10.1093/nar/gnf121.

[79] X. Michalet, S. Weiss, and M. Jager. Single-molecule fluorescence studies of protein folding and conformational dynamics. *Chem Rev*, 106(5):1785–813, 2006.

[80] Marvin Minsky. Microscopy apparatus, 1961.

[81] W. E. Moerner and L. Kador. Optical detection and spectroscopy of single molecules in a solid. *Phys. Rev. Lett.*, 62: 2535–2538, May 1989. doi: 10.1103/PhysRevLett.62.2535.

[82] Tanmoy Mondal, Markus Rasmussen, Gaurav Kumar Pandey, Anders Isaksson, and Chandrasekhar Kanduri. Characterization of the rna content of chromatin. *Genome Research*, 20(7): 899–907, 2010. doi: 10.1101/gr.103473.109.

[83] Violette Morales and Helene Richard-Foy. Role of histone n-terminal tails and their acetylation in nucleosome dynamics. *Mol Cell Biol.*, 20(19):7230–7237, 2000.

[84] B. K. Muller, E. Zaychikov, C. Brauchle, and D. C. Lamb. Pulsed interleaved excitation. *Biophys J*, 89(5):3508–22, 2005.

[85] A. Muschielok and J. Michaelis. Application of the nanopositioning system to the analysis of fluorescence resonance energy transfer networks. *J Phys Chem B*, 115 (41):11927–11937, 2011.

[86] A. Muschielok, J. Andrecka, A. Jawhari, F. Bruckner, P. Cramer, and J. Michaelis. A nano-positioning system for macromolecular structural analysis. *Nat Methods*, 5(11):965–71, 2008.

[87] Adam Marek Muschielok. *Development and Application of a Quantitative Analysis Method for Fluorescence Resonance Energy Transfer Localization Experiments*. PhD thesis, Ludwig-Maximilians-Universität München, 2011.

[88] D. Nettels, I. V. Gopich, A. Hoffmann, and B. Schuler. Ultrafast dynamics of protein collapse from single-molecule photon statistics. *Proc Natl Acad Sci U S A*, 104(8):2655–60, 2007.

[89] Heinz Neumann, Susan M. Hancock, Ruth Buning, Andrew Routh, Lynda Chapman, Joanna Somers, Tom Owen-Hughes, John van Noort, Daniela Rhodes, and Jason W. Chin. A method for genetically installing site-specific acetylation in recombinant histones defines the effects of h3 k56 acetylation. *Molecular Cell*, 36(1):153 – 163, 2009. doi: 10.1016/j.molcel.2009.07.027.

[90] E. Nir, X. Michalet, K. M. Hamadani, T. A. Laurence, D. Neuhauser, Y. Kovchegov, and S. Weiss. Shot-noise limited single-molecule fret histograms: comparison between theory and experiments. *J Phys Chem B*, 110(44):22103–24, 2006.

[91] Lukas Novotny and Bert Hecht. *Principles of nano-optics*. Cambridge University Press, 2006.

[92] B. Okumus and T. Ha. Real-time observation of g-quadruplex dynamics using single-molecule fret microscopy. *Methods Mol Biol*, 608:81–96, 2010.

[93] D.E. Olins and A.L. Olins. Chromatin history: our view from the bridge. *Nat Rev Mol Cell Biol*, 4(10):809–814, 2003.

[94] A. V. Orden and J. Jung. Review fluorescence correlation spectroscopy for probing the kinetics and mechanisms of dna hairpin formation. *Biopolymers*, 89(1):1–16, 2008.

[95] G Orphanides, T Lagrange, and D Reinberg. The general transcription factors of rna polymerase ii. *Genes Dev.*, 10:2657–2683, 1996.

[96] M. Orrit and J. Bernard. Single pentacene molecules detected by fluorescence excitation in a *p* -terphenyl crystal. *Phys. Rev. Lett.*, 65:2716–2719, Nov 1990. doi: 10.1103/PhysRevLett.65.2716.

[97] N. Panchuk-Voloshina, R.P. Haugland, J. Bishop-Stewart, M.K. Bhalgat, P.J. Millard, F. Mao, W.Y. Leung, and R.P. Haugland. Alexa dyes, a series of new fluorescent dyes that yield exceptionally bright, photostable conjugates. *J Histochem Cytochem.*, Sep;47(9):1179–88, 1999.

[98] Young-Jun Park, Pamela N. Dyer, David J. Tremethick, and Karolin Luger. A new fluorescence resonance energy transfer approach demonstrates that the histone variant h2az stabilizes the histone octamer within the nucleosome. *The Journal of Biological Chemistry*, 23(4):24270–24282, 2004.

[99] F. Perrin. Mouvement brownien d'un ellipsoide-i. dispersion diélectrique pour des molécules ellipsoidales. *Journal de Physique et le Radium*, 5(10):497–811, 1934.

[100] F. Perrin. Mouvement brownien d'un ellipsoide (ii). rotation libre et dépolarisation des fluo-rescences. translation et diffusion de molécules ellipsoidales. *Journal de Physique et le Radium*, 7(1): 1–11, 1936.

[101] Raymond A. Poot, Ludmila Bozhenok, Debbie L. C. van den Berg, Soren Steffensen, Fernando Ferreira, Margaret Grimaldi, Nick Gilbert, Joao Ferreira, and Patrick D. Varga-Weisz. The williams syndrome transcription factor interacts with pcna to target chromatin remodelling by iswi to replication foci. *Nat Cell Biol*, 6(12):1236–1244, 2004. 10.1038/ncb1196.

[102] E. S. Price, M. S. DeVore, and C. K. Johnson. Detecting intramolecular dynamics and multiple forster resonance energy transfer states by fluorescence correlation spectroscopy. *J Phys Chem B*, 114(17):5895–902, 2010.

[103] Lisa R. Racki, Janet G. Yang, Nariman Naber, Peretz D. Partensky, Ashley Acevedo, Thomas J. Purcell, Roger Cooke, Yifan Cheng, and Geeta J. Narlikar. The chromatin remodeller acf acts as a dimeric motor to space nucleosomes. *Nature*, 462(7276): 1016–1021, 2009. doi: 10.1038/nature08621.

[104] L.R. Racki and G.J. Narlikar. Atp-dependent chromatin remodeling enzymes: two heads are not better, just different. *Curr Opin Genet Dev*, 18:137–144, 2008.

[105] P. J. J. Robinson and D Rhodes. Structure of the '30 nm' chromatin fibre: a key role for the linker histone. *Curr Opin Struct Biol*, 16 (3):336–343, 2006.

[106] B. Rotman. Measurement of activity of single molecules of -d-galactosidase. *Proceedings of the National Academy of Sciences of the United States of America*, 47(12):1981, 1961.

[107] R. Roy, S. Hohng, and T. Ha. A practical guide to single-molecule fret. *Nature Methods*, 5:507–516, 2008.

[108] Matthew E. Sanborn, Brian K. Connolly, Kaushik Gurunathan, and Marcia Levitus. Fluorescence properties and photophysics of the sulfoindocyanine cy3 linked covalently to dna. *The Journal of Physical Chemistry B*, 111(37):11064–11074, 2007. doi: 10.1021/jp072912u.

[109] Y. Santoso, C. M. Joyce, O. Potapova, L. Le Reste, J. Hohlbein, J. P. Torella, N. D. Grindley, and A. N. Kapanidis. Conformational transitions in dna polymerase i revealed by single-molecule fret. *Proc Natl Acad Sci U S A*, 107(2):715–20, 2010.

[110] Yusdi Santoso and Achillefs N. Kapanidis. Probing biomolecular structures and dynamics of single molecules using in-gel alternating-laser excitation. *Analytical Chemistry*, 81(23):9561–9570, 2009. doi: 10.1021/ac901423e. PMID: 19863108.

[111] J. Schaffer, A. Volkmer, C. Eggeling, V. Subramaniam, G. Striker, and C. A. M. Seidel. Identification of single molecules in aqueous solution by time-resolved fluorescence anisotropy. *The Journal of Physical Chemistry A*, 103(3):331–336, 1999. doi: 10.1021/jp9833597.

[112] T. Schalc h, S. Duda, D.F. Sargent, and T. J. Richmond. X-ray structure of a tetranucleosome and its implications for the chromatin fibre. *Nature*, 436(7047):138–141, 2005.

[113] Martin Sikor. *Single-molecule fluorescence studies of Protein Folding and Molecular Chaperones*. PhD thesis, Ludwig-Maximilians-Universität München, 2012.

[114] Matthew D. Simon, Feixia Chu, Lisa R. Racki, Cecile C. de la Cruz, Alma L. Burlingame, Barbara Panning, Geeta J. Narlikar, and Kevan M. Shokat. The site-specific installation of methyllysine analogs into recombinant histones. *Cell*, 128(5):1003–1012, 2007.

[115] S. Sindbert, S. Kalinin, H. Nguyen, A. Kienzler, L. Clima, W. Bannwarth, B. Appel, S. Muller, and C. A. Seidel. Accurate distance determination of nucleic acids via forster resonance energy transfer: implications of dye linker length and rigidity. *J Am Chem Soc*, 133(8):2463–80, 2011.

[116] Devinderjit Sivia. *Data Analysis, 2nd edition*. Oxford University Press, USA, 2006.

[117] John Skilling. Nested sampling for general bayesian computation. *Bayesian Analysis*, 1, 2006.

[118] Carlas S. Smith, Nikolai Joseph, Bernd Rieger, and Keith A. Lidke. Fast, single-molecule localization that achieves theoretically minimum uncertainty. *Nat Meth*, 7(5):373–375, 2010. doi: 10.1038/nmeth.1449.

[119] John E. Stone, David J. Hardy, Ivan S. Ufimtsev, and Klaus Schulten. Gpu-accelerated molecular modeling coming of age. *Journal of Molecular Graphics and Modelling*, 29(2):116–125, 2010.

[120] M. D. Stone, M. Mihalusova, M. O'Connor C, R. Prathapam, K. Collins, and X. Zhuang. Stepwise protein-mediated rna folding directs assembly of telomerase ribonucleoprotein. *Nature*, 446(7134):458–61, 2007.

[121] E. Tan, T. J. Wilson, M. K. Nahas, R. M. Clegg, D. M. Lilley, and T. Ha. A four-way junction accelerates hairpin ribozyme folding via a discrete intermediate. *Proc Natl Acad Sci U S A*, 100(16):9308–13, 2003.

[122] A Thastrom, P.T Lowary, H.R Widlund, H Cao, M Kubista, and J Widom. Sequence motifs and free energies of selected natural and non-natural nucleosome positioning dna sequences. *Journal of Molecular Biology*, 288(2):213 – 229, 1999. doi: 10.1006/jmbi.1999.2686.

[123] Susanne Till and Andreas G. Ladurner. Rna pol iv plays catch with argonaute 4. *Cell*, 131(4):643–645, 2007.

[124] M. Tomschik, H. Zheng, K. van Holde, J. Zlatanova, and S. H. Leuba. Fast, long-range, reversible conformational fluctuations in nucleosomes revealed by single-pair fluorescence resonance energy transfer. *Proc Natl Acad Sci U S A*, 102(9):3278–83, 2005.

[125] T. Torres and M. Levitus. Measuring conformational dynamics: a new fcs-fret approach. *J Phys Chem B*, 111(25):7392–400, 2007.

[126] B. Treutlein, A. Muschielok, J. Andrecka, A. Jawhari, C. Buchen, D. Kostrewa, F. Hög, P. Cramer, and J. Michaelis. Dynamic architecture of a minimal rna polymerase ii open promoter complex. *Molecular Cell*, 46:1–11, 2012. doi: 10.1016/j.molcel.2012.02.008.

[127] P Török and T Wilson. Rigorous theory for axial resolution in confocal microscopes. *Optics Communications*, 137(1-3):127 – 135, 1997. ISSN 0030-4018. doi: 10.1016/S0030-4018(96)00771-7.

[128] Jay R. Unruh, Giridharan Gokulrangan, G. H. Lushington, Carey K. Johnson, and George S. Wilson. Orientational dynamics and dye-dna interactions in a dye-labeled dna aptamer. *Biophysical Journal*, 88(5):3455–3465, 2005.

[129] R. D. Vale. Myosin v motor proteins: marching stepwise towards a mechanism. *J Cell Biol*, 163(3):445–50, 2003.

[130] G. Vamosi, C. Gohlke, and R.M. Clegg. Fluorescence characteristics of 5-carboxytetramethylrhodamine linked covalently to the 5′ end of oligonucleotides: multiple conformers of single-stranded and doubl e-stranded dye-dna complexes. *Biophys J*, 71:972–994, 1996.

[131] M. Wahl, I. Gregor, M. Patting, and J. Enderlein. Fast calculation of fluorescence correlation data with asynchronous time-correlated single-photon counting. *Opt Express*, 11(26):3583–91, 2003.

[132] M. I. Wallace, L. Ying, S. Balasubramanian, and D. Klenerman. Non-arrhenius kinetics for the loop closure of a dna hairpin. *Proc Natl Acad Sci U S A*, 98(10):5584–9, 2001.

[133] S. Weiss. Measuring conformational dynamics of biomolecules by single molecule fluorescence spectroscopy. *Nat Struct Biol*, 7 (9):724–9, 2000.

[134] J. Widengren, R. Rigler, and Ü. Mets. Triplet-state monitoring by fluorescence correlation spectroscopy. *Journal of Fluorescence*, 4(3):255–258, 1994.

[135] Roy S. Wu and William M. Bonner. Separation of basal histone synthesis from s-phase histone synthesis in dividing cells. *Cell*, 27(2):321–330, 1981.

[136] Joanna Wysocka, Tomek Swigut, Hua Xiao, Thomas A. Milneand So Yeon Kwon, Joe Landry, Monika Kauer, Alan J. Tackett, Brian T. Chait, Paul Badenhorst, Carl Wu, and C. David Allis. A phd finger of nurf couples histone h3 lysine 4 trimethylation with chromatin remodelling. *Nature*, 442:86–90, 2006.

[137] Kazuhiro Yamada, Timothy D. Frouws, Brigitte Angst, Daniel J. Fitzgerald, Carl DeLuca, Kyoko Schimmele, David F. Sargent, and Timothy J. Richmond. Structure and mechanism of the chromatin remodelling factor isw1a. *Nature*, 472:448–453, 2011.

[138] J. G. Yang, T. S. Madrid, E. Sevastopoulos, and G.J. Narlikar. The chromatin-remodeling enzyme acf is an atp-dependent dna length sensor that regulates nucleosome spacing. *Nat. Struct. Mol. Biol.*, 13(12):1078–1083, 2006.

[139] Yin Ye, Yi Xiao, Wenting Wang, Qien Wang, Kurtis Yearsley, Altaf A. Wani, Qintao Yan, Jian-Xin Gao, Brandon S. Shetuni, and Sanford H. Barsky. Inhibition of expression of the chromatin remodeling gene, snf2l, selectively leads to dna damage, growth inhibition, and cancer cell death. *Molecular Cancer Research*, 7(12):1984–1999, 2009.

[140] Xiaowei Zhuang, Laura E. Bartley, Hazen P. Babcock, Rick Russell, Taekjip Ha, Daniel Herschlag, and Steven Chu. A single-molecule study of rna catalysis and folding. *Science*, 288(5473): 2048–2051, 2000.

[141] Xiaowei Zhuang, Harold Kim, Miguel J. B. Pereira, Hazen P. Babcock, Nils G. Walter, and Steven Chu. Correlating structural dynamics and function in single ribozyme molecules. *Science*, 296(5572):1473–1476, 2002.

[142] J. Zlatanova, T. C. Bishop, J.-M. Victor, V. Jackson, and K. van-Holde. The nucleosome family: dynamic and growing. *Structure*, 17(2):160–171, 2009.

[143] Martin Zofall, Jim Persinger, Stefan R. Kassabov, and Blaine Bartholomew. Chromatin remodeling by isw2 and swi/snf requires dna translocation inside the nucleosome. *Nat Struct Mol Biol*, 13(4):339–346, 2006. doi: 10.1038/nsmb1071.